DEENAPANRAY, P N K

ELECTRICAL CHARACTERISATION OF PLASMA PROCESSING INDUCED DEFECTS IN SILICON

MSc UP 1997

Electrical characterisation of plasma processing induced defects in silicon

by

P.N.K. Deenapanray

Submitted in partial fulfillment of the requirements for the degree

MSc (Physics)

in the

Faculty of Science (Department of Physics)

University of Pretoria

Pretoria

July 1997

SUMMARY

Electrical characterisation of plasma processing induced defects in silicon

by

P.N.K. Deenapanray

Promoter : Professor F.D. Auret

Co-promoter : Professor G. Myburg

MSc (Physics) - Department of Physics

Plasma processing techniques have become vital for the fabrication of sub-micron size semiconductor devices. For instance, sputter deposition is used during metallization steps for the deposition of refractory metals and the stoichiometric deposition of alloys. Plasma or dry etching is used for the transfer of patterns onto semiconductors with sub-micron line-width resolution. Sputter deposition and sputter etching make use of low energy noble gas ions (0.2-2 keV), which impinge on the exposed substrate during processing to create damage in the semiconductor lattice. The defects thus produced modify the electrical, optical and structural properties of the semiconductor and of devices fabricated thereon. The extent of the property modifications depends critically on the plasma parameters, such as plasma operation mode (dc or rf), etch rate, pressure and power, amongst others. In order to avoid the deleterious effects of these defects or to use them to engineer the semiconductor properties during processing, it is essential to know the electrical, optical and structural properties of the defects. This exercise also leads to process optimisation. Finally, the annealing properties of the processing-induced defects must be known so that they can be removed, if required, by in-situ or post-processing high temperature treatments.

Sputter deposition of TiW and Au contacts on n-Si introduced electrically active defects in the substrate. The barrier height of the Schottky diodes were lower than those of control diodes fabricated by resistive evaporation. Furthermore, the barrier height of the sputter deposited diodes decreased with decreasing plasma pressure, suggesting that more donor-type defects are introduced with decreasing pressure. Sputter etching in an Ar plasma also introduced several electrically active defects in n-Si. The amount of damage was found to increase with decreasing plasma pressure. Donor-type defects, responsible for the degraded quality of the diodes fabricated on the etched surfaces by resistive evaporation, were found to be confined close to the metal-semiconductor interface. Acceptor-type defects caused a reduction in the free carrier concentration of the semiconductor to depths much larger than the theoretical range of the low energy Ar ions. This suggests that some defects migrate away from the region where they are produced during processing.

The amount of residual damage was observed to decrease with increasing etch time up to 6 min, and thereafter increased. For relatively low etch periods of time, defect accumulation dominates over their removal by physical sputtering. Etching for more than 6 min is speculated to introduce extended defects or amorphize the near surface region. Isochronal annealing studies showed that most of the defects could be removed by annealing above 500 °C. However, a prominent secondary defect which was stable at 650 °C was introduced during annealing.

Low energy noble gas ion bombardment created different defects compared to 5.4 MeV alpha-particle irradiation of n-Si. This has been explained by considering the energy loss mechanisms of the ions in these energy ranges. It is shown that large vacancy clusters and non-radiative recombination centres are produced during the low energy noble gas ion bombardment of n-Si.

OPSOMMING

Elektriese karakterisering van plasma-prosessering geïnduseerde defekte in silikon

deur

P.N.K. Deenapanray

Studieleier : **Professor F.D. Auret**

Mede-studieleier : **Professor G. Myburg**

Plasma-prosesseringstegnieke se belangrikheid in die vervaardiging van submikron grootte halfgeleier gebaseerde komponente het met verloop van tyd onmiskenbaar toegeneem. Voorbeelde hiervan is die opdamping van oorgangsmetale met behulp van verstuiwing en die stoichiometriese opdamping van legerings. Plasma of droë etsing word weer vir die oordra van patrone, met submikron lynwydtes, op halfgeleiers gebruik. Opdamping en etsing met behulp van verstuiwing maak gebruik van lae energie edelgas-ione (0.2-2keV), wat tydens prosesering op die substraat gerig word. Hierdie energieke ione rig, bo en behalwe die opdamp- en etsfunksies, ook skade aan die kristalrooster van die halfgeleiermateriaal aan. Die defekte wat sodoende geskep word, modifiseer die elektriese, optiese en strukturele eienskappe van die halfgeleiermateriaal en dus ook die komponente wat daarop vervaardig word. Die mate waartoe hierdie eienskappe gemodifiseer word, hang sterk van die plasmaparameters af, soos byvoorbeeld die tipe intreedrywing (gs of rf), etstempo, druk en drywing. Kennis van hierdie defekte se elektriese, optiese en strukturele eienskappe is van die uiterste belang om die negatiewe effekte daarvan te vermy, of om hulle positief aan te wend om tydens prosessering die eienskappe van die halfgeleiermateriaal kunsmatig te verander. Hierdie oefening lei ook tot prosesoptimering. Laastens is dit ook belangrik om die uitgloei-karakteristieke van proses-geïnduseerde defekte te ken, sodat indien nodig, hulle deur 'n finale hoë temperatuur hittebehandeling verwyder kan word.

Verstuiwing van TiW- en Au-kontakte op n-Si het elektries-aktiewe defekte in die substraat tot gevolg, met verlaagde walhoogtes van Schottky-diodes wat op hierdie wyse vervaardig is, teenoor kontrole diodes wat met behulp van weerstandsverdamping vervaardig is. Verder verlaag die walhoogtes van die verstuifde diodes met afname in plasmadruk, wat suggereer dat meer skenkertipe defekte geskep word, soos die plasmadruk afneem. Etsing deur vertuiwing in 'n Ar-plasma skep ook verskeie elektries-aktiewe defekte in n-Si. Daar is gevind dat die hoeveelheid skade toeneem met afname in plasmadruk. Daar is ook gevind dat die skenker-tipe defekte, wat verantwoordelik is vir die degradering van die kwalitiet van diodes wat met behulp van weerstandsverdamping op verstuifde oppervlakke vervaardig is, beperk is tot die nabye gebied van die metaal-halfgeleierintervlak. Ontvangertipe defekte het 'n afname in die vrydraerdigtheid tot gevolg gehad en wel tot op dieptes dieper as die teoreties voorspelde reikwydtes van lae energie Ar-ione. Dit suggereer dat sommige defekte weg migreer vanaf die gebied waar hulle tydens prosessering geskep is.

Daar is gevind dat die hoeveelheid oorgeblewe skade afneem met toename in etstyd tot en met 6 minute en daarna neem dit weer toe. Vir relatiewe kort etsperiodes domineer die akkumulasie van defekte bo die verwydering daarvan deur verstuiwing. Daar word gespekuleer dat tydens etsperiodes langer as 6 minute, uitgebreide defekte geskep word of dat die naby-oppervlakgebied geamorfiseer word. Isokroniese uitgloei-studies het aangetoon dat die meeste van die defekte deur uitgloeiing bo 500°C verwyder kan word. Daarenteen is 'n prominente sekondêre defek tydens genoemde uitgloeiing geskep, wat stabiel was by 650°C.

Lae energie edelgas-ioon bombardering skep defekte verskillend van die wat deur 5.4 MeV alfapartikel bestraling in n-Si geskep word. Dit kan verklaar word deur energie-verliesmeganismes van die ione in hierdie energiegebiede. Daar is aangetoon dat groot saamgegroepeerde leë roosterruimtes en nie-stralingsherkombinasie sentrums deur die bombardering van n-Si met lae energie edelgas-ione, veroorsaak word.

To Mama and Papa

ACKNOWLEDGEMENTS

I am indebted to Prof. F.D. Auret for having given me his full support, in the capacity of being my supervisor as well as a friend, during the course of my study. I am also grateful to him for the many stimulating discussions that we have had and for supporting my trips to international conferences and to work at other South African institutions.

I am thankful to Prof. G. Myburg for both his technical and supervising assistance. His guidance concerning the properties of metal-semiconductor contacts has been most valuable.

I thank Walter E. Meyer for his tremendous help with the instrumentation part of this study and for his support when I first joined Prof. Auret's group.

I am also grateful to Pierre de Villiers for all his help, especially concerning the making of my posters at times when I most needed it.

Prof. J.B. Malherbe and Prof. D.J. Brink are acknowledged for their help regarding low energy noble gas ion bombardments and PL measurements, respectively.

I am most grateful to Dr. C. Schutte for making the Universal Sputtering Machine at DETEK available for my experiments. The technical assistance of C. du Toit, M. Le Roux and W. Engelbrecht are kindly acknowledged. The staff at DETEK is thanked for their warm welcome during my many visits.

I am grateful to the University of Pretoria for awarding me Research Assistantship and a Tuition Fee Scholarship, without which I would not have been able to undertake this study. The financial assistance of the Carl and Emily Fuchs Institute for Microelectronics (UP) and the Institude of Applied Materials (UP) are warmly acknowledged.

I take this opportunity to thank Dr. M.C. Ridgway (ANU) for introducing me to the field of Electronic Materials Engineering and for his continuous support since 1992. I also thank him for the fruitful collaboration that we have had over the past 18 months.

I am most grateful to the Auret family for all their support and kindness.

I would finally like to express my sincere gratitude to the tremendous support that I have obtained from Anneloes Smitsman. She has, in fact, been the main driving force to make me finish this work on schedule.

TABLE OF CONTENTS

CHAPTER 1

INTRODUCTION

The interaction between microelectronics device technology and the control of defects has been strong since the first transistor. It has been known for a very long time that, under suitable conditions, defects and impurities can modify in a positive way the properties of semiconductor materials. The immense and unparalled development of this technology together with the thrive for ULSI require that the density of defects within the critical volume of a device be contained reciprocally to a minimum, lest the ineffectiveness of the device. Consequently, defects induced in semiconductor materials during growth and subsequent device fabrication steps such as, ion implantation and plasma-related processing, are now mostly considered to be undesirable. However, the great progress in the understanding and control of point defects over the past three decades has led to the new field of defect engineering, wherein knowledge about defects is used to improve and even modify the properties of materials. Any successful application of defect engineering through the reproducible and controlled introduction of defects to tailor the properties of semiconductors requires the following information to be known:

i) The defect's atomic and electronic configurations are needed for the positive identification of the defect and the basic understanding of its properties.
ii) The defect's electrical levels in the forbidden gap in the semiconductor material.
iii) The defect's formation mechanisms and introduction rates.
iv) The defect's diffusion mechanisms and rates are required to understand its interaction with impurities in the semiconductor lattice.
v) An understanding of the influence of process parameters on the concentrations of defects, which invariably leads to process optimization, is needed. For instance, the concentrationss of defects introduced during ion implantation must be established as a function of irradiation fluence, dose rate, ion energy and implant temperature.
vi) The annealing behaviour of the defect in order to learn about its removal rate through high temperature treatments. Annealing studies also yield valuable information about secondary defects which could form during any subsequent high temperature processing of the semiconductor material.

Plasma-based processes are routinely used for submicron size device fabrication. For example, sputter deposition is used during metallisation for the stoichiometric deposition of compounds and refractory metals on semiconductors. Compared to conventional deposition techniques, such as resistive evaporation, it offers the possibility of metallisation at highly controlled rates and yields better metal adhesion to the substrate. Furthermore, dry etching techniques such as ion beam or sputter etching and reactive ion etching are preferred over traditional wet etching techniques because of their ability to provide fine line definition and highly directional or anisotropic etching. These attributes of plasma etching are used for the faithful transfer of patterns to semiconductors with submicron scale resolution. Modern industrial plasma reactors now offer the possibility for the combined etching of semiconductors prior to sputter deposition of metal contacts without breaking vacuum. However, these plasma-related processes are not "defect-free". During sputter deposition and sputter etching, noble gas ions and neutral atoms with energies typically between 0.5-1 keV impinge on the semiconductor surface to create lattice damage. Further damage can be produced by low energy electrons and electromagnetic energy in the form of X-rays and ultaviolet light, and in the case of sputter deposition, also by target metal atoms interacting with the exposed semiconductor.

In order to understand the effect of these processes on the properties of semiconductors, and therefore on the properties of devices fabricated thereon, the characteristics of the plasma processing-induced defects have to be established. Since no single technique can be used to fully characterize any defect, one has to rely on the use of a set of complimentary characterization techniques. For instance, magnetic resonance techniques such as electron paramagnetic resonance (EPR) and optically detected magnetic resonance (ODMR) are used to study the structure of defects, photoluminescence (PL) to investigate their optical properties, and junction spectroscopy including deep level transient spectroscopy (DLTS) are used to extract the electrical properties of defects. Each of these techniques can be used in conjunction with annealing experiments. However, by matching the electronic properties of an unknown defect to one of which the structure is known, or by correlating their annealing behaviours, DLTS can be used to shed light on the structure of defects. The properties of devices fabricated on the plasma-processed semiconductors can also be used to monitor the type and extent of the damage. Furthermore, the effects of

different plasma parameters on device properties can be used to achieve process optimization.

In this dissertation a comprehensive study of the electronic properties of defects introduced in silicon during sputter deposition of metal contacts and sputter etching in an argon plasma was compiled, using DLTS. Optimization of the two plasma processes were also investigated by monitoring the changes in electrical properties of Schottky barrier diodes (SBDs) using current-voltage (I-V) and capacitance-voltage (C-V) measurements. In order to learn more about the structure of these defects, their electronic properties were correlated to those of defects formed during high energy (MeV) alpha-particle, electron and proton irradiation of the same substrates. Furthermore, to establish whether any of the plasma processing-induced (PPI) defects could be noble gas species-related, their electronic properties were compared to the defects created by low energy (1 keV) noble gas ion bombardment of the same materials. The annealing behaviours of the PPI and low energy noble gas ion created defects was also investigated. Finally, a discussion is made on the effects of some low energy noble gas ion implantation parameters on optically active defects in n-Si.

Chapters 2 and 3 discuss the fundamentals of plasma physics and introduce the principles of sputter deposition and sputter etching, respectively. The essential theoretical background on metal-semiconductor contacts and experimental techniques are provided in Chapters 4 and 5. The experimental procedures and results are discussed in Chapters 6 and 7, respectively. Chapter 8 summarises the general conclusions.

CHAPTER 2

FUNDAMENTALS OF PLASMA

The fabrication of complex integrated circuits (ICs) utilizing CMOS and bipolar silicon technologies requires a sequence of 9-13 individual mask steps to complete the process. The need for submicron line width resolution during pattern transfer onto semiconductors together with the need for anisotropic etching of masking layers and the deposition of stoichiometric compounds for interconnects have made plasma-based processes vital technologies in microelectronics device fabrication. Since the physics of a plasma are complex and beyond the scope of this study, no attempt is made here to be comprehensive. This chapter aims at providing the necessary information concerning the plasma state and its generation, and discusses the fundamentals of particle interaction in a plasma.

2.1 The Plasma State

A plasma, often called the fourth state of matter, is a gas containing charged and neutral species, including some or all of the following particles: electrons, positive ions, negative ions, atoms and molecules. Though a plasma is on average electrically neutral, the individual densities of positive and negative charges may be quite high. Because electrons have a much higher mobility, any surface in contact with the plasma will develop a floating potential, $-V_f$, with respect to the plasma. Plasmas are initiated and maintained by applying an electric potential (dc or ac or a combination of both) across the neutral gas. However, there is no distinct phase change in going from a neutral gas to the plasma state. In steady state, the rate of ionization must be equal to the rate at which charged particles are lost from the plasma volume through recombination and diffusion or convection to the boundary. An important parameter of a plasma is the degree of ionization, which is the fraction of the original neutral species which have become ionized. Process or cold plasmas are weaky ionized (10^{-6} - 10^{-4}) and neutral species dominate their behaviour [1]. On the other hand, interstellar plasmas can be characterised as being fully ionized with a degree of ionization approaching unity. Plasmas generated by an electric discharge are also referred to as

glow discharges and the terms will be used interchangeably. In a weakly ionized plasma with electron densities between 10^9 - 10^{12} cm^{-3}, the temperature of electrons ranges from 10^3 K to 10^5 K, while neutrals have temperatures approaching 500 K.

2.2 Generating a Plasma

The plasmas considered here are generated by electric fields which are produced by either direct current (dc) or alternating current (ac) power supplies. Typical excitation ac frequencies are 100 kHz, at the low end of the spectrum, 13.56 MHz in the radio frequency (rf) range and 2.45 GHz in the microwave region. The initiation of a plasma will be considered using a parallel plate or planar reactor. The geometry of other types of reactors and plasmas formed therein are discussed elsewhere [2,3]. When a glow discharge is initiated after breakdown, it does not completely cover the cathode surface. It operates at near constant voltage in this regime, called the normal discharge, with the current increasing as the cathode coverage increases. Eventually, the glow expands to cover the whole cathode surface and a further increase in power causes both current and voltage to increase. This is called the abnormal glow. The important characteristic of a plasma is that free electrons are created by ionization and secondary electron generation from ion impact of surfaces. When the plasma power is sufficiently high to heat the cathode, thermionic emission may become the dominant electron generation process.

2.2.1 DC Glow Discharge

The initiation of a dc glow discharge follows the breakdown of the neutral gas. Consider the schematic of a low pressure Ar discharge prior to breakdown as illustrated in Figure 2.1. The resistance of the Ar is much greater than that of the ballast resistor R, so the entire voltage V_{dc}, is dropped across the electrodes, a distance d, apart. An electron created by photodesorption at the cathode is accelerated through the electric field $E = V_{dc}/d$, towards the anode and ionizes Ar atoms through inelastic collisions. The resulting electrons also gain kinetic energy in the electric field and cause further ionization. Townsend's first ionization coefficient α, denoting the probability per unit length that ionization will occur, is used to describe the net ionization probability, including losses. Furthermore, Ar ions strike the cathode when

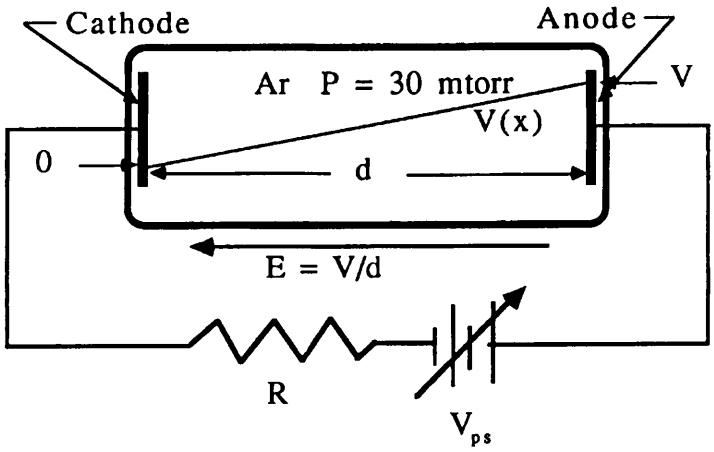

Figure 2.1: Schematic of an Ar discharge prior to breakdown. The entire voltage is dropped across the tube because the impedance of the Ar is much higher than that of the ballast resistor R (ref [1]).

accelerated by the electric field and secondary electrons are emitted with an emission probability γ. The secondary electrons in turn gain energy and create more ionization. Consequently, the number of electrons increases exponentially and the ionization process can be characterized by an Avalanche breakdown. The breakdown voltage $V_B = E_B/d$ can be expressed as:

$$V_B = A(Pd)/\left(C + \ln(Pd)\right), \qquad (2.1)$$

where A and C are constants which depend on the gas and P is the gas pressure. A graph of the breakdown condition for Ar is shown in Figure 2.2. The minimum breakdown voltage is called the Paschen minimum.

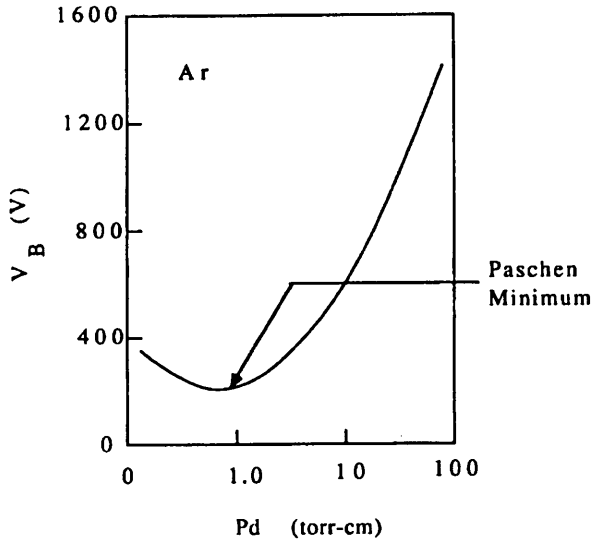

Figure 2.2: Plot of the minimum breakdown voltage for Ar as a function of the product of the Ar pressure, P, and spacing, d, of the electrodes (ref [1]).

The plasma geometry is such that after breakdown the plasma particles rearrange themselves in a self-consistent fashion which ensures that the discharge is self-sustained. Hence, the dc discharge is comprised of distinct regions which are illustrated in Figure 2.3 [4]. The potential drop across the electric discharge is not uniform [Figure 2.3(b)], but the drop in the cathode sheath region [Figure 2.3(b)] can be assumed to be linear. Ions formed in the Crooke dark space (cathode sheath) and negative glow regions are accelerated by the cathode electric field towards the cathode

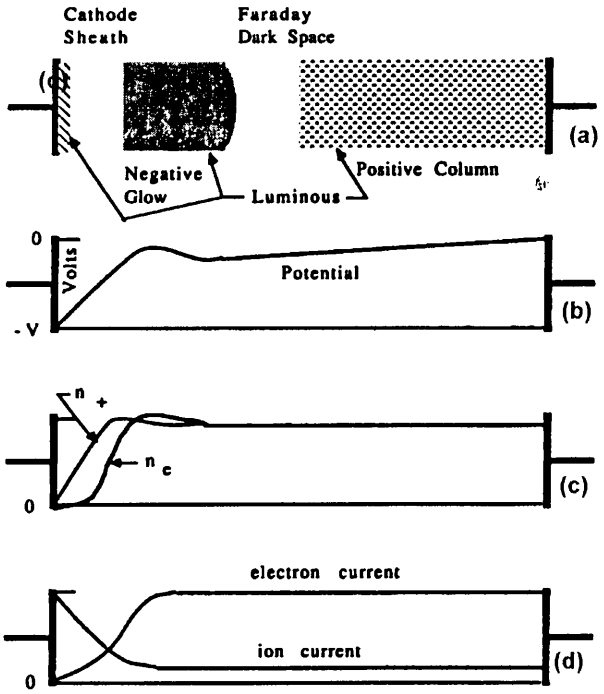

Figure 2.3: After breakdown, the discharge arranges itself into characteristic regions to provide for particle and energy input. Most of the potential is dropped across the cathode sheath region, which contains ions but very few electrons. There are almost equal number of ions and electrons in the negative glow, Faraday dark space and positive column (ref [1]).

where they cause secondary electron emission and sputtering [Figures 2.3(c) and 2.3(d)]]. The secondary electrons are accelerated back across the cathode sheath and cause ionization, either directly or by transferring energy to electrons in the plasma. Additionally, a dc glow discharge may have another dark space beyond the negative glow (Faraday dark space) and a positive column. In these regions, electrons are excited by the local electric field, which results in a balance between ionization and losses of charged particles. When the positive column is present, it serves to connect the anode electrically to the remainder of the discharge [5]. In dc discharge plasmas, the floating potential, V_f, is usually a few volts.

2.2.2 RF Glow Discharge

In a dc glow discharge, only 10 % of the power is stored in the negative glow from secondary electrons being accelerated in the cathode sheath region owing to the very low secondary electron coefficient. This feature makes the dc glow a rather inefficient plasma reactor. Furthermore, the cathode must be at least partially conducting so that the plasma can be sustained through the emission of secondary electrons. The use of an ac power source can overcome these shotcomings of the dc plasma.

The ac glow discharge is ignited by applying a large enough potential to cause breakdown. The plasma is self-sustained by electrons oscillating in the alternating electric field and causing ionization. Under equilibrium conditions the rate of loss of charged plasma particles must be equal to the rate at which they are generated. The ac plasma has the same configuration as the one depicted in Figure 2.3(a). In order to highlight the specific properties of the ac plasma, the electrodes of the planar reactor will be assumed to be insulated. When a very low frequency ac power supply is connected to the electrodes, the reactor behaves like a parallel plate capacitor that is charged in alternate directions by the plasma particles (Figure 2.4). If the frequency of the ac supply is increased to the point where the charging time is much longer than the period of the ac signal (50 - 100 kHz), a current flows in the plasma for the entire ac cycle. New phenomena start to appear as the frequency of the supply exceeds 1 MHz.

Since most commercial plasma reactors, including the Leybold-Haraeus Universal Sputtering Machine used in this study, are designed to operate at the internationally assigned frequency of 13.56 MHz [6,7], the salient features of high frequency plasmas will be discussed at this nominal frequency. Due to their high inertia, ions, such as Ar^+, do not respond to the rf electric field in the sheath regions at an excitation frequency of 13.56 MHz. Only the lighter electrons respond to the electric fields and owing to their higher mobilities, significant time-average dc biases occur at the electrodes. The dc voltage developed at the anode is called the plasma voltage, V_p, and the negative dc potential at the cathode with respect to the discharge is called the dc self-bias, V_{dc}. It will be shown below that the self-bias voltage can be a few hundred volts in reactors having a non-symmetric planar electrode configuration.

2.2.2.1 Self Bias and Plasma Potential

Consider the discharge system with one small electrode connected to an rf power source through a coupling capacitor and an impedance matching unit illustrated in Figure 2.4(a) [top]. Because of the much higher electron mobility, any given positive

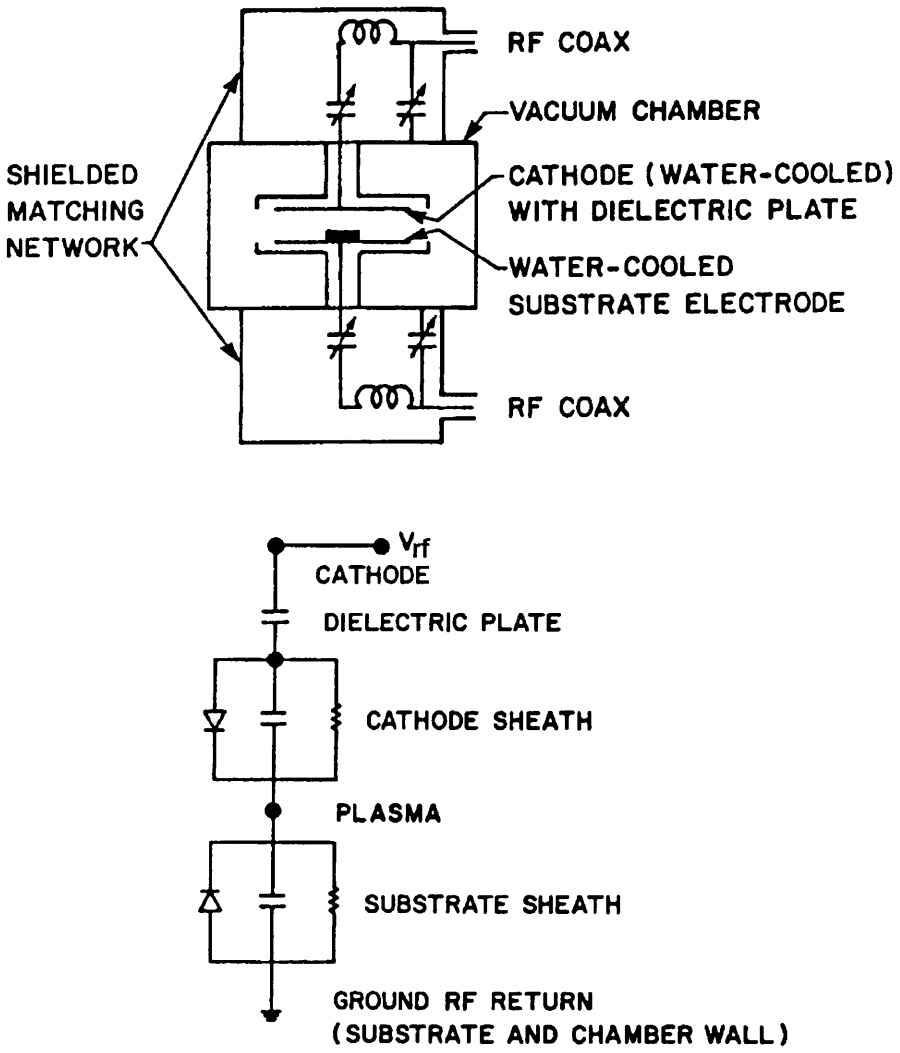

Figure 2.4: Schematic of a typical parallel plate reactor with an rf matching network (top). The bottom drawing illustrates the equivalent circuit of the rf planar reactor and shows that the anode and cathode regions can be modelled as blocking diodes (ref [1]).

voltage will result in a much larger electron current than the ion current flowing for the same negative voltage. Consequently, the anode and cathode sheath regions can be equivalently described as having rectifying properties [Figure 2.4(b)-bottom]. The importance of the self bias voltage on the smaller electrode can be best demonstrated by considering a square wave voltage, V_1, which is applied across the plasma. Figure 2.5 illustrates the square wave signal together with the discharge voltage V_2. The shaded areas represent the electron and positive ion (Ar^+) currents during alternate cycles of the square waveform. Initially, the potential V_1 is dropped across the plasma and the coupling capacitor is charged through the effective resistance of the plasma by the electron current. The discharge voltage V_2 decays fast because of the relatively high electron current. During the following half cycle of the square wave, the voltage drop across the plasma drops instantaneously by $-2V_1$, after which it decays with a longer time constant associated with the smaller Ar^+ current. Eventually, the time-average electron and Ar-ion current become equal in magnitude as time-average dc potentials develop on the electrodes [8]. Figure 2.6 shows the time variation of the plasma potential with the self bias voltage on the small electrode. It is seen from Figure 2.6 that even with the self bias, the small electrode is positive during part of positive half-cycles, so the time average plasma potential is usually higher than for the dc case. Massive ions (Ar^+) which cannot respond to the rf signal bombard the small electrode after being accelerated through the voltage difference between the time-average plasma potential and the time-average self bias. The magnitude of the self bias depends on the pressure of neutral particles [9]. Alternatively, it can be said that the self bias varies with the plasma pressure since the glow discharge is made up of only 1 % ionized particles. The self bias is decreased with an increase in pressure at constant rf power. This can be explained in part by the decrease in rf voltage droped across the plasma due to the decrease in plasma impedance with increase in pressure. Alternatively, the discharge does not require as high a sheath field to sustain itself, since it is speculated that at higher densities the plasma is able to put energy directly into the glow electrons through a "surf riding" effect [10]. No self bias is generated for the case of a symmetric discharge (electrodes with equal areas). The time-average plasma potential will be much larger than for the dc case and although there is no self bias, energetic ions will bombard the electrodes. If the electrodes are conducting,

these bombardments will generate secondary electrons which will help to sustain the glow discharge as is the case for dc plasmas.

2.3 Properties of Plasma Particles

In plasma processes, plasma particles and photons from the glow discharge interact with the exposed semiconductor substrate. Typically, the substrate is mounted on the cathode and the extent of the interaction depends on the energy of the plasma particles. It is, therefore, important to understand the energy distribution of these particles, especially in the cathode sheath region, and to understand the effect of changes in plasma parameters on their energy distribution. The main collisional process in a wealky ionized plasma, together with the increased ionization efficiency in a plasma when a magnetic field is superimposed on the electric discharge, are also discussed.

2.3.1 Mean Free Path of Particles in the Cathode Region

If there were no neutrals present in the dark space region, the positively charged ions, say Ar^+, would be accelerated towards the cathode through potential difference, V_k, between the plasma and the cathode. Hence, Ar ions would bombard the cathode with energy, E_m, given by:

$$E_m = eV_k \ , \qquad (2.2)$$

As mentioned earlier, the plasma is made up of mostly neutral atoms or molecules. Owing to their thermal energies, these neutrals diffuse out of the glow discharge into the cathode sheath where they interact with the positively charged ions, e.g. Ar^+. Because of their random motion, the neutral atoms collide with Ar ions causing the latter to lose kinetic energy. Charge transfer may also take place during these collisions. The energy with which the ions reach the substrate is dictated by their mean free path between collision with Ar atoms. Since the mean free path is inversely proportional to the density of the neutral particles for weakly ionized glow discharges [11], the kinetic energy of the bombarding Ar ions is decreased with increasing plasma pressure. Eq. (2.2), therefore, gives the maximum energy of an ion reaching the cathode. Furthermore, the mean free path between collision of the neutral particles

is also decreased with an increase in plasma pressure, so that they too will impinge the cathode with reduced energy.

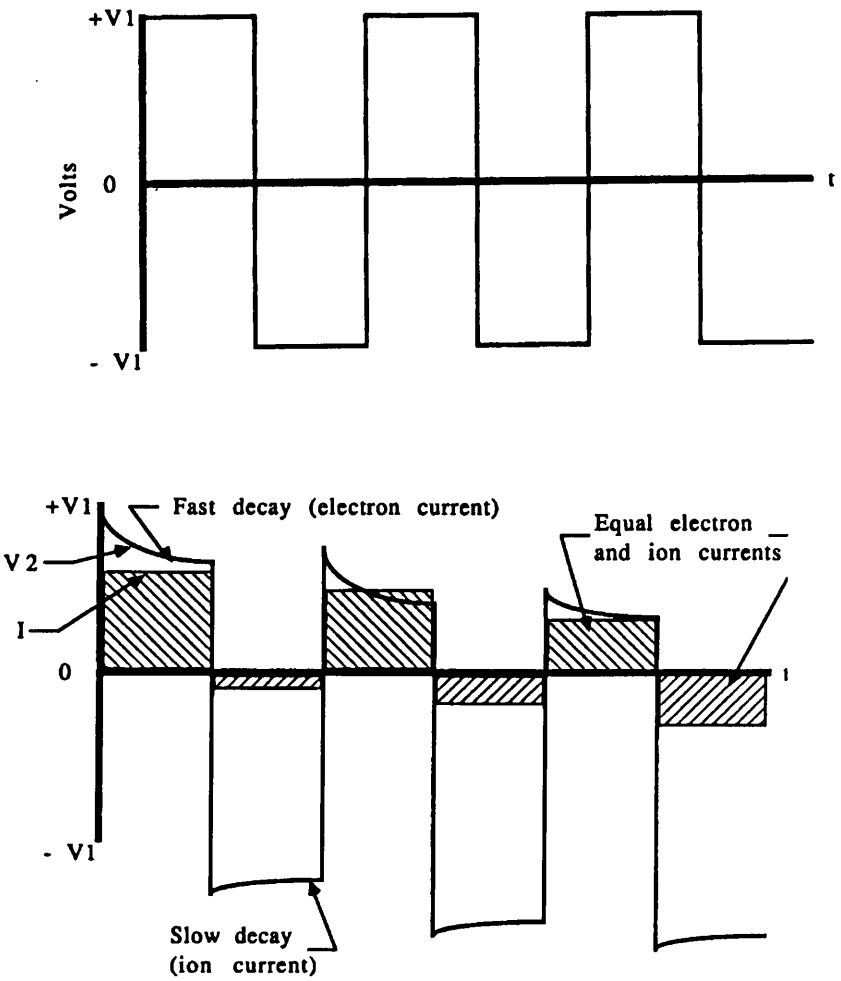

Figure 2.5: Output square wave of peak V_1 which is used for the circuit shown in Figure 2.4(a) [top]. Behaviour of the discharge voltage V_2, [bottom] as the self bias develops to produce equal electron and ion currents. On each half cycle, the current decays as the capacitor charges from the plasma. On the half cycle where electron current flows, the decay is faster because the plasma has an effectively lower impedance owing to the greater mobility of the electrons (ref [1]).

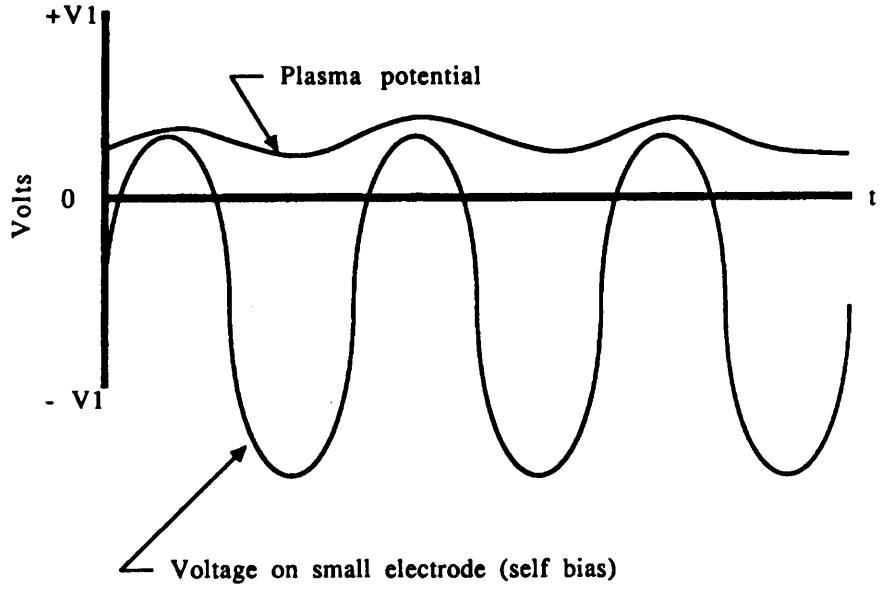

Figure 2.6: Time variation of the plasma potential shown with the self bias voltage on the small electrode. In the absence of collisions in the sheath, the ion energy at the small electrode (cathode) is the difference between the average potential and average self bias (ref [1]).

2.3.2 Electron-Neutral Elastic Collisions

The dominance of electron-neutral collisions is responsible for the general character of weakly ionized glow discharges. Any collision can be described by a cross section, σ, which is a measure of the probability that the event will take place. Collisions between electrons and neutrals can be described by the "hard sphere" model for elastic collisions as illustrated in Figure 2.7. The mean free path between collisions, λ, can be expressed as:

$$\lambda = \left(N\sigma_N\right)^{-1}, \qquad (2.3)$$

where σ_N is the elastic cross-section for electron-neutral collision, which depends on the electron velocity, and N is the neutral density. For the electron-Ar system, σ_N has is a minimum when the electron energy is 1 eV and shows a maximum value at approximately 16 eV. At higher electron energies, the interaction time is shortened, so

that the cross-section for elastic collision decreases monotically. Eq. (2.3) gives the average distance travelled by an electron between collisions. If the electron velocity is v, the collision frequency, ν, is then given by:

$$\nu = N\sigma_N v \ . \qquad (2.4)$$

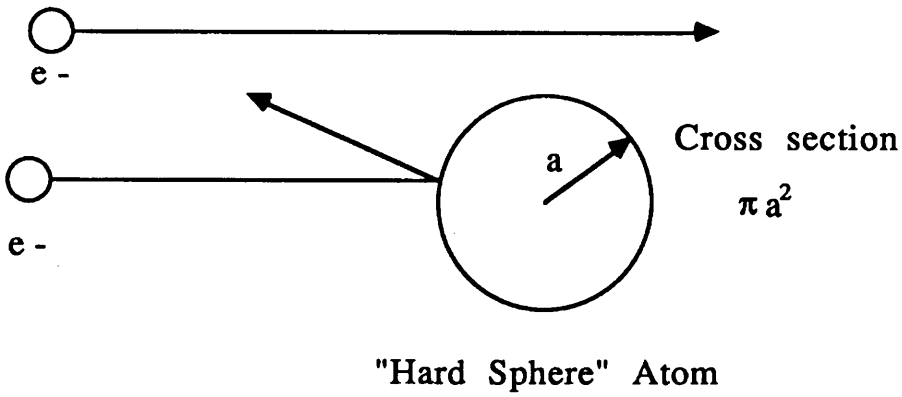

Figure 2.7: "Hard sphere" atom cross section. Electrons that approach within a distance a of the centre will undergo a collision, while those that have a larger impact parameter will not collide (ref [1]).

The average amount of energy the electron transfers to the neutral is E_t, given by [11]:

$$E_t = \frac{2m}{M} E^2 \ , \qquad (2.5)$$

where E is the electron energy, and m and M are the electron and neutral masses, respectively. In the case of an Ar plasma, $(2m/M) = 1/40{,}000$, and very little energy is transferred to the Ar atoms during the elastic collision. However, the electron experiences a significant change in its direction, and its momentum is thus altered.

An important consequence of electron-neutral collision in a dc glow discharge is that the directed energy which the electrons gather by being accelerated through the static electric field is converted into random energy. Eventually, a steady state must be reached whereby the energy gained by the electrons between collisions is equal to their energy lost during collisions. Since the energy lost is quite small, the electrons will "heat up" to a sufficiently high temperature to establish this equilibrium. The random velocities of the electrons is, therefore, much larger than the directed velocity. The small fraction of the total electron energy transferred to the neutrals implies that

the internal energy of the latter does not change significantly [12]. In the case of the ac glow discharge, an electron reaches its maximum kinetic energy when the frequency of the ac power supply, ω, is equal to the collision frequency, ν, i.e. the electron reaches a state of resonance. If $\omega << \nu$, the particles make numerous collisions during one ac cycle, which prevents them from reaching maximum energy during the ac oscillation. On the other hand, if $\omega >> \nu$, the particles undergo many oscillations between collisions, but this does not increase their energy. For a planar reactor with an electron density of 10^{10} cm^{-3} and operating at a frequency of 13.56 MHz, the wavelength of the rf power is over 20 m, whereas $\nu \approx 1$ GHz. Since the wavelength of the energy signal supplied by the power supply is much larger than the dimensions of the reactor, the rf plasma responds similarly to a dc field. This condition is described as the "near zone" [13].

2.3.3 Particle Orbits

The charged particles in a plasma will respond to electric and magnetic fields. These fields may arise from external sources or from collisions between the plasma particles. In this section, the motion of charged particles in electric and magnetic fields, and the increased ionization probability of neutrals in the presence of a magnetic field are discussed.

In the presence of an electric field **E** and magnetic field **B**, a particle of charge q and velocity **v** will experience a force **F** given by:

$$\mathbf{F} = q\mathbf{E} + q\mathbf{v} \times \mathbf{B} . \qquad (2.6)$$

For a particle of mass m, the corresponding acceleration **a** is obtained from:

$$\mathbf{F} = m\mathbf{a} . \qquad (2.7)$$

Typical particle motions in glow discharges can be illustrated by considering the following cases:

Case 1: E = constant and B = 0

From Eqs. (2.6) and (2.7), a particle will experience a constant acceleration in the direction of **E** given by:

$$\mathbf{a} = q\mathbf{E}/m \ . \qquad (2.8)$$

Case 2: E = 0 and B = constant

The magnetic force acts in a direction perpendicular to the velocity of the charged particle. The components of the nonzero particle velocity parallel and perpendicular to **B** can be defined as $v_{||}$ and $v_{\perp}$, respectively. If $v_{||} = 0$, the particle moves along a circular trajectory normal to the magnetic field with an orbital radius, also called the gyro radius, ρ, given by:

$$\rho = mv_{\perp}/qB\,, \qquad (2.9)$$

where B is the magnitude of **B**. Since the perpendicular magnetic field does not the accelerate the particle, the gyro radius can be written in terms of the kinetic energy W of the particle as:

$$\rho = (2mW)^{1/2}/qB\,. \qquad (2.10)$$

Therefore, for particles having the same energy, the heavier species will have larger circular orbits. Plasma reactors employing magnetic field, usually in a transverse direction to the electric field, are called *magnetron* systems. In magnetron-type reactors, the electrons are confined to execute circular orbits near the cathode such that their collisional interaction with neutrals is enhanced, leading to an increased ionization probability. Magnetron discharges, therefore, have a higher densities of charged particles and are preferred over dc and rf plasmas for sputter deposition and sputter etching. Heavy ions such as Ar^+ will have gyro radii much larger than the reactor size and will be largely unaffected by the magnetic field. The heavier plasma particles will in general reach the cathode in a direction perpendicular to its surface.

The frequency of rotation of a particle in a magnetic field is called the gyro frequency or cyclotron frequency, ω, and is given by:

$$\omega = 2\pi f = qB/m \ . \qquad (2.11)$$

Although the gyro radius was seen to increase with particle energy, the cyclotron frequency is independent of particle energy. An important feature of ac magnetron

reactors is that energy can be coupled directly to plasma electrons by using an ac power supply with a frequency equal to the natural rotational frequency of the electron in a magnetic field. The magnetic field has no effect on $v_{||}$ and if $v_{||} \neq 0$, the charged particle will move along a helical path. Particles with different charge signs will rotate in opposite directions.

Case 3: E and B are both constant

If **B** is parallel to **E**, it does not have any effect on the component of velocity parallel to itself and the situation is reduced to the one described in *Case 1*. If **B** is, however, perpendicular to **E**, then the particles will experience a drift velocity in a direction perpendicular to both fields, and will have a magnitude, v_{ExB}, given by:

$$v_{E\times B} = E / B . \qquad (2.12)$$

This drift will act on electrons in the cathode region of a magnetron, where the cathode electric field has a component perpendicular to the magnetic field, and the electron gyro radius is small. As stated earlier, the heavy plasma ions are not affected because their gyro radii are larger than the reactor dimensions. The gyro motion of the particles may be interrupted by collisions, in which case Eq. (2.12) is no longer valid.

Case 4: Nonuniform Fields

A time-dependent electric field will result in an acceleration which changes in space. A quantitative discussion of this case can be found in the ref. [14]. On the other hand, a nonuniform magnetic field will result in additional drift motion. A drift velocity, v_g, given by Eq. (2.13) will be produced from a field gradient. This drift velocity is perpendicular to both the magnetic field and the field gradient.

$$v_g = \left(v_\perp{}^2 / \omega\right)\left(\mathbf{B} \times \nabla\mathbf{B} / 2\mathbf{B}^2\right). \qquad (2.13)$$

The gradient drift, $\mathbf{B}\times\nabla\mathbf{B}$, depends on the particle mass, charge and velocity. Furthermore, if the magnetic field is curved, the particle will experience a drift velocity, v_c, which is perpendicular to both the field and its direction of curvature and is given by:

$$v_c = \left(v_{\parallel}^{\,2} / \omega\right)\left(\mathbf{R_c} \times \mathbf{B}\right) / \left(\mathbf{B}\mathbf{R_c}^{\,2}\right), \qquad (2.14)$$

where $\mathbf{R_c}$ is the radius of curvature of the field. The drift velocity too depends on the particle mass, charge and velocity. The magnetic field in most magnetron discharges will have both curvature and gradient, such that the drifts in Eqs. (2.13) and (2.14) will affect the electrons in the discharge, given the rate of collisions is low enough to allow the electrons to execute their gyro motion [15].

REFERENCES

[1] J.L. Cecchi, in Handbook of Plasma Processing Technology, ed. by S.M. Rossnagel, J.J. Cuomo and W.D. Westwood, Chapter 2 (Noyes Publications, New Jersey, 1990).

[2] J.M. Moran and D. Maydan, Bell System Tech. J. **58**, 1027 (1979).

[3] S. Matatsuo and Y. Adachi, Jpn. J. Appl. Phys. **21**, L4 (1982).

[4] K. Wasa and S. Hayakawa, Handbook of Sputter Deposition Technology (Noyes Publications, New Jersey, 1991), p. 85.

[5] Sanborn C. Brown, Introduction to Electrical Discharges in Gases (John Wiley and Sons, New York, 1966), p. 213.

[6] D.L. Flamm, J. Vac. Sci. Tech. **A4**, 729 (1986).

[7] J.L. Cecchi, in Handbook of Plasma Processing Technology, ed. by S.M. Rossnagel, J.J. Cuomo and W.D. Westwood (Noyes Publications, New Jersey, 1990), p. 59.

[8] H.R. Koenig and L.I. Maissel, IBM J. Res. Dev. **14**, 168 (1970).

[9] D.L. Flamm and V.M. Donnelly, Plasma Chemistry and Plasma Processing **1**, 317 (1981).

[10] M.J. Kushner, IEEE Trans. Plas. Sci. **PS-14**, 188 (1986).

[11] K. Wasa and S. Hayakawa, Handbook of Sputter Deposition Technology (Noyes Publications, New Jersey, 1991), p. 71.

[12] B. Chapman, Glow Discharge Processes (John Wiley and Sons, New York, 1980), p. 12.

[13] J.D. Jackson, Classical Electrodynamics (John Wiley and Sons, New York, 1975).

[14] Sanborn C. Brown, Introduction to Electrical Discharges in Gases (John Wiley and Sons, New York, 1966), p. 166.

[15] J.A. Thornton and A.S. Penfold, in Thin Film Processes, ed. J.L. Vossen and W. Kern (Academic, Orlando, 1978), p. 75.

CHAPTER 3

SPUTTER DEPOSITION AND SPUTTER ETCHING

The plasma-related processes investigated in this study employ low energy (0.2-1 keV) Ar ion bombardment. Three main effects resulting from ion bombardment are chemical reactions, sputtering and implantation. The deposition and etching techniques of interest here proceed through nonreactive, or physical sputtering so that plasma chemistry will not be a main focus in this chapter. However, the underlying principles behind plasma deposition and etching techniques utilizing reactive ions will be outlined. During sputter deposition, a metal target is bombarded with Ar ions and the sputtered metal atoms are deposited on the semiconductor surface through a mask. In the case of sputter etching, the energetic ions are directed onto the semiconductor surface resulting in the physical removal of the topmost atomic layers. In both processes the exposed semiconductor surface is subject to energetic plasma particles which introduce damage in the lattice. Furthermore, damage can be created by electromagnetic radiation (X-rays and UV) from the glow discharge and electrons in certain plasma reactors. Consequently, the structural, electrical and optical properties of the semiconductor are altered, and these changes are reflected in changes in the performance of devices fabricated on the processed semiconductor material. This chapter describes the physical sputtering mechanism for elemental targets, such as a Si crystal and Au, and describes the process of ion implantation induced damage by considering the nuclear energy stopping by low energy particles. A brief discussion on the structural and surface morphology changes which occur during plasma particle-semiconductor interactions is also included. The extent to which the structural, electrical and optical properties of the semiconductor is changed depends critically on the plasma conditions, that is on the ion species, ion energy, plasma pressure, and time of exposure. An attempt is made throughout the discussion to highlight the effects of these plasma parameters, especially those of changes in plasma pressure, on the various mechanisms taking place during sputter deposition and sputter etching.

3.1 The Physical Sputtering Process

In a plasma, sputtering can be effected by ions, neutral atoms, electrons and photons. Since most relevant sputtering applications are performed under bombardment with ions, this section deals with that particular process. The nonreactive or physical sputtering process can proceed via different mechanisms depending on the energy and atomic masses of the target and the bombarding ion. Sputtering using noble gas ions in the low energy regime (0.2-10 keV) of interest here can be described by binary collision events, and Sigmund's linear cascade theory can be applied [1]. Most of the extensive studies on sputtering have been conducted using ion beams whereby the beam energy and its angle of incidence on the target can be controlled. Furthermore, modern ion sources offer the possibility of controlling the beam uniformity by focusing and rastering systems. A somehow different scenario applies in the case of sputtering in a glow discharge wherein the ion energies and their directionality must be described in terms of probability functions. In addition, the effect of neutral atoms, which constitute approximately 99 % of the glow discharge (see Chapter 2), on the sputtering process cannot be measured exactly. Before the sputtering process in a glow discharge is described, the fundamental sputtering mechanism in the low energy regime together with the related sputtering parameters are discussed.

3.1.1 Mechanism of Ion Beam Sputtering and Sputter Yield

The underlying principle for sputtering in the energy regime applicable in this study, is momentum transfer between the bombarding ions and the surface atoms of the target. A threshold energy is required for an incoming ion to knock off a surface atom and cause sputtering. This threshold energy depends on the nature of the target (i.e., the surface binding energy, mass, and atomic number of the substrate atoms) and on ion species. Typically, the threshold energy, E_{th}, for elemental targets can be assumed to be equal to four times the surface binding energy, U_0, of the target matrix for most inert gases [2]. Based on a few-collision model, an analytical relation was derived for E_{th} at a not-too-oblique angle of incidence by Yamamura and Bohdansky [3]. By considering the possible collision sequences for near-threshold sputtering, they found that for small angles of incidence θ, the sputter threshold energy is given by:

$$E_{th} = \frac{U_0}{\gamma \sin^{12}\left(\frac{2\pi + \theta}{6}\right)}, \quad \text{for } M_1 \geq M_2 \tag{3.1}$$

and γ is the energy transfer factor given by:

$$\gamma = \frac{4 M_1 M_2}{(M_1 + M_2)^2}, \tag{3.2}$$

where M_1 and M_2 are the mass numbers of the incident ion and target atoms, respectively. For silicon, $U_0 = 137.9$ kcal/mol or 5.98 eV/atom [4]. When the bombarding ions have energies larger than the threshold energy for sputtering, they result in collision cascades during which the primary ions may become implanted with the ejection of target atoms through near-surface recoil collisions. Figure 3.1 illustrates the collision of a primary particle (bombarding ion) with a solid surface and the emission of secondary particles (target atoms).

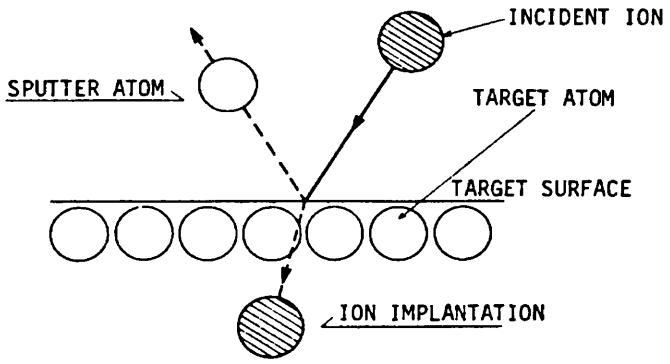

Figure 3.1: Illustration of the physical sputtering process. The energy transfer between an incident ion and a surface target atom results in the latter being "knocked-off" from the lattice, while the incident ion becomes imbedded below the target surface (Wasa and Hayakawa, in Handbook of Sputter Deposition: principles, technology and applications, (Noyes Publications, New Jersey, 1991).

The sputtering process is quantified by the sputter yield, Y, which is defined as the mean number of target atoms removed per incident ions, that is:

$$Y = \frac{\text{number of sputtered atoms}}{\text{number of incident ions}}. \tag{3.3}$$

The factors influencing the sputter yield are discussed in the next section. An important remark concerning the sputtering of a homogeneous multicomponent target can be made. At equilibrium, the composition of the sputtered flux must be stoichiometric, that is the same as the bulk composition of the target [5]. This is true even though the components of the matrix may differ significantly in their relative sputtering yields. At the onset of sputtering, the component with the higher sputtering yield is eroded faster, depleting the target surface of that component. This region is called the "altered region" and subsequent sputtering yields tend to even out. Hence, at the steady-state sputtering of a binary alloy AB, the ratio of the sputtered atoms n_A of component A to n_B of component B must be equal to the ratio of the target concentrations C_A/C_B. Using Eq. (3.3), the following expression can, therefore, be written:

$$Y_A / Y_B = C_A / C_B = n_A / n_B \ . \tag{3.4}$$

In general, the total sputter yield Y of a multicomponent target can be written as the sum of the partial sputter yields Y_i of each atomic species i:

$$Y = \sum_i Y_i \ . \tag{3.5}$$

3.1.2 Sigmund Theory for Linear Cascade Sputtering

Sputtering can be classified into three categories: the single knock-on regime, linear cascades, and non-linear cascades or spikes. In the single knock-on regime, the incident ion imparts sufficient energy to a surface atom during a head on collision for the latter to be sputtered. This mechanism is predominant when the bombarding ions have energies near the threshold energy. When the incident ions have larger energies, they undergo a series of collision cascades through recoil collisions. If the collision cascades reach the surface region sputtering can take place. The difference between the linear cascade regime and the spike regime is that the spatial density of a collision cascade is much smaller in the former case. In the linear cascade theory, a Boltzmann transport equation is used to describe collision cascades. The collisional events are assumed to be binary between point-like objects and to take place between a moving

atom and a stationary atom. Neglecting inelastic energy losses during the binary events, the sputter yield can be expressed as:

$$Y = 0.042\alpha\left(M_2 / M_1,\theta\right)S_n\left(E,Z_1,Z_2\right)/U_0\ , \qquad (3.6)$$

where the dimensionless factor α, represents the fraction of energy available for sputtering, S_n is the nuclear stopping cross-section, E is the ion energy, and Z_1 and Z_2 are the atomic numbers of the bombarding ion and target atom, respectively. It is evident from Eq. (3.6) that the sputter yield will be influenced by: (a) the energy of the incident ions, (b) the target material, and (c) the incident angle of the bombarding ions. In addition, the crystal structure of the target surface plays an important role in determining the sputter yield. The typical dependencies of the sputter yield on the ion energy and on the atomic numbers of the substrate and ion species, as predicted by Eq. (3.6), can be found in references [6,7].

3.1.2.1 Ion Energy

The sputter yield is zero for ion energies lower than the threshold energy for sputtering. At energies slightly larger than the threshold energy, that is in the single knock-on regime, the sputter yield is small. The yield increases with ion energy to reach a maximum that ranges between 10-100 keV depending on the universal stopping power. This is attributed to the increase in collision cascades and their density which result in increased transport of energy to the surface until the stopping reaches a maximum. Further increases in energy result in the ions becoming imbedded deeper into the target and a decreased fraction of energy is deposited in the near surface layers.

3.1.2.2 Mass of Target and Bombarding Ion

For any ion energy larger than the threshold energy, the sputter yield increases with increasing atomic mass of both target atoms and bombarding ions [6,7]. This is due to the increased nuclear energy deposited to the target lattice when using heavier targets and incident ions. The nuclear stopping cross-section S_n in Eq. (3.6) can be written as:

$$S_n(\varepsilon) = 4\pi a Z_1 Z_2 e^2 \frac{M_1}{M_1 + M_2} s_n(\varepsilon) \quad , \tag{3.7}$$

where $s_n(\varepsilon)$ is a universal function, depending on the detailed form adopted for the screened Coulomb interatomic potential. The reduced energy parameter ε [dimensionless Thomas-Fermi (TF) energy] is given by:

$$\varepsilon = \frac{4\pi\varepsilon_0 a M_2}{Z_1 Z_2 e^2 (M_1 + M_2)} E \quad , \tag{3.8}$$

where e is the electronic charge, ε_0 is the permittivity of free space, a is the screening radius and the remaining variables hold their previously defined meanings. Amongst others [8,9], the screening radius can be expressed as the Thomas-Fermi screening length a_{TF} given by:

$$a_{TF} = \frac{0.8853 a_0}{\left(Z_1^{2/3} + Z_2^{2/3}\right)^{1/2}} \quad , \tag{3.9}$$

where $a_0 = 0.529$ Å is the Bohr radius. Furthermore, as will be shown later, the projected range of the bombarding ions in the target decrease with increasing target and ion mass numbers, such that nuclear energy deposited by the incoming ions to the substrate is confined to the near surface layers and in denser collision cascades. Eq. (3.6) does not hold when the reduced energy of the bombarding ions is larger than 1 ($\varepsilon \geq 1$), since then the electronic stopping becomes predominant. The energy loss mechanisms will be discussed in more detail in the section on ion implantation.

3.1.2.3 Angle of Incidence

The angular dependence of the sputter yield can be investigated by considering the factor α in Eq. (3.6). In the energy regime important for sputtering (i.e., $\varepsilon \leq 1$), α is, for all practical purposes, independent of the ion energy. If the bombarding ions impinge on the target with an angle of incidence θ, then α is given by [1]:

$$\alpha(M_2, M_1, \theta) = \alpha(M_2 / M_1)\cos^{-f}\theta$$

$$\text{with } f \approx \frac{5 \pm 2}{3} \text{ and } (\theta \leq 60°) \ , \qquad (3.10)$$

where the factor $\alpha(M_2/M_1)$ can be expressed using Eqs. (3.11) to (3.13) depending on the ratio M_2/M_1 [Eq. (3.14)]. The following expressions were obtained by Gries and Strydom [10-12] after solving Eq. (3.6) for α by substituting 620 measured sputter yield values of monoelemental targets and using the heats of sublimation for surface binding energies.

$$\alpha\left(M_2 / M_1\right) = 0.120 \ , \text{for } l \leq -1.2 \qquad (3.11)$$

and

$$\alpha\left(M_2 / M_1\right) = 0.0857l^5 + 0.289l^4 + 0.402l^3 + 0.350l^2 + 0.220l + 0.189 \ ,$$

$$\text{for } -1.2 < l \leq -0.144 \qquad (3.12)$$

and

$$\alpha\left(M_2 / M_1\right) = 0.0449l^6 - 0.107l^5 - 0.209l^4 + 0.314l^3 + 0.207l^2 + 0.156l + 0.183 \ ,$$

$$\text{for } -0.144 < l \leq 1.8 \qquad (3.13)$$

where

$$l = \log_{10}\left(M_2 / M_1\right). \qquad (3.14)$$

The increase in α in Eq. (3.10), and hence in Y in Eq. (3.6), with increasing θ, is due to the increasing density of energy deposition near the target surface. Alternatively, the range of the bombarding ions in a direction perpendicular to the target surface decreases with increasing θ. Depending on the target-primary ion combination, the sputter yield reaches a maximum at angles between 60° and 80° [13]. For angles of incidence larger than 80° (i.e., at oblique angles), the atomic interaction between the incident ions and target atoms decreases so that the sputter yield decreases. However, one serious shortcoming of Eq. (3.10) is that it wrongly predicts the penetration depth of the bombarding ions with increasing angle of incidence. Yamamura applied the

single knock-on model to analyse the sputter yield by light ions [14], and proposed the following empirical formula for the angular dependence of the sputter yield:

$$Y(\theta)/Y(0) = \left(\cos^{-f}\theta\right)\exp\left[\sum\left(1-\frac{1}{\cos\theta}\right)\right]. \qquad (3.15)$$

The first term is identical to the angular term in Eq. (3.10), which represents a longer ion path length near the substrate surface with an increase in θ. The second term takes the angular penetration probability into account. The following expression is obtained for *f* by taking a least-squares fit to experimental values of sputter yield:

$$f = U_0^{1/2}\left(0.94 - 0.0133 M_2 / M_1\right). \qquad (3.15)$$

3.1.2.4 Crystal Structure of Target

The crystal structure of a mono-crystalline target also affects the sputter yield. This dependence can be explained by considering the following two cases. Firstly, the atomic interaction, and hence nuclear stopping, between the bombarding ions and target atoms will be larger when the former are incident along a direction normal to a closely packed atomic plane, say (111), compared to a plane with a lower atomic density, e.g., (100). Secondly, if the bombarding ions are incident along a low crystallographic direction, they penetrate to larger depths below the crystal surface as would be the case if the target matrix were amorphous. This condition is known as "channelling" and is characterised by a critical angle, ψ_c [15]. When $\theta < \psi_c$, as can be the case at the low energies often used in processing technology, the bombarding ions are guided deeper into the target so that the energy deposited in the near-surface region is decreased. It can, therefore, be concluded that the sputter yield is lower when the primary ions are either incident normal to a relatively less dense crystallographic plane or directed along a direction of low crystallographic index.

3.2 Ion Implantation

During sputtering in the linear cascade regime the incident ions become trapped or implanted inside the substrate. While the ions are slowed down in the semiconductor lattice, host atoms are displaced through energetic recoils and damage is introduced in

the crystal lattice. This implantation-induced damage continues as long as the ions have energies larger than the displacement energy, E_d, of the lattice atoms. The amount of damage created depends on the energy deposited per unit volume by the implanted ions, which in turn determines the extent to which the properties of the semiconductor are changed. The two main energy loss mechanisms of an energetic particle in a solid together with some defect reactions are considered in the following discussion. The removal of radiation damage through post-bombardment high temperature treatments is briefly discussed.

3.2.1 Energy-Loss Mechanisms

An energetic ion undergoes two major mechanisms of energy loss: (1) screened Coulomb collisions with target atoms (nuclear stopping), and (2) interactions with bound or free electrons in the solid (electronic stopping). The relative effect of the two mechanisms depends on the energy and the mass of the incident ion, as well as the mass of the target atoms. Figure 3.2 summarises the velocity ($\varepsilon^{1/2}$) dependence of the two energy-loss processes, nuclear stopping $(d\varepsilon/d\rho)_n$ and electronic stopping $(d\varepsilon/d\rho)_e$, in terms of the dimensionless Thomas-Fermi (TF) energy, ε, and path length, ρ [16] . The energy unit ε is defined as the ratio a/b, where a is the TF screening length [Eq. (3.9)] and b is the distance of closest approach in an unscreened head-on collision. The laboratory energy, E (keV), of the incident ion can be expressed in terms of the dimensionless TF energy using Eqs. (3.8) and (3.9). For $\varepsilon < 1$, b is greater than a and hence all collision processes occur in a screened Coulomb field.

Using the reduced TF energy provides two advantages, namely: (1) nuclear stopping and associated quantities such as sputtering and damage production can be expressed by a universal curve for all ion-target combinations (Figure 3.2), and (2) ion bombardment studies can be separated into two distinct regimes. In the first regime, also called the ion implantation regime ($\varepsilon < 10$), both nuclear and electronic stopping have significant contributions, and theoretical treatments in this regime are complex. In the nuclear analysis regime ($\varepsilon >> 10$) consisting of sufficiently fast ions virtually stripped of all their electrons, electronic stopping is the predominant energy-loss process. The ion trajectory is almost linear, sputtering and collision cascade effects are

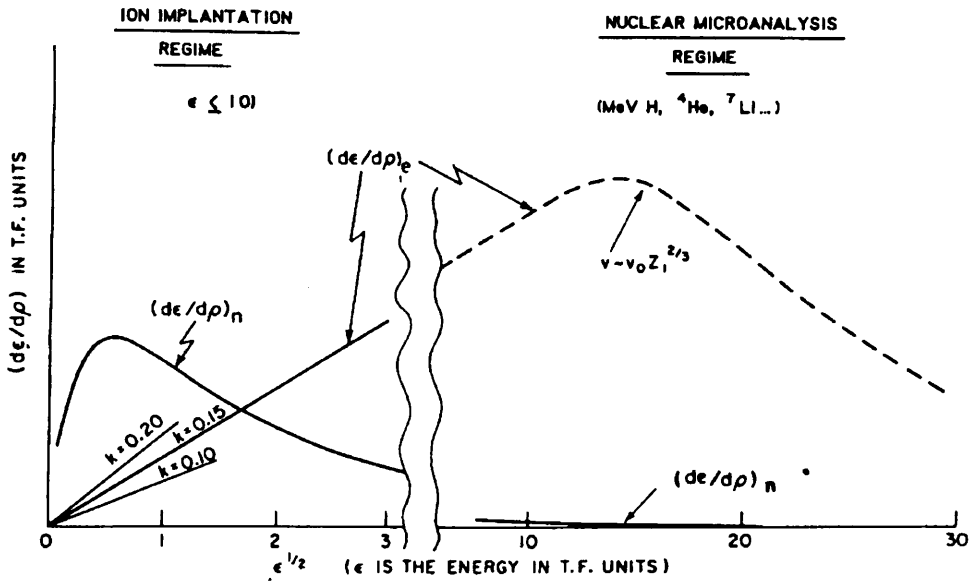

Figure 3.2: Nuclear and electronic stopping powers versus the dimensionless Thomas-Fermi energy of an implanted ion (J.A. Davies, MRS Bulletin, June 1992, p. 26).

practically negligible, and the Bethe-Bloch formalism can be used for accurately determining energy loss and penetration phenomena [17].

Figure 3.2 shows that at low energies relevant to sputtering, nuclear stopping is the more important process and that it reaches a maximum value around $\varepsilon = 0.35$ and thereafter falls off. Conversely, electronic stopping increases linearly with velocity and becomes the dominant energy-loss mechanism for $\varepsilon > 4$. It should be noted that $(d\varepsilon/d\rho)_e$ does not exhibit true ε-scaling and cannot, therefore, be described by a universal curve. The values of ε/E (keV^{-1}) for the noble gas species are given in Table I.

Table I: *Ratio of reduced TF energy, ε, to laboratory energy, E (keV), for different noble gas species.*

Noble gas species	He	Ne	Ar	Kr	Xe
ε/E ($x10^{-3}$ keV^{-1})	373.9	41.8	15.0	3.963	1.691

3.2.2 Range Distribution of Implanted Ions

The mean depth, or range, R, of a bombarding ion with initial energy, ε_0, is given by:

$$R = \int_{\varepsilon_0}^{0} \frac{1}{(d\varepsilon / d\rho)_{total}} d\varepsilon \quad , \tag{3.16}$$

where

$$(d\varepsilon / d\rho)_{total} = (d\varepsilon / d\rho)_n + (d\varepsilon / d\rho)_e . \tag{3.17}$$

When $M_1 \geq M_2$, the projected range, R_p, in the direction of the ion beam is obtained by applying a correction factor approximately equal to $(1 + M_2/3M_1)^{-1}$ to Eq. (3.16). It should be noted that when the ion is incident normal to the target surface, the mean and projected ranges are equal. In the case of a monocrystalline target, the deviations in predicted and measured ion ranges could be significantly different (more than 20 %) when channelling effects take place [20]. Alternatively, the Nielsen approximation can be used over the energy range $0.1 < \varepsilon < 10$ to predict the mean range, R (nm), usually with an accuracy of around 30 % [21]:

$$R = E \times 13.0 \frac{1 + M_2 / M_1}{g Z_1^{2/3}} \quad , \tag{3.18}$$

where g is the density of the substrate in g/cm^3.

A more exact knowledge about the entire depth distribution calls for an evaluation of the straggling range. In the absence of straggling, the spatial distribution of implanted ions is approximately Gaussian, and can, therefore, be described by the standard deviation ΔR. The Lindhard-Scharff-Schiott (LSS) theory [16] predicts that for $\varepsilon < 3$, the total straggling in ion path length, i.e., $\Delta R/R$, approaches a constant value of:

$$\Delta R / R = 0.35 \frac{2(M_1 M_2)^{1/2}}{M_1 + M_2} \quad . \tag{3.19}$$

As the electronic stopping increases at higher energies, the relative straggling becomes smaller. The relative straggling in projected range, $\Delta R_p/R_p$, is almost identical to $\Delta R/R$ since the path length correction terms for the numerator and

denominator are virtually identical. Considering the projected range distribution, the Gaussian approximation gives the implant concentration $N(\rho)$ as:

$$N(\rho) = \frac{\phi}{\Delta R_p \sqrt{2\pi}} \exp\left[-\frac{(\rho - R_p)^2}{2\Delta R_p{}^2} \right], \qquad (3.20)$$

where ϕ is the fluence, or ion dose and ρ is measured along the direction of the beam. It should be noted that the implant profile given by Eq. (3.20) ignores *in-situ* diffusion, as well as channelling and ion beam mixing effects. Through the use of additional moments, such as skewness and kurtosis, the Pearson-IV distribution [21] and other higher order descriptions can accurately fit implanted ion depth distributions. Monte Carlo based computer simulations of implant profiles can be produced using the TRIM (TRansport of Ion in Matter) code of Biersack and Haggmark [22]. It should be born in mind that TRIM assumes the target to be amorphous, or equivalently, disregards channelling effects. An extensive review of computer simulations of ion-solid interactions has recently been conducted by Eckstein [23]. Although being widely used, theoretical predictions should always be applied with caution, especially in crystalline substrates, as they take no account of channelling , nor of possible diffusion effects during and after the implantation.

3.2.3 Radiation Damage and its Distribution

The energy transferred from the bombarding ion to the target atoms is usually sufficient to displace the host atom from its lattice site. Typically, the implanted ion is able to knock-off a target atom from its lattice site if the ion energy is larger than the threshold energy for displacement, E_d, of the host atom. This displaced atom may in turn displace other atoms and so on, thus creating a cascade of atomic collisions, and a distribution of vacancies, interstitial atoms and higher order defects, including complexes, in the region surrounding the ion track (Figure 3.3). The size of the collision cascades is governed by nuclear and electronic energy-loss processes. However, only the nuclear component contributes to the production of energetic recoil atoms. The incident ion energy can be partitioned into its two components, ν and η, where ν is the energy translated into atomic motion, and η is the total energy

transferred to electrons, i.e., $\varepsilon = \nu + \eta$ [24]. For $\varepsilon < 1$ (linear cascade regime for sputtering), a constant fraction of approximately 80 % of the total energy ($\nu/\varepsilon \approx 0.8$) is consumed in recoil processes, whereas the ratio ν/ε falls rapidly when $\varepsilon > 1$. The number of displaced atoms N_d in a collision cascade can be estimated from $\nu(E)$ through the modified Kinchin-Pease relationship derived by Sigmund [25]:

$$N_d = \xi \frac{\nu(E)}{2E_d}, \qquad (3.21)$$

where E_d is the displacement energy threshold of the lattice, which for Si is approximately 15 eV, $\nu(E) = E$ x ν/ε, is the total energy deposited in atomic motions, and $\xi \sim 0.8$ is a correction factor. Eq. (3.21) often overestimates the amount of

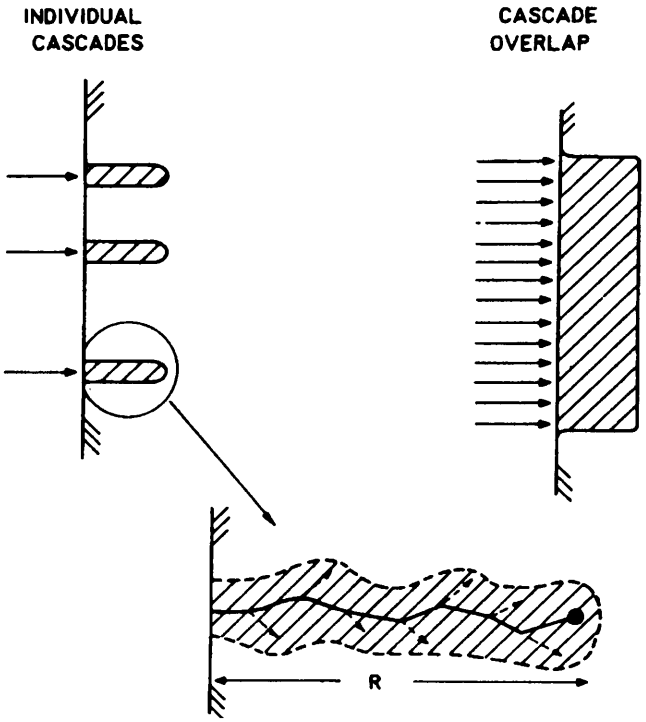

Figure 3.3: Collision cascade schematic illustrating spatially separated individual collision cascades and the result of their overlap [J.W. Mayer, L. Erikson and J.A. Davies, Ion Implantation in Semiconductors (Academic Press, New York, 1970)].

disorder since it overlooks the effects of ion channelling and of vacancy-interstitial recombination within the cascades. The amount of energy deposited into energetic recoils and the total number of vacancies produced for given ion-target interactions can also be simulated using TRIM. Since an ion requires an amount of energy greater

than E_d for the production of damage, the maximum of the damage distribution is always closer to the surface then the maximum of the ion depth distribution.

Another important point to note is that Eq. (3.21) is valid for low density collision cascades which in general are also spatially well separated. This condition is, however, not fulfilled in many low-E high-Z cascades, as in low energy (0.3-1 keV) Ar-ion bombarded Si, and the resulting spike effect [26] may sometimes create higher disorder levels than predicted by Eq. (3.21). For instance, as the low energy Ar ion slows down, its energy decreases, and since the nuclear stopping increases with decreasing ion energy, the ion will interact more strongly with the Si lattice and will dislodge more atoms, thereby creating a higher density of vacancies at the end of its range. Figure 3.4 shows the depth distribution of 1 keV Ar-ions in Si as well as the nuclear energy deposited per unit path length to the lattice.

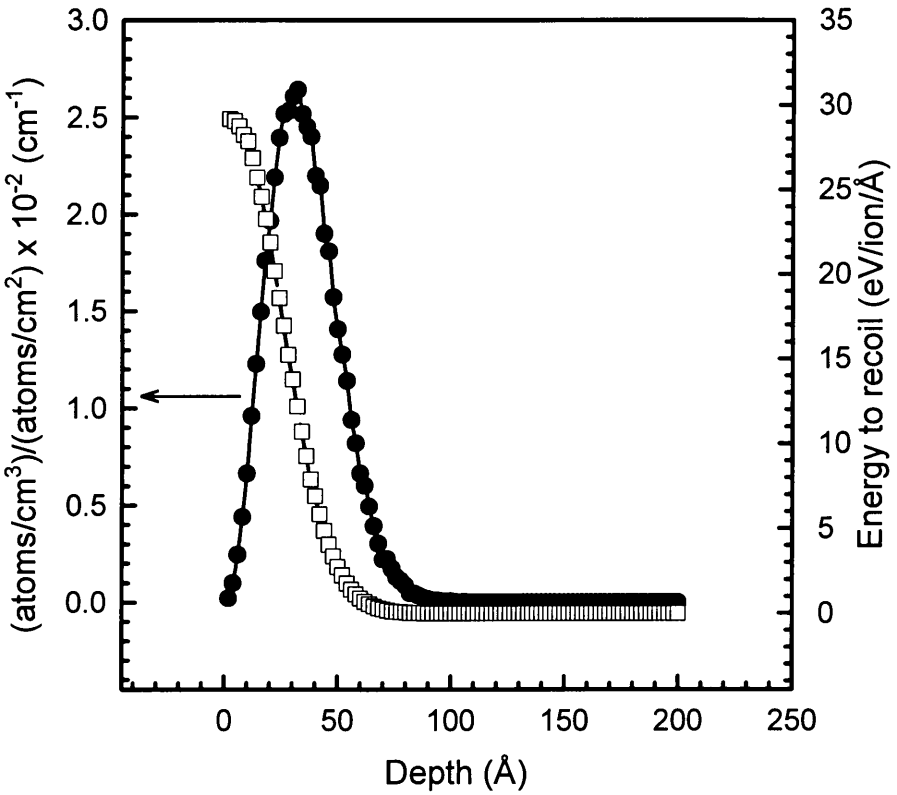

Figure 3.4: Depth distribution of 1 keV Ar-ions in Si (solid circles) and their nuclear energy deposited to elastic recoils as obtained from TRIM [22] simulations.

A useful criterion for defining the onset of spike behaviour is the density of energy deposited, E_0, per atom along an individual ion track. Whenever E_0 exceeds some

critical value, typically ~ 1-5 eV per atom, then the possibility of some collective spike phenomenon exists. Thompson and Walker have, nevertheless, demonstrated that nonlinear effects (i.e. deviations from linear cascade regime) can take place in Si when the average energy density is as low as 0.1 eV/atom [27]. A dominant spike effect that takes place during elastic collisions is the "displacement spike". Brinkman [28-29] has described a displacement spike to evolve when the mean distance between displacement collisions approach the mean interatomic distance, causing a net outward motion of the host atoms along the incident ion direction. The result will be to produce a vacancy rich central core surrounded by an outer shell which is rich in interstitial atoms. When the individual high density collision cascades overlap, there is a structural change in the lattice from being crystalline to becoming amorphous (Figure 3.3). A review of various spike phenomena can be found in ref [30].

3.3 Defect Reactions

3.3.1 Point Defects, Vacancy Clusters and Defect Complexes

Defect formation is dictated by the energy deposited per unit path length of the implanted ion. As the nuclear component of energy-loss of an ion is increased, the defects form and change from one configuration into another one in an evolutionary sequence, i.e., from point defects to extended defects to an amorphous region. Vacancies and interstitial Si atoms are the elementary defects formed during ion bombardment of Si, and because the former have been studied extensively using electron paramagnetic resonance (EPR), the discussion is focused mainly on vacancy-related defects. Single vacancies are highly mobile at low temperatures (~ 77 K) and, therefore, have very short lifetimes since they are either annihilated by recombining with self-interstitials or combine with other impurities to form complexes. For instance, a single vacancy can combine with another single vacancy to form a divacancy (V_2), or be trapped at an impurity site such as, oxygen, phosphorous or boron, to form a vacancy-impurity pair. The single vacancy, divacancy and vacancy-impurity pair are called point defects and their structures have been established, using EPR, by Watkins and Corbett [31-33]. Furthermore, the vacancy-oxygen (VO-centre) and the carbon-phosphorous (CP-centre) show metastability: the ability to achieve different electronic configurations while retaining their basic structures [34,35]. These

defects can also have different charge states, such as, for instance the singly positive and negative S = 1/2 charge states of the divacancy [36]. Divacancy-oxygen complexes have also been identified after ion bombardment of oxygen-rich (CZ) Si [37]. All of these defects introduce electronic states in the forbidden gap of Si and hence alter its electrical properties. Evidently, the degree to which a particular deep level affects the semiconductor properties depends on its position from the band edges and its concentration. For example, the VO-centre is known to be an efficient recombination centre and has, therefore, been used in defect engineering to tailor the minority carrier lifetime in pn-junctions irradiated with high energy electrons [38].

Higher order vacancy defects or vacancy clusters like the trivacancy (V_3), tetravacancy (V_4) and pentavacancy (V_5) have also been identified, using EPR, in ion implanted Si [39]. The planar tetravacancy is believed to form through the combination of two mobile divacancies and it is, in theory, possible for still larger vacancy clusters to form by this mechanism. Although the structure of the hexavacancy has not yet been established experimentally, Weiser [40] has assigned a puckered six-membered ring configuration to the cluster. Taking the interatomic spacing in Si to be 5.43 Å, the TRIM simulations in Figure 3.4 demonstrate that the average nuclear energy deposited by a 1 keV Ar ion exceeds the threshold energy for the initiation of spike effects throughout most of its range. Similar effects were obtained with other noble gas species, including He and Ne. Hence, it is conceivable that in the low energy regime wherein spike effects dominate, vacancy clusters larger than the divacancy can be produced. Theoretical simulations have been made which show that low energy noble gas ions, as employed during ion beam and plasma etching, can also become incorporated in these higher order vacancy defects [41,42]. The well-known 1018 meV vibrionic band in Si is speculated to be due to a multi-vacancy defect. Weber *et al* have shown through photoluminescence (PL) studies that the 1018 meV vibrionic band is shifted during low energy (200-2000 eV) noble gas bombardment of Si, and that the shift was noble gas species dependent [43-44]. They further showed that the incorporation of noble gas atoms was thermally activated with the PL intensities of the shifted I_1 peaks reaching a maximum at 350 °C. However, based on theoretical modelling, Estreicher and Weber have recently postulated that the intrinsic I_1 defect was most probably due to the neutral divacancy [45]. The above

discussion demonstrates that more experimental work has yet to be conducted in order to identify the structure of the I_1 defect and of noble gas-related defects in ion bombarded Si.

Complexes related to oxygen interstitials and carbon interstitials form a major class of defects in bombarded Si. For instance, the carbon interstitial-carbon substitutional (C_i-C_s) and carbon interstitial-oxygen interstitial (C_i-O_i) are amongst the dominant defects in Si substrates rich in carbon and oxygen [46]. However, Benton *et al* have demonstrated that these C_i-related defects could be observed in oxygen- and carbon-free Si substrates after reactive ion etching in CCl_4 [47]. These defects are both electrically and optically active, and their presence, therefore, affects the electrical and optical properties of the bombarded Si lattice. The C_i-C_s defect is metastable in nature and is responsible for the G luminescence line (969.5 meV), while the C_i-O_i defect produces the C luminescence line (789.4 meV) [47]. In addition, these two impurities react with P and B dopant ions to give the impurity (C,O) - dopant (B,P) pairs [48-50], which are also electrically active.

When spike effects become dominant, the point defects can combine to form extended defects and an amorphous layer is eventually formed. As opposed to the above-mentioned defects which introduce discrete electronic levels in the band gap, extended defects introduce a continuous band of energy levels [51]. As will be explained in Chapter 5, the thermal emission rate from a deep level is maximum at a specific temperature which allows one to determine its exact position in the band gap. On the other hand, the emission from a continuous distribution of energy levels is not defined by a maximum at a specific temperature. The temperature range over which the thermal emission takes place depends on the spread of the levels in the band gap as well as the density and uniformity of their distribution [52]. Finally, amorphisation results in a structural change in the Si substrate. The amorphous layer is also electrically different from the crystalline lattice because it has a larger mean band gap (1.8-2.4 eV), a higher resistivity and contains defect densities of 10^{15} /eV cm^{-3} which pin the Fermi level at the middle of the band gap [52].

3.3.2 Thermal Annealing of Processing-Induced Defects

Defects introduced during semiconductor processing (e.g., sputter etching and sputter deposition) have deep trapping and compensating states, and may have deleterious effects on the properties of the semiconductor. Some of these deep levels can also act as recombination centres. On the other hand, certain defects such as the shifted I_1 defects, have to be thermally activated before any of their optical properties can be used to alter those of the semiconductor material in a controlled fashion. Furthermore, Er-related defects in Si are known to luminesce at 1.5 μm, the absorption minimum of waveguides, and that these defects become optically active after thermal activation [53]. Consequently, the annealing behaviour of defects has to be understood for their potential application in defect engineering (Chapter 1), or their thermal removal rates known in order to avoid their negative effects on semiconductors and, therefore, device properties. Though there are various annealing methods available, e.g., pulsed laser beam, rapid thermal annealing (RTA), CW laser, incoherent light and thermal radiation, conventional furnace annealing domintes in the manufacturing industry for reproducibility and higher throughput.

Thermal annealing studies also play an important role in helping to identify the structure of defects. Defect characterisation techniques such as, deep level transient spectroscopy (DLTS) and photoluminescence (PL) cannot be used to identify the structure of defects. The only way to match a defect whose structure has been identified by electron paramagnetic resonance (EPR) to one identified by DLTS or PL, is through thermal annealing studies. Figure 3.5 (top) shows the annealing stages of various vacancy defects studied by EPR, while Figure 3.5 (bottom) illustrates the annealing behaviour of some prominent vacancy-related defects which have been characterised using DLTS [54,55].

Caution must be applied when using high temperature treatments on processed semiconductors for the following reasons: (a) with increasingly stringent demands for ultra large scale integration (ULSI), the need for shallower dopant depth distributions is becoming a limiting factor. During high temperature annealing, the dopant atoms diffuse into the substrate thereby increasing the junction depth. Any overlapping of adjacent shallow junctions or the overlap of a junction with an interconnect will

decrease device yield; (b) the defects are driven further away from the semiconductor surface and start to affect previously "defect-free" regions; (c) the initial defects may react with other defects at higher temperatures to form new classes of defects, also called “secondary defects”, which may be stable to higher temperatures. It is conceivable that divacancies can combine at higher temperatures to form planar or non-planar tetravacancies (Figure 3.5). Sawyer *et al* have recently demonstrated that the shifted I_1 defect can be completely removed at 550 °C, and that a completely new class of defects are created at 650 °C [56]. They further showed that annealing of Ar-etched samples at 1050 °C causes a structural change in the Si lattice through the formation of Ar bubbles with an average diameter of about 5 nm; (d) the solid phase epitaxial recrystallisation of an amorphous Si layer [57] is always accompanied by the

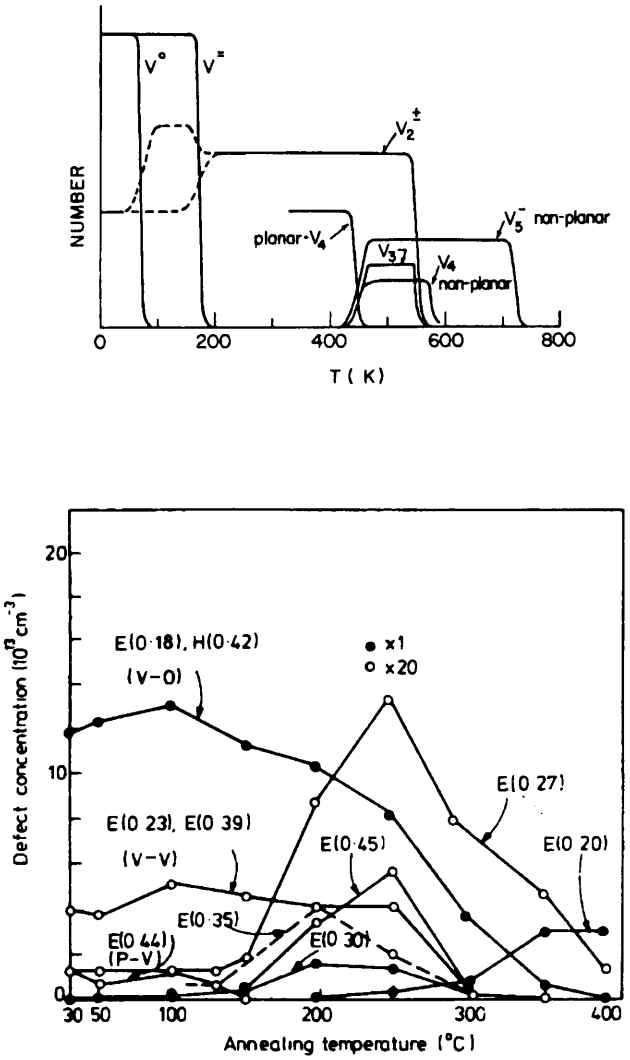

Figure 3.5: Schematic representation of the recovery of intrinsic vacancy-related defects in silicon (top) [54]. Isochronal annealing stages of point defects in electron irradiated n-Si (bottom) [55].

release of dislocation loops and smaller aggregates of Si interstitial atoms, which in turn may act as recombination centres for minority carriers or induce stresses in the lattice; and (e) Ashok *et al* have recently demonstrated that the formation of a silicide phase at a metal-Si interface during thermal annealing injects vacancies into the substrate [58]. They have successfully used this silicidation technique to remove interstitial-related defects in processed p-type Si. On the other hand, it can be argued that annealing of a metal contact to an n-type Si substrate containing primary defects can lead to increased concentrations of vacancy-type defects.

3.4 Sputter Deposition and Etching in a Glow Discharge

The following sub-sections address the principles of sputter deposition and sputter etching. It will be shown that, although, the nuclear energy loss during plasma particles-semiconductor interactions is used to describe damage creation in the exposed semiconductor surfaces during both processes, the role of energetic neutral atoms, electromagnetic waves (photons and X-rays) and electrons have to be considered, in addition to energetic ions. Compared to an ion beam, the energy distribution of plasma particles reaching the semiconductor surface as well as their angular distributions can only be approximated or defined using statistical approaches. It will also be demonstrated that pressure is the main plasma parameter that determines the energy and angular distributions of the sputtered metal atoms and of the plasma particles reaching the semiconductor surface. A major advantage of plasma-processing is that sputter deposition for metallization and nonreactive anisotropic etching can be conducted in the same reactor. The magnetron reactor as well as the design constraints to achieve anisotropic and uniform etching are also discussed. Brief discussions on the type and extent of defects induced in Si during plasma processing together with the resulting structural changes in the sputter etched substrate are also included. Finally, a summary of reactive plasmas and their properties is given.

3.4.1 The Magnetron Plasma Reactor

Magnetron reactors have become widely accepted in the past decade and are routinely used to rapidly deposit thin metal (elemental and alloy) films and for high-rate sputter

etching. Magnetron reactors are a class of cold cathode discharge devices used in generally the diode mode (planar reactor described in Chapter 2). The plasma is initiated by either applying an ac or dc potential across the electrodes. For the reasons discussed in Chapter 2, rf excitation is often preferred. In the magnetron system, a magnetic field is applied parallel to the cathode surface which confines the electrons to move in helical loops. The increased path length of electrons in a magnetron increases the ionization efficiency of the plasma. The result of the high density plasma and its proximity to the cathode is a high current, relatively low voltage discharge. Typical discharge parameters for a magnetron might be a voltage of 500 V and a current of 5 A, whereas a non-magnetised diode may operate at 2500 V and 0.5 A. The high magnetron discharge currents results in the ability to sputter the cathode at a higher rate. Furthermore, the kinetic energy of Ar ions is minimised resulting in less damage introduced in the semiconductor lattice during sputter etching.

Due to the effective trapping of the energetic secondary electrons close to the cathode, a high plasma density can be sustained at significantly lower plasma pressures than a similar rf or dc diode glow discharge. A magnetron operates at a pressure ranging from about $1x10^{-3}$ mbar to $4x10^{-2}$ mbar, whereas a typical rf diode might operate at 0.015-0.200 mbar. The low operating pressure results in a significant reduction in plasma particle scattering so that higher anisotropic etching can be achieved as well as an increase in the probability of sputtered atom transport from the cathode to the substrate. The planar magnetron (Chapter 2) such as, the Leybold Hearaeus Universal Sputtering Machine, is one of the most commonly used industrial reactors. Other reactor configurations are the cylindrical and conical designs [59]. Most plasma reactors are preconditioned for etching before wafers are placed to warm the reactor and to reduce wafer contamination. Wafers are introduced to the reactor through a load lock to minimize atmospheric contamination, especially water vapour.

3.4.2 Sputter Deposition

During sputter deposition of thin metal films onto a semiconductor, the metal target is placed on the top electrode (cathode) to which a negative dc bias, $-V_b$, is applied while the substrate is placed on the grounded anode. The positive Ar ions are accelerated across the sheath, and assuming they are not scattered, they bombard the target with

an maximum energy equal to $e(V_{self} + V_b)$ eV. Typically, the dc bias can be varied between 200 V and 1000 V. In this energy regime, the sputtering process is governed by direct knock-on collisions (section 3.4.1). Consequently, metal atoms are sputtered from the target, together with secondary electrons, X-rays and backscattered Ar atoms. For an alloy target, the features of the sputtered atoms are similar to those of the single element target. Under low incident ion energy most of the sputtered atoms are composed of single element of the alloy. Clusters become predominant when the ion energy is higher than 10 keV. The ionization probability of the sputtered metal atoms can, for all practical purposes, be assumed to be zero. Sputter yields for most gas-cathode combinations range from 0.1 to 3, implying that most of the incident ion energy is lost to cathode heating. In general, the functional limit to high power, high rate magnetron sputtering is almost always the ability to cool the cathode. In this study, the sputtered metal atoms were deposited onto Si substrates through a metal contact mask. The sputter deposition process is illustrated in Figure 3.6(a).

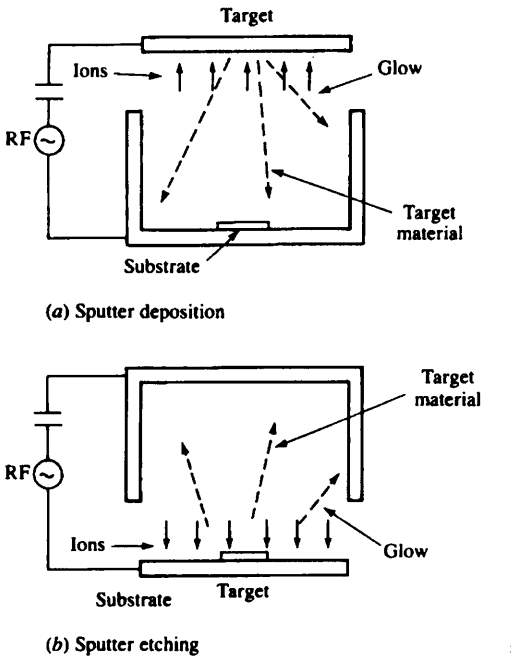

Figure 3.6: Two modes of operation of a parallel plate rf sputtering system (ref [59]).

3.4.2.1 Energy and Mean Free Path of Sputtered Atoms

The average energy of sputtered neutral atoms is much higher than that of thermally evaporated atoms in vacuum, and depends on both the incident ion species and its

energy and incident bombardment angles. In general, the average energy of a sputtered atom is between 10 to 30 eV, which is more than 100 times higher than thermal evaporation energy. The dependence of the energy of sputtered atoms on the bombarding ion species, ion energy and incident angle is similar to that of sputter yield. Hence, for any given ion-target combination, the energy of sputtered metal atoms will increase with increases in ion energy and angle of incidence until the nuclear energy deposited to the near-surface target atoms decreases at higher ion energies and for oblique angles of incidence (i.e., $\theta > 60\text{-}80°$). Evidently, bombarding the metal target with Xe ions rather than Ar ions will also result in the sputtered atoms having more kinetic energy. Table II summarises the measured and calculated arrival energies of various metals for Ar sputtering [60].

Table II: Measured and calculated energy arrival rates for Ar sputtering.

Metal	Atomic Weight	Planar Magnetron (eV/atom)	Theoretical Values (eV/atom)
Al	27.0	11	13
Cr	52.0	16	16
Ni	58.7	15	19
Ta	181	96	38
W	184	98	40

Before deposition, the sputtered atoms travel through the discharge where they collide with mostly neutrals Ar atoms. Their mean free path before they collide to discharge gas molecules is given by :

$$\lambda_1 \approx c_1 / \nu_{12} \ , \qquad (3.22)$$

where c_1 is the mean velocity of sputtered atoms and ν_{12} is the mean frequency between sputtered atoms and discharge gas atoms. Since the velocity of sputtered particles is much larger than the gas molecules, ν_{12} can be written as:

$$\nu_{12} \approx \pi (r_1 + r_2)^2 c_1 n_2 \ , \qquad (3.23)$$

where r_1 and r_2 are the atomic radius of sputtered atoms and discharge gas atoms, respectively, n_2 is the density of discharge gas. The mean free path is then given by:

$$\lambda_1 \approx 1/\pi(r_1 + r_2)^2 n_2 \ . \qquad (3.24)$$

In the case of Ar ion bombardment of a Au target, taking $r_1 = 1.79\text{x}10^{-8}$ cm, $r_2 = 1.82\text{x}10^{-8}$ cm, and $n_2 = 3.5\text{x}10^{16}$ cm^{-3} (at 0°C, 1 Torr), λ_1 becomes $6.98\text{x}10^{-3}$ cm. These estimated values are slightly longer than the mean free path between neutral gas atoms at room temperature.

3.4.2.2 Interactions at the Sample Surface

Compared to the conventional resistive deposition technique, sputter deposition of thin metal films offers the advantages of controlled higher deposition rates and better film adhesion, being able to deposit refractory metals, the stoichiometric deposition of alloys and its ability to be coupled with plasma etching of the substrate without breaking vacuum. An advantage of the thermal deposition process is that it practically introduces no damage is introduced in the semiconductor lattice. During sputter deposition, the substrate is bombarded by a wide range of energetic plasma particles and electromagnetic radiations. Since the substrate is grounded during magnetron sputter deposition, very few Ar ions and electrons interact with the semiconductor. Damage is caused to the lattice by neutrals that are elastically reflected from the target, Auger neutralised ions that have been accelerated to high energy to the target surface and which may reflect with up to several hundred eV of kinetic energy, sputtered metal atoms, X-rays which are emitted when Ar ions bombard the target and photons from the glow discharge. The nature and extent of the defects produced in an n-type and p-type single crystal silicon wafer during sputter deposition of a thin metal film have been investigated by measuring the electrical characteristics of the resulting metal-semiconductor contacts. The current-voltage (I-V) and capacitance-voltage (C-V) measurements showed that the defects were donor-type [61-63]. Typically, the Schottky barrier height to n-type Si is decreased during sputter deposition and the relative decrease depends on the concentration of damage induced in the surface and near-surface region of the semiconductor. The opposite effect is observed during metallization to p-type Si [61].

The extent of the sputter deposition induced damage depends mainly on the energy with which the neutral Ar atoms reach the semiconductor surface. More damage is created when both the negative dc bias on the cathode and the self-bias voltage (i.e., using a larger rf excitation potential) are increased. Mullins and Brunnschweiler [61] have shown that the rectifying properties of molybdenum Schottky diodes deposited by dc sputtering on n-Si became poorer when the cathode voltage and the deposition time were increased. As mentioned previously, the energy and angular distributions of the particles traversing the glow discharge depend on their scattering frequencies, and thus on the plasma pressure. Eq. (3.23) shows that the frequency of collision of particles in the glow discharge is proportional to the plasma density (i.e., pressure), so that the energy with which the neutral Ar ions reach the Si substrate decreases with increasing plasma pressure. Furthermore, the energy required to sustain the electric discharge decreases with increasing pressure, causing a self-bias, V_{self}, and hence the amount of damage, to decrease. Despite the numerous studies on the effects of various plasma parameters on the electrical characteristics of sputter deposited metal-Si contacts, very little work has been devoted to studying the electrical and annealing properties of sputter deposition induced defects.

3.4.3 Magnetron Nonreactive Sputter Etching

Nonreactive sputter etching makes use of a noble gas glow discharge (e.g., Ar). The reactor configuration is similar as in the case of sputter deposition with the only difference being that the substrate is placed on the cathode which now is the bottom electrode [Figure 3.7(b)]. A negative bias, $-V_b$, is usually applied to the cathode and Ar ions are accelerated across the cathode sheath to bombard the exposed semiconductor material with a maximum kinetic energy of $e(V_{self} + V_b)$ eV. During ion bombardment two competing processes take place, namely: (a) damage creation at and close to the semiconductor surface, and (b) removal of the topmost damaged atomic layers by physical sputtering. The relative effect of these two processes depends critically on the rate of sputtering, which is defined as the product of sputter yield and ion flux reaching the substrate. Another important effect that takes place during sputter etching is in-diffusion of defects to depths much larger than the projected range of the implanted Ar ions. Contamination of the substrate surface with heavy

metals and the uniformity of the sputter etched substrate surface are also important considerations. The end-product of nonreactive sputtering is a substrate of which the surface structure, electrical and optical properties have been altered. For instance, physical sputtering effects manifest themselves in etched silicon in changes in surface properties [64], in changes in generation lifetimes [65], in changes in doping activation [66-68], and can even result in changes in diffusion lengths [69]. Capacitor structures fabricated on dry-etched Si surfaces show that the oxides display increased interface state densities which are strongly dependent on the etching ion species and energy [70] as well as the dielectric breakdown that also depend on etching history [71-73]. Furthermore, sputter etching induced damage and contamination can result in degraded electrical properties of metal-Si interfaces [74-76]. All of these various effects of etching on materials properties propagate into devices and may have deleterious effects on their performance. However, a better understanding of the properties of sputter etching induced defects may lead to their use in tailoring materials properties or, moreover, to minimise their adverse effects on device properties.

3.4.3.1 Transport Effects in the Cathode Sheath

The Ar ions will bombard the substrate with maximum energy only when the plasma pressure is sufficiently low such that the mean free path before collision of an ion is larger than the sheath thickness, *d*. In this case, the ions can also be assumed to impinge on the substrate in a direction normal to its surface. However, complexities arise in determining the ion energy and angular distributions of the ions when collisional effects start to take place in the cathode dark space. The probability of having no collision in travelling a distance x is given by $\exp(-x/\lambda)$, where λ is the mean free path [77]. The probability of having no collision in travelling the sheath thickness, P_d, is therefore given by:

$$P_d = \exp\left(-\frac{d}{\lambda}\right) \quad , \tag{3.25}$$

where the mean free path of ions in neutrals is given by [78]:

$$\lambda = \left[\pi n_i {d_i}^2 (2)^{1/2} + \pi n_n \left(\frac{d_i + {d_n}^2}{2} \right)^{1/2} \left(1 + \frac{M_i}{M_n} \right)^{1/2} \right]^{-1} . \qquad (3.26)$$

The relationship gives good order of magnitude agreement with experiments for the slightly ionized gases, typical of plasma processing. In Eq. (3.26), n is the number density, d is the molecular or atomic diameter, M is the molecular or atomic weight, and the subscripts i and n, respectively, are for ions and neutrals. The mean free path decreases with increasing pressure. The sheath thickness also decreases with increasing pressure but at a much lower rate. Thus as pressure decreases, d/λ decreases and the probability of having no collision [Eq. (3.25)] approaches unity.

As apparent from Eq. (3.25), the probability of collision in the sheath approaches zero when d/λ is much less than unity, which occurs when the pressure is less than 0.01 mbar. When the sheath thickness is large relative to the mean free path, the average ion energy E_i can be expresses as [79]:

$$E_i = \lambda_i q E_j \ , \qquad (3.27)$$

where E_j is the electric field across the sheath. Since the mean free path is inversely proportional to pressure, P, it should be noted that the ion energy is proportional to E_j/P. Thus, the ion energy is the same if E_j/P is the same. The ion flux can be determined from the measured root mean square (rms) current although both electrons and ions contribute to the current in alternating frequencies. The ion flux is less than the current flux but is nevertheless proportional to the current density. Field and co-workers [80-81] have shown that the ion energy distribution (IED) is affected by both momentum-transfer scattering and charge exchange in the cathode sheath whereas the ion angular distribution (IAD) is dictated wholly by momentum-transfer collisions. They found that during low pressure (< 0.01 mbar) collisionless interactions, most of the ions bombard the substrate at an angle of more than 86° with respect to its surface, but that the IAD randomly distributed up to angles of ~50° when the plasma pressure was increased to 0.1 mbar. This increase in angular distribution is also accompanied by a net shift of the IED towards lower energies.

3.4.3.2 Sputter Etching Induced Damage and Contamination

The damage caused to the substrate lattice during sputter etching is attributed to nuclear energy deposited by the energetic noble gas ions. As discussed previously, a residual thin amorphous layer is produced when spike effects take place. The displacement of bonding damage layer can extend to hundreds of angstroms below the receding semiconductor surface and is characterised by the projected range of the implanted ions. The sputtering process, therefore, involves the simultaneous introduction of damage in the substrate lattice and the physical removal of the top-most damaged atomic layers. In addition, the defects induced in the substrate diffuse away from the surface and can be detected to depths as large as 1 μm [43]. The accumulation of damage is critically dependent on the sputter rate, and hence on the sputter yield of the noble gas ion species and substrate combination. Higher etch rates ensure that most of the damage is removed and that diffusion effects are minimised [82,83]. Figure 3.7 shows the sputter yields for Si bombarded with Ne and Ar ions at different energies. It can be inferred from Figure 3.7 that, for the ion energies less than 600 eV, more residual damage will be found in Ne-ion etched Si compared to Ar-ion etching. The presence of water vapour in the reactor chamber can result in the introduction of hydrogen in the Si substrate, which can diffuse to depths several microns below the surface [84].

The effects of sputter etching damage are easily seen with the very simple yet very sensitive monitor provided by current-voltage characteristics of metal-semiconductor contacts made on etched surfaces. As is the case for sputter deposited metal-Si contacts, sputter etching damage causes metal-Si contact barrier heights to decrease on n-type Si and increase on p-type Si. The relative change in Schottky diode barrier height is indicative of the concentration of sputter damage. In fact, this damage-caused barrier height shift at etched Si surfaces is enhanced with increased cathode biasing voltage or decreased pressure (i.e., with increased bombarding ion energy). This shift in barrier height is known to occur for ion beam-etched Si [85,86] and reactive-ion-etched Si [64,87]. Interestingly, it is also found to occur for Ar ion-implanted Si [88]. Because the effect is independent of etching tool and etching chemistry and is present in inert gas ion implantation, this barrier height change effect is attributed to physical damage caused by ion bombardment [87].

Metallic impurities due to "scrubbing" of the reactor chamber and fixturing have been found to deposit on reactive ion etched surfaces [73,89,90]. Since residue cleaning procedures, including RCA cleans, were not able to remove this metallic contamination, it has been suggested that the metallic permeation could have premeated (~ 100 Å) into silicon during reactive ion etching (RIE) [91]. In general, the presence of metallic impurities can affect subsequent processing and device performance. For example, in cases where RIE was done prior to junction formation, it has been found that high leakage currents are present. These high leakage currents are believed to be due to stacking faults, which are nucleated and made electrically active by metallic contaminants from the etching chamber [91].

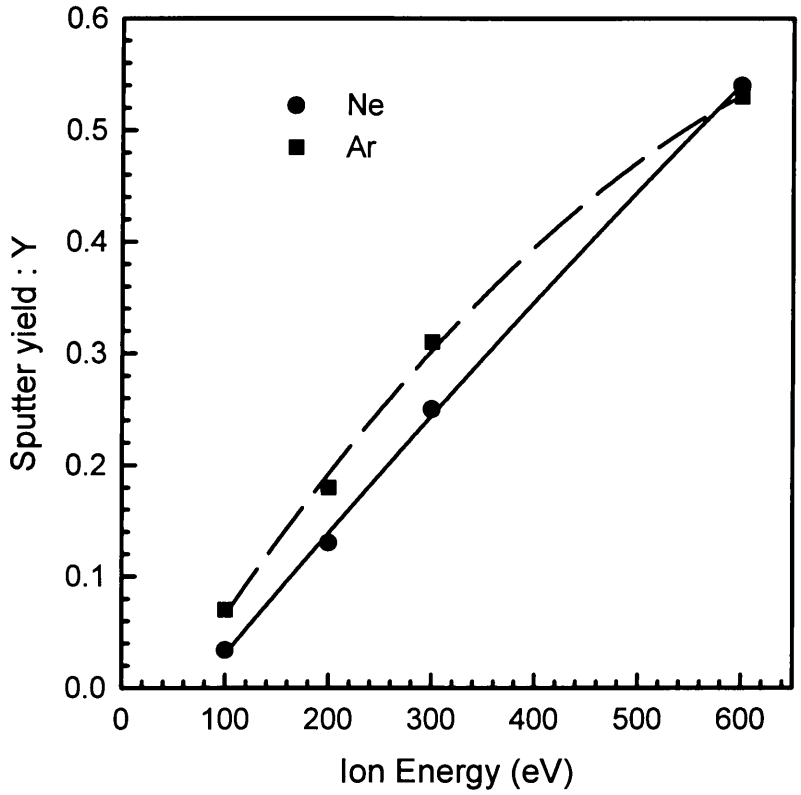

Figure 3.7: Sputter yields of low energy (100-600 eV) Ne- (circles) and Ar-ions (squares).

3.4.3.3 Etch Uniformity

In addition to achieving highly anisotropic etching, plasma reactors are designed to yield optimum etching uniformity. This uniformity depends on factors such as the surface morphology of the starting material, the distribution of the Ar ions over the

substrate surface, the plasma pressure, the presence of metallic impurities on the surface and the degree of re-deposition of sputtered atoms, amongst others. As pointed out in section 3.4.1.4, the sputter yield depends on crystal orientation. It is, therefore, conceivable that when the surface of the substrate prior to sputter etching is rough, the plasma ions will bombard the latter along different crystallographic directions resulting in preferential etching. Furthermore, non-uniform distribution of ions on the surface will also lead to uneven etching. High plasma pressures are desired for higher etching rates and thus for minimising residual bonding damage. However, when pressure is increased, the electrode spacing becomes be very small (of the order of 1 cm), and therefore the degree to which the two electrodes are parallel to each other can have significant effect on the uniformity because of the difference in electric field from one point to the other. Metallic impurities have different sputter yields than the substrate and because of their shielding effect will cause non-uniform etching. The shielding effect is further increased by re-deposited sputtered Si atoms.

3.5 Reactive Ion Etching (RIE)

The unique feature of RIE as compared to physical sputtering lies in the gasification of substrate at the surface by reactive species generated in the plasma. The modification of substrate surfaces by bombarding ions significantly increasing the rate of gas-solid reaction is more important than the nature of the reactive species. This effect is clearly demonstrated in Figure 3.8. When both Ar and XeF_2 are used, the etch

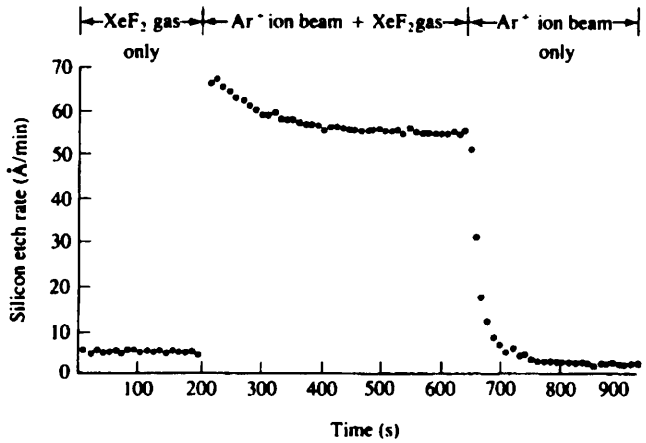

Figure 3.8: Synergistic effect of reactive and non-reactive (Ar) ions yields an enhanced etch rate. Etch rate of the mixture of gases is much higher than the sum of the etch rates of the individual components (ref [59]).

rate becomes much greater than the sum of the individual rates. The higher reactive ion etching rate results in less residual damage in the semiconductor substrate. Noble gas species are often mixed with the reactive plasma in low concentrations to, firstly, reduce the etching rate to achieve higher anisotropy and etch uniformity, and secondly, to stabilise the plasma thermally. RIE is ion-induced if no etching takes place in the absence of ions, and it is ion-enhanced if etching can take place in the absence of ions, but is greatly enhanced by ion bombardment. In either case, the physical momentum transfer from colliding ions is the initiator for plasma etching. Table III summarises the etching properties of various RIE techniques.

Table III: Properties of dry etching techniques

TECHNIQUE	PRESSURE (mbar)	ETCH MECHANISM	SELECTIVITY	rf /dc	PROFILE
Downstream Etching	10^{-1} - 10^{0}	chemical	excellent	rf	isotropic
Barrel Etching	10^{-1} - 10^{0}	chemical	excellent	rf	isotropic
Plasma Etching (PE)	10^{-1} - 10^{1}	chemical	good	rf	isotropic or anisotropic
Ion Etching	10^{-3} - 10^{-1}	physical	poor	rf	anisotropic
Reactine Ion Etching (RIE)	10^{-3} - 10^{-1}	chemical-physical	good	rf	isotropic or anisotropic
Magnetron Ion Etching (MIE)	10^{-3} - 10^{-2}	physical	poor	rf	anisotropic
Magnetron Reactive Ion Etching (MRIE)	10^{-3} - 10^{-2}	chemical-physical	good	rf	anisotropic
Triode Etching	10^{-3} - 10^{-2}	chemical-physical	good	rf	anisotropic
Ion Beam Etching (IBE)	$\approx 10^{-4}$	physical	poor	dc	anisotropic
Reactive Ion Beam Etching (RIBE)	$\approx 10^{-4}$	chemical-physical	good	dc	anisotropic
Chemically Assisted Ion Beam Etching (CAIBE)	$\approx 10^{-4}$	chemical-physical	good	dc	isotropic or anisotropic

REFERENCES

[1] P. Sigmund, Phys. Rev. **184**, 383 (1969).

[2] G.K. Wehner and G.S. Anderson, in Handbook of Thin Film Technology, Chap. 3, Eds. L. Maissel andR. Glang (McGraw-Hill, New York, 1970).

[3] Y. Yamamura and J. Bohdansky, Vacuum **35**, 561 (1985).

[4] A.J. Moses, in The Practising Scientist's Handbook, Chap. IX (Van Nostrand Reinhold, New York, 1978).

[5] L. Maissel, in Handbook of Thin Film Technology, Chap. 4, Eds. L. Maissel and R. Glang (McGraw-Hill, New York, 1970).

[6] W.H. Gries, Mikrochimica Acta [Wien] **Suppl. 11**, 33 (1985).

[7] W.H. Gries, Pure Appl. Chem. **64**, 545 (1992).

[8] J.P. Biersack and J.F. Ziegler, Nucl. Instrum. Method **194**, 93 (1982).

[9] O.B. Firsov, Zh. Eksp. Teor. Fiz. **34**, 447 (1958).

[10] W.H. Gries and H.J. Strydom, Fres. Z. Anal. Chem. **319**, 727 (1984).

[11] H.J. Strydom and W.H. Gries, Rad. Eff. Lett. **86**, 145 (1984).

[12] H.J. Strydom and W.H. Gries, *A table of normalized sputtering yields for mono- elemental polycrystalline targets*. SMAT3, Materials Characterization Division, Council for Scientific and Industrial Research, Pretoria, South Africa, 1984.

[13] H.H. Anderson and H.L. Bay, in Sputtering by Particle Bombardment I, Ed. R. Behrisch (Springer Verlag, Berlin, 1981), p. 202.

[14] Y. Yamamura, Nucl. Instrum. Method **B2**, 578 (1984).

[15] J.S. Williams and R.G. Elliman, in Ion Beams for Materials Analysis (Academic Press, Sydney, 1989), Chap. 6.

[16] L. Lindhard, M. Scharff and H.E. Schiott, Kgl. Dan. Vid. Selsk. Mat. fys. Medd. **33** (14), (1963).

[17] H. Bethe, Z. Phys. **76**, 293 (1932).

[18] F. Bloch, Ann. Physik **16**, 287 (1933).

[19] F. Bloch, Z. Phys. **81**, 363 (1933).

[20] J. Lindhard, Kgl. Dan. Vid. Selsk. Mat. fys. Medd. **34** (14), (1965).

[21] W.K. Hofker, Philips Research Reports **Suppl. 8**, (1975).

[22] J.P. Biersack and L.G. Haggmark, Nucl. Instrum. Methods **174**, 257 (1980).

[23] W. Eckstein, in Computer Simulation of Ion-Solid Interactions, Springer Ser. Mat. Sci., Vol. 10 (Springer, Berlin, Heidelberg 1991).

[24] J. Lindhard, V. Nielsen, M. Scharff and P.V. Thompsen, Kgl. Dan. Vid. Selsk. Mat. fys. Medd. **33** (10) (1963).

[25] P. Sigmund, Appl. Phys. Lett. **14**, 114 (1969).

[26] P. Sigmund, Appl. Phys. Lett. **25**, 169 (1974); plus erratum in **27** (197) p. 52.

[27] D.A. Thompson and R.S. Walker, Rad. Effects **36**, 91 (1978).

[28] J.A. Brinkman, J. Appl. Phys. **25**, 961 (1954).

[29] J.A. Brinkman, Amer. J. Phys. **24**, 246 (1956).

[30] D.A. Thompson, Rad. Effects **56**, 105 (1981).

[31] G.D. Watkins, Trans. IEEE **NS-16** (6), 13 (1969).

[32] G.D. Watkins and J.W. Corbett, Phys. Rev. **121**, 1001 (1961).

[33] J.W. Corbett and G.D. Watkins, Phys. Rev. Lett. **7**, 314 (1961).

[34] G.E. Jellison, J. Appl. Phys. **53**, 5715 (1982).

[35] L.W. Song, B.W. Benson and G.D. Watkins, Phys. Rev.B **33**, 1452 (1986).

[36] E.E. Klontz and J.W. MacKay, J. Phys. Soc. Japan **8** (Suppl. III), 216 (1963).

[37] K.L. Brower, Rad. Eff. **8**, 213 (1971).

[38] V. Rianeri, G. Fallica and S. Libertino, J. Appl. Phys. **79**, 9012 (1996).

[39] Y.H. Lee and J.W. Corbett, Phys. Rev. B **8**, 2810 (1973).

[40] K. Weiser, Phys. Rev. **126**, 1427 (1962).

[41] A.V. Mudryi, A.L. Pushkarchuk, V.D. Tkachev and A.G. Ul'yashin, Phys. Status Solidi B **125**, K75 (1984).

[42] A.V. Mudryi, A.L. Pushkarchuk and A.G. Ul'yashin, Sov. Phys. Semicond. **19**, 225 (1985).

[43] J. Weber, R.J. Davis, H.-U. Habermeier, W.D. Sawyer and M. Singh, Appl. Phys. A **41**, 175 (1986).

[44] J. Weber, Physica B **170**, 201 (1991).

[45] S.K. Estreicher, J. Weber, A. Derecskei-Kovacs and D.S. Marynick, Phys. Rev. B **55**, 5037 (1997).

[46] J. Weber and M. Singh, Appl. Phys. Lett. **49**, 1617 (1986).

[47] J.L. Benton, B.E. Weir, D.J. Eaglesham, R.A. Gottscho, J. Michel and L.C. Kimerling, J. Vac. Sci. Technol. B **10**, 540 (1992).

[48] E. Gürer and B.W. Benson, Mat. Res. Soc. Symp. Proc. **163**, 295 (1990).

[49] L.C. Kimerling, M.T. Asom, J.L. Benton, P.J. Drevinsky and C.E. Caefer, Materials Science Forum **38-41**, 141 (1989).

[50] E. Gürer. B.W. Benson and G.D. Watkins, Materials Science Forum **83-87**, 339 (1992).

[51] W. Schroter, J. Kronewitz, U. Gnauert, F. Riedel and M. Seibt, Phys. Rev. B **52**, 13 726 (1995).

[52] T. Markvart, D.P. Parton, J.W. Peters and A.F.W. Willoughby, Materials Science Forum **143-147**, 1381 (1993).

[53] S. Libertino, S. Coffa, G. Franzo and F. Priolo, J. Appl. Phys. **78** (6), 3867 (1995).

[54] J.W. Corbett, J.P. Karins and T.Y. Tan, Nucl. Instrum. Methods **182-183**, 457 (1981).

[55] L.C. Kimerling, Inst. Phys. Conf. Ser. **31**, 221 (1977).

[56] W.D. Sawyer, J. Weber, G. Nabert, J. Schmalzlin and H.-U. Habermeiser, J. Appl. Phys. **68**, 6179 (1990).

[57] J.S. Williams, Mat. Res. Soc. Symp. Proc. 51, 83 (1985).

[58] Dong-Zhi Chi and S. Ashok, Mat. Res. Soc. Symp. Proc. **442**, (1997)

[59] Hong. H. Lee, in Fundamentals of Microelectronics Processing, Chapter 5 (McGraw Hill, Singapore, 1990).

[60] I.A. Morozov, Yu.V. Esipchuk, G.N. Tilinin, A.V. Trofimov, Yu.A. Sharov and G.Ya. Shchepkin, Sov. Phys. Tech. Phys. **17**, 38 (1972).

[61] F.H. Mullins and A. Brunnschweiler, Solid-State Electron. **19**, 47 (1976).

[62] L.P. Andersson and A.O. Evwaraye, Vacuum **28**, 5 (1978).

[63] H. Norström, E. Grusell, L.P. Andersson and S. Berg, Phys. Scr. **18**, 421 (1978).

[64] S.J. Fonash, Solid State Technol. **28**, 201 (1985).

[65] J.P. Gambino, C.C. Parks, G.S. Oehrlein and M.A. Jaso, Abstract 205, p. 304, The Electrochemical Society Extended Abstracts, Vol. 89-1, Los Angeles, CA, May 7-12, 1989.

[66] X.-C. Mu, S.J. Fonash and R. Singh, Appl. Phys. Lett. **49**, 67 (1986).

[67] S.J. Jeng and G.S. Oehrlein, Appl. Phys. Lett. **50**, 1912 (1987).

[68] J.M. Heddleson, M.W. Horn and S.J. Fonash, J. Vac. Sci. Technol. **B6**, 280 (1988).

[69] R. Herlocher III and S.J. Fonash, in Plasma Processing, eds. G.S. Mathad and D.W. Hess, The Electrochemical Society Softbound Proceedings Series, Pennington, NJ (1990) p. 304.

[70] S.W. Pang, D.D. Rathman, D.J. Silversmith, R.W. Mountain and P.D. DeGraff, Appl. Phys. Lett. 54, 3272 (1983).

[71] T. Wantanabe and Y. Yoshida, Solid State Technol. 27, 263 (1984).

[72] F.J. Montillo, R.G. Frieser and W.K. Chu, Abstract 279, p. 681, The Electrochemical Society Extended Abstracts, Vol. 81-2, Denver, CO, Oct. 11-16, 1981.

[73] F.K. Moghadam and X.-C. Mu, IEEE Trans. Electron Dev. **36**, 1602 (1986).

[74] M. Hirai, H. Iwakuro, J. Ohno and T. Kuroda, IEEE Trans. Components Hybrids and Manufacturing Technology **13** (4), 629 (1990).

[75] P. Spirito, C.M. Ranson and G.S. Oehrlein, Solid-State Electron. **29**, 607 (1986).

[76] T.J. Faith, J.J. O'Neill, R.S. Irven, J.L. Vossen, J.M. Shaw and J.H. Thomas, J. Electrochem. Soc. **134**, 665 (1987).

[77] B.N. Chapman, in Glow Discharge Processes, Wiley, New York, 1980.

[78] E.W. McDaniel, in Collision Phenomena in Ionized Gases, Wiley, New York, 1964.

[79] W.D. Davis and T.A. Vanderslice, Phys. Rev. **131**, 219 (1963).

[80] D. Field, D.F. Klemperer, P.W. May and Y.P. Song, J. Appl. Phys. **70** (1), 82 (1991).

[81] P.W. May, D. Field and D.F. Klemperer, J. Appl. Phys. **71** (8), 3721 (1992).

[82] F.D. Auret, G. Myburg, W.E. Meyer, P.N.K. Deenapanray, H. Nordhoff, S.A. Goodman, M. Murtagh, Shu-Ren Ye and G.M. Crean, Appl. Phys. Lett. **71**, (1997).

[83] M. Meyyappan, H.S. Lee, D. Eckart, M. Namaroff and J. Sasserath, J. Vac. Sci. Technol. B **10**, 1215 (1992).

[84] S.J. Fonash, J. Electrochem. Soc. **137**, 3885 (1990).

[85] S. Ashok, S.J. Fonash and R. Singh, Appl. Phys. Lett. **39**, 423 (1981).

[86] R. Singh, S.J. Fonash, P.J. Caplan and E.H. Poindexter, Appl. Phys. Lett. **43**, 502 (1983).

[87] S.J. Fonash, S. Ashok, and R. Singh, Appl. Phys. Lett. **39**, 423 (1981).

[88] S. Ashok, P. Chow and B.J. Baliga, Appl. Phys. Lett. **42**, 687 (1983).

[89] S. Ashok and A. Mogro-Campero, IEEE Electron Device Lett. **EDL-5**, 48 (1984).

[90] S. Pang, Solid State Technol. **27**, 249 (1984).

[91] F.K. Moghdam and X.-C. Mu, IEEE trans. Electron Dev. **36**, 1602 (1989).

CHAPTER 4

METAL-SEMICONDUCTOR CONTACTS

Metal-semiconductor contacts had been used as radio wave detectors in the early days of wireless telegraphy in the form of point contact diodes. After being replaced by vacuum diodes in the early 1920s, the applications of point contact diodes as frequency converters and low-level microwave detectors were revived during the Second World War. Point contact diodes, however, proved to be highly unreliable and were subsequently replaced by rectifiers obtained by depositing a thin metallic film on a clean semiconductor surface. Metal-semiconductor contacts or Schottky barrier diodes (SBDs) now provide an enabling technology for ultra-high frequency (Terahertz) applications. Unlike conventional p-n junction diodes, SBDs do not display minority carrier effects such as junction capacitance and reverse recovery time. This chapter discusses the principles of barrier formation and of current transport mechanisms over the barrier between a metal contact to an n-type semiconductor. A similar approach can be used for a metal contact on p-type semiconductor. Furthermore, details concerning the experimental set-up used to measure the electrical properties of SBDs are also given.

4.1 Formation of an Ideal Metal-Semiconductor Junction

According to the Schottky-Mott theory [1,2], the potential barrier which arises at a metal-semiconductor interface results from the difference in work functions of the two materials. The work function of a metal, ϕ_m, is defined as the amount of energy required to raise an electron from the Fermi level to the vacuum level, ie., an energy state just outside the metal wherein the electron has zero kinetic energy [Figure 4.1(a)]. The work function has a volume contribution due to potential of the metal lattice and a surface contribution arising from any surface dipole layers. The semiconductor work function, ϕ_s, is defined in a similar way and is a variable quantity depending on the position of the Fermi level (i.e., doping level) [Figure 4.1(a)].

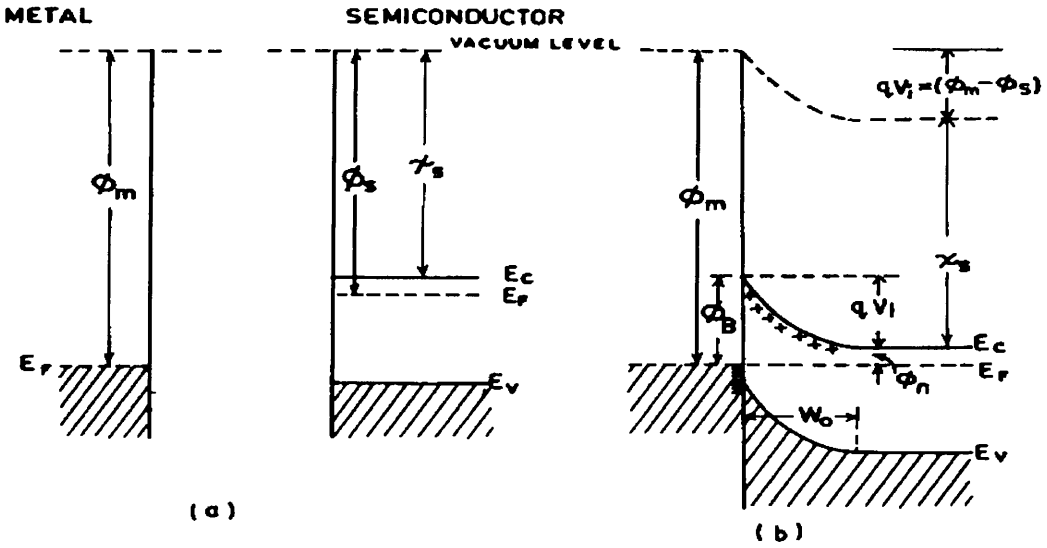

Figure 4.1: Electron energy band diagrams of metal contact to n-type semiconductor with $\phi_m > \phi_s$. (a) Neutral materials separated from each other and (b) thermal equilibrium [M.S. Tyagi, in "Metal-Semiconductor Schottky Barrier Junctions and Their Applications" (Ed. B.L. Sharma), Plenum Press, New York, 1984].

Another important parameter which is independent of the semiconductor doping level is the electron affinity, χ_s. As seen from Figure 4.1(a), χ_s is the energy difference of an electron between the vacuum level and the conduction band edge, and also contains a surface dipole term. ϕ_s and χ_s are related as follows:

$$\phi_s = \chi_s + \xi \ , \tag{4.1}$$

where ξ is the energy difference between the conduction band and the Fermi level, and is given by:

$$\xi = kT \ln\left(N_C / N_D\right), \tag{4.2}$$

where k is the Boltzmann constant, T is the temperature in Kelvin, N_C is the effective density of states in the conduction band and N_D is the free carrier concentration.

When the metal and semiconductor are brought into intimate contact electrons from the conduction band of the semiconductor flow into the metal until the Fermi level on the two sides of the interface coincide. Due to the decrease in free carriers on the semiconductor side adjacent to the interface, and given that the Fermi level remains constant throughout under thermal equilibrium, the conduction band edge of the

semiconductor bends up as depicted in Figure 4.1(b). Consequently, a positively charged space-charge region of width, w, is formed on the semiconductor side of the interface, while a thin negatively-charged layer contained within the Thomas-Fermi screening distance (~0.5 Å) from the interface is formed on the metal side. The metal-semiconductor junction thus formed is similar to the p^+-n junction, and the potential barrier, ϕ_B, also known as the Schottky barrier, is given by (Schottky-Mott theory):

$$\phi_B = \phi_m - \chi . \tag{4.3}$$

It can be seen from the above discussion that the metal-semiconductor junction is rectifying when $\phi_m > \phi_s$. For an n-type semiconductor, an ohmic contact is formed when $\phi_m < \phi_s$. The opposite behaviour is observed in the case of a p-type semiconductor.

4.1.1 The Depletion Approximation

The exact shape of the potential barrier can be calculated from the charge distribution within the depletion layer. Assuming the junction is abrupt and the doping level in the space charge region to be constant and equal to N_D (the depletion approximation), the magnitude of the electric field at a distance, x, from the interface can be obtained from Gauss' theorem as:

$$E(x) = -\frac{qN_D}{\varepsilon_s}(w - x) . \tag{4.4}$$

The magnitude of E increases linearly from 0 at $x = w$ to reach its maximum value of qN_Dw/ε_s at the interface (ε_s being the permittivity of the semiconductor). Taking the electrostatic potential, V, to be zero within the neutral region of the semiconductor, the potential at x is given by:

$$V(x) = \int_x^w E(x)\,\mathrm{d}x = -\frac{qN_D}{2\varepsilon_s}(w - x)^2 . \tag{4.5}$$

The magnitude of the electrostatic potential, therefore, rises quadratically as the metal is approached and has a value $qN_Dw^2/2\varepsilon_s$ at the interface. Since $V(0)$ is equal to the diffusion potential, V_d, the width of the depletion layer, w, can be expressed as:

$$w = \sqrt{\frac{2\varepsilon_s V_d}{qN_D}} \ . \tag{4.6}$$

If the total charge per unit area due to uncompensated donors in the depletion region is defined as $Q_d = qN_D w$, then V_d can be written as:

$$V_d = \frac{Q_d^2}{2\varepsilon_s qN_D} \ . \tag{4.7}$$

According to Eqn. (4.7), the differential capacitance per unit area is given by:

$$C = \frac{\partial Q_d}{\partial V_d} = \left(\frac{\varepsilon_s qN_D}{2V_d}\right)^{1/2} = \frac{\varepsilon_s}{w} \ . \tag{4.8}$$

In the depletion approximation, a reverse biased Schottky barrier diode can be regarded as a parallel plate capacitor, whereby the depletion layer acts as a dielectric between the conducting metal and neutral region of the semiconductor. Although the doping concentration in the depletion layer can be tailored to be constant, the transition between the space-charge layer and the neutral region of the semiconductor occurs smoothly over a distance equal to the Debye length, in which the bands bend by about $3kT/q$.

4.2 The Generalised Bardeen Model

The Schottky-Mott theory assumed that the semiconductor did not contain any charge at the surface such that the Fermi level was constant throughout the material [Figure 4.1(a)]. Furthermore, it was assumed that the surface dipole contributions to ϕ_m and ϕ_s remained unchanged after the metal made contact with the semiconductor. In practice, the barrier height of covalent semiconductors (e.g., Si and GaAs) is less sensitive to ϕ_m as predicted by Eqn. (4.3). Bardeen [3] explained this discrepancy in terms of localized states at the surface of the semiconductor (Figure 4.2).

The surface of covalently bonded semiconductors are characterised by a disruption in the periodic structure of the crystal lattice. Dangling bonds at the semiconductor surface give rise to localized states which, usually, have a continuous distribution of energy levels in the forbidden gap. These surface states are characterised by a neutral

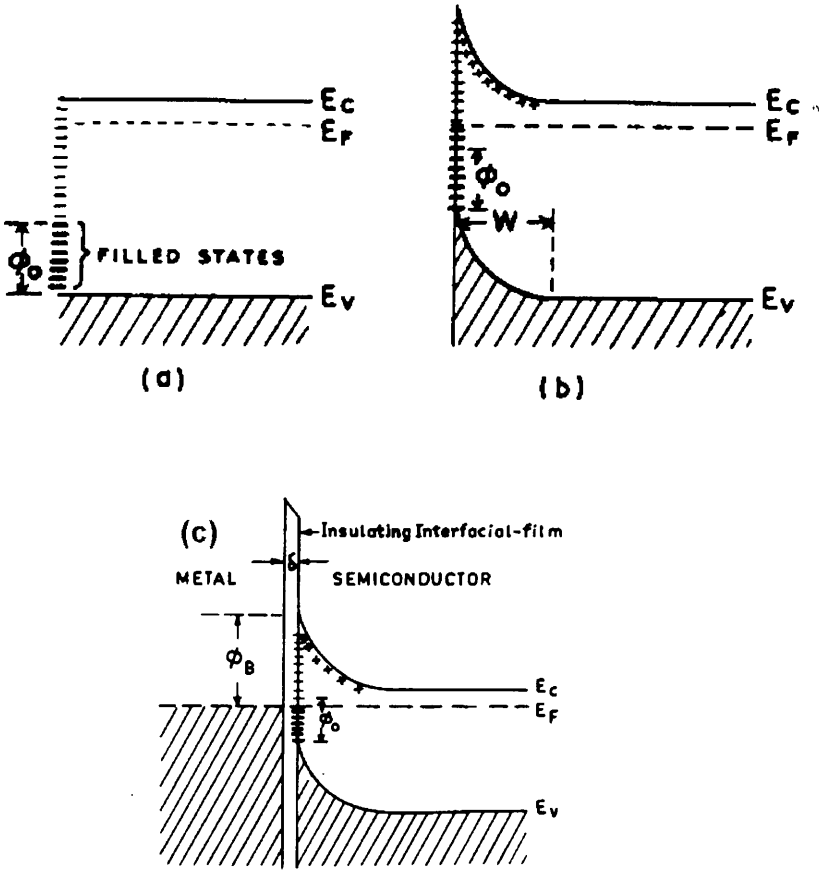

Figure 4.2: Electron energy band diagrams on n-type semiconductor with surface states and a thin interfacial layer. The diagrams show: (a) flat band at the surface, (b) surface in thermal equilibrium with the bulk, and (c) semiconductor in contact with metal [M.S. Tyagi, in "Metal-Semiconductor Schottky Barrier Junctions and Their Applications" (Ed. B.L. Sharma), Plenum Press, New York, 1984].

level, ϕ_0, wherby all the states below ϕ_0 are filled (donor-type states), while those above it are empty (acceptor-type). Furthermore, chemical cleaning of the semiconductor prior to metallization invariably leaves a thin insulating oxide layer(~20 Å) on the surface. The presence of a native oxide layer, adsorbed contaminants and processing-induced defects (for instance, see Chapter 3 for a description of sputter deposition and plasma etching-induced damage in Si) will produce interfacial states and alter their densities [4]. The energy band diagram of a metal-semiconductor contact with surface states and an interfacial layer of thickness, δ, is illustrated in Figure 4.2(c). In this case, the barrier height can be written as [5]:

$$\phi_B^0 = \gamma(\phi_m - \chi) + (1-\gamma)(E_g - \phi_0), \qquad (4.9)$$

where

$$\gamma = \frac{\varepsilon_i}{\varepsilon_i + q^2 \delta D_s}, \qquad (4.10)$$

E_g is the band gap, ε_i is the permittivity of the interfacial layer and D_s is the density of interface states per eV per unit area in the band gap. As shown in Figure 4.2(b), equilibrium is reached when electrons from the semiconductor adjacent to the surface occupy the states above ϕ_0. This results in the semiconductor surface becoming negatively charged together with the formation of a depletion region near to the surface. When a metal is brought into contact with the semiconductor, charge exchange takes place between the metal and the semiconductor surface states leaving the depletion region virtually unperturbed.

It may be observed that $\phi_B{}^0$ tends to the Schottky-Mott limit (ϕ_m - χ) as $D_s \rightarrow 0$ and to the so-called Bardeen limit (E_g - ϕ_0) as $D_s \rightarrow \infty$. In the latter case, the barrier height is said to be "pinned" by surface states, and becomes essentially independent of ϕ_m.

4.2.1 Electric Field Dependence of the Barrier Height

The flat band barrier height $\phi_B{}^0$ in Eqn. (4.9) is obtained when there is no electric field in the semiconductor. As discussed above, a linear electric field is present in the depletion region of the unbiased junction, and this makes the barrier height a function of the voltage. The zero bias barrier height is, therefore, not equal to the flat band barrier height. Only two of the dominant causes which make the barrier height depend on the electric field in the depletion region will be considered here.

Firstly, the presence of an electric field in the semiconductor alters the potential drop in the interfacial layer. The consequent change in the barrier height can be expressed as [5]:

$$\phi_B = \phi_B^0 - \alpha E_{\max}, \qquad (4.11)$$

where

$$\alpha = \frac{\delta \varepsilon_s}{\varepsilon_i + q^2 \delta D_s}. \qquad (4.12)$$

When $\delta < 20$ Å, the difference between ϕ_B and $\phi_B{}^0$ is insignificant at all forward biases and also at small reverse biases.

The image force barrier lowering is the second effect which makes the barrier height depend on the electric field in the depletion region, and occurs even in the absence of the an interfacial layer. This barrier lowering results from the electric field produced by an electron moving towards the metal surface. If the electron is at a distance, x, from the interface, its potential can be calculated by assuming a hypothetical positive image charge q located at a distance, $-x$, inside the metal. The Coulombic attraction between the electron and its image charge is $q^2/4\pi\varepsilon_d(2x)^2$ and the electron will have a negative potential energy $-q^2/16\pi\varepsilon_d x$ relative to an electron at infinity. This potential energy is added to the Schottky barrier energy $-qEx$ to obtain the total energy of the electron. The magnitude, $\Delta\phi_B$, of the barrier lowering of the resultant potential can be expressed as [6]:

$$\Delta\phi_B = \left[\frac{q^3 N_D}{8\pi^2 \varepsilon_d^2 \varepsilon_s}(V_i - V)\right]^{1/4}, \qquad (4.13)$$

where V_i is the built-in potential, V is the applied voltage and ε_d is the image force permittivity, which for all practical purposes can be taken as being equal to ε_s. It should be noted that when the barrier height is measured by a method which does not require transport of electrons over the barrier (e.g., capacitance-voltage measurements), the image force lowering of the barrier need not be accounted for.

4.3 Current Transport Mechanisms

The electrical properties of a Schottky diode are determined by the transport mechanisms across the barrier. The mechanisms by which electrons are transported across a metal-semiconductor junction under forward bias are:

(a) emission of electrons from the semiconductor over the top of the barrier into the metal;

(b) quantum-mechanical tunnelling through the barrier;

(c) recombination in the depletion region;

(d) recombination in the neutral region (hole injection).

The inverse processes occur under reverse bias. Diodes in which (a) is the dominant transport mechanism are referred to as near-ideal. The remaining processes cause departures from ideality.

According to Bethe's thermionic-emission theory, the assumption is made that the current-limiting process under forward bias is the transfer of electrons across the interface. In this case, the Fermi level of the semiconductor is raised relative to that of the metal, resulting in a decrease in band bending and a decrease in the barrier "seen" by electrons in the semiconductor. The inverse process under reverse bias is analogous to thermionic emission from a metal into a vacuum but with the barrier height, ϕ_B, replacing the metal work function, ϕ_m. In near-ideal Schottky diodes fabricated on Si with doping concentrations in the 10^{15} - 10^{17} cm^{-3} range, the dominant mechanism for reverse bias and small forward bias is thermionic emission. By assuming that the velocity distribution of the electrons in the conduction band to be Maxwellian, the current density, J, flowing across the barrier can be written as:

$$J = A^* T^2 \exp\left(-\frac{q\phi_B}{kT}\right)\left\{\exp\left(\frac{qV}{kT}\right) - 1\right\}. \qquad (4.14)$$

A^* is the effective Richardson constant and T the temperature of the junction. For non-ideal diodes with series resistance, R_s, and $V > 3kT/q$, the current-voltage characteristics are given by:

$$J \approx J_0 \exp\left\{\frac{q(V - IR_s)}{nkT}\right\}. \qquad (4.15)$$

In Eqn. (4.15) J_0 is the saturation current density and n the ideality factor. The ideality factor can be extracted from the experimental J/V characteristic, for $V > 3kT/q$, through the relationship:

$$n = \frac{q}{kT}\left\{\frac{\partial V}{\partial(\ln J)}\right\}. \qquad (4.16)$$

The ideality factor was introduced in Eqn. (4.15) to account for the non-ideal behaviour of manufactured diodes. In order to obtain meaningful values of barrier

height from current-voltage (I-V) measurements, the ideality factor should be less than 1.05. The saturation current density, J_0, can be expressed as:

$$J_0 = A^* T^2 \exp\left\{-q\left[\frac{\phi_{B0} - \Delta\phi_B}{kT}\right]\right\}, \qquad (4.17)$$

where ϕ_{B0} is the zero bias barrier height and $\Delta\phi_B$ is given by Eqn. (4.13). The effective zero bias barrier height, $\phi_{e0} = \phi_{B0} - \Delta\phi_B$.

4.4 Current-Voltage (I-V) and Capacitance-Voltage (C-V) Measurements

The diode parameters n, J_0 and R_s can be determined from the characteristic ln(J) versus V curve (i.e., the I-V characteristic curve). A least squares fitting procedure is applied to the forward bias region ($V > 3kT/q$) of the graph, and the ideality factor is extracted using Eqn. (4.16). The value of J_0 is obtained by extrapolating the linear fit to $V = 0$ V, while the zero bias barrier height can be calculated from Eqns. (4.17) and (4.13). The free carrier concentration of the semiconductor material can be extracted from capacitance-voltage (C-V) measurements.

In C-V measurements, the diode capacitance is measured as a function of applied reverse bias. When a small, high-frequency (1 MHz) ac voltage of a few mV is applied to the reverse biased diode, the depletion region capacitance, C, is given by the relation:

$$C = S\left[\frac{\varepsilon_s q N_D}{2(V_i + V_R - kT/q)}\right]^{1/2}, \qquad (4.18)$$

where S is the electrically active area of the Schottky contact, V_R is the applied reverse bias, and all other symbols have their usual meanings. In Eqn. (4.18) it is assumed that $\delta < 20$ Å and that the n-type semiconductor has a uniform donor concentration, N_D. A plot of $1/C^2$ versus V_R gives a straight line with slope $2/S^2\varepsilon_s q N_D$ and an intercept on the voltage axis $V_0 = (V_i - kT/q)$. The slope of the line is used to determine the value of N_D and the C-V barrier height, ϕ_B^{CV} (i.e., the flat band barrier height) can be calculated from:

$$\phi_B^{CV} = \left(qV_0 + \xi + kT\right) . \qquad (4.19)$$

If N_D is not constant, as shown in Figure 4.3, the differential capacitance method is used to determine the doping profile. Assuming that a small increase in reverse bias,

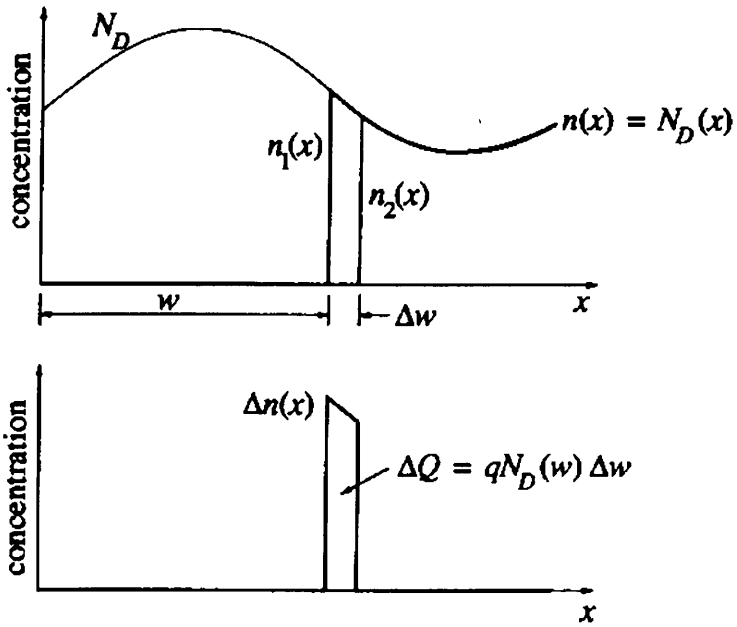

Figure 4.3: The charge distribution in the depletion region of a non-uniformly doped semiconductor (courtesy of Mr. W.E. Meyer).

ΔV_R, increases the width of the depletion layer by Δw, and that the concentration of free carriers before and after increasing V_R are $n_1(x)$ and $n_2(x)$, the decrease in majority carriers per unit area, ΔQ, can be written as:

$$\Delta Q = \int_0^\infty \Delta n(x)dx . \qquad (4.20)$$

If Δw is small, the above equation can be simplified to:

$$\Delta Q = qN_D(w)\Delta w . \qquad (4.21)$$

The increase in the applied voltage can be found by calculating the increase in the potential at the interface due to the change in charge distribution, yielding:

$$\Delta V_R = qN_d(w)w\Delta w / \varepsilon_s . \qquad (4.22)$$

Using Eq. (4.8) in conjunction with Eq. (4.22), the free carrier density can be found from the measured capacitance per unit area:

$$N_D(w) = -\frac{C^3}{q\varepsilon_s}\left(\frac{dC}{dV}\right)^{-1}. \qquad (4.23)$$

The barrier height of a Schottky diode can also be calculated from activation energy measurements. In this case, the forward current, I_F, at a fixed forward bias, V_F, is measured at different temperatures, and a graph of $\ln(I_F/T^2)$ versus $1/T$ is drawn. This Arrhenius plot can be expressed as:

$$\ln\left(\frac{I_F}{T^2}\right) = \ln\left(SA^{**}\right) - \frac{q}{kT}\left(\phi_{0K}^{Act} - V_F\right), \qquad (4.24)$$

where A^{**} is the experimentally determined value of the Richardson constant and ϕ_{0k}^{Act} is the value of the barrier height at $T = 0$ K which is extracted from the gradient of the Arrhenius plot. The intercept at $1/T = 0$ K gives the value SA^{**}. Experimentally determined values of A^{**} are significantly smaller than those of A^{*} because the former include the effect of processes such as phonon scattering and quantum mechanical tunnelling and reflection. A typical value for A^{**} in Si is $112\text{x}10^4$ $\text{Am}^{-2}\text{K}^{-2}$.

The experimental set-up used to measure the I-V and C-V properties of the metal-semiconductor diodes used in this study is illustrated in Figure 4.4.

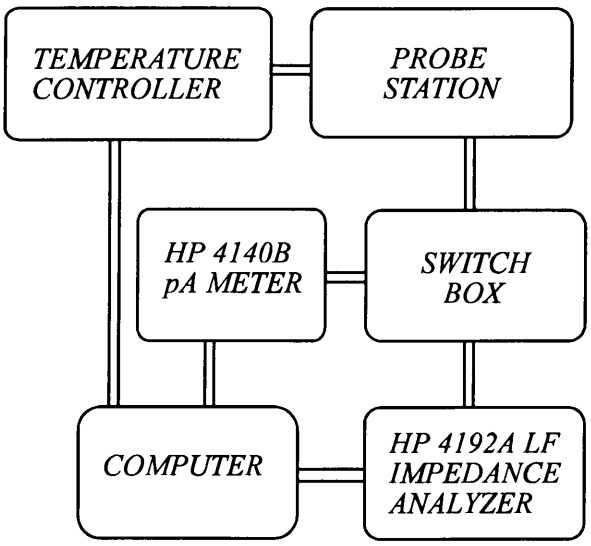

Figure 4.4: Schematic of the automated station used for the I-V and C-V measurements in this study (courtesy of Dr. S.A. Goodman).

REFERENCES

[1] W. Schottky, Naturwissenschaften **26**, 843 (1938).

[2] N.F. Mott, Proc. Camb. Phil. Soc. **34**, 568 (1938).

[3] J. Bardeen, Phys. Rev. **71**, 717 (1947).

[4] W.E. Spicer, N. Newman, C.J. Spindt, Z. Liliental-Weber and E.C. Weber, J. Vac. Sci. Technol. A **8**, 2084 (1990).

[5] E.H. Rhoderick and R.H. Williams, in Metal-Semiconductor Contacts, Clarendon Press, Oxford (1988).

[6] S.M. Sze, in Physics of Semiconductor Devices, John Wiley and Sons, New York (1981).

CHAPTER 5

DEEP LEVEL TRANSIENT SPECTROSCOPY

The success of the microelectronics industry relies on the fact that the electrical conductivity of semiconductor materials can be modified through the controlled addition of dopant atoms (e.g. P or B for Si) in the lattice. The electrically active dopant ions introduce either shallow donor (P^+) or acceptor (B^-) electronic states near the bottom of the conduction band or the top of the valence band. These substitutional impurities often create optically active defects which can be studied using luminescence techniques. On the other hand, defects created in semiconductors during growth and subsequent processing steps are usually non-radiative and introduce levels in the forbidden gap which lie farther away from the band edges, hence the terms *deep levels* or *traps*. Deep level transient spectroscopy (DLTS) was first introduced by Lang in 1974 [1,2], and has since emerged as a powerful tool for the electrical characterization of deep levels in semiconductors. Like any capacitance spectroscopy technique, DLTS monitors the change in capacitance of the depletion layer of a p-n junction or Schottky diode as a result of charge transfer between deep levels and the conduction or valence bands. DLTS yields information about a defect's thermal capture and emission rates for electrons and holes, its energy position in the bandgap and concentration. The discussion to follow will assume the depletion layer of a Schottky diode on an n-type semiconductor.

5.1 Theoretical aspects

5.1.1 Capture and emission of carriers by trapping centres

The emission and capture processes of carriers to and from the band edges are demonstrated in Figure 5.1. It can be seen that a deep level can act as an efficient recombination centre for electrons and holes. The electron and hole capture rates are given by:

$$c_n = \sigma_n \langle v_n \rangle n \ , \qquad (5.1)$$

and

$$c_p = \sigma_p \langle v_p \rangle p \ , \qquad (5.2)$$

where σ_n and σ_p are the defect's capture cross-sections for capturing electrons and holes, and n and p are the electron and hole concentrations and $\langle v_n \rangle$ is the thermal velocity:

$$\langle v_n \rangle = \sqrt{3kT / m^*} \ , \qquad (5.3)$$

where m^* is the effective mass of the electron, k is the Boltzmann constant, and T is the temperature in Kelvin.

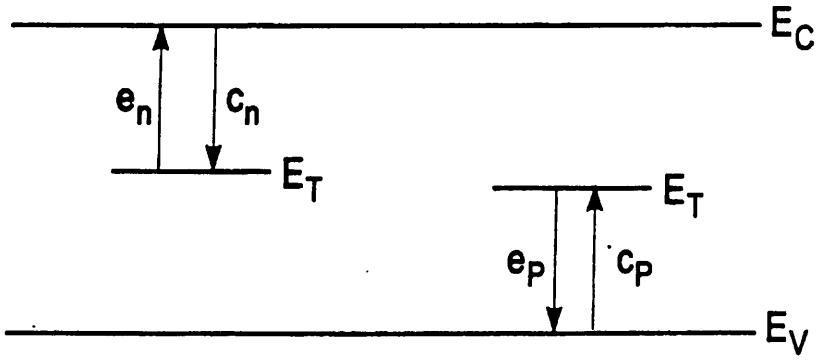

Figure 5.1: Thermal capture and emission processes. E_C - E_T is the binding energy for electrons and E_V - E_T is the binding energy for holes. Thermal emission (e_n, e_p) and capture (c_n, c_p) rates for elcetrons and holes.

A similar equation can be written for $\langle v_p \rangle$. The thermal emission rate, e_n, of an electron trap in an n-type semiconductor is proportional to a Boltzmann factor, $\exp(-\Delta E/kT)$, and can be written as [3]:

$$e_n = \frac{\sigma_n \langle v_n \rangle N_C}{g} \exp\left(-\frac{E_C - E_T}{kT}\right) \ , \qquad (5.4)$$

where N_C is the effective density of states in the conduction band and $\Delta E = E_C - E_T$, where E_C and E_T are the energies of the conduction band and the trap, respectively. The degenaracy, g, of the deep level can be equated to unity for simplicity. The parameter, ΔE, is the Gibbs free energy

$$E_C - E_T = \Delta E \equiv \Delta H - T\Delta S \ , \qquad (5.5)$$

where ΔH and ΔS are the changes in enthalpy and entropy due to the change in charge state of the deel level. A similar expression to Eq. (5.4) can be written for hole emission from a defect state to the valence band edge.

5.1.2 Electronic properties or "signature" of defect level

Using the depletion approximation, the depletion layer width of a Schottky diode was shown to vary with a voltage applied to the diode such that the junction capacitance was analogous to that of a variable-width parallel plate capacitor. Eqs. (4.6) and (4.8) show that a change in the charge density in the depletion region will result in a corresponding change in the depletion layer width and thus the junction capacitance is a direct measure of the total charge. If the concentrations of electrons and holes trapped at deep levels is changed by the thermal emission of carriers to the appropriate band edge, this change can be monitored by measuring the variation in the junction capacitance or capacitance transient at constant applied bias. The magnitude of the capacitance transient depends on the defect concentration, emission rate and temperature. Therefore, a study of the emission rate, e_n, as a function of temperature, T, can yield the signature of a defect level, i.e., its capture cross-section, σ_n, and activation energy, E_T.

The capacitance transient due to an electron trap of density N_T, capture cross-section σ_n and position E_C - E_T from the conduction band edge, after applying a filling pulse, V_p, to a junction under a quiescent reverse bias, V_r, is depicted in Figure 5.2. The unbiased energy band diagram is illustrated in Figure 5.2(a). When the barrier is reverse biased [Figure 5.2(b)], the depletion layer has a magnitude, w, which is larger than for the unbiased junction. If V_r is sufficiently large such that the electronic level of the defect is above the Fermi level, E_F, of the semiconductor, the former will be devoid of electrons and said to be empty. During the application of V_p, the width of the depletion layer is reduced [Figure 5.2(c)] and the portion of the deep level previously above E_F is filled with electrons. It is assumed here that the pulse width, t_p, is large enough to allow for complete filling of the trap states. The quiescent bias is thereafter restored resulting in electrons from the traps being emitted to the conduction band [Figure 5.2(d)] with an emission rate given by Eq. (5.4). The capacitance transient shown in Figure 5.2(e) is obtained by plotting the capacitance of

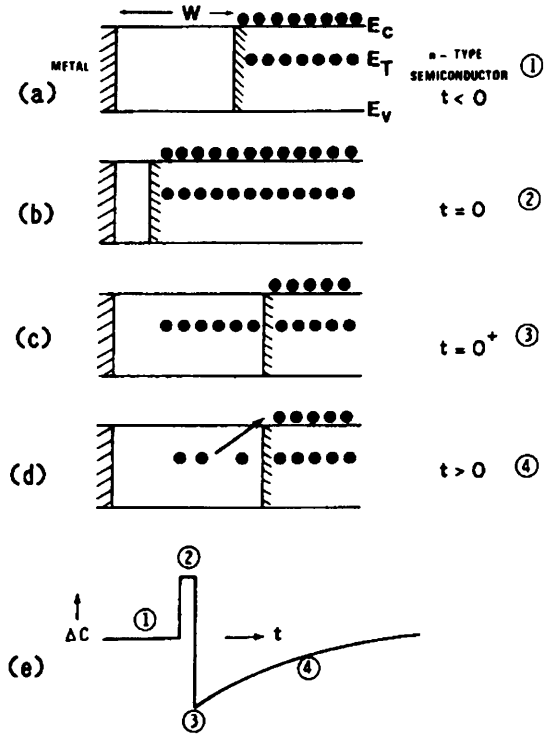

*Figure 5.2: Energy band diagram and capacitance transient resulting from a majority carrier pulse [A.R. Leitch, F.D. Auret and J.S. Vermaak, S. Afr. J. Phys. 7, **83** (1984)].*

the Schottky barrier as a function of time t starting with the reverse biased junction. The characteristic decay time constant, τ, of the capacitance transient is related to the emission rate, e_n, by:

$$e_n = 1/\tau \quad . \tag{5.6}$$

DLTS is a high frequency (MHz range) junction capacitance technique consisting of repetitively pulsing a reverse biased Schottky diode and thus generating a series of capacitance transients with a constant repetition rate. The transients are then detected by a synchronous detection system [3,4,5]. The lock-in amplifier technique used to analyse thermal emission transients and the DLTS instrumentation are discussed in section 5.2. The decay time constant of the emission transient can be varied by changing the sample temperature, and the output signal is maximised when the emission rate falls within the "rate window" of the synchronous detection system [2].

A DLTS spectrum is obtained by plotting the output signal as a function of sample temperature and an electrically active majority carrier trap is observed as a defect peak

at the temperature corresponding to its thermal emission activation energy. The temperature of the peak can be shifted by varying the rate window of the synchronous detector such that the emission rate of the trap can be calculated as a function of temperature. Assuming that the trap concentrations are small so that the change in capacitance ΔC is small compared to the total capacitance C (i.e. $\Delta C << C$), the thermal emission capacitance transient decays exponentially. Furthermore, assuming that the product $N_c\langle v_n\rangle$ in Eq. (5.4) has a T^2 dependence and neglecting the temperature dependence of σ_n, the DLTS signature of a majority carrier trap can be determined from an Arrhenius plot of the $\ln(T^2 e_n^{-1})$ versus $1000/T$. The activation energy, E_T, for electron emission to the conduction band is obtained from the slope of the Arrhenius plot. In fact, the value, E_T, represents the enthalpy of the trap plus any residual temperature dependence of σ_n or equivalently the free energy at $T = 0$ K. Since measurements are usually not done at 0 K, an accurate determination of E_T is possible only when the temperature dependence of the bandgap is known [6]. The capture cross-section, σ_n, is extracted from the intercept of the plot. Figure 5.3 shows a typical DLTS spectrum from a 5.4 MeV alpha-particle irradiated n-Si sample and the inset depicts the Arrhenius plots from which the signature of the prominent defects were obtained. The defect peaks Eα178 and Eα251 have been identified as the VO centre and $V_2^{=/-}$, respectively, while Eα445 is the superposition of the VP pair and $V_2^{-/0}$ [7]. The activation energy of $V_2^{-/0}$ (Eα435) was determined after removing the VP pair (Eα415) by annealing at 180 °C for 30 minutes. The low energy peaks Eα088 and Eα143 are the C-related metastable defects [8]. In the nomenclature used, "E" denotes an electron trap, "α" indicates that the defect was introduced upon alpha-particle irradiation, and the number represents the position of the level in meV below the conduction band.

The electron capture cross section may also be dependent on temperature such as during non-radiative carrier capture by multiphonon emission (MPE) via lattice relaxation or through the Auger effect [9]. In these cases, the capture cross-section takes the form:

$$\sigma_n = \sigma_\infty \exp\left(-\Delta E_\infty / kT\right), \qquad (5.7)$$

where σ_∞ is the capture cross-section extrapolated to $T = \infty$, and ΔE_∞ is the thermal activation energy of the capture cross-section (i.e. thermal barrier for carrier capture). The temperature dependence of the capture cross-section can be determined by plotting $\ln(\sigma_n)$ versus $1/T$. The slope of this line gives the value of ΔE_∞ and the y-intercept yields the capture cross-section extrapolated to $T = \infty$. If a deep level exhibits a temperature-dependent capture cross-section, then its corrected activation energy E_0 may be obtained from:

$$E_0 = E_T - \Delta E_\infty \ . \qquad (5.8)$$

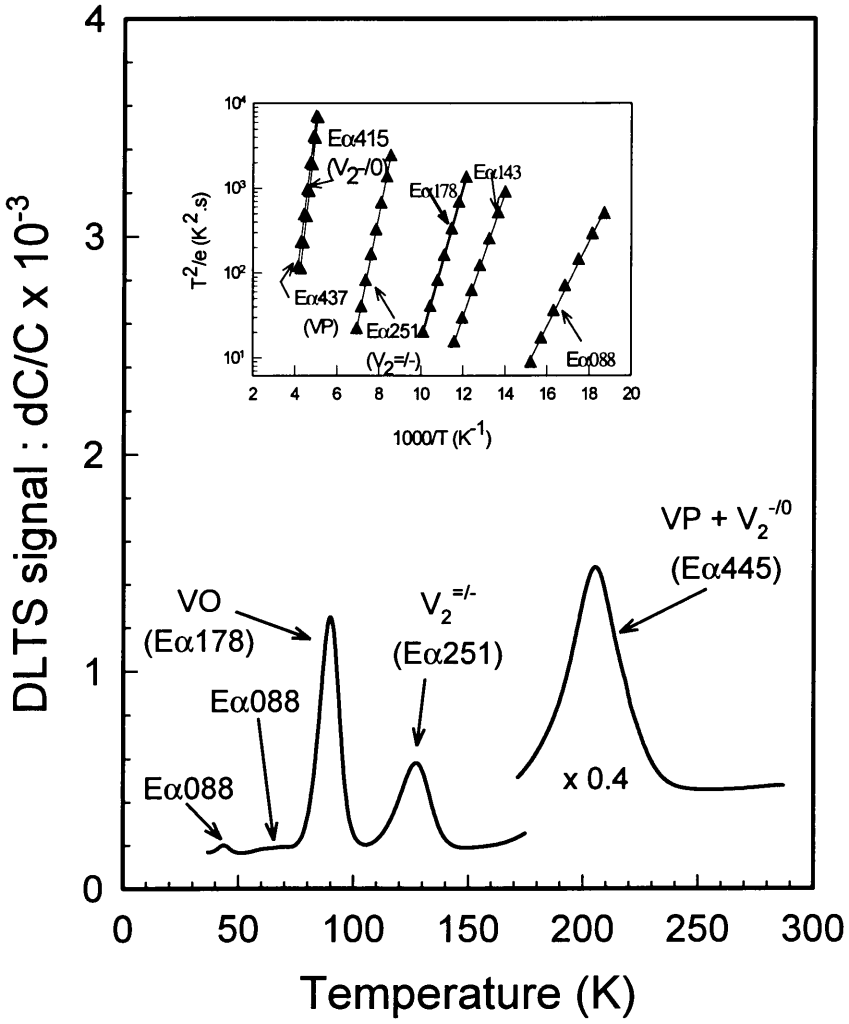

Figure 5.3: Typical DLTS spectrum of 5.4 MeV alpha-particle irradiated n-type Si containing O and C. The "signatures" of the defects are extracted from the Arrhenius plots shown in the inset. The second charge state of the divacancy ($V_2^{-/0}$) can be observed by annealing the VP pair at 180 °C for 30 minutes.

5.1.3 Defect depth profiling

In the small signal regime ($\Delta C << C$), the DLTS signal from a defect is directly related to its concentration. A determination of the defect density, N_T, allows the defect introduction rate and its spatial distribution to be computed. This defect property is required in order to assess the extent to which a particular defect can alter the properties of the semiconductor. Lang [1] proposed that by applying a sufficiently large filling pulse all the defects in the depletion region could be filled. The density of a defect, N_T, could simply be calculated using:

$$N_T = 2(\Delta C / C)(N_D - N_A) \ , \qquad (5.9)$$

where ΔC is the change in capacitance after removing the pulse and (N_D - N_A) is the net donor concentration. Since Eq. (5.9) does not take into account the edge region it usually yields significant underestimation of N_T, especially at low reverse bias voltages. The edge region is the transition region wherein the deep level lies below the Fermi level. The traps in the edge region are occupied and do not contribute to a change in capacitance when a filling pulse is applied. The width of the edge region is given by:

$$\lambda = \left\{ \frac{2\varepsilon(E_T - E_F)}{q^2 N_D} \right\}^{1/2} . \qquad (5.10)$$

In this study we have used the "fixed bias-variable pulse" methodology [4] together with the edge region correction proposed by Zohta and Watanabe [10] to determine defect concentrations. The fixed bias-variable pulse technique relies on the change in depletion width when the majority carrier pulse, V_p, is changed by a small increment, δV_p. The corresponding incremental change in the relative capacitance signal due to the traps being filled by the pulse increment, $\delta(\Delta C/C)$, may be determined using:

$$\delta\left(\frac{\Delta C}{C}\right) = \left(\frac{\varepsilon_s}{qw^2 N}\right)\frac{N_T(x)}{N(x)}\delta V_p \ , \qquad (5.11)$$

where x is the width of the depletion layer during the filling pulse, q is the electronic charge, and C, w and N are the values of the junction capacitance, width of the depletion region and ionized shallow level concentration, respectively, corresponding to the steady-state quiescent bias. $N(x)$ is obtained from C-V measurements. The depletion region within a distance, $x = w - \lambda$, below the metal-semiconductor interface can be probed by applying successively larger increments (multiples of δV_p) of V_p till the flat-band condition is reached. Taking into account the influence of carriers in the edge region an accurate determination of the deep level concentration can be made using [10]:

$$N_T = 2(\Delta C / C) N_D \left[\left(\frac{x - \lambda}{x} \right)^2 - \left(\frac{x_p - \lambda_p}{x} \right)^2 \right]^{-1}, \qquad (5.12)$$

where λ and λ_p are the widths of the edge region before and after applying the filling pulse, and x and x_p are the depletion region widths before and after pulsing, respectively.

It must be pointed out that the sensitivity of the junction to trapped charge varies linearly from zero at the junction ($x = 0$) to a maximum at the edge of the depletion region ($x = w$). Therefore, DLTS cannot be used to measure the trap concentration close to the metal-semiconductor interface accurately. Furthermore, for large trap concentrations, the capacitance transients obtained at constant reverse bias are non-exponential and the above analyses are no longer valid [11].

5.2 DLTS instrumentation

The DLTS spectrometer consists of three main components: a pulse generator to provide the desired quiescent bias voltages and filling pulses to the diode and a synchronous pulse to the other instruments, a fast (1 MHz range) capacitance meter to detect the capacitance transient, and a signal detector to analyse the emission transient and generate the DLTS spectrum. As discussed in section 5.1.2, the output signal is maximised when the thermal emission rate matches the "rate window" of the signal detector. Originally, the rate window was implemented by the double boxcar averager [1,2] which samples the capacitance transient at two fixed times, t_1 and t_2, after the

trailing edge of the filling pulse. For an exponential capacitance transient, the normalised DLTS signal is:

$$S(T) = [C(t_1) - C(t_2)] / \Delta C(0) = \exp(-t_1 / t)[1 - \exp(\Delta t / t)] \ , \qquad (5.13)$$

where $\Delta C(0)$ is the magnitude of the transient at $t = 0$, $\Delta t = t_1 - t_2$ and $\tau = 1/e_n$. By setting the derivative of Eq. (5.13) with respect to τ equal to zero, the transient time constant giving rise to the maximum output may be written as:

$$\tau_{max} = \frac{t_1 - t_2}{\ln(t_1 / t_2)} \ , \qquad (5.14)$$

with the signal to noise ratio being proportional to the square root of the gate width $(t_1 - t_2)$ [2].

An alternative straightforward method of analysing the capacitance transient makes use of a lock-in amplifier [3,6]. The rate window is set by altering the frequency of the lock-in amplifier (LIA). One disadvantage of the LIA technique is the excess noise generated by the capacitance-spike obtained upon application of the filling pulse. The spike is gated off using a sample and hold circuitry [3] and the resulting capacitance transient is partially exponential. The LIA response to this transient signal is the integral of the product of the LIA square-weighting function and the first Fourier component of the signal. Alternatively, sine and cosine weighting functions can be used. The DLTS signature of deep levels were extracted by varying the LIA frequency, f, between 1 Hz and 220 Hz in steps chosen to yield uniformly spaced data points on the Arrhenius plot of $\ln(T^2/e_n)$ versus $1000/T$.

Figure 5.4 depicts the phase setting for the "bias-pulse phase reference" mode used in analysing the capacitance transient [6]. In this mode, the lock-in zero crossing is set at the end of the bias pulse [Figure 5.4 (a) and (c)]. The partially exponential capacitance transient obtained after a total gate off time, $t_p + t_d$, is illustrated in Figure 5.4(b). The LIA registers the phase and first Fourier of the partially exponential waveform and the LIA output can be written as:

$$S_{exp} = (2T_0 / \pi)[a_1 \sin(2\pi t_d / T_0) + b_1 \cos(2\pi t_d / T_0)] \ , \qquad (5.15)$$

where a_1 and b_1 are the Fourier coefficients of the first Fourier component of the partially exponential capacitance transient [6] and $T_0 = 1/f$. The maximum value of the

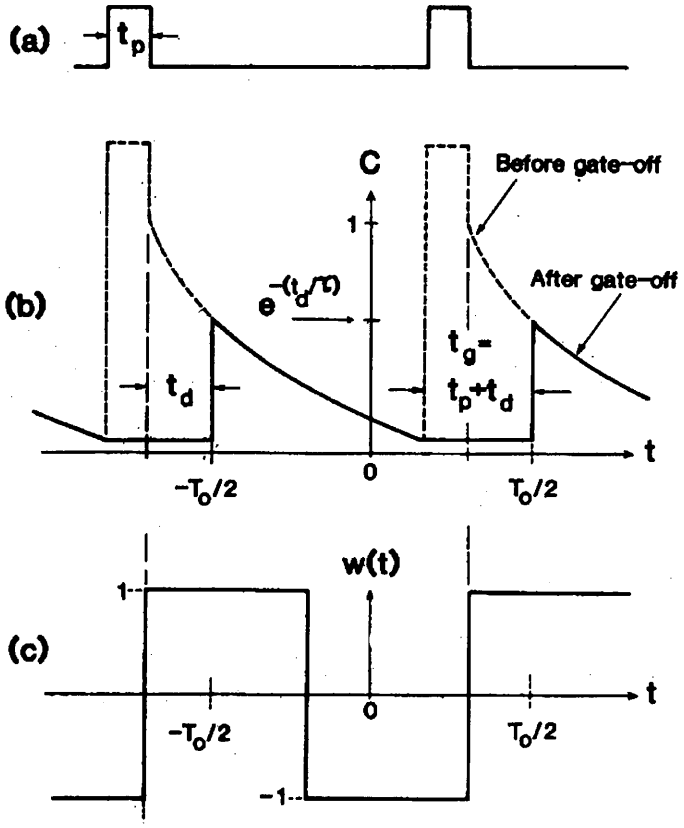

Figure 5.4: Phase setting for the "bias-pulse phase reference" mode: (a) filling pulse of width t_p and frequency $f = 1/T_0$; (b) normalized exponential capacitance transient before (broken curve) and after gate-off (solid curve); (c) lock-in amplifier weighting function set in phase with the falling edge of the filling pulse (ref [5]).

decay time constant, τ_{max}, is obtained by setting the derivative of Eq. (5.13) with respect to τ equal to zero. For $1\ \text{Hz} < f < 220\ \text{Hz}$ and $t_d = 2t_p$ ($t_p = 0.2$ ms), an approximate value of τ_{max} can be derived from the expression:

$$\tau_{max} = 0.42 / f \quad . \tag{5.16}$$

A schematic of the DLTS system used in this study is shown in Figure 5.5. The sample holder is designed to ensure that the sample is in thermal equilibrium even at high scan rates and the system allows DLTS scans to be recorded between 20 K and 375 K.

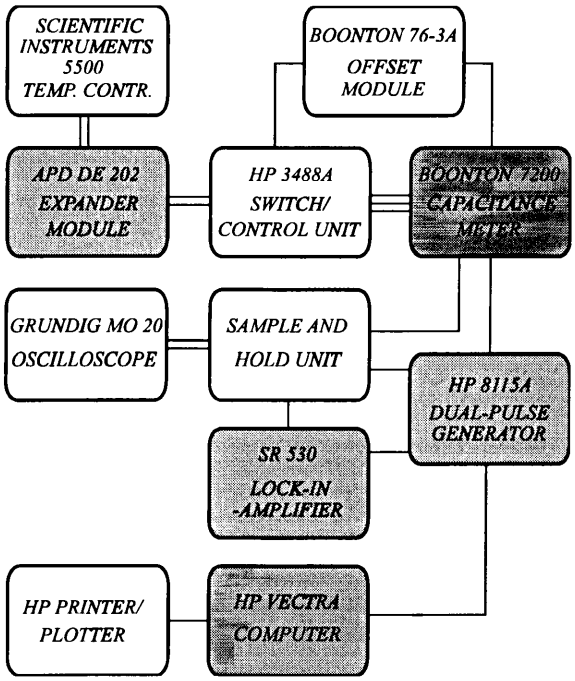

Figure 5.5: Schematic of the DLTS system used in this study. The shaded blocks show the main components of the capacitance spectroscopy technique (courtesy of Dr. S.A. Goodman).

REFERENCES

[1] D.V. Lang, J. Appl. Phys. **45**, 3014 (1974).

[2] D.V. Lang, J. Appl. Phys. **45**, 3023 (1974).

[3] G.L. Miller, D.V. Lang and L.C. Kimerling, Ann. Rev. Mater. Sci. **7**, 377 (1977).

[4] D.V. Lang, In "Thermally Stimulated Relaxation of Solids" (P. Braunlich, ed.) pp. 93-133, Springer-Verlag, Berlin, 1979.

[5] F.D. Auret, Rev. Sci. Instrum. **57**, 1597 (1986).

[6] H.G. Grimmeiss, E. Janzén and B. Skarstam, J. Appl. Phys. **51**, 3740 (1980).

[7] J.R. Troxell, Solid State Electron. **26**, 539 (1983).

[8] J.L. Benton, T. Asom, R. Sauer and L.C. Kimerling, Mater. Res. Soc. Proc. **104**, 85 (1988).

[9] C.H. Henry and D.V. Lang, Phys. Rev. B **15**, 989 (1977).

[10] Y. Zohta and M.O. Watanabe, J. Appl. Phys. **53**, 1809 (1982).

[11] A.C. Wang and C.T. Sah, J. Appl. Phys. **55**, 565 (1984).

CHAPTER 6

EXPERIMENTAL DETAILS

6.1 Plasma Processing

The sputter deposition of TiW and Au on n-Si were done in a Leybold-Heraeus Universal Sputtering Machine at DETEK. The samples were loaded in the main chamber through a load-lock system, which was then pumped down to $2x10^{-5}$ mbar. High purity Ar (5N) was then leaked into the main chamber to a pressure of $5x10^{-3}$ mbar and the plasma ignited using either dc or rf excitation. Deposition of Au was done in the dc mode by applying a potential of 400 V on the cathode (top electrode of parallel plate reactor) containing the Au target. On the other hand, TiW (10%:90% by mass) contacts were deposited in the rf mode by applying a 13.56 MHz , peak-to-peak voltage of 1.5 KV on the target. In both cases, the Schottky diodes were deposited through a metal contact mask on the n-Si substrates which were mounted on the water-cooled anode (bottom plate of reactor). Calibration runs were conducted to measure the deposition rate prior to each experiment, and the thickness of the deposited metal contacts were measured afterwards using a step-profiler (profilometer).

Sputter etching of n-Si substrates were performed in the same system by reversing the polarity on the two electrodes [Figure 7(b)]. All sputter etching experiments were conducted in the rf mode with a negative dc bias applied to the substrate holder and with the top electrode at earth potential. The pressure of the Ar plasma was limited between $1x10^{-3}$ mbar and $1.2x10^{-2}$ mbar, while the dc bias could be varied between 200 V and 800 V. The sputter deposition and sputter etching processes made use of different electrodes in order to minimise the effect of metallic contamination.

6.2 Ion Irradiation of n-type Silicon

6.2.1 Low Energy (1 keV) Noble Gas Ion (NGI) Bombardments

The 1 keV He-, Ne-, Ar- and Xe-ion bombardments were done using a PHY-type ion gun in a Auger system. The ion fluence was varied between $1x10^{10}$ cm^{-2} and $1x10^{15}$ cm^{-2} and

the dose rate was $1x10^{11}$ $cm^{-2}s^{-1}$ for ion fluences larger than $1x10^{12}$ cm^{-2}, and two orders of magnitude smaller for the lower doses. High purity (5N) noble gas species were fed into the target chamber when the base pressure was ~$1x10^{-9}$ mbar. The low energy NGI bombardments were done at a pressure of ~$5x10^{-5}$ mbar.

6.2.2 Medium Energy NGI and MeV ^{28}Si Implantations

He and Ar ions with energies ranging from 25-150 keV were implanted in n-type Si in a Varian ion implanter at the Carl and Emily Fuchs Institute for Microelectronis (CEFIM). The implantations were done to a fluence of ~$1x10^{10}$ cm^{-2} at room temperature and the beam current was of the order of 1 nA. The samples were mounted on a rotating sample holder using a conductive carbon glue which could easily be removed in acetone. Implantations were conducted at a pressure of ~10^{-7} mbar.

The high energy $^{28}Si^{4+}$ implantations (5.4 MeV) were done in a 1.7 MV Tandem ion implanter at the Australian National University. The n-type Si substrates were implanted at room temperature to doses between $1x10^{9}$ cm^{-2} and $2x10^{10}$ cm^{-2} using a beam current of ~$1x10^{9}$ nA . Samples were mounted on a rotating Tantalum block using a conductive silver paint which was removed using acetone prior to metallization. Implantations were performed at a base pressure of $2x10^{-7}$ mbar.

6.2.3 Electron and Alpha-particle Irradiations

Electron irradiation was done by exposing the epitaxial n-Si layers to a disc-shaped strontium source (^{90}Sr) which has an activity of 20 mCi. The ^{90}Sr radionuclides first decay to Y with an emission of an 0.5 MeV electron (halflife 28.5 yrs) and then to Zr with the emission of a 2.3 MeV electron (halflife 64.1 h). The energy distribution of the electrons is continuous with approximately 70% having an energy above 250 eV [1].

An Am source having an activity of 0.39 μCi and a disc shape of 9.7 mm diameter was used as a source of high energy alpha-particles. During the decay of ^{241}Am to ^{237}Np, 85.5% of the alpha particles are emitted with a sharply defined energy peak at 5.484 MeV, while 12.3% have an energy of 5.441 MeV and 1.5% have an energy of 5.387 MeV. The

^{241}Am can therefore be regarded as a monoenergetic source of 5.4 MeV alpha-particles [1].

6.3 Schottky Diode Fabrication for Electrical Characterization

The fabrication of Schottky diodes by sputter deposition is described in section 6.1. Metal contacts were made on the epitaxial sides of sputter-etched and ion-bombarded samples by resistive evaporation of Au and Pd, through a metal contact mask. The diameter of the diodes were 0.77 mm and the thicknesses were 1000 Å and 3000 Å for Pd and Au contacts, respectively. Prior to metal deposition, the samples were chemically cleaned using degreasing in boiling trichloroethylene and iso-propanol, followed by rinses in de-ionised (DI) water (18 MΩcm) and etching in a mixture of NH_4OH-H_2O_2-H_2O (1:1:5 by volume). After rinsing thoroughly in DI water, the native oxide layers were stripped by immersing in buffered HF for 10-15 s (HF:NH_4F in 1:6 by volume). Several other cleaning procedures were assessed and these are described in Chapter 7. Prior to electrical characterisation, ohmic contacts were made on the n^+-substrates on the samples using an In-Ga eutectic mixture.

6.4 Electrical Characterizations

Current-voltage (I-V) and capacitance-voltage (C-V) measurements were used to assess the rectifying properties of the Schottky diodes and to monitor the amount and type of damage induced by ion-processing of the epitaxial substrates. The measurements were made using the automated system illustrated in Figure 4.4.

The electrically active defects introduced by ion-processing of the n-Si samples were characterised using capacitance deep level transient spectroscopy (DLTS). The activation energy, E_T, and capture cross-section, σ_n, of the processing-induced defects were extracted from Arrhenius plots of $\ln(T^2/e)$ versus $1000/T$ as described in Chapter 5. The set-up of the DLTS instrumentation used is illustrated in Figure 5.5. The "fixed bias variable pulse" methodology, as described in Chapter 5, was employed to determine the spatial distribution of the electrically active defects below the metal-semiconductor junction.

6.5 Optical Characterization of Defects

Optically active defects created during ion-processing on n-Si were studied using photoluminescence spectroscopy (PL). The photoluminescence analyses were carried on processed samples without metal contacts. Measurements were taken using the 514 nm line of an argon-ion laser, a 0.64 μm infra red monochromator (resolution 1.4 Å), a cooled germanium detector and conventional lock-in amplifier techniques. Samples were mounted in a closed cycle helium-cooled cryostat and the temperature could be varied between 11-295 K. The laser power was fixed at 200 mW and it had a spot size of approximately 0.2 mm.

6.6 Atomic Force Microscopy (AFM) Measurements

A Park Scientific Autoprobe CP was used in the AFM investigation of the surface morphology of chemically cleaned samples. Scan sizes of 3 x 3 μm^2 were recorded using a 200 μm long rectangular cantilever with a force constant of 0.02 Nm^{-1} and a torsion force constant of 0.008 $Nrad^{-1}$ with an integrated silicon nitride tip. These tips were 3 μm long of which the sharpened part was 0.2 μm and had a pyramidal shape. All the images were acquired at a scan rate of one line per sec to minimize any artefacts due to piezo-material creep or feedback response time. The images were acquired automatically and their processing was done using the software supplied by the manufacturer.

REFERENCES

[1] F.D. Auret, S.A. Goodman, G. Myburg, W.E. Meyer, Appl. Phys. A **56**, 547 (1993)

CHAPTER 7

PUBLISHED AND OTHER RESULTS

7.1 Cleaning Procedures

(1) P.N.K. Deenapanray, F.D. Auret, G. Myburg, K.T. Hillie and C.M. Demanet, "Effect of Cleaning Procedures on the Quality of Palladium Schottky Barrier Diodes Fabricated on Epitaxially Grown n-Si", Proceedings of ECASIA'97, (Ed. C. Briggs), Wiley, 1997 (to be published).

7.2 Sputter Deposition

(1) P.N.K. Deenapanray, F.D. Auret, G. Myburg, M. Hayes, W.E. Meyer and C. Schutte, "Defect Formation by Low Energy Ions During Sputter Deposition of TiW and Au on Epitaxially Grown n-Si at Different Plasma Pressures", Materials Science Forum **248-249**, 249 (1997).

7.3 Sputter Etching

(1) P.N.K. Deenapanray, F.D. Auret, C. Schutte, G. Myburg, W.E. Meyer, J.B. Malherbe and M.C. Ridgway, "Electronic Properties of Defects Formed in n-Si During Sputter Etching in an Ar Plasma", Mat. Res. Soc. Symp. Proc. 442, **87** (1997).

(2) P.N.K. Deenapanray, F.D. Auret and G. Myburg, "Electrical Characterisation and Annealing Behaviour of Defects Introduced in Si During Sputter Etching in an Ar Plasma", submitted to J. Vac. Sci Technol A, July 1997.

7.4 Low Energy Noble Gas Ion Bombardment

(1) F.D. Auret, P.N.K. Deenapanray, S.A. Goodman, J.B. Malherbe, W.E. Meyer, G. Myburg and M. Hayes, "Electronic Properties of Defects Created in n-Si by Low Energy He and Ar-Ions", Nucl. Instr. and Meth. in Phys. Res B **127-128**, 393 (1997).

(2) P.N.K. Deenapanray, N.E. Perret, F.D. Auret, J.B. Malherbe and M. du Plessis, "Electronic and Optical Properties of Defects Formed in Si During Low Energy Noble Gas Ion Bombardment", 1996 Conference on Optoelectronic and Microelectronic Materials and Devices (COMMAD'96) Proceedings, (Ed. C. Jagadish) IEEE, Piscataway, NJ (USA), 1997 (to be published).

(3) P.N.K. Deenapanray, N.E. Perret, D.J. Brink, F.D. Auret and J.B. Malherbe, "Characterisation of Optically Active Defects Created by Noble Gas Ion Bombardment of Silicon", J. Appl. Phys. (accepted for publication).

(4) F.D. Auret, P.N.K. Deenapanray, S.A. Goodman, W.E. Meyer and G. Myburg, "Electrical Characterization of Low-Energy He-ion Bombardment Induced Defects in Epitaxially Grown n-Si", unpublished.

(5) P.N.K. Deenapanray, F.D. Auret, G. Myburg, J.B. Malherbe, M.C. Ridgway and S.A. Goodman, "DLTS Characterisation of 1 keV He, Ne, Ar Ion Bombarded Epitaxially Grown n-Si", J. Appl. Phys. (submitted July 1997).

(6) P.N.K. Deenapanray, F.D. Auret, G. Myburg, W.E. Meyer and S.A. Goodman, "Electrical and Optical Characterisation of Defects Induced in Epitaxially Grown n-Si During 1 keV Noble Gas Ion Bombardment", presented at ICDS'19, Aveiro, Portugal, 21-25 July 1997.

Effect of Cleaning Procedures on the Quality of Palladium Schottky Barrier Diodes Fabricated on Epitaxially Grown n-Si

P.N.K. Deenapanray,[1] F.D. Auret,[1] G. Myburg,[1] K.T. Hillie[2] and C.M. Demanet[2]

[1] Department of Physics, University of Pretoria, Pretoria, 0002, South Africa
[2] Department of Physics, University of Transkei, Umtata, 5100, South Africa

1. Introduction

Schottky barrier diodes (SBDs) are extensively used microelectronic devices for ultra-high frequency applications. Furthermore, SBDs are routinely used in deep level transient spectroscopy (DLTS) for the electrical characterisation of processing-induced defects in semiconductor materials. It is, therefore, crucial to fabricate reliable SBDs with reproducible electrical properties. However, numerous studies have shown that the quality of metal-semiconductor interfaces are highly dependent on the substrate cleaning methods [1-3]. Current-voltage (I-V) and capacitance-voltage (C-V) measurements were used in a systematic study of the effect of eight cleaning procedures on the eletrical properties of Pd/n-Si contacts. Atomic force microscopy (AFM) was also employed to study the surface morphology of the chemically cleaned samples. A correlation between the surface roughness of the samples and the rectifying properties of the diodes fabricated thereon is made.

2. Experimental

Epitaxially (CVD) grown (111) oriented n-Si samples, doped to $5\text{x}10^{15}$ cm^{-3} with P, and grown on n^+-substrates were chemically cleaned using the procedures outlined in Table I. Circular Pd Schottky contacts of 0.77 mm diameter and 100 nm thickness were deposited by resistive evaporation on one set of samples. I-V and C-V measurements were performed using a HP 4140B picoammeter and a HP 4192A impedance analyzer (1 MHz), respectively. A Park Scientific Autoprobe CP was used in the AFM investigation of the surface roughness of a second set of samples. The I-V characteristics were extracted assuming the thermionic-emission theory [4], while the C-V parameters were obtained from graphs of $1/C^2$ vs V.

3. Results and Discussion

The rms roughness, R_{rms}, of a surface was calculated from :

$$R_{rms} = \left\{ \left[\sum_{p=1}^{P} (z_p - \bar{z})^2 \right] / (P-1) \right\}^{1/2} , \qquad (1)$$

where z_p is the height measurement of pixel p (P pixels in total) and $\bar{z}$ is the arithmetic mean height. The I-V (ϕ_b^{IV}) and C-V (ϕ_b^{CV}) barrier heights, ideality factor, n, and current, I_R, at a reverse bias of 1 V of the SBDs are summarised in Table II. The values of R_{rms} and free carrier concentration, N_D, extracted from C-V measurements are also given in the same table as a function of cleaning procedure.

Table I. Summary of cleaning procedures.

Number			Procedure
WM1	(a)	(i)	Immerse in boiling TCE[1] (≈3 min)
		(ii)	Immerse in boiling iso-propanol (≈3min)
		(iii)	Three rinses in H_2O (≈20 sec each)
	(b)	(i)	Immerse in 5:1:1 H_2O:NH_4OH:H_2O_2 for 10 min (75-80 °C
		(ii)	Quench in H_2O for 1 min
		(iii)	(a) (iii)
	(c)	(i)	Immerse in 6:1:1 H_2O:HCl: H_2O_2 for 10 min (75-80 °C)
		(ii)	As in (b) (ii)-(iii)
	(d)	(i)	Etch in 2:15:5 HF:HNO_3:CH_3COOH[2] for 3-4 sec
		(ii)	(a) (iii)
	(e)	(i)	Immerse in 1:6 HF:NH_4F[3] for 5 sec
		(ii)	(a) (iii)
	(f)		Dry in N_2-flow
WM2	(a)		As in 1(a) to 1(c)
	(b)		Immerse in 1:50 HF:H_2O[4] for 15 sec
	(c)		As in 1(a) (iii) and 1(f)
WM3	(a)	(i)	As in 1(a) to 1(c)
		(ii)	As in 1(e) and 1(f)
WM4		(i)	As in 1(a) and 1(b)
		(ii)	As in 1(d)
		(iii)	As in 1(b) and 1(c)
		(iv)	As in 2(b) and 2(c)
WM5		(i)	As in 4(a) (i)-(iii)
		(ii)	As in 1(e) and 1(f)
WM6		(i)	As in 4(a) (i)-(ii)
		(ii)	As in 1(b)
		(iii)	As in 2(b) and 2(c)
WM7		(i)	As in 6(a) (i)-(ii)
		(ii)	As in 3(a) (ii)
WM8		(i)	As in 4(a) (i)
		(ii)	As in 3(a) (ii)

[1] TCE: Trichloroethylene
[2] Planar etch for n(111) Si: ≈5 µm/min at 25 °C
[3] SiO_2 etch: ≈20 Å/sec at 25 °C
[4] SiO_2 etch: ≈10 to 100 nm/min at 25 °C

HNO_3 - 70 %; NH_4OH - 25 %
H_2O_2 - 30 %; HCl - 37 %
CH_3COOH - 96 % (glacial)
HF - 40 %; NH_4F - 40 %

It can be inferred from these results that a linear relationship exists between I_R, n and barrier heights, and R_{rms}. Diodes fabricated on chemically cleaned surfaces may show non-ideal properties ($n > 1$), such that differences, $\Delta\phi_b = |\phi_b^{CV} - \phi_b^{IV}|$, larger than 0.02 eV (experimental error) cannot solely be attributed to image-force lowering of the barrier. Values of $\Delta\phi_b > 0.02$ are usually attributed to the presence of donor-type interfacial states. Consequently, these diodes show poorer rectifying qualities and yield underestimated values of N_D by a factor n due to slope-shifts in the $1/C^2$ vs V curves. However, if the effective diode contact area, A^*, is not taken into account when surface roughness is increased, an overestimated value of N_D is obtained. Assuming a constant free carrier density, we have normalized the corrected values

N_D^* ($N_D^* = nN_D$) with respect to that corresponding to the near-ideal diode obtained using WM7 [$N_D^*(7)$], and calculated A^* for the remaining SBDs using:

$$A^* = A \times \sqrt{N_D^* / N_D^*(7)} \quad , \qquad (2)$$

where $A = 0.47$ mm^2. Table II also summarizes the calculated values of A^* and N_D^*.

Table II. Summary of results. A 10 % error is attributed to N_D* and the error in A^* is ± 0.02 mm^2. The untreated sample had a surface roughness of 17 ± 11 Å.

Cleaning procedure	n	ϕ_b^{CV} (eV)	ϕ_b^{IV} (eV)	$\lvert\Delta\phi_b\rvert$ (eV)	I_Rx10^{-8} (A)	N_D^* x10^{15} (cm^{-3})	A^* (mm^2)	R_{rms} (Å)
WM1	1.15	0.76	0.73	0.03	84.5	10.1	0.63	16.0 ± 10
WM2	1.10	0.79	0.74	0.05	34.2	7.7	0.55	10.0 ± 4
WM4	1.06	0.75	0.73	0.02	7.0	5.7	0.47	5.5 ± 0.5
WM3	1.05	0.80	0.76	0.04	4.7	7.0	0.52	3.5 ± 0.8
WM5	1.05	0.74	0.75	0.01	7.8	5.9	0.48	2.5 ± 0.5
WM6	1.04	0.77	0.75	0.02	4.2	7.6	0.55	1.5 ± 0.5
WM7	1.03	0.75	0.76	0.01	3.8	5.6	0.47	2.0 ± 1
WM8	1.05	0.82	0.75	0.07	4.4	6.4	0.50	1.0 ± 0.5

The cleaning procedures and corresponding diodes can be evaluated by classifying them under two groups: (i) group A for WM1, WM2 and WM4 ($R_{rms} > 5$ Å), and (ii) group B for the remaining procedures ($R_{rms} < 3$ Å). Group A diodes had poorer rectifying properties, with reverse currents 20 times larger than those fabricated on near-atomically flat surfaces. The high etch rate of HF:HNO_3:CH_3COOH (planar etch mixture) produced a rough surface (WM1) with a high density of interfacial states and the corresponding diode was significantly more leaky. Better quality diodes could be obtained by either omitting the planar etch step (WM2) or by using a H_2O_2/NH_4OH step just after (WM4-WM7). Furthermore, the results shown in Table II reveal that the free carrier density obtained from C-V measurements can, in our case, be grossly overestimated by 40-80 % when 10 Å < R_{rms}, due to larger effective areas of contact.

Group B cleaning procedures produced surfaces with roughness less than 3 Å, which yielded near-ideal diodes with $n < 1.05$. The values of ϕ_b^{IV} for the group B diodes were 0.75-0.76 eV and match the reported values for Pd_2Si/n-Si contacts [5]. A close inspection of Table II shows that the effective area of contact cannot be used to explain fluctuations in N_D* for Schottky diodes fabricated on near-atomically flat surfaces. The relatively higher values of N_D* obtained using WM3 and WM4 are thus attributed to higher densities of interfacial states introduced by these cleaning methods at the Si surface. The presence of higher densities of interfacial states is reflected in the correspondingly higher values of ϕ_b^{CV} (shift in the V-intercept of the curve $1/C^2$ vs V) and $\Delta\phi_b$ for these diodes. It can, therefore, be concluded that WM7 introduced the least amount of interfacial states and produced a smooth surface, and consequently yielded diodes with the best rectifying properties. Although, WM6 and

WM8 produced marginally smoother surfaces than WM7, their corresponding diodes had slightly inferior ideality factors and higher reverse currents. Moreover, the relatively higher value of N_D^* attributed to WM6 suggests that the latter also introduced high densities of interfacial states.

Finally, the following remarks can be made regarding the various cleaning procedures investigated in this study. A comparison of WM2 and WM3, WM4 and WM5, and WM6 and WM7, respectively, reveals that the use of a buffered HF solution (HF-NH_4F) as a final step for native oxide removal results in less rough surfaces than when using a diluted HF solution (2 % HF). This observation is consistent with the results by Becker *et al* [6], who showed using STM that an HF solution of high pH yielded smoother surfaces on Si(111) than one of lower pH. By comparing WM4 to WM6 and WM5 to WM7, respectively, it is concluded that the quality of SBDs became marginally poorer when a heavy metal etch step (H_2O-HCl-H_2O_2) was included.

4. Conclusion

We have used AFM in conjunction with I-V and C-V measurements of Pd/n-Si diodes to evaluate various cleaning procedures on Si(111). We showed that near-atomically flat surfaces ($R_{rms} \approx 1$ Å) could be obtained starting with a surface with an average roughness of 17 Å. Diodes fabricated on surfaces with roughness larger than 5 Å had poorer electrical properties compared to those fabricated on surfaces with $R_{rms} < 3$ Å. For instance, diodes corresponding to $R_{rms} \approx 16$ Å had reverse currents 20 times larger than those fabricated on a surface with $R_{rms} \approx 1$ Å. Cleaning procedures which produced near-atomically flat surfaces yielded near-ideal diodes with $n < 1.05$ and I-V barrier heights between 0.75 eV and 0.76 eV. However, cleaning procedures producing equally smooth surfaces did not yield diodes with similar electrical properties, and we have attributed this to the different densities of interfacial states introduced by the chemical procedures. We have unambiguously showed that the free carrier density can be grossly over-estimated when the surface roughness exceeds 10 Å. Buffered HF solutions used for native oxide removal produced smoother surfaces on Si(111) than diluted HF solutions, and including a heavy metal etch step yielded diodes with marginally poorer electrical characteristics.

References

1. F.D. Auret, *J. Electrochem. Soc.*, **129**, 2752 (1982).
2. C.M. Garner, C.Y. Su, W.A. Saperstein, K.G. Jew, C.S. Lee, G.L. Pearson and W.E. Spicer, *J. Appl. Phys.*, **50**, 3376 (1979).
3. D. Schmidt, H. Niimi, B.J. Hinds, D.E. Aspnes and G. Lucovsky, *J. Vac. Sci. Technol.*, **B 14(4)**, 2812 (1996).
4. M.S. Tyagi, in *Metal-Semiconductor Schottky Barrier Junctions and Their Applications*, ed. by B.L. Sharma, Plenum Press, New York (1984), p. 14.
5. S.P. Murarka, in *Silicides for VLSI Applications*, Academic Press, New.York (1983).
6. R.S. Becker, G.S. Higashi, Y.J. Chabal and A.J. Becker, *Phys. Rev. Lett.*, **65**, 1917 (1990).

Tel. No. : +27-12-420-2684
Fax. No. : +27-12-342-4143
e-mail : sdeenapa@scientia.up.ac.za

DEFECT FORMATION BY LOW ENERGY IONS DURING SPUTTER DEPOSITION OF TiW AND Au ON EPITAXIALLY GROWN n-Si AT DIFFERENT PLASMA PRESSURES

P. N. K. Deenapanray, F. D. Auret, G. Myburg, M. Hayes, W. E. Meyer and C. Schutte

Department of Physics, University of Pretoria, Pretoria 0002, South Africa

Keywords: sputter deposition, magnetron system, defects, DLTS.

Abstract: The electronic and annealing properties of the main defects introduced during RF sputter deposition of TiW and Au contacts on n-Si were investigated using current-voltage (IV) and deep level transient spectroscopy (DLTS) techniques, combined with isochronal and isothermal annealing, respectively. It was found that the barrier heights of the sputter deposited diodes were lower than that of a control diode fabricated using resistive evaporation. Furthermore, the barrier heights of the sputter deposited diodes were found to decrease with a decrease in the Ar-plasma pressure used. Sputter deposition of Au and TiW introduced five and four prominent levels below the conduction band, respectively. No direct evidence could be obtained for the introduction of V_2- and VP-centres during sputtering. The sputter-deposition-induced (SDI) defects may, amongst others, be attributed to impurities in the Si, and to energetic metal and Ar atoms from the plasma impinging the Si.

I. Introduction

Sputter deposition is a versatile technique used during metallization for the stoichiometric deposition of compounds and refractory metals on semiconductors. Compared to other deposition techniques such as resistive evaporation, sputtering also offers the possibility of control over the deposition rate and better film adhesion to the substrate [1]. During sputter deposition, both the metal contact and the semiconductor substrate material are subject to bombardment by energetic particles. These particles include low energy Ar ions from the plasma, neutral Ar atoms which are backscattered from the target, sputtered metal atoms, energetic electrons, X-rays and photons [2]. The interaction between these particles and the substrate results in the introduction of donor-type defects [3] at and close to the metal-semiconductor interface, which modify its barrier height. In addition, the electrical, optical and structural properties of the semiconductor, and hence the characteristics and performance of the devices fabricated on them, can be adversely affected. Hence, a reproducible and controlled introduction of these defects can be used to obtain barrier heights of specific values. Other Schottky barrier diode (SBD) parameters such as the reverse leakage current and ideality factor, are also affected by sputter-deposition-induced damage. The extent of this damage depends on the deposition parameters such as deposition time and rate, sputter mode and bias conditions, as well as gas pressure and species.

In order to either predict the influence of defects on device characteristics or be able to successfully use them in any form of defect engineering [4,5], it is essential that their electrical and structural properties be established. Several electron and hole traps introduced during sputter deposition on bulk grown Si have been studied using DLTS [6,7]. In this study, SDI defects were characterised and barrier height changes monitored after the sputter deposition of Au and TiW on epitaxially grown Si at different plasma pressures in a magnetron-type system.

II. Experimental

Epitaxially grown (111) oriented n-type Si layers with a free carrier concentration of $6x10^{15}$ /cm^3, grown on n^+-substrates, were used in this study. The samples were chemically cleaned after which circular TiW and Au Schottky contacts of 0.75 mm diameter, and 200 nm and 500 nm thick, respectively, were sputter-deposited through a metal contact mask in an RF magnetron-type

sputtering system at plasma pressures of $2x10^{-3}$, $7x10^{-3}$, and $2x10^{-2}$ mbar, respectively. For control purposes, 300 nm thick circular Au contacts were resistively deposited through the same contact mask. Ohmic contacts were formed on the n^+-substrates by using a liquidus In-Ga alloy prior to diode and defect characterization.

The quality of the SBDs were evaluated by I-V and C-V measurements. The barrier heights (ϕ_b^{IV}) for TiW diodes were extracted from the log I-V curves by using the Beguwala and Crowell three-point method [8]. The C-V barrier height (ϕ_b^{CV}) was calculated from a graph of $1/C^2$ vs V_R by using a reverse bias, V_R, of between 0 and 1 V, while the section $1 < V_R < 3$ V of the same graph was used to determine the free carrier density. The defects induced during the sputter deposition process were characterised by deep level transient spectroscopy (DLTS) [9]. The DLTS "signatures" (energy level, E_t, and apparent capture cross-section, σ_a) of the defects were determined from DLTS Arrhenius plots of $\log(e/T^2)$ vs $1/T$, where e is the emission rate at a temperature T.

Isochronal annealing of the Au sputter-deposited SBD ($7x10^{-3}$ mbar) was performed between 50 and 200°C (in steps of 50°C) in an argon atmosphere for 15 min periods. I-V and C-V measurements were used to monitor the changes in the non-ideality factor (n) of the diodes and their barrier heights, and the Si free carrier density. To study the removal rates of two defects, with overlapping DLTS peaks at approximately 63 K (see section on **"Results and discussion"**), isothermal annealing experiments were conducted at 75 °C.

III. Results and discussion

A. I-V and C-V results

The I-V barrier heights of the SBDs analyzed were found to be lower than those by the C-V method. The greater fluctuations observed for C-V than for I-V measurements are explained by the deviation from linearity of the $1/C^2$ vs V_R curve in the region below 1.0 V reverse bias.[10] Since this deviation leads to inaccuracies in the C-V measurements, the discussion that follows will be based on the I-V results.

Fig. 1 shows the variation of barrier heights (ϕ_b^{IV} and ϕ_b^{CV}) as a function of the argon plasma pressure for Au SBDs. It is observed that ϕ_b^{IV} increases from (0.731 ± 0.007) eV at a pressure of $2x10^{-3}$ mbar to approximately (0.74 ± 0.01) eV at a pressure of $2x10^{-2}$ mbar. In the case of TiW diodes, the barrier height was (0.54 ± 0.01) eV and (0.52 ± 0.01) eV at $2x10^{-3}$ and $2x10^{-2}$ mbar, respectively. Mullins and Brunnschweiler [3] have proposed that sputter damage creates donor-type traps close to the semiconductor surface which result in the lowering of the I-V barrier height in n-type material. Applying the above model to our results reveals that less sputter-deposition induced damage is created when the sputter pressure is increased. We explain this by noting that for a given target and plasma, the mean free path is inversely proportional to the pressure during sputtering. Hence, the mean free path between collision of the particles in the plasma and the target atoms will decrease when the sputter pressure is increased. The particles (mostly sputtered metal and argon atoms) which bombard the semiconductor surface in a denser plasma, are less energetic and therefore create less damage [11].

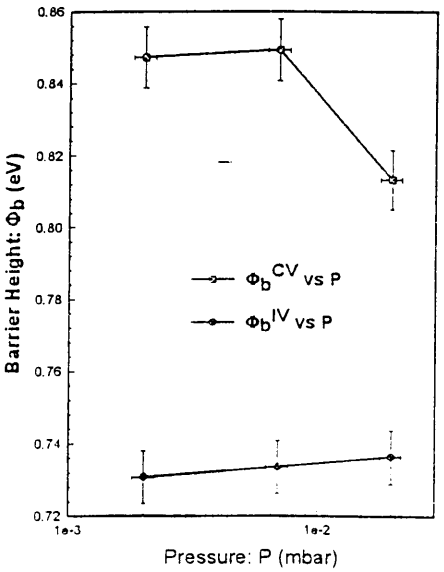

Fig. 1 Au/n-Si SBD barrier heights (I-V and C-V) as a function of argon plasma pressure.

The changes in barrier heights (ϕ_b^{IV} and ϕ_b^{CV}) and non-ideality factor as a function of isochronal annealing temperature are shown in Fig. 2 for a diode deposited at a pressure of $7x10^{-3}$ mbar. It is observed that the ϕ_b^{IV} and ϕ_b^{CV} values follow opposite trends and converge for

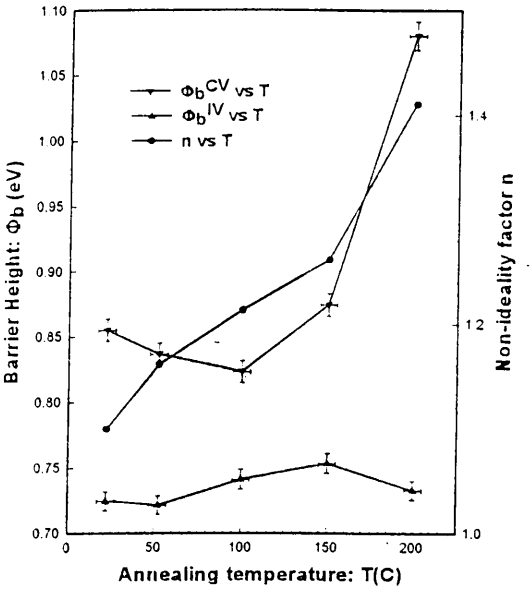

Fig. 2 IV and CV barrier heights and non-ideality factor as a function of annealing temperature for a Au sputter deposited diode at a plasma pressure of $7x10^{-3}$ mbar.

annealing temperatures up to 150 °C. The I-V barrier height is found to increase from (0.73 ± 0.01) eV before annealing to (0.76 ± 0.01) eV after annealing at 150 °C, which is close to the value of ϕ_b^{IV} = (0.76 ± 0.02) eV for our resistively deposited control sample. As expected, this increase in ϕ_b^{IV} with temperature is characteristic of damage removal. Furthermore, the free carrier density was found to increase from its partially compensated value of $5.1x10^{15}$ /cm^3 after sputter deposition to approximately $5.9x10^{15}$ /cm^3 after annealing at 150 °C, which is also indicative of damage recovery during annealing. However, Fig. 2 also shows that the values of ϕ_b^{IV} and ϕ_b^{CV} start to diverge from each other for annealing temperatures higher than 200 °C. The sharp increase in the non-ideality factor shows substantial degradation of the diode with temperature such that the thermionic emission theory used to extract ϕ_b^{IV} is no longer valid.

B. DLTS results

Sputter deposition of Au and TiW introduced five and four prominent traps, respectively, below the conduction band. The electronic properties of these defects are summarised in Table1. Although we have determined the electronic properties of the main SDI defects, their structures remain unknown. To learn more about the structures of SDI defects we have compared them to the primary defects (most of which have been structurally identified) introduced during high energy alpha-particle irradiation [12] and those created during low energy Ar-ion bombardment. Fig. 3 shows the DLTS spectra of RF sputter-induced defects together with the spectra of 1 keV Ar ion bombarded and 5.4 MeV alpha-particle irradiated n-Si. It is observed that EAu2 and ETiW2 are identical to the VO-complex (A-centre). However, no direct evidence was obtained regarding the possible introduction of V_2- ($V_2^{-/0}$ and $V_2^{=/-}$) and VP-centres during sputter deposition of Au and TiW. It has been observed that EAu4 is due to the superposition of 2 or more defect peaks which may include both the $V_2^{-/0}$ and the VP-centre. These overlapping peaks could not be totally separated using different biases and frequencies, or narrow (20 ns) filling pulses. We are currently conducting further isochronal annealing studies (above 200 °C) to investigate the presence of the $V_2^{-/0}$ and VP-centres after sputter deposition. It can be argued that $V_2^{=/-}$ could not be detected because of the presence of stress fields due to extended defects in the region probed by DLTS [13]. EAu1 was observed to anneal out at room temperature. Fig. 4 shows the DLTS spectra of the isothermal annealing of EAu1 and EAu2 at 75 °C for three successive 10 min periods. In this figure it is demostrated that EAu1 is the result of two overlapping defects having almost similar activation energies. We are also conducting further isothermal annealing studies to determine the removal rates of the main SDI defects.

Table 1 Electronic properties of the main SDI defects.

Defect (Au)	E_t (eV)	σ_n (cm^2)	Defect (TiW)	E_t (eV)	σ_n (cm^2)	Defect structure
EAu1	0.112	5.0e-16	ETiW1	0.111	5.5e-16	Ar-related?
EAu2	0.172	1.1e-15	ETiW2	0.174	1.7e-15	V0-centre
EAu3	0.313	2.4e-16				
EAu4	0.379	1.2e-17	ETiW3	0.374	2.8e-17	
EAu5	0.392	3.5e-19	ETiW4	0.449	2.9e-18	

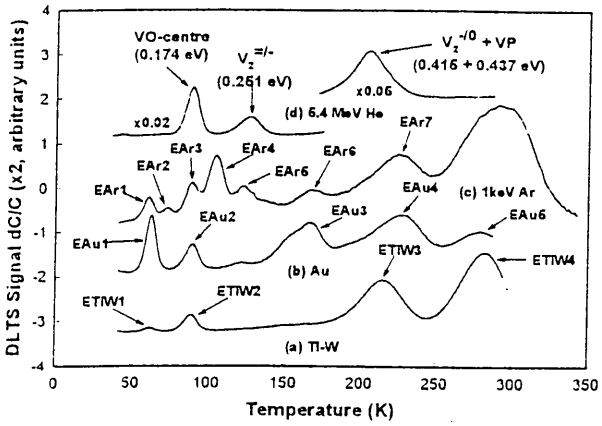

Fig. 3 DLTS spectra of (a) sputter deposited TiW, (b) sputter deposited Au, (c) 1 keV Ar ion bombardment, and (d) 5.4 MeV alpha-particle irradiation of n-Si.

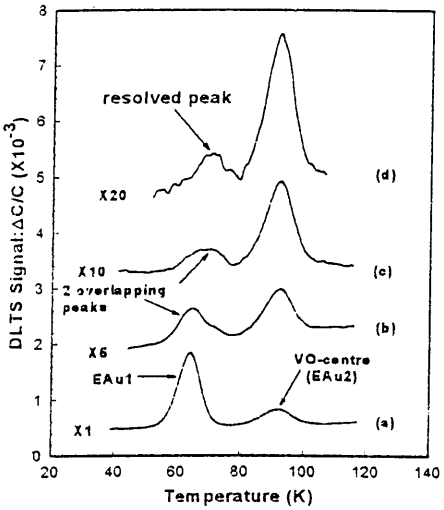

Fig. 4 DLTS spectra showing successive isothermal annealing periods of EAu1 and EAu2 at 75 °C for a Au sputter-deposited diode:(a) unannealed sample, (b) 10 minutes, (c) 20 minutes, and (d) thirty minutes.

III. Conclusions

We have demonstrated that RF sputter deposition of Au and TiW introduces defects near the semiconductor interface. I-V measurements confirm that sputter-induced damage results in a lowering of the barrier height on n-Si. The barrier height is also observed to decrease with a decrease in plasma pressure and this is attributed to an increase in the mean free path of the plasma particles at lower pressures. No direct evidence could be obtained to show the presence of V_2- and VP-centres in our samples. The absence of V_2=/- could be due to the presence of stress fields caused by the presence of extended defects. EAu2 and ETiW2 have been identified to be the VO-complex. Using our Arrhenius diagram, EAu1 is due to the overlapping of two defects. An increase in the barrier height as well as in the free carrier density from its compensated value after sputter deposition during isochronal annealing are characteristic of damage removal. We are currently conducting further annealing experiments to investigate the presence of V_2-and VP-centres together with the removal rates of the main SDI defects.

Acknowledgments

We are grateful for the financial assistance of the South African Foundation for Research and Development and the Carl and Emily Fuchs Institute for Microelectronics. The technical assistance of C. du Toit and J. P. Le Roux is kindly acknowledged. We are thankful to DETEK for making available their sputtering system for this study.

References

[1] L. I. Maissel: Handbook of Thin Film Technology, ed. L. I. Maissel and R. Glan, McGraw Hill, New York, 1 (1970).
[2] E. Ohta, K. Kakishita, H. Y. Lee, T. Sato and M. Sakata, J. Appl. Phys., **65**, 3938 (1989).
[3] F. H. Mullins and A. B. Brunnschweiler, Solid-State Electron., **19**, 47 (1976).
[4] S. Brotherton and P. Bradley, J. Appl. Phys., **53**, 5720 (1982).
[5] V. Rianeri, G. Fallica and S. Libertino, J. Appl. Phys., **79**, 9012 (1996).
[6] O. Paz, F. D. Auret and J. F. White, J. Electrochem. Soc., **127**, 1573 (1980).
[7] F. D. Auret, O. Paz and N. A. Bojarczuk, J. Appl. Phys., **55**, 1581 (1984).
[8] M. Beguwala and C. R. Crowell, J. Appl. Phys., **45**, 2792 (1974).
[9] G. L. Miller, D. V. Lang and L. C. Kimerling, Ann. Rev. Mater. Sci.,7, 203 (1961).
[10] F. D. Auret, M. Nel and N. A. Bojarczuk, J. Vac. Sci. Techno., **B 4**, 1168 (1986).
[11] P. N. K. Deenapanray, F. D. Auret, W. E. Meyer and G. Myburg, unpublished.
[12] J. R. Troxell, Solid-State Electronics, **26**, 539 (1983).
[13] B. G. Svensson, B. Mohadjeri, A. Allen, J. H. Svensson and J. W. Corbett, Phys. Rev. B **43**, 2292 (1991).

ELECTRONIC PROPERTIES OF DEFECTS FORMED IN n-Si DURING SPUTTER-ETCHING IN AN Ar PLASMA

P.N.K. DEENAPANRAY *, F.D. AURET *, C. SCHUTTE *, G. MYBURG *,
W.E. MEYER *, J.B. MALHERBE *, and M.C. RIDGWAY **
*Department of Physics, University of Pretoria, Pretoria 0002, sdeenapa@scientia.up.ac.za
**Department of Electronic Materials Engineering, Australian National University, Canberra, ACT 2601

ABSTRACT

We have employed current-voltage (IV), capacitance-voltage (CV) and deep level transient spectroscopy (DLTS) techniques to characterise the defects induced in n-Si during RF sputter-etching in an Ar plasma. The reverse leakage current, at a bias of 1 V, of the Schottky barrier diodes fabricated on the etched samples was found to decrease with etch time reaching a minimum at 6 minutes and thereafter increased. The barrier heights followed the opposite trend. The plasma processing introduced six prominent deep levels below the conduction band of the substrate. A comparison with the defects induced during high energy (MeV) alpha-particle, proton and electron irradiation of the same material revealed that plasma-etching created the VO- and VP-centres, and $V_2^{-/0}$. Some of the remaining sputter-etching-induced (SEI) defects have tentatively been related to those formed during either 1 keV He- or Ar-ion bombardment.

INTRODUCTION

Plasma processes are versatile techniques which are routinely used for submicron scale device fabrication. For instance, sputter deposition is used during metallization for the stoichiometric deposition of compounds and refractory metals on semiconductors. However, it has been shown that sputter deposition introduces donor-type defects at and close to the metal-semiconductor interface [1]. Plasma-based dry etching techniques such as sputter etching, ion beam etching (IBE) and reactive ion etching (RIE), are also used for the anisotropic etching of semiconductors. These plasma processes also result in lattice damage at and below the semiconductor surface which alters its electrical, optical and structural properties [2,3]. Little information on the structure of defects caused by sputter-etching is available [4,5]. The extent of the sputter-etching damage depends on the etching parameters such as etching time and rate, etching mode and bias conditions, as well as gas pressure and species. The type and extent of the sputter-etching induced (SEI) defects as a function of etch time are presented in this paper. To better understand the structure and electronic properties of the SEI defects we have compared them to those introduced during high energy (MeV) alpha-particle, proton and electron irradiation [6], and low energy (1 keV) He- and Ar-ion bombardment of the same material. We have also monitored the barrier heights and reverse leakage currents of the Schottky barrier diodes (SBD) fabricated on the etched surfaces.

EXPERIMENTAL PROCEDURE

Epitaxially grown (111) oriented n-type Si, doped to $5x10^{15}$ cm^{-3} with P, and grown on n^+-substrates were used in this study. The samples were chemically cleaned before being sputter-etched for 2, 4, 6, 8 and 10 minutes in an rf-excited (13.56 MHz) plasma. The plasma pressure and dc bias were kept constant at $5x10^{-3}$ mbar and 400 V, respectively. Circular Pd Schottky contacts of 0.77 mm diameter and 100 nm thickness, were then resistively deposited on the etched

samples through a metal contact mask. For control purposes, 100 nm thick Pd contacts were resistively deposited through the same mask on chemically cleaned but unetched (t = 0 min) Si. Ohmic contacts were formed on the n^+-substrates using a liquidus In-Ga alloy.

I-V and C-V measurements were used to monitor the quality of the SBDs. The C-V barrier height (ϕ_b^{CV}) was calculated from a graph of $1/C^2$ vs V_R by using a reverse bias, V_R, of between 0 and 1 V. The SEI defects were characterised using deep level transient spectroscopy (DLTS) [7]. The energy levels, E_T, and apparent capture cross-sections, σ_a, of the defects were determined from DLTS Arrhenius plots of $\log(e/T^2)$ vs $1/T$, where e is the emission rate at a temperature T. The depth profiles were determined using the method of Zotha *et al* [8].

RESULTS AND DISCUSSION

I-V and C-V results

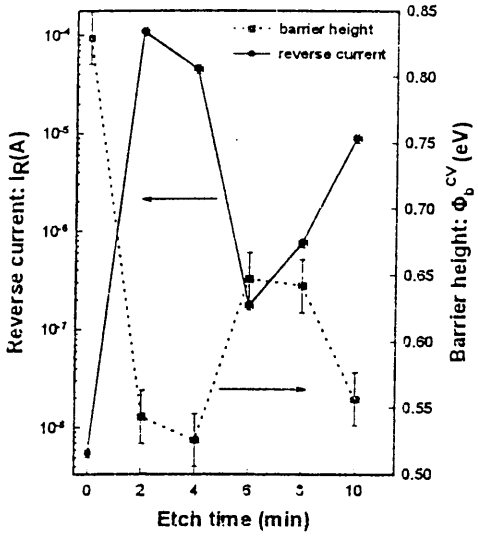

Figure 1: Variation of leakage current (I_R) at 1 V reverse bias and C-V barrier heights (ϕ_b^{CV}) of Schottky barrier diodes (SBD) fabricated on the sputter-etched samples in an Ar plasma at a pressure of $5x10^{-3}$ mbar and a dc bias of 400 V, as a function of time.

The diodes fabricated on the etched samples were found to be very leaky at room temperature. Hence, the leakage currents at 1 V reverse bias together with their C-V barrier heights were extracted at 250 K. The high ideality factors (n > 1.1) of the diodes suggested that the current transport mechanism over the barrier was not dominated by thermionic emission [9], so that the measured I-V barrier heights were not meaningful. Figure 1 shows that the leakage current decreases with sputter time to reach its minimum at 6 min, and increases thereafter. The diode barrier heights were found to follow the opposite trend. It has been proposed by Fonash *et al* [10] that sputter-etching may induce donor levels at and below the Si surface resulting in a lowering of barrier height. However, the high carrier compensation (C-V depth profiles) in the sample etched for 2 min indicates that sputter-etching introduced acceptor levels. We have, therefore, accounted for the changes in the measured barrier heights to be due to the introduction of a continuous distribution of near-surface states during etching, which pin the Fermi level in the band gap. Consequently, the least amount of defects are produced for 6 min etch times, when the effect of Fermi level pinning is least. This would correspond to a steady state regime proposed by Hirai *et al* [5]. It is speculated that for t > 6 min, the higher doses (constant etch rate) of Ar ions impinging the exposed surface results in the formation of extended defects and may even amorphise the sub-surface region. These results are in agreement with the defect depth profiling studies which are discussed below. The presence of extended defects has been correlated to baseline skewing of the DLTS spectra corresponding to etch times of 8 and 10 min, respectively, as has been proposed by Auret *et al* for GaAs [11]. Glancing angle Rutherford backscattering spectroscopy (RBS) and transmission electron microscopy (TEM) experiments to detect the presence of amorphous layers in our etched samples are in progress.

DLTS results

A typical DLTS spectrum for a sputter-etched sample is shown in curve (b) of Fig. 2. The defects are labelled P1 through to P8, and are identified in the form, for instance EP088 (P1), where "E" denotes an electron trap, "P" for plasma-etching induced and 088 the position in meV of the specific level below the conduction band. Three well resolved peaks EP088 (P1), EP143 (P2) and EP454 (P8) were identified, whereas EP183 (P3) and EP310 (P6) could be resolved only after using filling pulses of narrow widths (ns). Furthermore, the "signature" of P7 (EP326) was extracted after annealing the etched sample at 260 °C for 30 minutes.

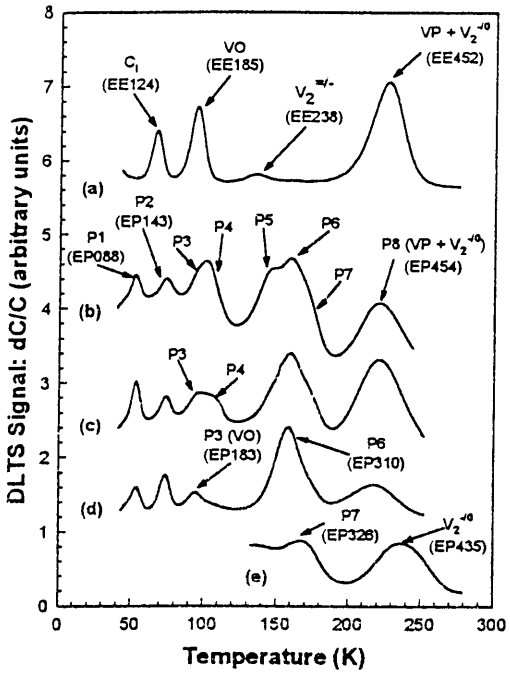

Figure 2: DLTS spectra of epitaxially grown n-Si bombarded with high energy (MeV) electrons [curve (a)], and sputter-etched in an Ar plasma [curve (b)] using 0.2 ms filling pulses. Curves (c) and (d) were obtained using filling pulse widths of 500 ns and 25 ns, respectively. Curve (e) was obtained after annealing the etched sample at 260 °C. All curves were recorded at a lock-in amplifier frequency of 46 Hz, $V_r = 1$ V and $V_p = 1.4$ V.

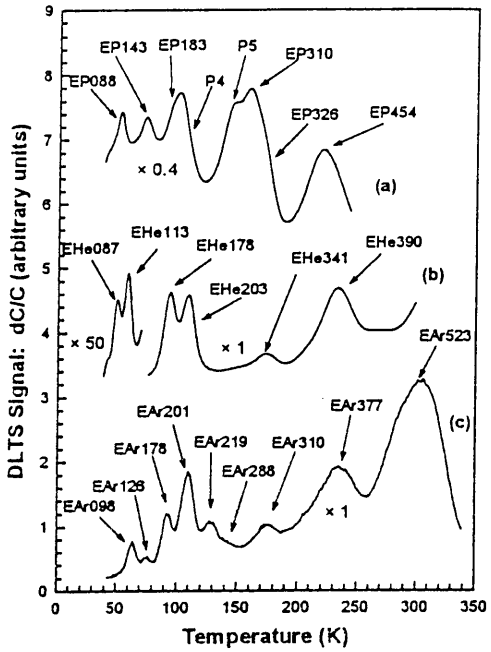

Figure 3: Comparison of DLTS spectra of epitaxially grown n-Si doped to $5x10^{15}$ cm^{-3} with P. (a) Sputter-etched in an Ar plasma at a pressure of $5x10^{-3}$ mbar (dc bias of 400 V), (b) bombarded with 1 keV He ions and (c) 1 keV Ar ions. A lock-in amplifier frequency of 46 Hz was used to extract the data.

Though the SBDs had leaky I-V characteristics, the DLTS results presented here are reliable because the activation energies of the SEI defects are less than the calculated barrier height of the most degraded diode (t = 4 min) [12]. To learn more about the structure of the SEI defects, we compared them with the primary defects induced in Si during high energy (MeV) electron, proton and alpha-particle irradiation [6,13]. Curve (a) [Fig. 2] shows the DLTS spectrum of the defects induced in n-Si during irradition with high energy (MeV) electrons. In addition to VO- and VP-centres, $V_2^{=/-}$ and $V_2^{-/0}$, high energy alpha-particle and proton irradiation introduced levels at E_c - 0.08 eV and E_c - 0.14 eV. However, no level at E_c - 0.124 eV was introduced during high energy proton and alpha-particle irradiation. After annealing the

electron irradiated sample at 180 °C for 30 minutes, EE124 annealed out and levels at E_c - 0.141 eV and E_c - 0.085 eV, which have similar electronic "signatures" (activation energy, E_T and apparent capture cross-section, σ_n) as EP143 and EP088, respectively, emerged [14]. A comparison between the SEI defects and primary defects revealed that P3 is electronically the same as the VO-centre while P8 is the superposition of the VP-centre and $V_2^{-/0}$ (EP435 resolved as per curve (e) [Fig. 2]). EP088 and EP143 are tentatively assigned the C_i-C_s structure [15]. Note that no direct evidence could be obtained from our results to show the detection of $V_2^{=/-}$. Since $V_2^{-/0}$ is observed after the VP-centre anneals out, the proposal from Svensson *et al* [16] is used to argue that the high level of damage induced in our samples results in stress fields which prevent the complete filling of $V_2^{=/-}$.

During the sputter-etching process, the Si samples were subjected to bombardment by energetic Ar ions and Ar atoms (energy between 0.4 and 1 keV) from the plasma. In order to characterise the SEI defects we have compared them with those introduced during 1 keV Ar-ion bombardment of the same material. In order to establish whether any of the SEI defects are noble gas species dependent, we have also compared them with defects created by 1 keV He-ion bombardment. Figure 3 shows the DLTS spectra of defects created during low energy Ar- [curve (c)] and He-ion [curve (b)] bombardment. From the curves in Fig. 3, P4 is tentatively matched to EAr201 and EHe203, which have similar "signatures". Annealing studies at 350 °C are scheduled to monitor the annealing of the VO-centre and to resolve P4 if it is indeed similar to EAr201/EHe203 (anneal out at 500 °C). EP310 could be similar to EAr310 since they have similar electronic properties. The properties of the SEI defects are summarised in Table I.

Table I : Summary of electronic and structural properties of the main SEI defects

Defect	P1	P2	P3	P4	P6	P7	P8
E_T (meV)	88	143	183		310	326	452
σ_a (cm^2)	$3.7x10^{-16}$	$5.7x10^{-15}$	$3.4x10^{-15}$		$1.6x10^{-15}$	$1.5x10^{-15}$	$4.2x10^{-16}$
T_{peak}[(b)] (K)	54	74	94		158	167	237
Similar defects	C_i-C_s [14]	C_i-C_s [14]	VO [6]	EAr201/ EHe203?	EAr310?		VP + $V_2^{-/0}$ [6]

(b) Peak temperature at a lock-in amplifier frequency of 46 Hz (decay time constant of 9.23 ms).

The peak DLTS signal intensities of the main SEI defects for Vr = 1 V and Vp = 1.4 V are plotted as a function of etch time in Fig. 4. It is observed that the intensities of the main defects reach a minimum in the sample etched for 6 min, and thereafter increase with etch time, which is in agreement with our I-V and C-V results. The DLTS signal for t = 2 minutes should be treated with caution because of the high carrier compensation in that sample. This result suggests that a high concentration of defects are introduced in the samples for t < 6 min, and decrease with time to reach a minimum at 6 min. The gradual increase in the defect densities for t = 8 min and t = 10 min, respectively, could be due to the creation of extended defects.

Figure 5 shows the depth profiles of P6 as a function of etch time. For the reason already specified, the depth profile corresponding to an etching time of 2 minutes is not included. The depth profiles shown here are accurate since the diodes had relatively lower leakage currents and higher barrier heights at 160 K compared to those at 250 K. A close inspection of Fig. 5 shows that the depth profiles can be separated into two distint regions - (1) a region labelled A which is

within a depth of 0.1 μm of the metal-semiconductor interface, and (2) a region B starting at a depth 0.1 μm and extending into the semiconductor. Close to the etched surface (region A), the

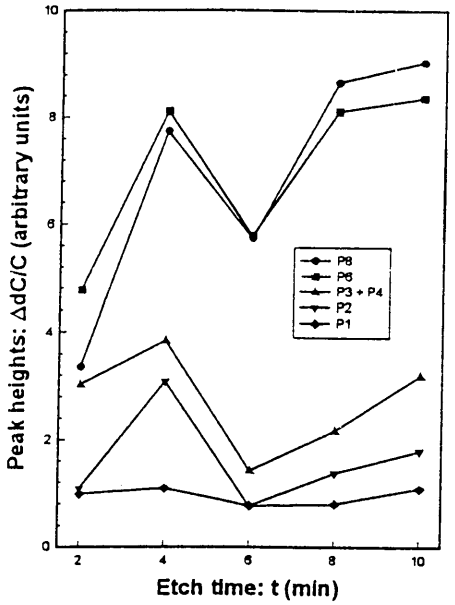

Figure 4: Peak DLTS intensity of the prominent SEI defects at V_r = 1 V and V_p = 1.4 V. None of the defects could be observed in the unetched sample. The data points for t = 2 min are not meaningful because of the heavy carrier compensation in the corresponding etched sample.

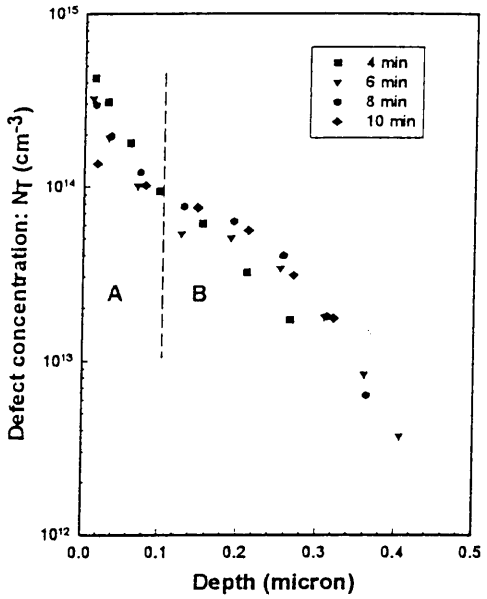

Figure 5: Depth profile (constructed from DLTS measurements using a lock-in amplifier frequency of 46 Hz) of defect P6 introduced in epitaxially grown n-Si doped to $5x10^{15}$ cm^{-3} with P, during plasma-etching in an Ar plasma at a pressure of $5x10^{-3}$ mbar and a dc bias of 400 V.

concentration of P6, [P6], is a maximum for t = 4 min, and that at 8 min slightly larger than at 6 min as expected. The lower than expected [P6] at t = 10 min is attributed to the presence of extended defects which resulted in baseline skewing of our DLTS spectra. Consequently, lower peak intensities of P6 were extracted under the successive application of forward filling pulses. Region B shows an opposite time dependence in the depth distribution of P6. The increasingly higher [P6] from t = 2 min to t = 10 min is expained by its in-diffusion, which is proportional to $\sqrt{t}$, into the epi-layer. This in-diffusion may also be assisted by recombination-enhanced diffusion [17].

CONCLUSIONS

The defects induced in n-Si by sputter-etching in an Ar plasma at a pressure of $5x10^{-3}$ mbar and a dc bias of 400 V, together with the electrical characteristics of the Schottky barrier diodes fabricated on the etched samples, have been studied as a function of etch time. We have proposed that sputter-etching has introduced acceptor-type defects in n-Si which caused an increase in the leakage currents of the diodes fabricated on the etched surfaces. The lowering of barrier heights has been explained by the introduction of a continuous distribution of near-surface states which result in the Fermi level pinning. The extent of the Fermi level pinning has been proposed to increase with the concentration of near-surface states. It has been shown that minimum damage was created for an etch time of 6 min and that extended defects could be introduced for etch times longer than 6 min. Some of the defects were successfully matched with primary defects which are introduced during high energy alpha-particle or electron irradiation,

whereas others have been tentatively identified to be noble gas-related. DLTS depth profiling of a defect P6 has revealed two distinct regions in its spatial distribution. The leakage currents of the diodes follow the same trend as the concentration of defect P6 in a region extending to approximately 0.1 μm below the interface. However, the concentration in a region extending beyond 0.1 μm increases with etch time, and has been attributed to the in-diffusion of the P6.

ACKNOWLEDGMENTS

The financial assistance of the FRD and CEFIM are gratefully acknowledged, as well as the technical assistance of J.P. le Roux and C.M. du Toit.

REFERENCES

1. F.H. Mullins and A. Brunnschweiler, Solid State Electron. **19**, p. 47 (1976).
2. S.J. Pearton, W.S. Hobson, U.K. Chakrabarti, G.E. Derkits, Jr., and A.P. Kinsella, J. Electrochem. Soc. **137** (12), p. 3892 (1990).
3. G.S. Oehrlein, Materials Science and Engineering B4, p. 441 (1989).
4. O.O. Awadelkarim, T. Gu, P.I. Mikulan, R.A. Ditizio and S.J. Fonash, Appl. Phys. Lett. **62** (9), p. 958 (1993).
5. M. Hirai, H. Iwakuro, J. Ohno, and T. Kuroda, IEEE Transactions on Components, Hybrids, and Manufacturing Technology **13** (4), p. 629 (1990).
6. J.R. Troxell, Solid State Electronics **26**, p. 539 (1983).
7. D.V. Lang, J. Appl. Phys. **45**, p. 3014 (1974).
8. Y. Zohta and M.O. Watanabe, J. Appl. Phys. **53**, p. 1809 (1982)..
9. E.H. Rhoderick and R.H Williams, Metal-Semiconductor Contacts, 2nd ed. (Clarendon Press, Oxford, 1988), p. 38.
10. S.J. Fonash, S. Ashok and Ranbir Singh, Thin Film Solids **90**, p. 231 (1982).
11. F.D. Auret, S.A. Goodman, R.M. Erasmus, W.E. Meyer and G. Myburg, Nucl. Instr. and Meth. **B 106** (1995) 323.
12. Q.Y. Ma, M.T. Schmidt, X. Wu, H.L. Evans and E.S. Yang, J. Appl. Phys. **64**, p. 2469 (1988).
13. L.C. Kimerling, Inst. Phys. Conf. Ser. **13**, p. 221 (1977).
14. P.N.K. Deenapanray, F.D. Auret, G. Myburg and W.E. Meyer, C.M. Demanet, unpublished.
15. J.L. Benton, M.T. Asom, R. Sauer and L.C. Kimerling in Identification of Interstitial Carbon Related Defects in Silicon, edited by M. Stavola, S.J. Pearton and G. Davies (Mater. Res. Soc. Proc. **104**, Pittsburgh, PA, 1988) pp. 85-91.
16. B.G. Svensson, B. Mohadjeri, A. Allen, J.H. Svensson and J.W. Corbett, Phys. Rev. **B 43**, p. 2292 (1991).
17. J.L. Benton, J. Michel, L.C. Kimerling, B.E. Weir and R.A. Gottscho, Journal of Electronic Materials **20**, p. 643 (1991).

ELECTRICAL CHARACTERISATION AND ANNEALING BEHAVIOUR OF DEFECTS INTRODUCED IN Si DURING SPUTTER ETCHING IN AN Ar-PLASMA

P.N.K. Deenapanray, F.D. Auret and G. Myburg

Department of Physics, University of Pretoria, Pretoria 0002, SOUTH AFRICA

ABSTRACT

We have employed current-voltage and capacitance-voltage measurements in conjunction with deep level transient spectroscopy to characterise the defects induced in n-Si during rf sputter-etching in an Ar plasma. The reverse current, at a bias of 1 V, of the Schottky barrier diodes fabricated on the etched samples decreased with etch time to a minimum at 6 min and, thereafter, increased. Furthermore, the reverse current increased with decreasing plasma pressure. The barrier heights of the diodes followed the opposite trend. Six prominent electron traps were introduced in the substrate during Ar sputter-etching. A comparison with the defects induced during high-energy alpha-particle, proton and electron irradiation of the same material revealed that sputter-etching created the VO and VP centres and $V_2^{-/0}$. The $V^{=/-}$ charge state of the divacancy was not detected in our plasma etched samples. We have attributed the non-detection of $V_2^{=/-}$ to the presence of defect-induced stress fields in the etched samples. A secondary defect which introduced an energy level at E_c - 0.219 eV was introduced during annealing and was found to be stable at 650 °C. This defect was introduced at the expense of a sputter-etching induced defect P4, which has similar electronic and annealing properties as EAr201 (E_c - 0.201 eV), created in Ar-ion bombarded n-type Si.

I. INTRODUCTION

Plasma processes are versatile techniques which are routinely used for submicron scale device fabrication. Sputter etching, ion beam etching (IBE) and reactive ion etching (RIE), are used for anisotropic etching and the transfer of patterns to semiconductor surfaces. These plasma etching techniques also result in lattice damage at and below the surface which alters the electrical, optical and structural properties.[1,2,3]

Traditionally, defects introduced during growth and subsequent processing have been considered undesirable. However, defect engineering[4] which relies on the controlled and reproducible introduction of defects, has recently been applied to control the lifetime of minority carriers,[5] tailor the barrier height of SBDs,[1] and control the band offset in heterojunction devices.[6] Any successful application of defect engineering requires that the introduction rates and concentrations of processing-induced defects, together with their physical nature and electronic properties, are well characterised.

During sputter-etching, the extent of damage depends on parameters such as etch time, temperature and rate, etching mode and bias conditions, as well as gas pressure and species. Extensive studies have been conducted to investigate the extent and type (donor or acceptor) of defects created during plasma etching and their effects on the barrier height modification of SBDs fabricated on the etched surfaces.[7-10] The sputter yield and the structural and bonding changes induced in Si by Ar ion-etching have also been studied.[11,12] Despite these studies, little information is available on the electronic properties, structure and thermal stability of defects introduced during sputter-etching of Si in an Ar plasma. In this paper, the electronic properties and annealing behaviour of sputter-etching induced (SEI) defects are reported. To better understand the nature of these defects, we have

compared their electronic properties to those of defects created during high-energy (MeV) alpha-particle, proton and electron irradiation, and low-energy (1 keV) He- and Ar-ion bombardment of the same material. We have also investigated the extent of SEI damage by monitoring the rectifying behaviour of the SBDs fabricated on the etched surfaces.

II. EXPERIMENTAL PROCEDURE

(111) oriented n-type Si layers of thickness 4 μm and doping concentration 4.8×10^{15} cm^{-3} with P were epitaxially grown on n^+-substrates by chemical vapour deposition (CVD). The samples were chemically cleaned before being sputter-etched in a Leybold-Heraeus Universal Sputtering machine using an rf-excited (13.56 MHz) plasma. One batch of samples were sputter-etched for 2-10 minutes with the plasma pressure kept constant at 5×10^{-3} mbar. A second batch of samples was etched at plasma pressures of 2×10^{-3} - 2×10^{-2} mbar for 6 min. For both experiments the dc bias on the rf electrode was fixed at 400 V. The samples were kept at room temperature by mounting them on a water cooled substrate holder.

Circular Pd Schottky contacts of 0.77 mm diameter and 100 nm thickness were resistively deposited on the etched samples through a metal contact mask. As a control, Pd contacts were also deposited on chemically cleaned but unetched Si. Ohmic contacts were formed on the n^+-substrates using a liquidus In-Ga alloy.

Current-voltage (I-V) and capacitance-voltage (C-V) measurements were used to monitor the quality of the SBDs. The C-V barrier height (ϕ_b^{CV}) was calculated from a graph of $1/C^2$ vs V_R by using a reverse bias, V_R, of between 0 and 1 V. The SEI defects were characterised using deep level transient spectroscopy (DLTS).[14] The energy levels,

E_T, and apparent capture cross-sections, σ_a, of the defects were determined from DLTS Arrhenius plots of $\log(e/T^2)$ vs $1/T$, where e is the emission rate at a temperature T. The defect depth profiles were determined using the method of Zotha *et al.*[15] Isochronal annealing experiments were conducted to 650 °C, at 50 °C intervals, for periods of 20 min under Ar flow and zero bias. DLTS was employed to monitor changes in the peak signal intensities of the prominent SEI defects as well as the introduction of secondary defects.

III. RESULTS

A. I-V and C-V characteristics of SBDs

Figure 1(a) shows the I-V characteristics, measured at 250 K, of the SBDs deposited on the etched Si samples as a function of etch time. The high ideality factors (n > 1.1) of the diodes suggested that the current transport over the barrier was not dominated by thermionic emission,[16] so that the measured I-V barrier heights (ϕ_b^{IV}) were not meaningful. It can be seen from Fig. 1(a) that the reverse current decreased with etch time to reach a minimum at 6 min, and increased thereafter. Plots of $\ln(J/T^2)$ vs $1000/T$ at a forward voltage of 0.1 V are depicted in Fig. 1(b) for diodes fabricated on samples etched for 2, 6 and 10 min. It can be seen from this graph that the temperature dependence of the forward current of the diodes shows two activation energies, suggesting that two different mechanisms are responsible for current transport over the Schottky barrier in the temperature range examined (120 - 300 K). The low temperature mechanism is dominant for a 2 min etch time whereas the high temperature mechanism is dominant for a 6 min etch time. The low values of activation energies [less than $(E_g - V_F)/2$] suggest that the transport mechanisms involve a combination of generation-recombination and tunneling.[17]

The above results are further substantiated by observing the change in barrier heights of the diodes as a function of etch time (Fig. 2). The barrier heights were extracted from CV measurements and compared with values calculated from Eqns. (1) and (2) using diode currents at a reverse bias of 1 V.

$$J_o = \frac{J}{\{\exp(qV / kT) - 1\}} \tag{1}$$

$$\phi_b{}^{eff} = -\frac{kT}{q}\ln\left(J_o / A^{**}T^2\right) \tag{2}$$

In the above equations, J is the current density, V is the reverse bias, A^{**} is the effective Richardson constant (112 x 10^4 A m^{-2} K^{-2} -assumed to be constant between 120-300 K), T is the measurement temperature, $\phi_b{}^{eff}$ is the effective barrier height, and the remaining symbols have their usual meaning. As anticipated, the barrier heights follow the opposite trend to the reverse current except for the relatively higher $\phi_b{}^{CV}$ of the diode fabricated on the 2 min sputter-etched sample. CV depth profiling (not shown) demonstrated that the free carrier compensation at depths < 0.5 μm below the interface after a 2 min etch was approximately 10 %, and hence $\phi_b{}^{CV}$ of the corresponding diode is higher than expected. In general, the differences between $\phi_b{}^{CV}$ and $\phi_b{}^{eff}$ can be attributed to: (a) the image-force lowering of barrier height was not taken into account in calculating $\phi_b{}^{eff}$, and (b) the measured $\phi_b{}^{CV}$ values could be over-estimated if the traps introduced during plasma-etching ionize under CV bias excursions.[18] The significant lowering in $\phi_b{}^{CV}$ of the diodes

fabricated on the etched samples compared to that of the control diode further revealed that the rectifying properties of Pd/n-Si SBDs fabricated on sputter-etched surfaces were poorer than those on unetched surfaces.

The variations in ϕ_b^{IV} and current, I_R, at a reverse bias of 1 V are plotted as a function of plasma pressure in Fig. 3(a), while Fig. 3(b) shows the pressure dependence of free carrier concentration of the etched samples. The lowering in barrier heights with decreasing plasma pressure observed in Fig. 3(a) is in agreement with the results obtained during sputter deposition of metals on n-Si[1,19] and with the proposal that ion-induced etching introduces donor-type levels at and below the semiconductor surface.[8] On the other hand, the reverse current is found to decrease with Ar pressure. The CV depth profiles shown in Fig. 3(b) demonstrated that sputter-etching introduced two types of defects in the Si lattice. The net decrease in free carrier concentration in the region extending beyond 0.45 μm suggested that sputter-etching created acceptor-type defects which migrated to depths much larger than the Ar ion projected range (21 Å for 400 eV Ar^+ [TRIM]). It is, furthermore, observed that the carrier compensation, and hence the amount of damage, increased with decreasing plasma pressure. The apparent increase in carrier concentration from a depth of approximately 0.45 μm towards the interface has been attributed to the presence of donor-type defects.

Capacitance-voltage measurements were conducted in the temperature range 40 - 100 K in order to study the apparent increase in free carrier concentration at depths of ~0.4 μm below the interface. Since this feature was common to all the sputter-etched samples, the sample etched for 6 min at a plasma pressure of $9x10^{-3}$ mbar was arbitrarily chosen for the measurements. Figure 4 shows that the free carrier compensation due to acceptor-type defects is observed at all temperatures. However, the apparent increase in

free carrier density could only be observed above 80 K, and its effect became more significant at 100 K. Furthermore, the increase in free carrier density could be observed deeper below the interface with increasing temperature.

B. DLTS results

A typical DLTS spectrum for a sputter-etched sample is shown in curve (b) of Fig. 5. The defects are labelled P1 through to P8, and are identified in the form, for instance EP088 (P1), where "E" denotes an electron trap, "P" stands for plasma-etching related defect and "088" corresponds to the position in meV of the trap below the conduction band. Three well resolved peaks EP088 (P1), EP143 (P2) and EP454 (P8) were observed under normal conditions (filling pulses of 0.2 ms width). Figure 5 (c) and (d) show that EP183 (P3) and EP310 (P6) could be resolved after using filling pulse widths as low as 20 ns, suggesting that their capture cross-sections are larger than those of P4, P5 and P7, respectively. We have also used current (I)-DLTS to monitor the presence of a shallow electron trap with a level at E_c - 0.056 eV, which could not be detected using conventional capacitance (C)-DLTS. The modified Arrhenius plots from which the activation energy, E_t, and apparent capture cross-section, σ_a, of the SEI defects were extracted are illustrated in Fig. 6.

Figures 7(a) and 7(b) illustrate the peak DLTS signal intensities of the prominent SEI defects as functions of etch time and plasma pressure, respectively. Figure 7(a) shows that the intensities of the SEI defects, and hence their concentrations, decreased with etch time to reach a minimum at 6 min, and thereafter increased. Due to the high degree of carrier compensation, the DLTS signals for t = 2 min have been grossly under-estimated and are, therefore, lower than the signals corresponding to t = 4 min. An increase in the

peak intensities of the defects was expected with decreasing pressure. The relatively lower intensities of the SEI defects for $2x10^{-3}$ mbar compared to $9x10^{-3}$ mbar [Fig. 7(b)] have also been attributed to the heavy carrier compensation sustained at the lowest pressure [Fig. 3(b)].

DLTS depth profiling of the samples etched for 6 min at different plasma pressures (not shown) revealed that the concentrations of the prominent defects EP310 and EP454 decreased exponentially according to Eqn. (3),

$$N_T(x) = N_{T0} \exp(-x / L) \qquad (3)$$

where N_{T0} is the defect concentration at the interface (x = 0) and L is the characteristic distribution length of the trap. The surface concentrations and characteristic lengths of EP310 and EP454 are summarised in Table I for different plasma pressures. The values of N_{T0} at $2x10^{-3}$ mbar were found to be marginally smaller than their corresponding values at $9x10^{-3}$ mbar for both EP310 and EP454. The DLTS depth profiles of EP454 are shown in Fig. 8 as a fucntion of etch time. We have explained the difference between the depth distributions in Fig. 8 by considering the following two competing time-dependent processes: (a) Ar-ion sputtering of the bombarded surface layers and (b) defect in-diffusion.

EP088 and EP143 were completely removed after annealing at 100 °C, whereas the overlapping P3 and P4 peaks were annihilated above 200 °C. The prominent defects EP310 and EP454 were annealed out at 300 °C and 200 °C, respectively. Isochronal annealing proved to be an efficient technique to resolve some of the overlapping DLTS defect peaks. The "signature" of P7 (EP326) was extracted after annealing an etched sample at 250 °C. The peak of P5, which has a level at E_c - 0.219 eV in the band gap, was identified after

removing both P6 and P7 at 300 °C. Figure 9 depicts the DLTS spectra from an annealed sputter-etched sample at various temperatures. It can be seen from Fig. 9 that EP454 was removed at 200 °C, after which an electron trap EP435, which was thermally stable up to 550 °C, could be observed. EP203 was the main defect after annealing at 450 °C and could not be detected above 550 °C. The intensity of a defect EP219 was observed to increase above 400 °C, while that of EP203 decreased. EP219 was the main defect above 450 °C and its magnitude decreased when annealing above 550 °C. This defect was however thermally stable at 650 °C.

IV. DISCUSSION

A. Electrical characteristics of SBDs and extent of SEI damage

The results presented above have shown that the rectifying properties of Pd SBDs fabricated on sputter-etched n-Si were poorer than those fabricated on a chemically cleaned but unetched substrate. We can explain the differences between the electrical properties of the diodes deposited on Si etched for different time periods by considering the following two competing time-dependent processes: (a) defect removal by Ar-ion sputtering and (b) defect in-diffusion. During the etching process, low-energy Ar ions sputter the Si surface whilst coming to rest, on average, at a depth of ~21 Å. The projected range of the ions depends on their energy, which will be assumed to be equal to qV_{dc} eV throughout this discussion (V_{dc} being the dc bias on the electrode and q the electron charge). The low-energy implanted Ar ions transfer energy to the Si lattice predominantly by nuclear stopping and create damage in the crystal by displacing substrate atoms. Sputtering also results in the simultaneous erosion of the topmost atomic layers, and hence the removal of ion-induced damage. The amount of damage removed is proportional to the etch time, t,

and is rivalled by the in-diffusion (proportional to $\sqrt{Dt}$) of the ion beam induced defects. For relatively small etch times, the in-diffusion of defects supersedes their removal leading to accumulation of damage below the semiconductor surface. Furthermore, the etch rate requires a definite time to equilibrate, such that for small etch times the accumulation of damage is predominant over the sputtering process. As shown in Figs. 1 and 2, the quality of the diodes improved with etch time up to 6 min. We have attributed the lower rectifying characteristics of the diodes corresponding to etch times larger than 6 min to the formation of an amorphous layer with a corresponding continuous distribution of electronic states in the band gap.[20] The amount of etching-induced damage were further substantiated by our DLTS results. Figure 7(a) showed that the peak DLTS signal intensities of the main SEI defects followed similar trends as the IV characteristics of the diodes. Furthermore, the DLTS depth profiles of EP454 (Fig. 8) and EP310[20] revealed that the defect distributions could be separated into 2 distinct regions - (1) a region labelled A of depth < ~0.10 μm, and (2) a region B of depth > ~0.10 μm below the interface. It is seen that the concentrations of EP454 decreased with etch time within region A, which is consistent with the proposal that defect diffusion dominates over their removal rates for relatively low etch periods of time. Region B revealed that the defects migrated to depths much larger than the projected range of 400 eV Ar ions (21 Å), suggesting that diffusion of the plasma-etching induced defects could have been assisted by recombination-enhanced diffusion or transient enhanced diffusion.[21,22]

The plasma pressure dependence of the rectifying characteristics of the diodes is explained by considering the mean free path, λ, between collision of Ar ions with neutral Ar atoms in the cathode sheath. Since λ is inversely proportional to the plasma density, the

frequency of collision of an Ar ion in a denser plasma is higher. The ion is thus accelerated over a shorter distance inside the discharge and its kinetic energy before a collision is lower compared to another ion in a less dense environment. The Ar ions in a low-pressure plasma, therefore, bombard the Si surface with higher energies compared to Ar ions in a denser plasma. The result is that more damage is introduced in the semiconductor lattice at lower plasma pressures. As shown in Fig. 3(a), the electrical properties of the diodes became poorer, while Fig. 3(b) illustrated that the compensation in free carrier concentration of the etched samples increased, with decreasing plasma pressure. The DLTS plots illustrated in Fig. 7(b) further validate our results. Since the DLTS signal is proportional to the carrier concentration, the peak signal intensities corresponding to a plasma pressure of $2x10^{-3}$ mbar were lower than at $9x10^{-3}$ mbar because of the higher incurred degree of free carrier compensation [Fig. 3(b)].

The CV depth profiles shown in Fig. 3(b) revealed that sputter etching introduced acceptor-type defects resulting in maximum free carrier compensation in a region 0.45 - 0.50 μm below the interface as well as donor-type traps which caused an apparent increase in the free carrier concentration at depths < ~0.40 μm below the interface. Figure 4 revealed that the effect of the donor-type defects on the free carrier density could only be observed above 60 K. It is, therefore, concluded that sputter-etching introduced donor-type defects close to the interface with shallow levels, which are filled at and below 60 K. In addition, I-DLTS measurements showed that an electron trap with a level at E_c - 0.056 eV was created during the plasma-etching process. An extended analysis of the effect of donor-type defects on the parameters extracted from CV measurements on n-type SBD has been proposed by Bauza.[18] Assuming that the traps introduced in sputter-etched Ti-W/n-Si

diodes decreased exponentially below the interface, he demonstrated that the apparent increase in free carrier concentration below the interface changed as functions of the trap activation energy and characteristic length.

B. Electronic, structural and annealing properties of SEI defects

Curve (a) of Fig. 5 shows the DLTS spectrum of the structurally identified defects induced in n-Si during MeV electron irradiation. We have observed that high energy alpha-particle and proton irradiation introduced levels at E_c - 0.08 eV and E_c - 0.14 eV, in addition to the VO- and VP-centres, and the two charge states of the divacancy ($V_2^{=/-}$ and $V_2^{-/0}$). $V_2^{-/0}$ is only detected after removing the VP-centre at 180 °C. EE124 (the second "E" in the nomenclature refers to "electron-irradiated") was removed and levels at E_c - 0.141 eV and E_c - 0.085 eV, which have similar electronic "signatures" as EP143 and EP088, respectively, emerged after annealing our electron-irradiated sample at 180 °C for 30 minutes. These strongly suggest that EE124 is structurally identical to the carbon interstitial (C_i). Since EP088 was reversibly removed after cooling under zero bias ($V_R = 0$ V) and re-introduced under a reverse bias excursion ($V_R = -2$ V) and noting that the intensity of EP143 increased and decreased, respectively, under these cycles, the two defects have been assigned the C_s-Si_i-C_s and C_i-C_s structures, respectively.[23] EP435 could be detected after removing EP454 at 180 °C [Fig. 5(e)] and its intensity was found to be approximately six times less than that of EP454 [Fig. 9(b)]. Furthermore, EP435 was observed to be thermally stable up to 500 °C [Fig. 9(b)]. The "signature" of EP454 together with its annealing behaviour suggest that it is the superposition of the VP-centre and $V_2^{-/0}$ (EP435). No direct evidence could be obtained from our results to show the

detection of $V_2^{=/-}$. Since $V_2^{-/0}$ is observed after the VP-centre anneals out, we argue that the high level of SEI damage in the region probed by DLTS created stress fields which prevented the complete filling of $V_2^{=/-}$.[24]

During any sputter-etching process, the substrate is subjected to bombardment by energetic noble gas ions from the plasma. In order to further characterise the SEI defects, we have compared them with those introduced during 1 keV Ar-ion bombardment of the same material. To establish whether any of the SEI defects are noble gas species dependent, we have also compared them with defects created by 1 keV He-ion bombardment. Photoluminescence experiments have demonstrated that low-energy, noble-gas-ion bombardment of Si created noble-gas-related defects.[25,26] Furthermore, we have recently shown that 1 keV He-ion bombardment of Si introduced a different set of defects compared to 5.4 MeV alpha-particle irradiation of the same material.[27] Figure 10 shows the DLTS spectra of defects created during 1 keV Ar- and He-ion bombardment of n-Si [curves (c) and (b), respectively]. From the curves in Figs. 9 and 10, P4 is matched to EAr201 and EHe203, since they have similar "signatures" and annealing properties. Since the electronic properties of EP310 and EP326 are similar within experimental error, to that of EAr310, we are currently conducting annealing studies on 1 keV Ar ion-bombarded Si samples to elucidate which of the two could be similar to EAr310. Furthermore, EP493, which is observed after annealing at 400 °C, has a similar “signature” to EAr377, while EP219 (dominant above 550 °C) is electronically similar to EAr219.

The fact that the intensity of EP219 increased while that of EP203 decreased during annealing above 450 °C suggest that they could be structurally similar defects. Based on results obtained from TRIM simulations, which show that the nuclear energy components

of 1 keV He- and Ar-ions are larger than the threshold energy for spike formation (~1-5 eV/atom), we have argued that the defects created by these ions could be vacancy clusters V_x ($x > 2$), the incorporation of the noble gas ions into these clusters or Si interstitials (Si_i).[27] On account of the following reasons, we tentatively propose that EP203 and EP219 are not noble gas species-related defects but are rather due to V_x or Si_i. Firstly, we have observed a defect with similar electronic properties to EHe203/EAr201 in 5.4 MeV Si-implanted n-Si. Secondly, a defect having an identical DLTS "signature" to EHe203 has been observed in 5.4 MeV alpha-particle irradiated Si after annealing above 180 °C. We are also conducting isochronal annealing experiments on MeV Si-, alpha-particle, and electron-irradiated n-Si to learn more about the natures of EHe203/EAr201 and EAr219, and thus about EP203 and EP219.

V. CONCLUSIONS AND SUMMARY

The electronic properties and concentration of defects introduced in n-Si during sputter-etching, together with the electrical characteristics of the Schottky barrier diodes fabricated on the etched samples, have been studied as a function of etch time and plasma pressure. Our results have shown that sputter-etching introduced both donor- and acceptor-type defects in n-Si. The donor-like traps caused an apparent increase in the free carrier concentration close to the interface resulting in a lowering of barrier heights of the SBDs. The acceptor-type defects resulted in free carrier compensation to depths much larger than the projected range of the implanted Ar ions. The rectifying properties of the SBDs were less degraded for relatively long etch periods and higher plasma pressure. An equilibrium between defect generation and defect removal could be achieved after etching for 6 min.

We have attributed the poorer qualities of SBDs for etch periods exceeding 6 min to the formation an amorphous layer with a continuous distribution of electronic states. Some of the SEI defects were successfully identified as being structurally identical to C_i-C_s, the VO- and VP-centres and $V_2^{-/0}$. The non-detection of $V_2^{=/-}$ has been attributed to the presence of stress fields in our sputter-etched samples. We have proposed some of the other SEI defects to be related to either vacancy clusters (larger than the divacancy) or Si interstitials. Our results have unambiguously demonstrated that sputter etching introduced electrically active defects in high concentrations which altered the electrical properties of Schottky barrier diodes fabricated on the etched surfaces. Annealing could remove the SEI defects but also introduced a prominent defect EP219 which was thermally stable at 650 °C. EP203 has a similar DLTS "signature" and annealing behaviour as EAr201, produced by 1 keV Ar-ion bombardment. A similar defect (EHe203) is also observed in low energy He-ion bombarded n-type Si.

ACKNOWLEDGMENTS

The financial assistance of the FRD and CEFIM are gratefully acknowledged, as well as the technical assistance of J.P. le Roux and C.M. du Toit. We also thank C. Schutte for making the Universal Sputter Machine at DETEK available to us. The authors are also thankful to Mark C. Ridgway for critically reviewing the paper and to J.B. Malherbe for the 1 keV He- and Ar-ion bombardments.

Table I: Surface concentrations, N_{T0}, and characteristic lengths, L, of EP310 and EP454 in 6 min sputter-etched n-Si in an Ar plasma at $2x10^{-2}$ mbar and $9x10^{-3}$ mbar.

Defect	*Pressure (mbar)*	N_{T0} *(cm^{-3})*	*L (nm)*
EP310	$2x10^{-2}$	$\sim 8x10^{12}$	95 ± 16
	$9x10^{-3}$	$\sim 8x10^{13}$	95 ± 16
EP454	$2x10^{-2}$	$\sim 4.6x10^{13}$	143 ± 2
	$9x10^{-3}$	$\sim 7.3x10^{13}$	143 ± 2

FIGURE CAPTIONS

FIG. 1.

Etch time dependence of: (a) the I-V characteristics, and (b) plots of $\ln(J/T^2)$ against $1000/T$ at a forward voltage of 0.1 V, for SBDs fabricated on plasma-etched n-Si at a pressure of 5 x 10^{-3} mbar and dc bias of 400 V.

FIG. 2.

Variation of C-V barrier heights [ϕ_b^{CV}] and barrier heights calculated from Eqns. (1) and (2) [ϕ_b^{eff}] as a function of etch time

FIG. 3.

Plots of (a) I-V barrier heights (ϕ_b^{IV}) and reverse current at a bias of -1 V (I_R), and (b) free carrier concentration of sputter etched samples as a function of plasma pressure.

FIG. 4.

Illustrates the effect of temperature on the apparent increase in free carrier concentration at and close to the metal-semiconductor interface for a 6 min etched sample at a plasma pressure of 9x10^{-3} mbar and dc bias of 400 V.

FIG. 5.

DLTS spectra of epitaxially grown n-Si doped to 5x10^{15} cm-3 with P, bombarded with high energy (MeV) electrons [curve (a)], and sputter-etched in an Ar plasma [curve (b)] using 0.2 ms filling pulses. Curves (c) and (d) from the same sample were obtained using filling pulse widths of 500 ns and 25 ns, respectively. Curve (e) was obtained after annealing at 260 °C. All curves were recorded at a lock-in amplifier frequency of 46 Hz, V_r = 1 V and V_p = 1.4 V.

FIG. 6.

Modified Arrhenius plots of $\log(e/T^2)$ vs $1000/T$ from which the activation energy, E_T, and apparent capture cross-section, σ_a, of the sputter-etching induced defects were extracted.

FIG. 7.

Illustrates the variations in peak DLTS signal intensities of the prominent SEI defects as a function of etch time [curve (a)] and plasma pressure [curve (b)].

FIG. 8.

DLTS depth profiles of EP454 (P8) for different etch times.

FIG. 9.

DLTS spectra of annealed sputter-etched n-Si at 100 °C [curve (a)], 400 °C [curve (b)], 450 °C [curve (c)] and 550 °C [curve (d)].

FIG. 10.

Comparison of DLTS spectra of epitaxially grown n-Si. (a) Sputter-etched in an Ar plasma at a pressure of $5x10^{-3}$ mbar (dc bias of 400 V), (b) bombarded with 1 keV He ions and (c) 1 keV Ar ions. A lock-in amplifier frequency of 46 Hz was used to extract the data.

REFERENCES

[1] F.H. Mullins and A. Brunnschweiler, Solid State Electron. **19**, 47 (1976).

[2] S.J. Pearton, W.S. Hobson, U.K. Chakrabarti, G.E. Derkits, Jr., and A.P. Kinsella, J. Electrochem. Soc. **137** (12), 3892 (1990).

[3] G.S. Oehrlein, Materials Science and Engineering **B4**, 441 (1989).

[4] M. Lannoo, Mat. Res. Soc. Symp. Proc. **262**, 775 (1992).

[5] S.D. Brotherton and P. Bradley, J. Appl. Phys. **53**, 5720 (1982).

[6] F. Capasso, A.Y. Cho, Khalid Mohammed and P.W. Foy, Appl. Phys. Lett. **46**, 664 (1985).

[7] S. Ashok, T.P. Chow and B.J. Baliga, Appl. Phys. Lett. **42**, 687 (1983).

[8] S.J. Fonash, S. Ashok and Ranbir Singh, Appl. Phys. Lett. **39**, 423 (1981).

[9] M. Hirai, H. Iwakuro, J. Ohno, and T. Kuroda, IEEE Transactions on Components, Hybrids, and Manufacturing Technology **13**, 629 (1990).

[10] O.O. Awadelkarim, T. Gu, P.I. Mikulan, R.A. Ditizio and S.J. Fonash, Appl. Phys. Lett. **62** (9), 958 (1993).

[11] M. Balooch, M. Moalem, Wei-E. Wang and A.V. Hamza, J. Vac. Sci. Technol. A **14**, 229 (1996).

[12] Ranbir Singh, S.J. Fonash, S. Ashok, P.J. Caplan, J. Shappirio, M. Hage-Ali and J. Ponpon, J. Vac. Sci. Technol. **A 1** (2), 334 (1983).

[13] J.R. Troxell, Solid State Electronics **26**, 539 (1983).

[14] D.V. Lang, J. Appl. Phys. **45**, 3014 (1974).

[15] Y. Zohta and M.O. Watanabe, J. Appl. Phys. **53**, 1809 (1982).

[16] E.H. Rhoderick and R.H Williams, Metal-Semiconductor Contacts, 2nd ed. (Clarendon Press, Oxford, 1988), p. 38.

[17] S.M. Sze, Physics of Semiconductor Devices, 2nd ed. (John Wiley and Sons, New York, 1981), p. 263.

[18] D. Bauza, J. Appl. Phys. **73**, 1858 (1993).

[19] P.N.K. Deenapanray, F.D. Auret, G. Myburg, M. Hayes, W.E. Meyer and C. Schutte, Materials Science Forum, Ed. Balogh, **248-249**, 249 (1997).

[20] P.N.K. Deenapanray, F.D. Auret, C. Schutte, G. Myburg, W.E. Meyer, J.B. Malherbe and M.C. Ridgway, Mat. Res. Soc. Symp. Proc. **442**, 87 (1997).

[21] J.L. Benton, J. Michel, L.C. Kimerling, B.E. Weir and R.A. Gottscho, Journal of Electronic Materials **20**, 643 (1991).

[22] B.G. Svensson, C. Jagadish and J.S. Williams, Phys. Rev. Lett. **70**, 3756 (1993).

[23] J.L. Benton, M.T. Asom, R. Sauer and L.C. Kimerling, Mater. Res. Soc. Proc. **104**, 85-91 (1988).

[24] B.G. Svensson, B. Mohadjeri, A. Allen, J.H. Svensson and J.W. Corbett, Phys. Rev. **B 43**, 2292 (1991).

[25] N. Bürger, K. Thonke, R. Sauer and G. Pensl, **Phys.** Rev. Lett. **52**, 1645 (1984).

[26] J. Weber, Physica B.**170** , 201 (1991).

[27] F.D. Auret, P.N.K. Deenapanray, W.E. **Meyer**, S.A. Goodman and G. Myburg, unpublished.

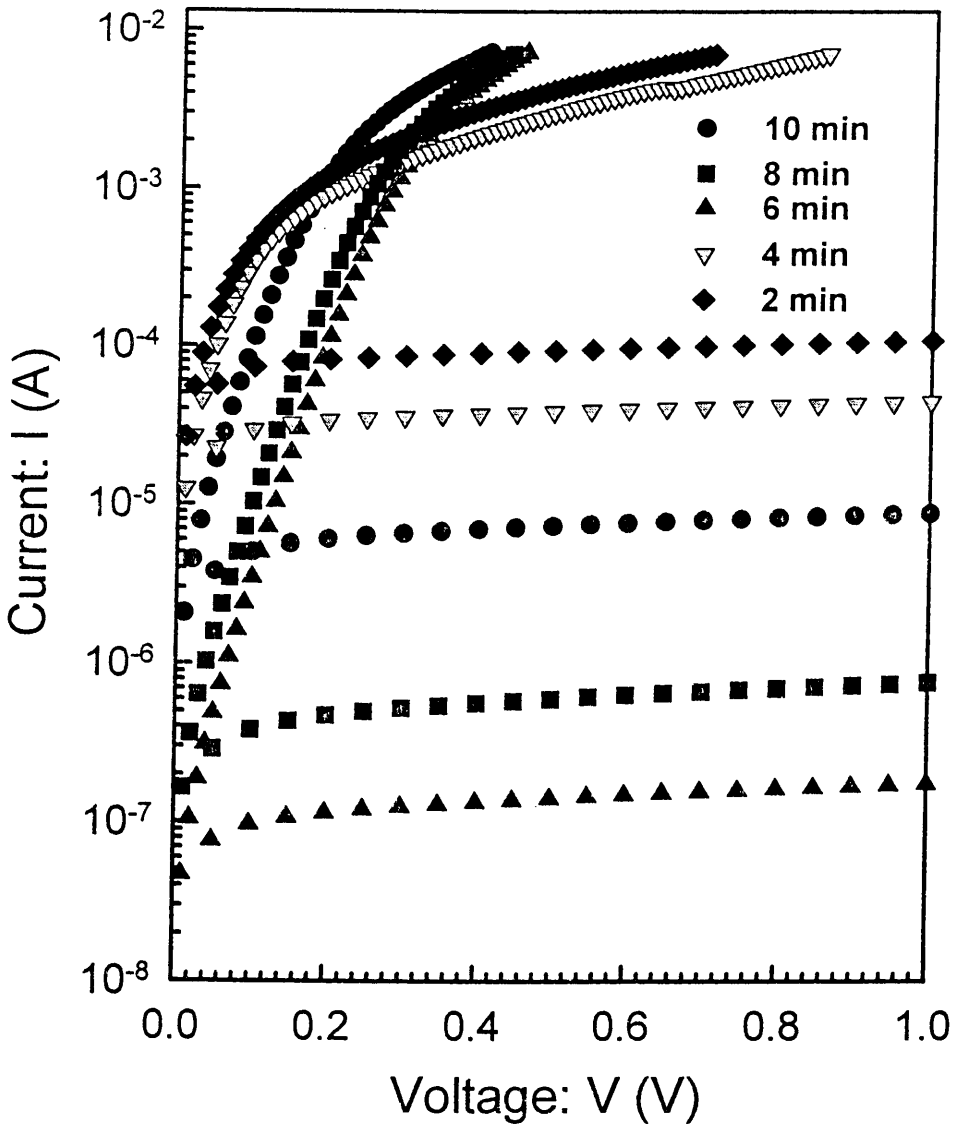

P.N.K. Deenapanray *et al* Fig. 1(a) of (10)

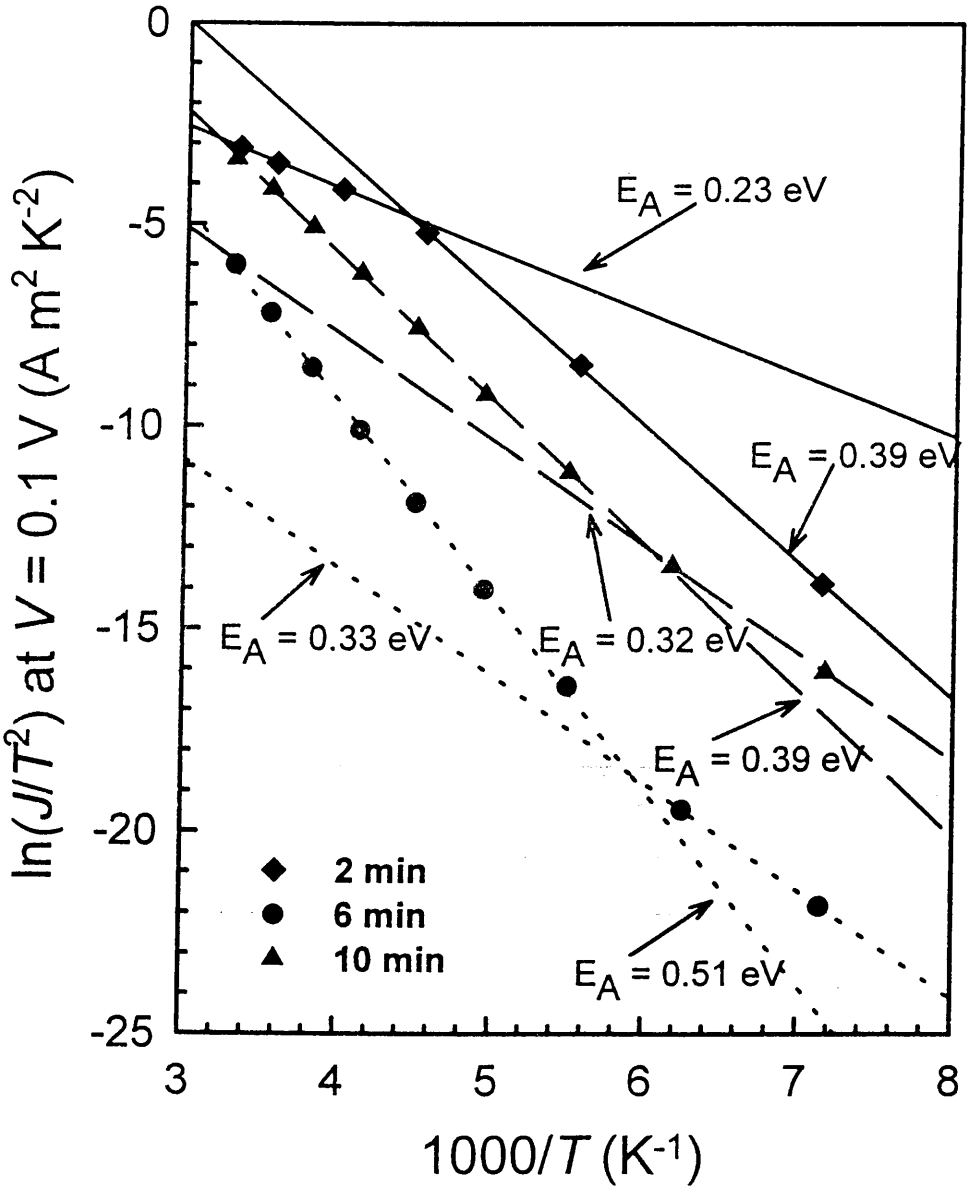

P.N.K. Deenapanray *et al* Fig. 1(b) of (10)

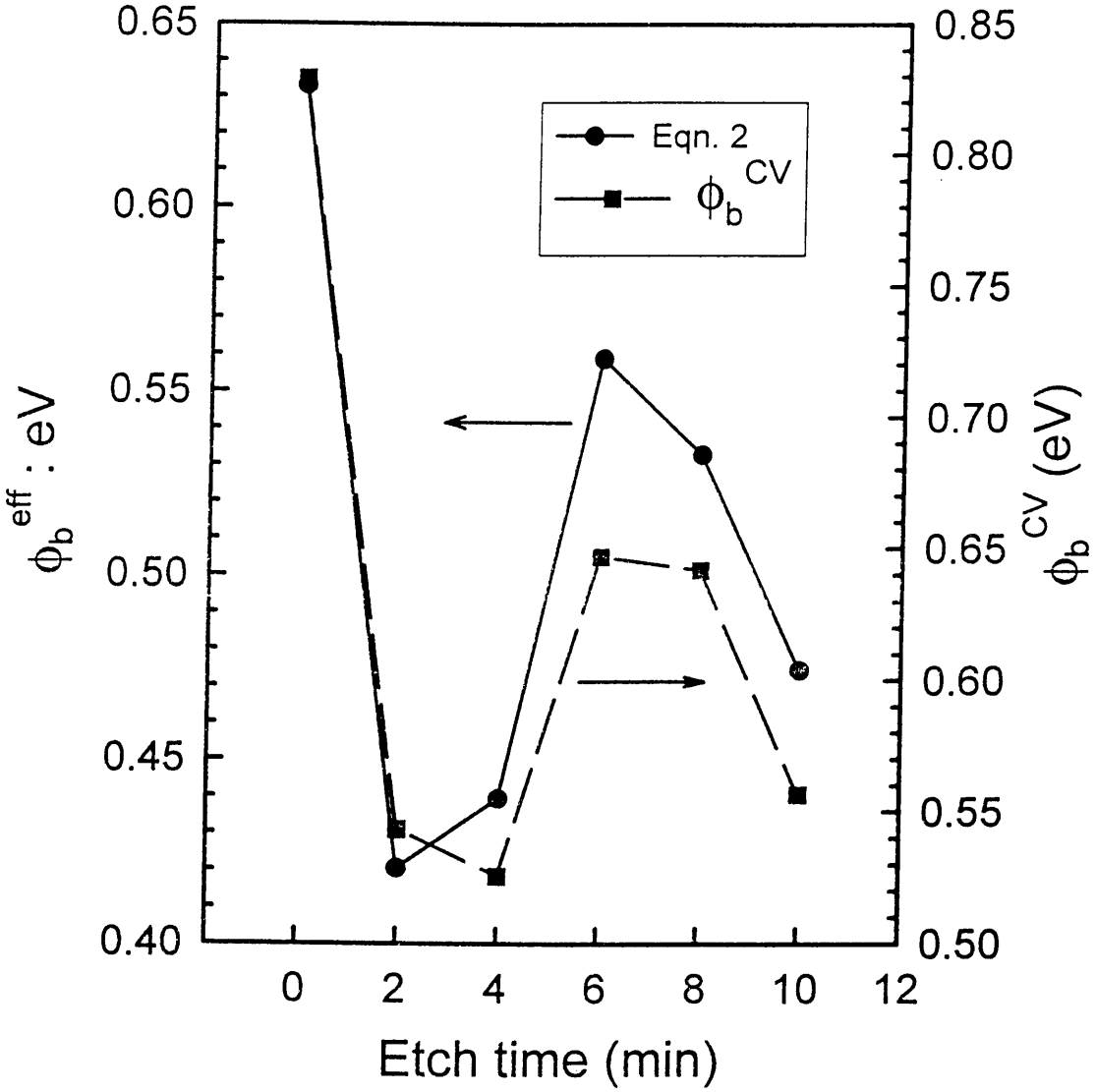

P.N.K. Deenapanray *et al* Fig. 2 of (10)

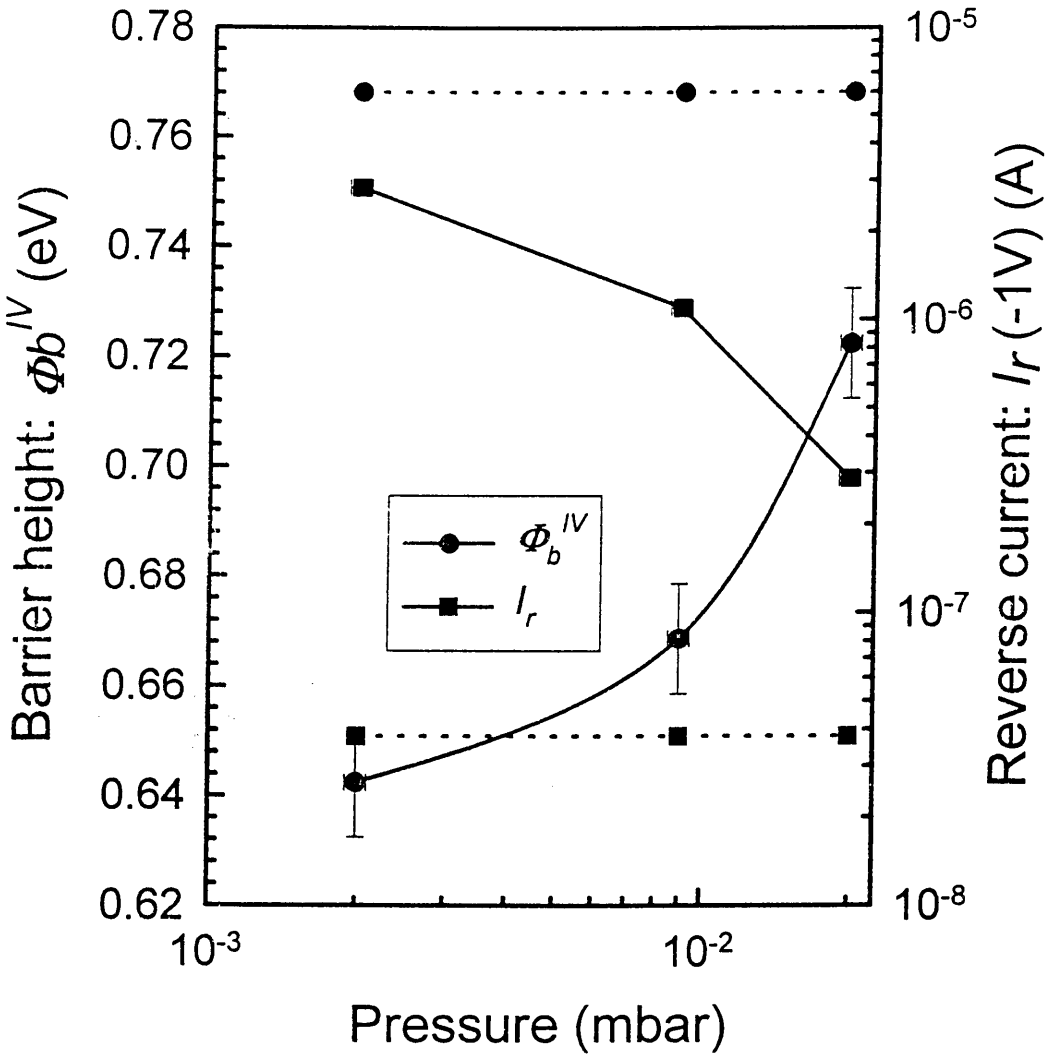

P.N.K. Deenapanray *et al* Fig. 3(a) of (10)

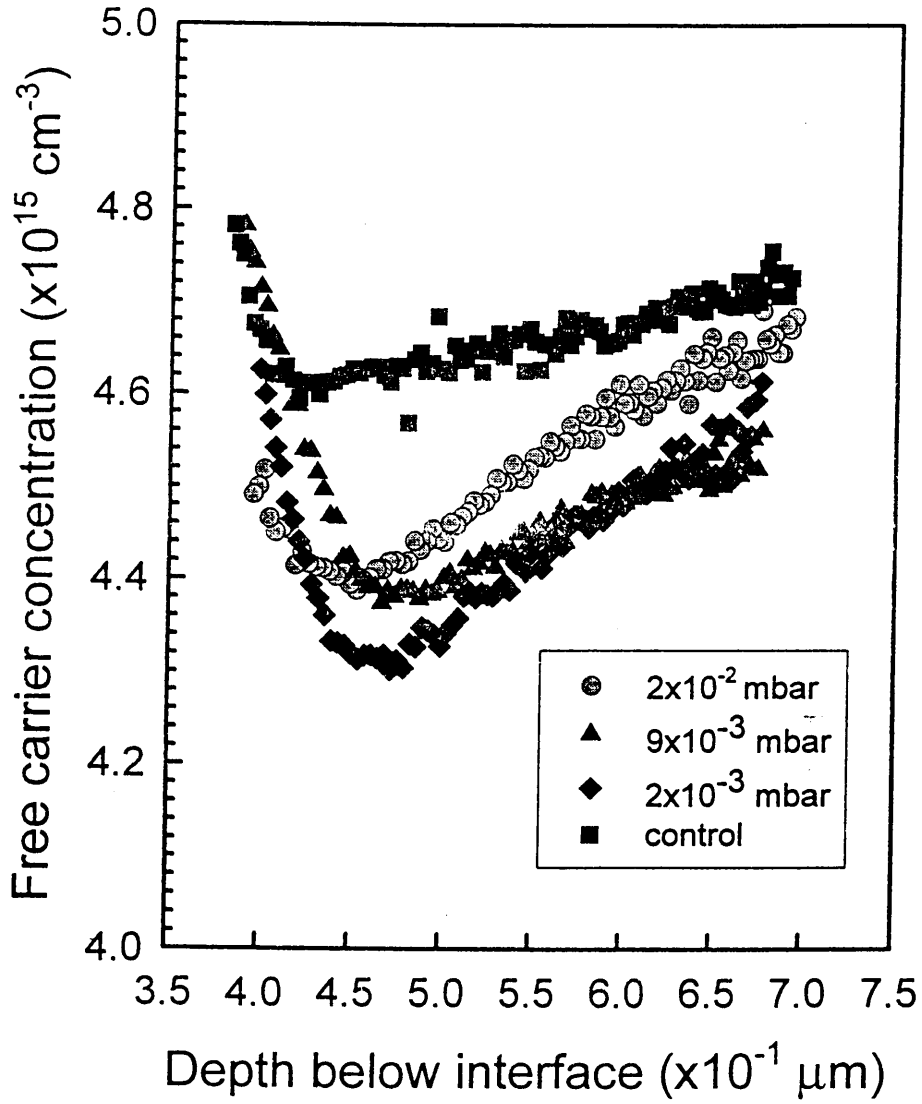

P.N.K. Deenapanray *et al* Fig. 3(b) of (10)

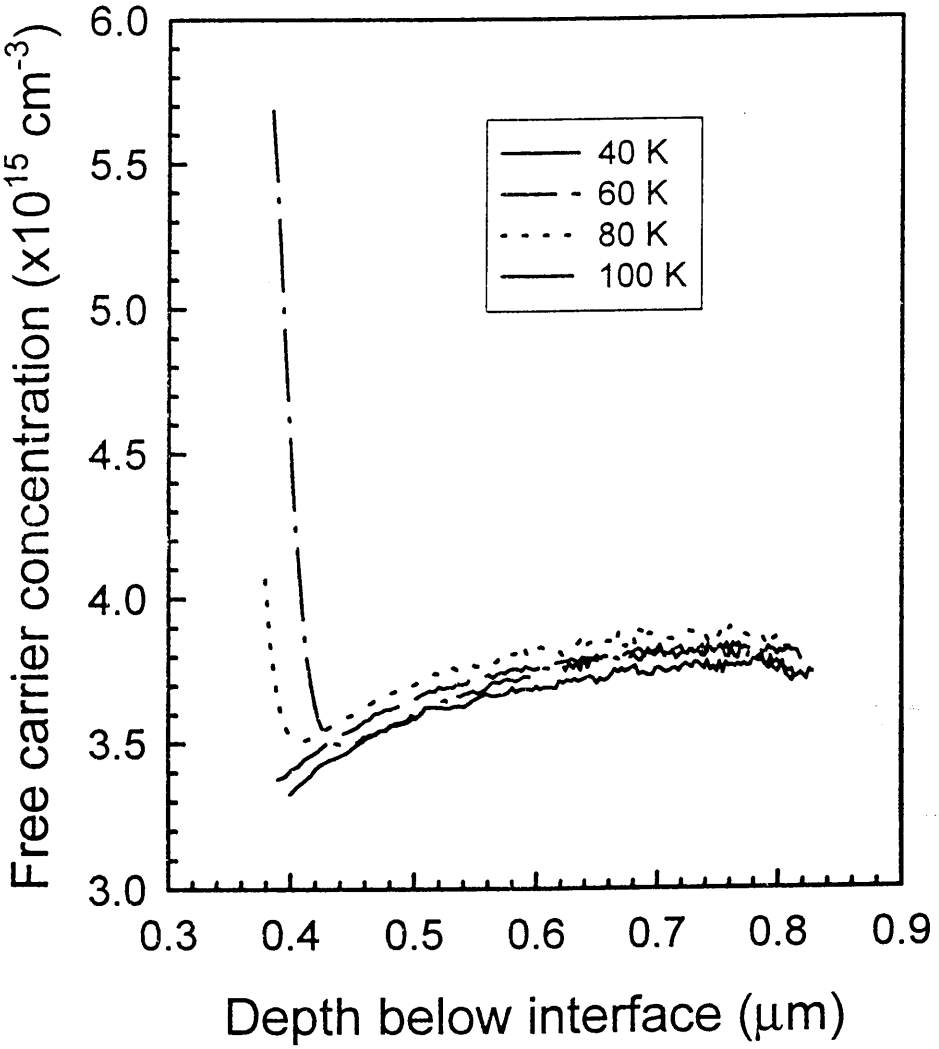

P.N.K. Deenapanray *et al* Fig. 4 of (10)

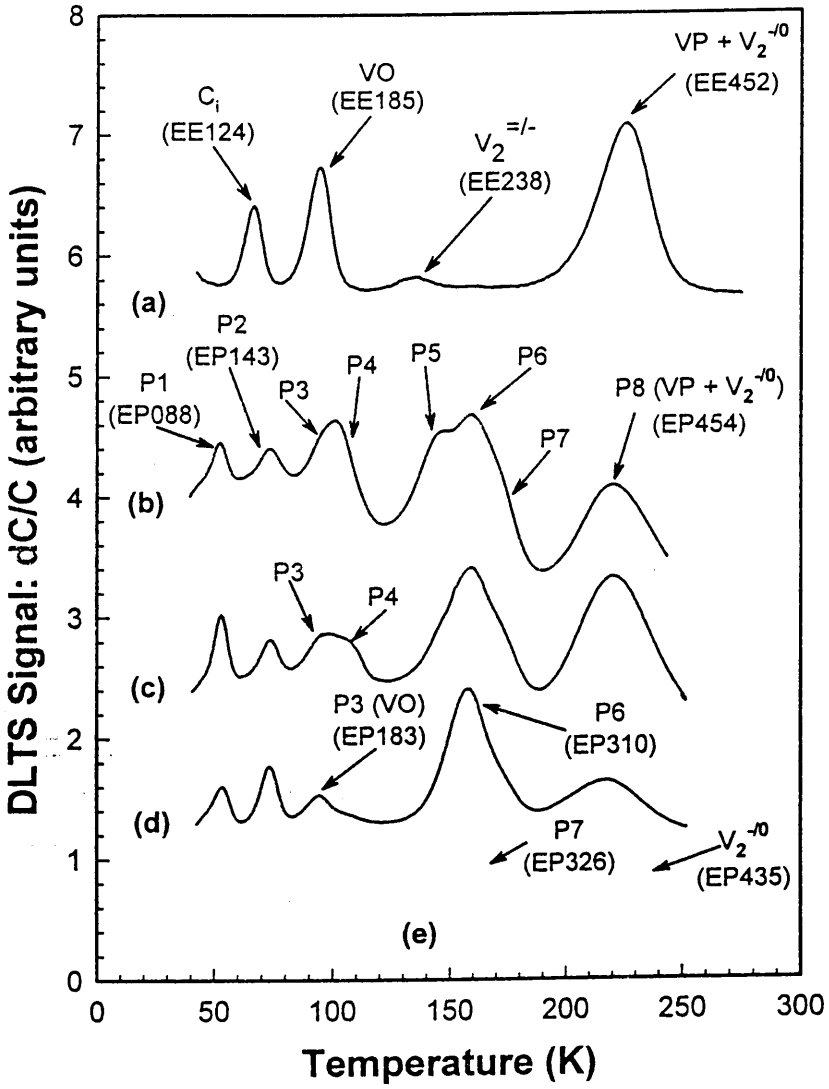

P.N.K. Deenapanray *et al* Fig. 5 of (10)

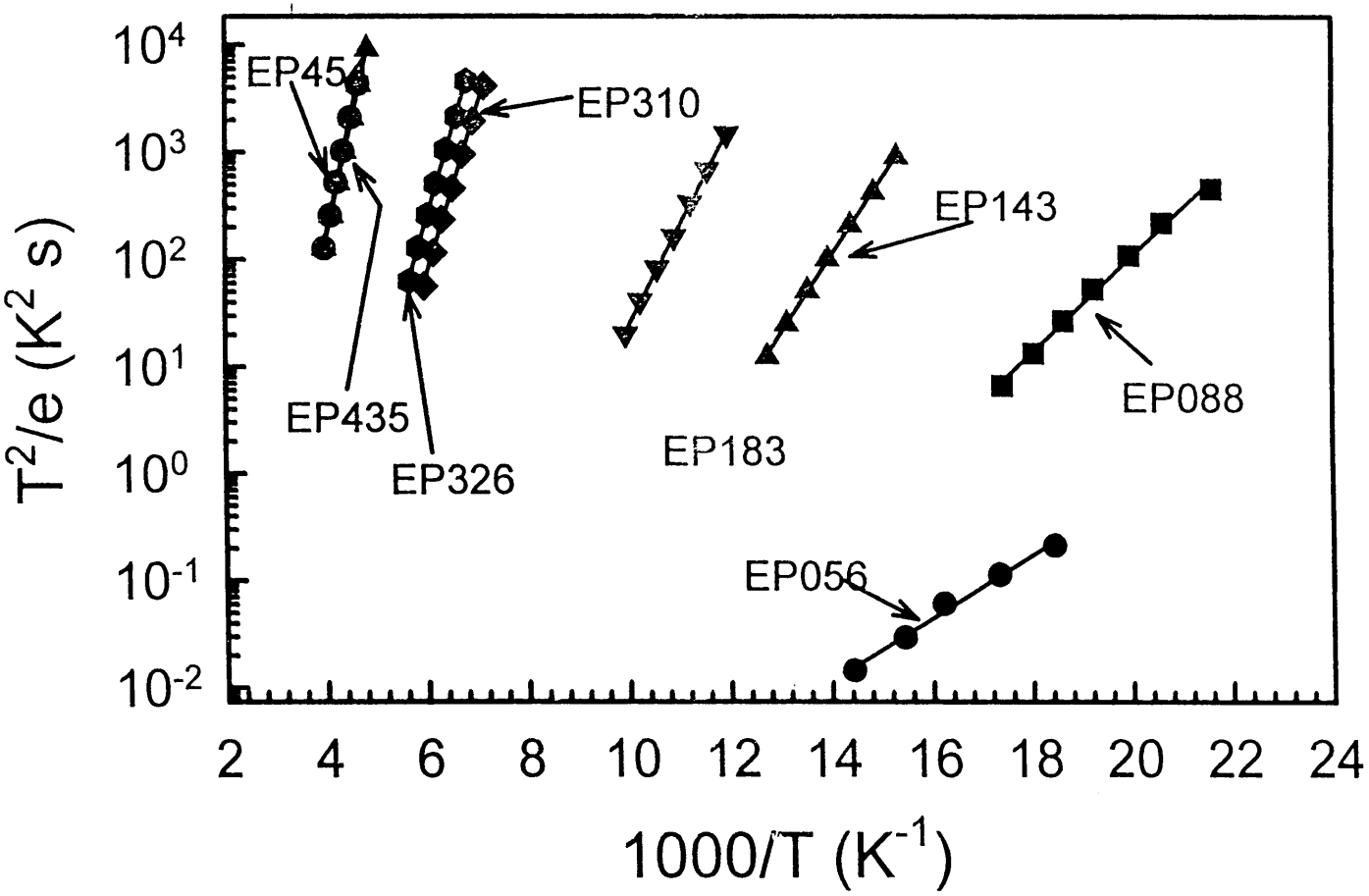

P.N.K. Deenapanray *et al* Fig. 6 of (10)

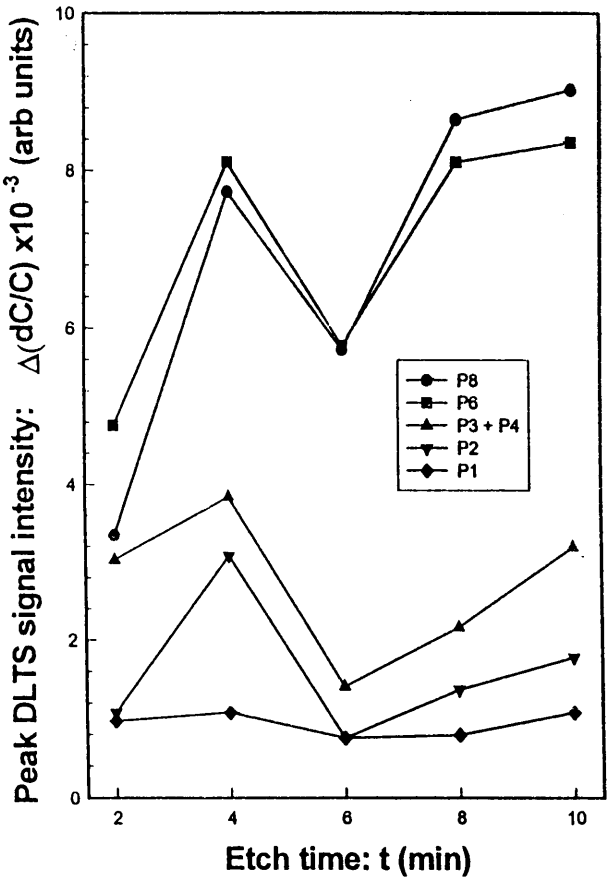

P.N.K. Deenapanray *et al* Fig. 7 [(a) and (b)] of (10)

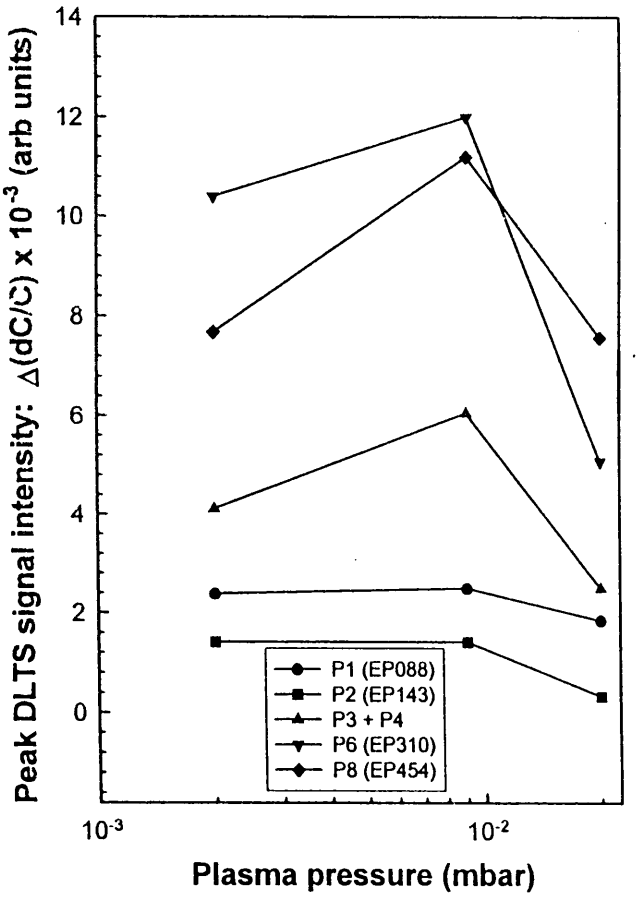

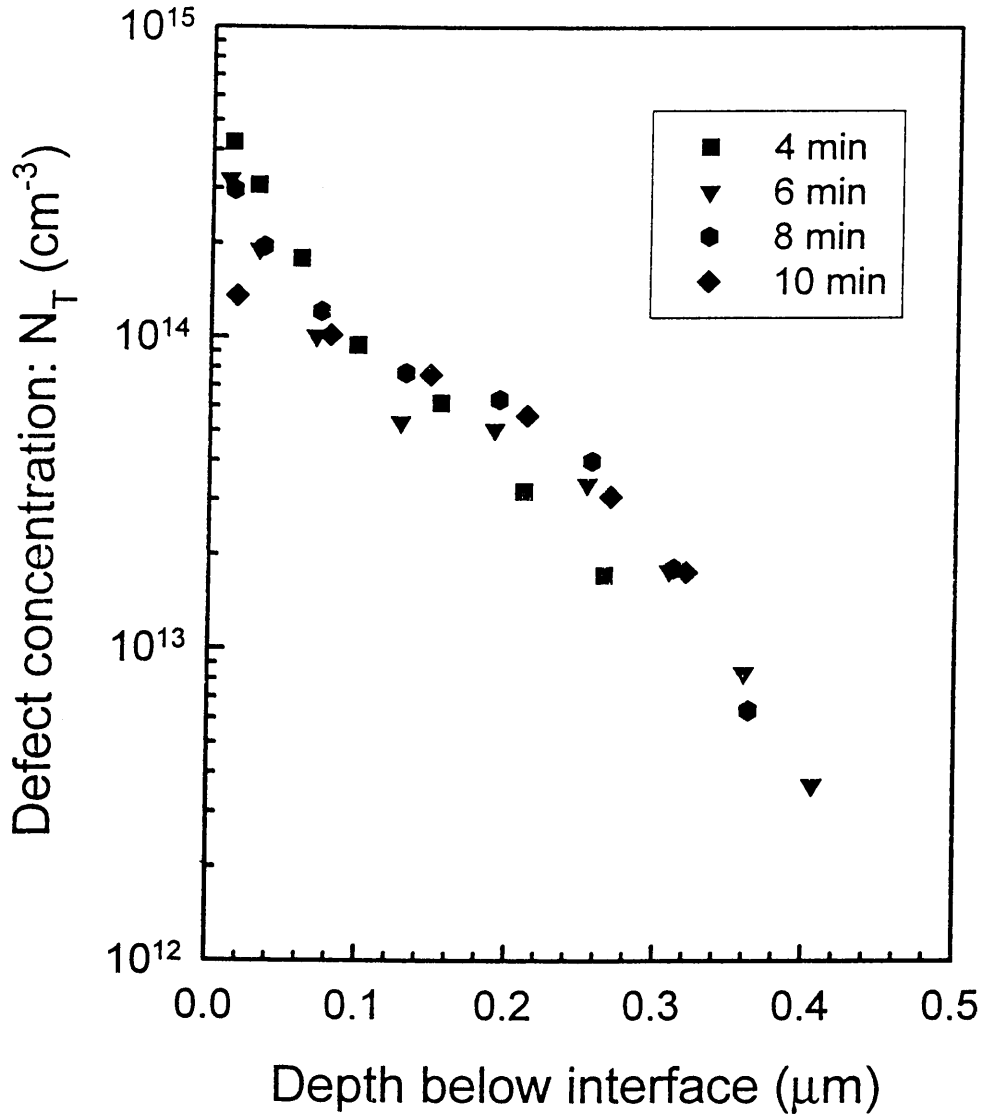

P.N.K. Deenapanray *et al* Fig. 8 of (10)

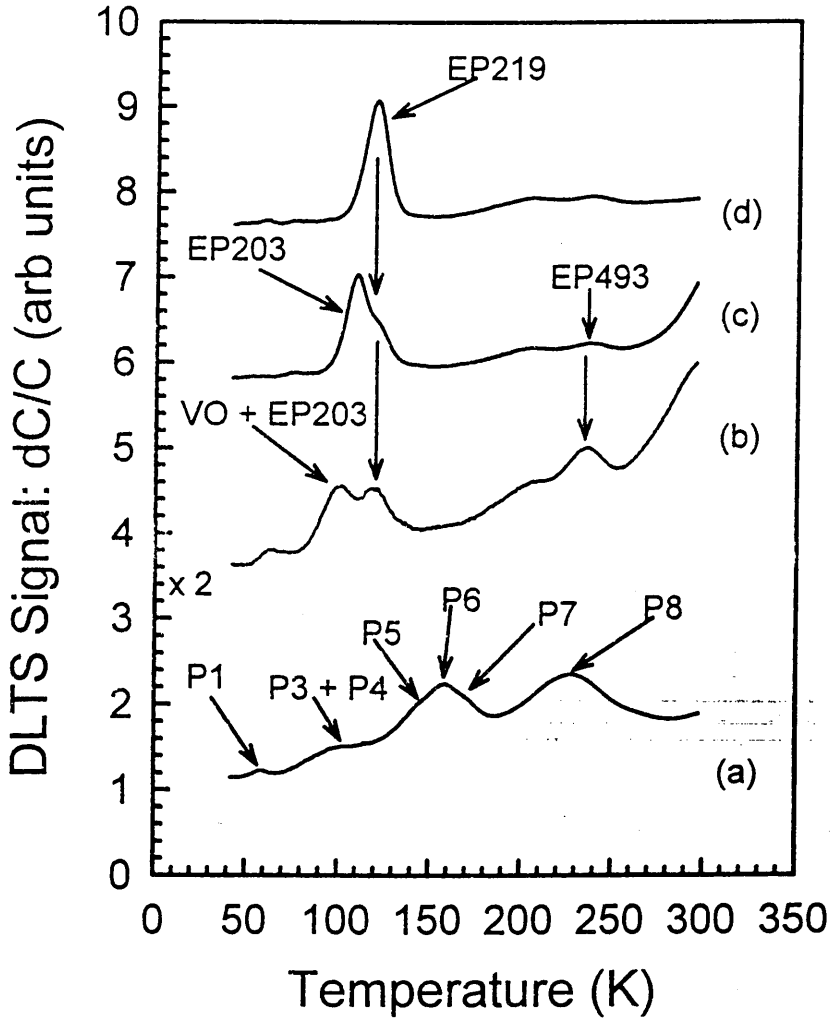

P.N.K. Deenapanray *et al* Fig. 9 (10)

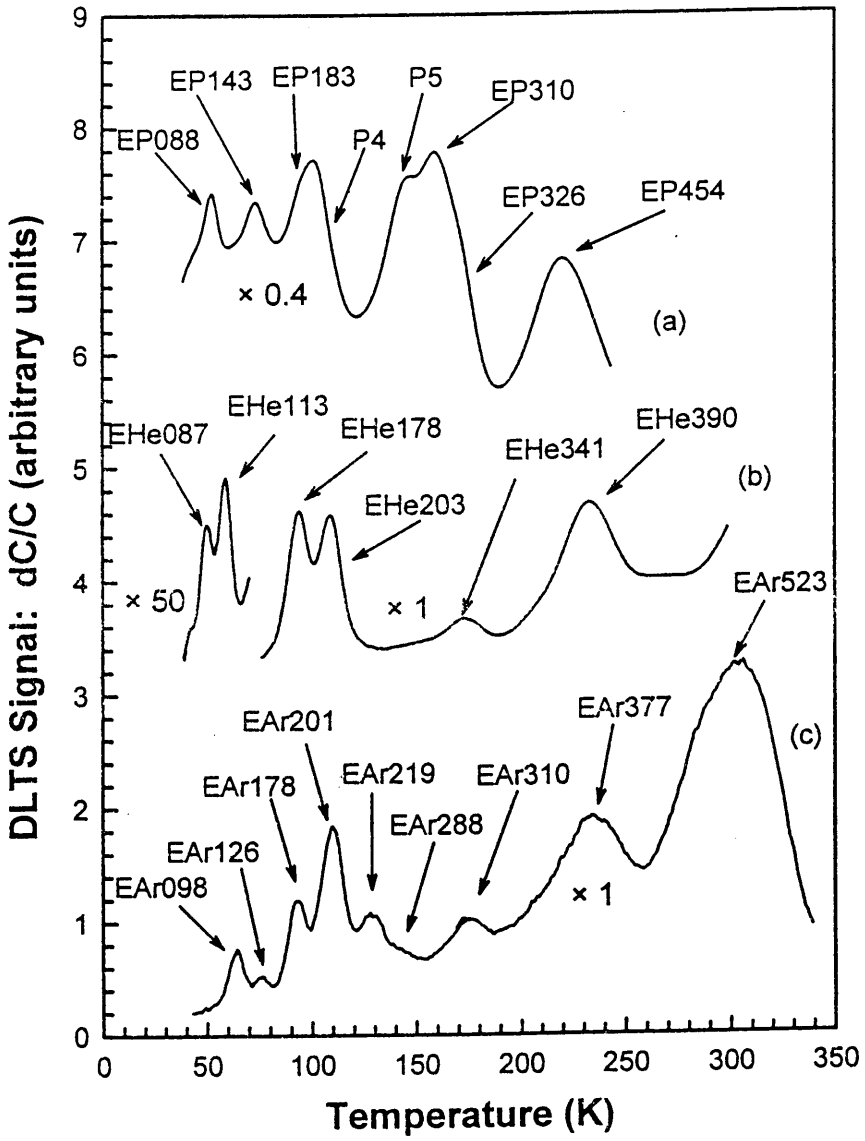

P.N.K. Deenapanray *et al* Fig. 10 of (10)

ELSEVIER

Nuclear Instruments and Methods in Physics Research B 127/128 (1997) 393–396

NIM B
Beam Interactions with Materials & Atoms

Electronic properties of defects created in epitaxially grown n-Si by low energy He and Ar ions

F.D. Auret, P.N.K. Deenapanray, S.A. Goodman, J.B. Malherbe, W.E. Meyer *, G. Myburg, M. Hayes

Department of Physics, University of Pretoria, Pretoria 0002, South Africa

Abstract

Ion beam etching with noble gases is routinely used in the fabrication of submicron-scale structures. Low energy ion bombardment, however, introduces near surface defects in semiconductors, which may alter their electrical properties, and may hence govern the properties of devices fabricated on these semiconductors. We have employed deep level transient spectroscopy (DLTS) to characterise the defects induced by low energy (1 keV) He- and Ar-ion bombardment of epitaxially grown n-type Si, each of which introduced several prominent electron traps. We found that the DLTS spectrum of low energy Ar-ion bombarded Si contained a number of peaks that that were not present in the low energy He-ion bombarded sample. The DLTS spectra of both low-energy bombarded samples displayed several peaks in addition to the V_2, VO and VP centres which are generally observed in the spectrum obtained from high energy (5.4 MeV) α-particle implanted Si. We attribute the differences in the defects induced by low energy He and Ar ions and high energy He ions to their different stopping powers, i.e. the different rate of energy loss in Si, as well as the inclusion of He and Ar ions in vacancy complexes.

1. Introduction

Ion beam (IB) etching employing noble gases is routinely used in the fabrication of sub-micron scale devices in microelectronics manufacturing. During IB etching, defects which alter the properties of semiconductors, and thus influence the properties of devices fabricated on them, are introduced at and below the semiconductor surface [1]. In order to understand and predict the influence of these defects on semiconductor properties and device behaviour, it is essential to know the electronic properties and structure of the defects and to quantify their dependence on ion species and processing parameters.

Although numerous studies have been performed regarding the influence of IB etching of Si on its properties and on those of devices fabricated on it, little is yet known about the structure of the IB induced defects. It was shown, using deep level transient spectroscopy (DLTS) [2], that IB etching of Si surfaces introduces donor type defects [3] which result in a lowering of the barrier height of Schottky barrier diodes (SBDs) on n-Si, while the opposite was found for p-Si [3]. Although the electronic properties of several low energy IB-induced defects in Si have been reported, no study has yet been conducted to correlate the type and concentration of defects formed with the ion species and energy used, or with the impurities in the Si.

Whereas Ar ions have traditionally been used for noble gas IB etching of Si, it is conceivable that, owing to their smaller mass, He ions may introduce different defects in the Si substrate after bombardment. The degree of damage created by ions depends on the nature and concentration of the ion-induced defects. We have used DLTS to characterise and compare the defects induced in Si by 1 keV He and Ar ions. To learn more about the nature of these defects, we compared their electronic and annealing properties to those of defects introduced in the same Si by 5.4 MeV He-ions of which the electronic properties *and structure* have been established.

2. Experimental procedure

P-doped (to 3×10^{16} cm^{-3}) n-type (111) oriented, 3 μm thick Si layers, grown by chemical vapor deposition on a P-doped n^+-Si substrate, were used for this study. After chemical cleaning, the epitaxial side of the wafer was bombarded with a fluence of 1×10^{12} cm^{-2} He or Ar ions at a dose rate of 2×10^{11} cm^{-2} s^{-1} and an energy of 1 keV. Other samples were implanted with He ions at energies of 5 keV, 150 keV and 5.4 MeV. The implantations at 1 keV and 5 keV were performed using an ion gun whereby the samples were tilted at an angle of 1° with

* Corresponding author. Fax: +27-12-342-4143; email: wmeyer@scientia.up.ac.za

PII S0168-583X(97)00074-8

respect to the ion beam. The implantation at 150 keV was done in an ion implanter at a dose of 1×10^{10} cm^{-2} and dose rate of 2×10^{9} cm^{-2} s^{-1}. The lower ion dose used for the 150 keV implantation ensured that less than 10% of the free carriers were removed at room temperature. The implanted samples were tilted 7° with respect to the beam to prevent ion channeling. An ^{241}Am radionuclide was used as a source of 5.4 MeV α-particles. The radionuclide has an emission rate of 7.1×10^{6} cm^{-2} s^{-1} and samples were exposed to achieve an irradiation dose of approximately 1×10^{12} cm^{-2}. After implantation, circular Pd contacts, 50 nm thick and 0.75 mm in diameter, were deposited onto the bombarded surface by resistive evaporation.

DLTS was used to study the bombardment induced defects. The DLTS "signatures" (energy level, E_t, and apparent capture cross-section, σ_a) of the defects were determined from DLTS Arrhenius plots of log (e/T^2) versus $1/T$, where e is the emission rate at a temperature T. To minimise electric field assisted emission [4], small biases and pulses ($V_r = V_p = 0.3$ V) were used for determining the "signatures".

3. Results and discussion

In Fig. 1 we compare the DLTS spectrum of 1 keV He-ion bombarded Si (curve b) to the DLTS spectrum of Si irradiated with alpha particles from an ^{241}Am radionuclide (curve a). The main electron traps introduced by high energy particles in Si have been shown [5,6] to be due to V_2, VO and VP centres. In this study the most prominent peaks were Eα178 (VO or A centre), Eα437 (VP or E centre) and two charge states of the divacancy, Eα251 ($V_2^{=/-}$) and Eα415 ($V_2^{-/0}$). The peaks of Eα415 and Eα437 overlap and after removing Eα437 (VP centre) by annealing at 180°C, the two charge states of the divacancy, Eα251 and Eα415, were present in the same concentration. (In the nomenclature used here, Eα251 refers to an electron trap 251 meV below the conduction band, produced by α-particle irradiation.)

The DLTS spectrum of the Si sample bombarded with low energy (1 keV) He ions (curve b) is considerably more complex, displaying six defect peaks EHe087, EHe113, EHe178, EHe203, EHe341 and EHe390. Except for EHe178 (that has electrical properties corresponding to the VO or A centre) none of the prominent peaks in the DLTS spectrum have electrical properties that correspond to those in the high energy alpha-particle implanted sample. However, the spectrum of the low energy bombarded sample does have a slight shoulder where the $V_2^{=/-}$ peak is expected, and the EHe390 peak obscures the position where the $V_2^{-/0}$ and the VP peaks would have been observed. It is, therefore, possible that the low energy sample could contain some divacancies and VP centres in relatively low concentrations.

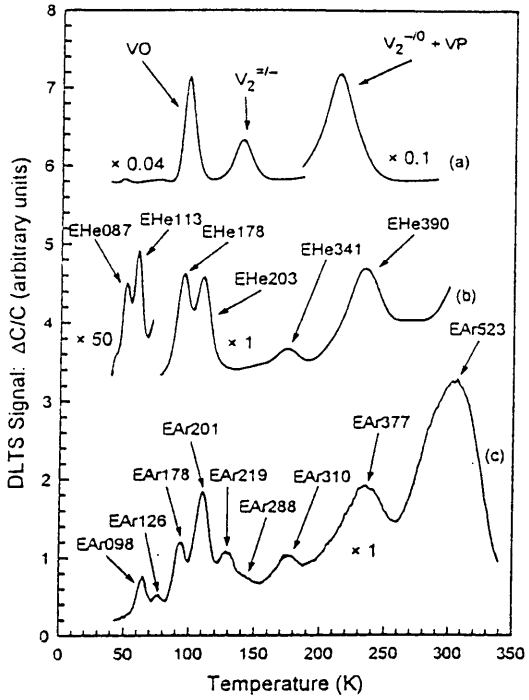

Fig. 1. DLTS spectra of epitaxially grown n-Si doped to 3×10^{16} cm^{-3} with P, bombarded with 5.4 MeV He-ions (curve a), 1 keV He ions (curve b) and 1 keV Ar ions (curve c). All curves were recorded at a lock-in amplifier frequency of 46 Hz, $V_r = 1$ V and $V_p = 1.6$ V.

The DLTS spectrum of low energy (1 keV) Ar-ion bombarded Si (Fig. 1c) is significantly more complex than that produced by the low-energy He-ion bombardment. The spectrum displays at least nine distinguishable peaks, some of which (e.g. the VO centre and EAr201) display properties similar to peaks found in the DLTS spectrum obtained from the low-energy He-ion bombarded sample. The most prominent peaks in the spectra are listed in Table 1. If a defect has electrical properties similar to one in another spectrum, it is indicated in the last column of the table. As the peaks are closely spaced, it was difficult to determine the positions of the peaks exactly, and consequently the error in the defect signatures is somewhat larger than would otherwise be expected. As was the case with the low-energy He-ion implanted sample, the DLTS spectrum does not rule out the possibility that some V_2 and VP centres may be present. However, they are present in significantly lower concentrations than the most prominent defects introduced by low energy ions. Because VP and VO centres are formed when single vacancies diffuse to sites where they recombine with O or with P, respectively, our results suggest that *low energy He- and Ar-ions create lower concentrations of freely diffusing vacancies (compared to other defects) than high energy He ions.*

In order to explain why neither 1 keV He ions nor 1 keV Ar ions create the same defects as 5.4 MeV He-ions in the region we probed by DLTS, consider the energy loss mechanisms which dominate in these energy ranges. 5.4 MeV He ions introduce only VO, VP and V_2 centres in the first micron below the surface of the Si studied here (Curve a in Fig. 1). This is expected because in this region electronic stopping dominates and mainly primary radiation induced defects are formed which combine to form VO, VP and V_2. For 1 keV He and Ar ions, nuclear stopping is the dominant mechanism for energy transfer to the lattice: For example, during almost the entire range of a 1 keV He ion in Si, it transfers at least 1.2 eV/Å to the Si lattice through elastic recoils [7], which is well above the critical value of the energy required for "spike" formation [8] — one mechanism of forming extended defects, such as vacancy clusters. Therefore, 1 keV He-ions create extended defects virtually throughout their range (145 Å on average, 90% of all ions in the first 300 Å, calculated using TRIM [9]). For Ar ions the same argument applies, except that the rate of energy transfer is higher since the range of Ar is less than that of He-ions.

Where these low energy ions come to rest, they may be incorporated in the vacancy clusters or, in the case of He, occupy tetrahedral interstitial sites [10]. The above argument for extended defect formation is supported by photoluminescence (PL) observations indicating that vacancy clusters of various sizes combine with these He and Ar atoms [11,12] are present in He- and Ar-ion bombarded Si. Based on these considerations, and since we observed no VP or V_2 centres, we propose that the defects we observed in the 1 keV He- and Ar-ion bombarded Si may be related to vacancy clusters of various sizes (larger than divacancies), combinations of these with He and Ar atoms, or He and Ar atoms incorporated into the Si lattice. Finally, note that some ions may channel deeper into the Si than predicted by TRIM because of their low energy and the low dose used.

Next, we discuss the differences in the DLTS spectra of 1 keV He- and Ar-ion bombarded Si and possible reasons for these differences. By comparing curve b in Fig. 1 with curve c in the same figure, it is clear that the spectrum of Ar-ion induced defects in Si is much more complex than that due to He-ion induced defects. We propose that the reason for this is at least twofold. Firstly, that the rate of energy loss of Ar to the Si by nuclear stopping as it enters the crystal is 31 eV/Å, which is much higher than the 1.2 eV/Å of He ions. This leads to the formation of more and larger vacancy complexes by Ar ions. Secondly, if we assume that some defect levels are caused by the incorporation of Ar or He ions in vacancy clusters or into the lattice, then it is clear that Ar, due to its larger mass than He, will result in a much different perturbation of the potential in and around the clusters or in the Si lattice. This in turn will result in different defect energy levels in the bandgap.

Fig. 2 shows the DLTS spectra obtained from n-Si implanted with He ions at different energies. These studies were performed in Si with a low oxygen content, consequently the VO centre is absent. Curve (a) shows the

Table 1
Electronic properties of defects introduced by He- and Ar-ions in epitaxially grown n-Si

Ion and energy	Defect	E_t (meV)	σ_a (cm^2)	$T^{a)}_{peak}$ (K)	Similar defects
He: 1 keV	EHe087	087 ± 2	8.2×10^{-16}	51	
	EHe113	113 ± 2	3.6×10^{-15}	60	EAr089?
	EHe178	178 ± 2	7.5×10^{-16}	93	VO
	EHe203	203 ± 3	1.1×10^{-15}	108	EAr201
	EHe341	341 ± 4	1.0×10^{-15}	176	EAr310?
	EHe390	390 ± 4	6.3×10^{-17}	225	EAr377?
Ar: 1 keV	EAr098	098 ± 2	6.6×10^{-17}	64	EHe113?
	EAr126	126 ± 2	2.2×10^{-16}	76	
	EAr178	178 ± 2	7.5×10^{-16}	93	VO
	EAr201	201 ± 3	9.7×10^{-16}	108	EHe203
	EAr219	219 ± 4	1.4×10^{-16}	128	
	EAr288	288 ± 4	$1.1 \times x10^{-15}$	149	
	EAr310	310 ± 4	1.6×10^{-16}	174	EHe341?
	EAr377	377 ± 5	1.1×10^{-17}	235	EHe390?
	EAr523	523 ± 6	2.8×10^{-17}	303	
He: 5.4 MeV	Eα178	178 ± 2	7.5×10^{-16}	93	VO
	Eα251	251 ± 3	1.3×10^{-15}	131	$V_2^{=/-}$
	Eα415	415 ± 4	1.9×10^{-16}	226	$V_2^{-/0}$
	Eα437	437 ± 4	2.4×10^{-15}	217	VP

a) Peak temperature at a lock-in amplifier frequency of 46 Hz, i.e. a decay time constant of 9.23 ms.

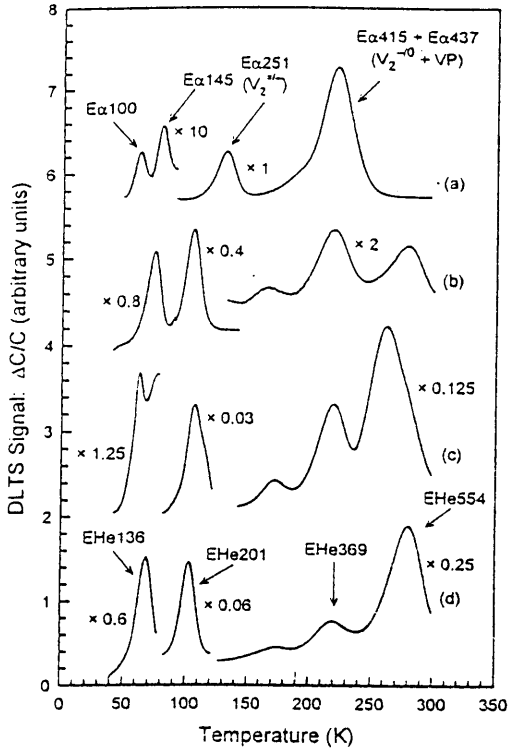

Fig. 2. DLTS spectra of epitaxially grown "low O" n-Si doped 6×10^{15} cm^{-3} with P and bombarded with He ions at an energy of (a) 5.4 MeV, (b) 150 keV, (c) 5 keV, and (d) 1 keV. All curves were recorded at a lock-in amplifier frequency of 46 Hz. $V_r = 1$ V and $V_p = 1.6$ V.

DLTS spectrum obtained from Si irradiated at 5.4 MeV. Except for the absence of the VO centre, the spectrum is similar to that in Fig. 1a. The DLTS spectrum obtained from 1 keV He-ion implanted "low-O" Si is shown in curve (d). When this spectrum is compared to the spectrum in Fig. 1b, a number of peaks, including the VO centre, are absent. By comparing the DLTS spectra obtained for samples that were implanted by lower energy He ions (1 to 150 keV, curves (b)–(d)) it is clear that the defects introduced by these particles, are different to those introduced by high energy alpha particles. Furthermore, it seems that for He ions with energies between 1 and 150 keV, the same set of defects are induced by the ions, irrespective of the energy of the ions, and only the relative concentrations of the induced defects vary.

4. Conclusions and summary

We have determined the energy levels and capture cross-sections of the electron traps introduced in epitaxially grown n-Si by 1 keV He- and Ar-ion bombardment. Our results showed unambiguously that the defects introduced by low energy ions are electronically, and therefore also structurally, different from primary radiation induced defects and their derivatives (V_2, VP and VO) in Si. We suggest that the most probable origin of these low energy ion-induced defects are the formation of Si vacancy clusters, the incorporation of ions into these clusters, or interstitial ions. We speculate that low energy He-ion induced defects have not been observed at the end-of-range in high energy He-ion bombarded Si because of, firstly, the large straggle in the range of high energy He-ions and, secondly, the high concentration of point defects created just before their end of range which impede detection of low energy ion induced defects.

Acknowledgements

We gratefully acknowledge the financial assistance of the Foundation for Research Development and the Carl and Emily Fuchs Institute of Microelectronics.

References

[1] S. Ashok, H. Krautle and H. Beneking, Appl. Phys. Lett. 45 (1984) 431.
[2] D.V. Lang, J. Appl. Phys. 45 (1974) 3014.
[3] E. Grusell, S. Berg and L.P. Andersson, J. Electrochem. Soc. 127 (1980) 1573.
[4] J. Frenkel, Phys. Rev. 54 (1938) 647.
[5] S.D. Brotherton and P. Bradley, J. Appl. Phys. 53 (1982) 5720.
[6] L.C. Kimerling, Inst. Phys. Conf. Ser. 31 (1977) 221.
[7] F.D. Auret, S.A. Goodman, G. Myburg, W.E. Meyer and P.N.K. Deenapanray, Appl. Phys. Lett., submitted.
[8] J.A. Davies, MRS Bull. (1992) p. 26.
[9] J.F. Ziegler, J.P. Biersack and U. Littmark, in: The Stopping and Range of Ions in Solids, Vol. 1, ed. J.F. Ziegler (Pergamon Press, New York, 1985).
[10] M. Alatalo, M.J. Puska and R.M. Nieminen, Phys. Rev. B 46 (1992) 12806.
[11] J. Weber, Physica B 170 (1991) 201.
[12] N. Burger, K. Thonke, R. Sauer and G. Pensl, Phys. Rev. Lett. 52 (1984) 1645.

Electronic and optical properties of defects formed in Si during low energy noble gas ion bombardment

P.N.K. Deenapanray, N. E. Perret, F.D. Auret, J.B. Malherbe, and M. du Plessis *

Department of Physics, University of Pretoria, Pretoria, South Africa
*Carl and Emily Fuchs Institute for Microelectronics, Department of Electrical and Electronics Engineering, University of Pretoria, Pretoria, South Africa

Abstract - We have used deep level transient spectroscopy (DLTS) and photoluminescence (PL) to determine the electronic and optical properties of the defects created during 1 keV He-, Ne- and Ar-ion bombardment. Except for their different relative concentrations, the defects induced by He- and Ne-ion bombardment were found to be similar. The different set of defects introduced by Ar ions has been associated with their higher rates of nuclear energy deposition in Si. Some of the low energy defects were found to be electronically similar to primary defects formed during 5.4 MeV alpha-particle irradiation, while some others are proposed to be noble gas species related. PL studies have shown that the intensities of the G- and C-lines decreased with increasing irradiation dose of Ne ions after reaching a maximum at $1x10^{12}$ cm^{-2}. The G-line intensity was found to decrease with the mass of noble gas used.

A. Introduction

Low energy processes using noble gas ions, such as plasma etching and sputter deposition, play an important role in microelectronics device fabrication. During these processes ions impinge on the semiconductor surface, whereby energy is transferred and some ions are embedded into the semiconductor, resulting in defect formation at and close to the surface [1]. The nature and concentration of defects depend on the species, energy and flux of the ions, the type of semiconductor and impurities therein. These defects alter the electrical, optical and micro-structural properties of semiconductors and consequently influence the characteristics of devices fabricated on them [2,3]. In order to understand and predict the influence of these defects on semiconductor properties and to successfully use them in any form of defect engineering [4,6], it is essential to know the electronic properties and structure of the defects and to quantify their dependence on noble gas ion species and processing parameters. Although the electronic properties of several low energy ion beam-induced defects in Si have been reported, few experiments have been done to correlate these defects with the ion species used. We have used deep level transient spectroscopy (DLTS) [5] and photoluminescence (PL) to characterise and compare the defects induced in Si by 1 keV He, Ne and Ar ions. To learn more about their nature, we compared their electronic properties to those defects induced in the same Si by 5.4 MeV alpha-particles of which the electronic properties and structure have been established.

B. Experimental Procedure

Epitaxially grown (111) oriented n-type Si layers, doped to $5x10^{15}$ cm^{-3} with P, and grown on n^+-substrates were used in this study. The epitaxial side of the wafer was bombarded with either He or Ne or Ar to a dose of $1x10^{12}$ cm^{-2} at an energy of 1 keV using an ion gun. Other samples were irradiated with 5.4 MeV alpha-particles using an ^{241}Am radionuclide. Ne ion bombardments (1 keV) to fluences of $5x10^{10}$, $1x10^{11}$, $1x10^{13}$ and $1x10^{14}$ cm^{-2} were also conducted. Circular Pd contacts, 100 nm thickness and 0.77 mm in diameter, were deposited on the irradiated samples by resistive evaporation for subsequent DLTS analyses.

The energy levels, E_T, and apparent capture cross-sections, σ_a, of the ion beam-induced defects were determined from DLTS Arrhenius plots of $\log(e/T^2)$ vs $1/T$, where e is the emission rate at a temperature T. The PL spectra of the bombarded samples were recorded at 11 K with an argon-ion laser, a cooled Ge detector, and conventional lock-in techniques. A laser power of 200 mW was used to illuminate the samples.

C. Results and Discussion

C.1 DLTS results

The DLTS spectra of n-Si bombarded with 1 keV He-, Ne- and Ar-ions to a fluence of $1x10^{12}$ cm^{-2} are shown in curves (b), (c) and (d) of Fig. 1, respectively. The defects are for instance identified in the form EHe178, where "E" denotes an electron trap, "He" for helium and "178" to the position in meV of the specific level below the conduction band. Fig. 2 shows the Arrhenius plots from which the activation energy, E_T and apparent capture cross-section, σ_a of the main bombardment-induced defects were extracted. To learn more about the structure of the low energy noble gas ion-induced defects, we have compared their electronic properties to those of the primary defects [6] introduced during 5.4 MeV alpha-particle irradiation of the same material [Fig. 1 curve (a)]. We observe from Fig. 1 that He and Ne ions introduce a similar set of defects in Si. The higher intensities of the Ne-ion induced defects are attributed to the larger energy deposited per unit length of 1 keV Ne ions owing to their higher mass. On the other hand, Ar ions introduce a more complex set of defects in Si. We have found EHe178, ENe183 and EAr178 to be electronically similar to the VO centre, while EHe113, ENe098 and EAr098 have been attributed to the presence of C_s-Si_i-C_s [7]. We also suspect EHe203, EAr201 and ENe223 to be the same defect due to their similar electronic properties. Except for EHe178 and ENe183 none of the prominent defects produced by He- and Ne-ions, respectively, have electrical properties that correspond to those of the primary defects. However, the spectrum of low energy He-ion bombarded Si has a slight shoulder where the $V_2^{=/-}$ is expected, and any presence of the $V_2^{-/0}$ and VP peaks is masked by the position of the EHe390 peak.

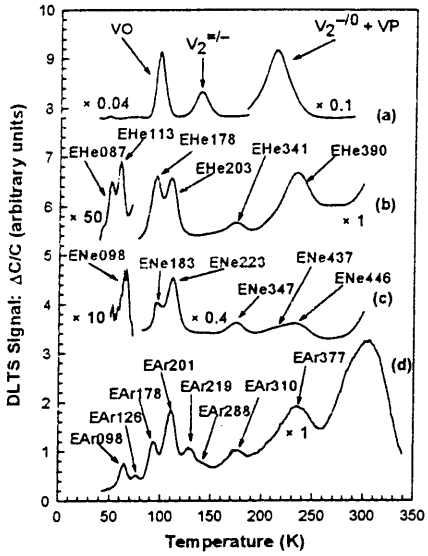

Figure 1 : DLTS spectra of n-Si bombarded with (a) 5.4 MeV alpha-particles, (b) 1 keV He-ions, (c) 1 keV Ne-ions and (d) 1 keV Ar ions. A fluence of $1x10^{12}$ cm^{-2} was used in the low energy bombardments. The data were extracted at a lock-in amplifier frequency of 46 Hz.

The ENe437 peak in the spectrum of Ne-bombarded sample, which could be resolved by using 50 ns filling pulses, has been attributed to the presence of VP-centres. A slight "hump" can also be observed where the $V_2^{=/-}$ is expected and the $V_2^{-/0}$ could be obscured by the position of ENe437. We, therefore, speculate that low-energy He- and Ne-ion bombardment of Si introduce divacancies and VP-centres in relatively low concentrations. Similarly, the introduction of divacancies and VP-centres during low energy Ar-ion bombardment are not ruled out. The more complex set of defects introduced by Ar-ions is due to their higher rates of energy deposition to the Si lattice.

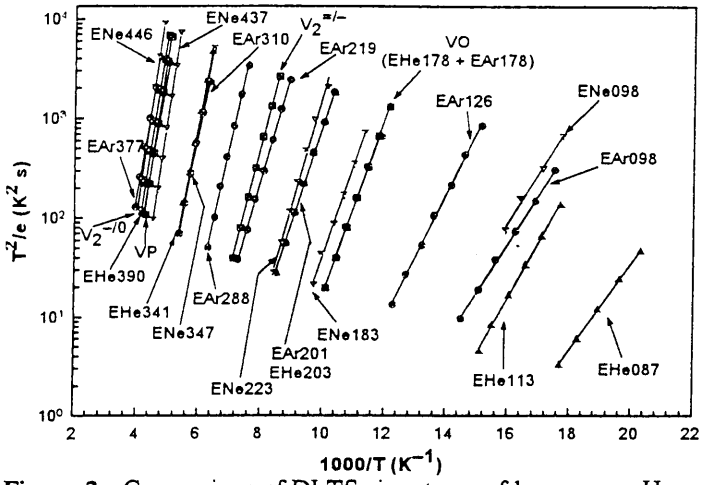

Figure 2 : Comparison of DLTS signatures of low-energy He-, Ne- and Ar-ion induced defects in n-Si with those introduced during high energy alpha-particle irradiation.

The results presented here suggest that low energy He-, Ne- and Ar-ions create lower concentrations of freely diffusing vacancies compared to high energy alpha-particles. This is explained by looking at the energy loss mechanisms of low (1 keV) and high (MeV) energy ions, respectively. Electronic stopping, which creates single vacancies and interstitials, is the predominant energy deposition mechanism when a high energy ions penetrates the Si lattice. Hence, the creation of a higher concentration of divacancies, VO- and VP-centres. On the other hand, the energy loss by a 1 keV ion is mainly due to nuclear stopping. We have calculated from TRIM [9] simulations the energy deposited to the Si lattice by a 1 keV He-ion to be at least 1.2 eV/Å (more for Ne- and Ar- ions), which is above the critical value required for "spike" formation [8]. Therefore, the 1 keV ions create extended defects virtually throughout their entire range. Furthermore, we have proposed that the noble gas ions may be incorporated into vacancy clusters (larger than divacancies) or occupy interstitial sites in the case of He and Ne [8]. This is further substantiated by observing the shifted I_1 defect [10] in our low energy noble gas ion-bombarded samples using PL.

C.2 Photoluminescence results:

After irradiating silicon samples containing carbon and oxygen as an impurities, at room temperature, two optical centers are commonly observed: a zero phonon line at 969 meV (often called G-line) and a no-phonon line at 789.4 meV (usually labelled C-line). The origin of these lines is still controversial. Two structures are currently suggested for the defect responsible for the G-line [11,12]: the carbon interstitial-carbon substitutional (C_i-C_s) configuration and an interstitial silicon between two substitutional carbon atoms (C_s-Si_i-C_s) configuration. The C-line defect is often assigned the C_i-O_i or Si-O_i-Si structure [11,13].

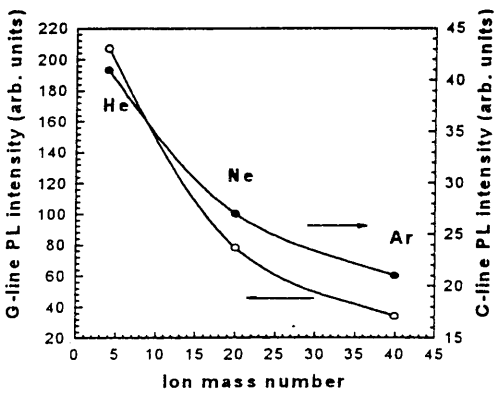

Figure 3: Ion mass dependence of the C-line and G-line intensities for 1 keV He^+, Ne^+ and Ar^+ bombardment at a fluence of $1x10^{12}$ ions/cm^2.

To date only few experiments have been carried out to study the effects of noble gas ion bombardment [14] on these transitions.

The dependence of the G-line and C-line intensities on ion mass have been investigated in this paper (Fig. 3). Further work is in progress to extend this study to other noble gases.

The PL intensity of both lines decreased with increasing ion mass. This mass dependence is again attributed to the different energy deposition rates of the different noble gas ions.

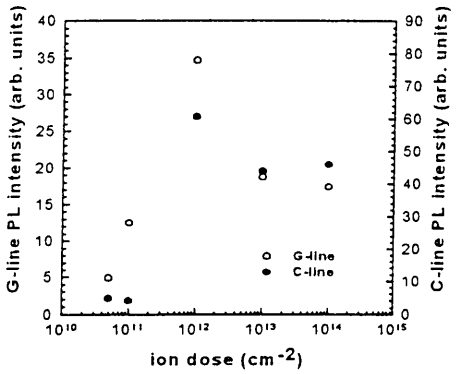

Figure 4: Dose dependence of the C-line and G-line intensities for 1 keV Ne^+ bombardment.

More complex clusters are likely to be created during high mass ion bombardment and, therefore, a lower concentration of Frenkel defects will lead to the formation of a lower number of defects responsible for the 969 meV and 789.4 meV transitions. The similar effect has been observed when increasing the ion energy [15].

The PL intensity of both lines has also been recorded as a function of ion dose (Fig. 4). Although they are expected to saturate at higher doses, the decrease observed in their intensities has been attributed to the creation of extended defects.

D. Conclusion

We have studied the electrical and optical properties of the defects induced by 1 keV energy He-, Ne- and Ar-ion bombardment of n-Si. Except for the A-centre, the low energy defects were different from the primary defects created during high energy (MeV) alpha-particle irradiation. These differences have been attributed to the different energy loss mechanisms of low and high energy ions. Moreover, our DLTS results have shown that Ar-ions introduced a different set of defects compared to those created by He- and Ne-ions. Low energy Ar ions are suspected to create vacancy clusters. The presence of the shifted I_1 defects in our samples favour the proposal that noble gas species related defects could be introduced in our samples. PL studies have revealed that the intensities of the G-line and C-line decreased with bombarding ion mass, which supports our DLTS results. Ne ion bombardments have also shown that the intensity of the lines reached a maximum at a dose of $1x10^{12}$ cm^{-2} and, thereafter, decreased due to the creation of extended defects.

The financial assistance of the South African Foundation for Research Development and the Carl and Emily Fuchs Institute for Microelectronics are gratefully acknowledged.

References

[1] S. Ashok, H. Krautle and H. Beneking, Appl. Phys. Lett. **45** (1984) 431.
[2] E. Grusell, S. Berg and L.P. Andersson, J. Electrochem. Soc. **127** (1980) 1573.
[3] S.J. Fonash, J. Electrochem. Soc. **137** (1990) 3885.
[4] V. Rianeri, G. Fallica and S. Libertino, J. Apply. Phys. **79** (1996) 9012.
[5] D.V. Lang, J. Appl. Phys. **45** (1974) 3014.
[6] S.D. Brotherton and P. Bradley, J. Appl. Phys. **53** (1982) 5720.
[7] L.C. Kimerling, M.T. Asom, J.L. Benton, P.J. Drevinsky and C.E. Caefer, Materials Science Forum **38-41**, p. 141 (1989).
[8] F.D. Auret, S.A. Goodman, G. Myburg, W.E. Meyer and P.N.K. Deenapanray, unpublished.
[9] J.F. Ziegler, J.P. Biersack and U. Littmark, "The Stopping and Range of Ions in Solids", vol. 1, ed. J.F. Ziegler, Pergamon Press, New York, 1985.
[10] J. Weber, Physica **B 170** (1991) 201.
[11] O.O. Awadelkarim, A. Henry, B. Monemar, J.L. Lindstrom, Y. Zhang and J. W. Corbett, Phys. Rev. **B 42** (1990) 5635.
[12] M. T. Assom, J. L. Benton, R, Sauer and L. C. Kimerling, Appl. Phys. Lett. **51** (1987) 256.
[13] J. Wagner, K. Thonke and R. Sauer, Phys. Rev. **B 29** (1984) 7051.
[14] J. Weber, R. J. Davis, H.-U. Habermeier, W. D. Sawyer and M. Singh, Appl. Phys. **A 41** (1986) 175.
[15] N.E. Perret, D.J. Brink, P.N.K. Deenapanray and F.D. Auret, unpublished.

CHARACTERISATION OF OPTICALLY ACTIVE DEFECTS CREATED BY NOBLE GAS ION BOMBARDMENT OF SILICON

P. N. K. Deenapanray, N. E. Perret, D. J. Brink, F. D. Auret and J. B. Malherbe

Physics Department, University of Pretoria, South Africa

Abstract

The modification in the G-line (969.5 meV) and the C-line (789.4 meV) PL intensities were studied as a function of the fluence, energy and the mass of the bombarding ions (He, Ne, Ar and Kr). The intensities of the luminescent lines induced by 1 keV Ne bombardment were found to decrease with increasing dose, after reaching a maximum at about $1x10^{12}$ ions/cm^2. Considerable reductions in the intensities of the G- and C-lines were also recorded during bombardment using heavier noble gas ions and these have been attributed to the higher rates of nuclear energy deposition with increasing bombarding ion mass. The incident ion energy at which the PL intensities of the spectral lines reached their maximum values were found to be dependent on the ion mass and fluence. We have explained the decrease in PL intensities of the G-line and C-line to be due to the introduction of increased amounts of non-radiative recombination centres with increasing incident ion dose and mass. Further, the integral sum of defects induced during bombardment as a function of projected ion range and excitation depth of the Ar-ion laser has been used to qualitatively describe the decrease in the intensities of the two lines.

1. INTRODUCTION

It is well known that low energy ion bombardment creates defects in the near-surface region of solids. In semiconductor processing, low-energy bombardment involving noble gas ions is commonly used, for instance during sputter etching and sputter deposition. The defects introduced during these processes can significantly alter the optical, electrical and micro-structural properties of the material. The creation of a class of optically active deep defects due to implantation of noble gas ions was previously reported.[1] Besides the well-known I_1 centre (1.018 eV), two characteristic luminescent lines termed G (969.5 meV) and C (789.4 meV) were observed in silicon containing carbon and oxygen after dry etching processes such as CF_4 reactive ion etching (RIE)[2] and ion beam etching (IBE)[1]. Reactive ion etching, routinely used during integrated circuit processing for anisotropic etching introduces defects in the near surface region. The I_1 centre are considered to interact with noble gas ions since the energy of the luminescence is significantly altered by the implantation of the ions and subsequent annealing.[1,3,4]

It is known that oxygen and carbon impurities play an important role in the creation of defects responsible for the G- and C-lines. This was really demonstrated as those luminescent lines introduced by IBE and RIE of Si strongly depended on the concentration of C and O.[5,6] Several studies have shown that the magnitude of G-line luminescence can be used as an accurate measure of the carbon content in Si crystals. The detection limit of carbon atoms by this analysis technique is more than an order of magnitude lower than the standard ASTM procedure.[2,7] After RIE in CF_4 + 8% O_2, the diffusion of the G-line and C-line defects was found to be limited by trapping of interstitial silicon atoms at impurity sites.[8]

Many studies have been carried out to determine the origin of these luminescent lines. It is proposed that the G-line luminescence[9] is related to an interstitial silicon atom Si_i located between two adjacent substitutional carbon atoms (C_s-Si_i-C_s). The C-line luminescence was

attributed to complexes composed of an interstitial carbon atom C_i and an interstitial oxygen atom O_i (C_i-O_i).[2,10,11] The mechanism responsible for the creation of these defects can be described as[9] interstitial silicon Si_i being trapped by a substitutional carbon C_s to create an interstitial carbon atom C_i ($Si_i + C_s \Rightarrow C_i + Si_s$). The mobile C_i may then react with oxygen and carbon atoms to create C_s - S_i - C_s ($C_i + C_s \Rightarrow C_s - S_i - C_s$) and C_i - O_i ($C_i + O_i \Rightarrow C_i - O_i$) complexes.[7] The 969.5 meV PL defect has been identified with the EPR-detected G11 centre,[12] whereas the 789.4 meV defect was identified as the EPR G15 centre,[13] with an energy level at 0.38 eV above the valence band.[14]

The concentration and type of defects primarily formed during irradiation depend on the fluence, energy and species of ions. Moreover, impurity-defect complexes are produced through the interaction between defects and impurities. It is important to study the dependences of ion mass, dose and energy on the luminescent lines by noble gas ion implantation. In the present study, we investigated the effect of mass, energy and fluence of bombarding noble gas ions on the intensities of the G- and C-lines luminescence. The electrical properties of the low energy bombardment-induced defects have also been studied by deep level transient spectroscopy (DLTS).[9,15]

II. EXPERIMENTAL PROCEDURE

Samples used were epitaxially grown (111) oriented Si layers on n^+-substrates and doped with $5x10^{15}$ cm^{-3} phosphorous. The epitaxial side of some samples were bombarded with 1 keV noble gas ions (He, Ne, Ar, Kr) at doses ranging from $1x10^{10}$ to $1x10^{15}$ ions/cm^2 using a sputter gun. Other samples were bombarded with He and Ar ions at fluences of $1x10^{10}$ and $1x10^{12}$ /cm^2 in the energy range 25 - 150 keV in an ion implanter.

The photoluminescence measurements were carried out using the 514 nm line of an argon-ion laser, a 0.64 μm infra red monochromator (resolution 1.4 Å), a cooled germanium detector and conventional lock-in amplifier technique. Samples were mounted in a closed cycle helium-cooled cryostat and the temperature could be varied between 11 K and 90 K. The laser power was fixed at 200 mW and it was focused to a spot of approximately 0.2 mm diameter.

Circular Pd Schottky contacts of 0.7 mm diameter and 100 nm thickness were resistively deposited on the bombarded samples through a metal contact mask for deep level transient spectroscopy (DLTS) analyses. Ohmic contacts were formed on the n^+-substrates using a liquidus In-Ga alloy immediately before defect characterisation. The energy levels, E_T, and apparent capture cross-sections, σ_a, associated with the defects were determined from DLTS Arrhenius plots of $\log(e/T^2)$ vs $1/T$, where e is the emission rate at a temperature T. For control purposes, PL and DLTS measurements were taken using Si samples which were not subject to noble gas ion bombardment.

III. RESULTS AND DISCUSSION

A. G-line transition characteristics

Figure 1 shows a typical PL spectrum of Si after irradiation with 5 keV He^+ to a dose of $1x10^{12}$ ions/cm^2. The broad peak to the left is also seen in untreated material and has previously been identified as a phonon replica of a bound exciton. The G- and C-lines are clearly visible, and were absent in untreated samples. The line width, power and temperature dependence of the G-line have been investigated. The spectral width of the lines observed on the photoluminescence (PL) spectra were to some extent limited by the resolution of our system. The total width of the G-line was found to be 5.1 Å, giving a deconvoluted full width at half maximum (FWHM) of appoximately 4.9 Å.

The sample temperature and laser power dependence of the G-line were also investigated. The intensity of the line was found to be directly proportional to the laser power in the range 10 mW - 350 mW. The activation energy of the optical transition responsible for the G-line was determined from the temperature dependence of the line (Fig. 2). The experimental data in the high temperature regime was fitted to the following equation:[16]

$$I(T) = I_o\,(1 + C\exp(-E_a/kT))^{-1} \qquad (1)$$

where C is a constant and E_a is the activation energy. From the line of best fit, the activation energy was found to be 0.055 eV.

B. Dose dependence

Figure 3 shows the G-line and the C-line intensities after 1 keV Ne ion bombardment as a function of fluence from $5\text{x}10^{10}$ to $1\text{x}10^{14}$ ions/cm^2. It is found that the intensity of optically active defects increased with increasing Ne ion dose. It is also found that the intensities decreased after reaching a maximum at a fluence of $1\text{x}10^{12}$ ions/cm^2. A saturation in the intensity of the defects is expected at higher doses since the number of defects is limited by the concentration of carbon and oxygen atoms originally present in the Si crystals. We attribute the reduction in the PL intensities of the G- and C-lines for higher doses to the formation of non-radiative recombination centres with either discrete levels related to vacancy-oxygen and vacancy-phosphorous pairs and divacancies[17,18] or continuous levels related to extended defects in the band gap. Furthermore, complexes composed of vacancies and neon atoms[19,20,21] could also increase the number of optically inactive recombination centres for bombardment doses larger than $1\text{x}10^{12}$ ions/cm^2. The higher concentrations of defects at higher doses are due to the

higher densities of collision cascades, and hence higher rates of nuclear energy deposition by the incoming ions.

Now we show the presence of discrete and continuous levels in 1 keV Ne implanted Si. Figure 4 shows the DLTS spectra obtained for n-Si after 1 keV Ne ion bombardments at different doses. The well known VO-centre has a level at E_c - 0.183 eV and is labelled ENe183. In the nomenclature used, "E" denotes an electron trap, "Ne" implies that the defect is Ne-ion induced and the number gives the position of the defect below the conduction band in meV. The peak labelled ENe437 is attributed to VP-centres. The second charge state of the divacancy, $V_2^{-/0}$, could be observed in low concentrations after removing the VP-centres by annealing at 180 °C for 30 min. We have attributed the nondetection of the first charge state of the divacancy, $V_2^{=/-}$, to the presence of stress fields in the 1 keV bombarded samples.[22] Three comments can be made about the spectra to validate the above discussion. Firstly, the intensities of the peaks (i.e., concentrations of defects) are found to increase with increasing ion dose. Secondly, a new prominent defect at E_c - 0.48 eV can be observed during bombardment at $1x10^{14}$ ions/cm^2. This defect, being close to the mid-bandgap position, could indeed be a recombination centre.[23] Finally, it is clear from Fig. 4 that the baseline "skewing" of the DLTS spectra increases with increasing ion dose. The baseline "skewing" phenomenon has previously been observed in 5.4 MeV electron irradiated GaAs and has been speculated to be due to the presence of extended defects.[24] Furthermore, the baseline "skewing" is accompanied by the broadening of some of the DLTS defect peaks such as ENe347 and those observed in the temperature range 200 - 280 K when the bombarding ion dose is increased. The peak broadening phenomenon is also indicative of the presence of extended defects.[25] It should be

noted that efficient recombination levels which could be present after bombarding at doses larger than $1x10^{12}$ ions/cm^2 cannot be detected by conventional DLTS.[26]

The non-radiative defects result in an increased amount of existing or new recombination paths such that the recombination of electrons and holes between the levels responsible for the G- and C-lines is decreased. Consequently, the luminescence from the G-line and C-line defects is reduced when the irradiation dose exceeds the critical level of $1x10^{12}$ ions/cm^2.

C. Incident ion mass and energy dependence

Figure 5 shows the variation in the PL intensities of the G- and C-lines after 1 keV He, Ne, Ar and Kr ion bombardments at a dose of $1x10^{12}$ ions/cm^2, as well as the nuclear energy deposited to recoils by each incident ion. The intensities of the two spectral lines were observed to decay almost exponentially with the mass of the bombarding ions. This mass dependence of the PL intensities is explained by considering the energy deposited by the different noble gas ions as they penetrate the Si lattice. Nuclear stopping is the dominant mechanism for energy transfer to the target during 1 keV He, Ne, Ar and Kr ion bombardments. As the incident ion mass is increased, the cross section for an elastic collision is also increased. This results in a higher density of recoil atoms being produced and consequently a higher rate of energy deposition. For instance, TRIM[27] simulations reveal that the nuclear energy loss to the Si lattice increases with incident ion mass as shown in Fig. 5. Since the energy deposited by a 1 keV He ion is well above the critical value of the energy required for non-linear effects such as energy spikes[28] - one mechanism of forming extended defects - the amount of damage introduced to the Si lattice is expected to increase drastically with the mass of bombarding ions. The lowering in the PL intensities of the G- and C-lines can thus be explained by the introduction of increased amounts of non-radiative recombination centres with increasing incident ion mass. Since the energy

deposited per unit length (eV/Å) is much higher than the threshold for spike formation, vacancy clusters (larger than divacancies) may be produced in large concentrations during 1 keV bombardments using the heavier noble gas ions. Using photoluminescence to study noble-gas-defects during ion-beam etching, Sawyer *et al.*[29] showed that 3-4 vacancies can be built into a noble gas defect when low energy ion beams are employed.

DLTS measurements have shown that 1 keV He and Ne ion bombardment of Si at a dose of $1x10^{12}$ ions/cm^2 introduced the same set of defects.[30] However, the concentration of the defects were found to be relatively higher during Ne ion irradiation. On the other hand, a more complex set of defects was created in the same material during Ar and Kr ion bombardments. We have also observed that, except for the VO- and VP-centres, the defects created by noble gas ion irradiation are different from the defects introduced by high energy (MeV) electron and alpha-particle irradiation. Furthermore, the low concentrations of $V_2^{-/0}$ in our samples indicate that vacancy clusters (larger than the divacancy) are predominantly formed by 1 keV noble gas ion bombardments. This was unambiguously demonstrated when we showed that 1 keV He-ion bombardment of n-Si containing low concentrations of oxygen introduced a completely different set of defects than irradiation by 5.4 MeV alpha-particles.[31] Thus our DLTS results agree with the TRIM simulation results presented above and can be used to confirm the propositions made to explain the reduction in PL intensities of the G- and C-lines with increasing bombarding ion mass. We have also noted significant baseline "skewing" of our DLTS spectra together with DLTS peak broadening during analysis of samples exposed to the heavier noble gas ions.

Figure 6 shows the PL intensities of the G- and C-lines as a function of incident ion energy for He ions at fluences of $1x10^{10}$ to $1x10^{12}$ ions/cm^2. The variation in the PL intensities of the two lines with ion energy for He and Ar ion bombardment at a dose of $1x10^{10}$ ions/cm^2 is depicted in Fig. 7. It is observed from Fig. 7 that the PL intensities of the G- and C-lines initially

increase to maximum values and thereafter decrease. A similar trend is observed from Fig. 6. These plots suggest that the maxima of the PL intensities of the G- and C-lines are both dose (Fig. 6) and mass (Fig. 7) dependent. We explain our results by considering energy, and mass dependence of the electronic and nuclear stopping of He ions in the Si crystal. In addition, we have considered the range of He ions with different bombarding energies together with the excitation depth of our Ar-ion laser. For any implanted ion, the nuclear stopping component of energy loss decreases as the energy of the ion is increased, whereas its electronic energy deposition increases.[32] The projected range and energy loss to recoils for He ions, as calculated from TRIM, in the energy range 1-150 keV are shown in Fig. 8.

For any implantation dose or noble gas ion used, the number of optically active defects increases from a minimum as the energy of the incident ion is increased. It can be deduced from Fig. 8 that a 150 keV He ion will create much fewer energetic recoil atoms in the first 100 Å below the semiconductor surface compared to a 1 keV He ion. However, as the 150 keV ion loses energy and slows down as it penetrates further into the Si lattice, its nuclear stopping increases. As a result, the ion produces increasingly more energetic recoil atoms and thus introduces increasingly more damage in the semiconductor as it continues to slow down over its range of approximately 8200 Å. TRIM simulations also show that of spike formation could occur when the energy of the ion is slightly less than 150 keV. Thompson *et al*[33] have shown that non-linear effects, such as the overlapping of individual collision cascades to form higher density ones, could occur in ion bombarded Si when the average deposited energy density is as small as 0.1 eV/atom. The integral sum of defects distributed over the penetration depth of $\sim \lambda/2 = 2570$ Å of the Ar-ion laser will, therefore, be larger for the 150 keV ion than for the 1 keV ion. Consequently, the Ar-ion laser "sees" more non-radiative recombination centres when PL measurements are taken on a sample bombarded with 150 keV He ions.

For all implantation doses or noble gas ion that were used, we found that the number of optically active defects increases from a minimum as the energy of the incident ion is increased. The intensities of the two transitions start to decrease at specific ion energies, which are dose and mass dependent, when the number of non-radiative recombination centres as discussed above provide alternative recombination paths to those responsible for the G- and C-spectral lines. For instance, the energy corresponding to maximum intensities of the G- and C-lines for a dose of $1x10^{10}$ He^{+}/cm^{2} is about 75 keV (Fig. 6), after which the sum total of defects increases, causing a reduction PL intensities. Since nuclear energy deposition increases with increasing bombarding ion dose, the energy corresponding to the maximum PL intensities of the two lines is lower for an irradiation dose of $1x10^{12}$ He^{+}/cm^{2} compared to $1x10^{10}$ He^{+}/cm^{2}. This dose dependence of the maximum is translated into a shift in the intensity curves in Fig. 6 to the left for the higher ion dose. A similar explanation can be used to describe the trend shown in Fig. 7. Since increasing ion mass and dose have the similar effects on the nuclear energy deposited, the PL intesity curves in Fig. 7 are also shifted to the left for Ar ion bombardment.

4. CONCLUSION

In this study, we have investigated the effect of ion dose, mass and incident energy on the intensities of the G- and C-line luminescence in Si induced by noble gas ions (He, Ne, Ar and Kr) bombardment. Bombardments using 1 keV Ne ions in the dose range $1x10^{10}$ cm^{-2} to $1x10^{15}$ cm^{-2} have shown that the PL intensities of the two lines increase to reach their maximum values at $1x10^{12}$ cm^{-2} and thereafter decrease with ion fluence. We have attributed the reduction in intensities beyond $1x10^{12}$ $Ne^{+}cm^{-2}$ to the introduction of non-radiative recombination centres, which provide alternative recombination paths to those responsible for the G- and C-transitions. DLTS results have indeed shown that higher concentrations of defects are introduced when ion

fluence is increased. A prominent new electron trap at E_c - 0.48 eV, which being close to the mid-bandgap position could be an efficient recombination centre, has been detected in $1x10^{15}$ Ne^+cm^{-2} bombarded material. Further, the baseline "skewing" and peak broadening phenomena observed in our DLTS spectra may suggest that extended defects, with a continuous distribution of deep levels in the bandgap, are introduced in our samples at irradiation doses higher than $1x10^{12}$ cm^{-2}. The PL intensities of the G- and C-lines were found to decrease almost exponentially with incident ion mass for 1 keV bombardments at $1x10^{12}$ cm^{-2}. The increasingly higher nuclear stopping component of energy deposited by the incident ions with higher mass results in larger amounts of damage to be created in the Si lattice. Consequently, the introduction of non-radiative recombination centres is increased resulting in a decrease in PL intensities of the luminescent lines. Finally, we have demonstrated that the incident ion energy at which the PL intensities reach their maximum values is mass and dose dependent. We have explained the observed trends qualitatively by considering the integral sum of defects produced over the excitation depth of the Ar-ion laser used in our PL experiments.

ACKNOWLEDGMENTS

We are grateful to the financial assistance of the South African Foundation for Research Development and the Carl and Emily Fuchs Institute for Microelectronics. The technical assistance provided by Willie Engelbrecht is kindly acknowledged.

REFERENCES

[1] N. Burger, K. Thonke, R. Sauer and G. Pensl, Phys. Rev. Lett. **52** (1984) 1645.

[2] J. Weber and M. Singh, Appl. Phys. Lett. **49** (1986) 1617.

[3] R.J. Davis, H.-U. Habermeier and J. Weber, Appl. Phys. Lett. **47** (1985) 1295.

[4] J. Weber, Physica **B 170** (1991) 201.

[5] J. Weber, R. J. Davis, H.-U. Habermeier, W. D. Sawyer and M. Singh, Appl. Phys. **A 41** (1986) 175.

[6] W.D.Sawyer, J. Weber, G. Nabert, J. Schmalzlin and H.-U. Habermeier, J. Appl. Phys. **68** (1990) 6179.

[7] M. Nakamura, E. Kitamura, Y. Misawa, T. Suzuki, S. Nagai and H. Sunaga, J. Electrochem. Soc. **141** (1994) 3576.

[8] J.L. Benton, B.E. Weir, D.J. Eaglesham, R.A. Gottscho, J. Michel and L.C. Kimerling, J. Vac. Sci. Technol. **B 10** (1992) 540.

[9] M. T. Assom, J. L. Benton, R, Sauer and L. C. Kimerling, Appl. Phys. Lett. **51** (1987) 256.

[10] O.O. Awadelkarim, A. Henry, B. Monemar, J.L. Lindstrom, Y. Zhang and J. W. Corbett, Phys. Rev. **B 42** (1990) 5635.

[11] J. Wagner, K. Thonke and R. Sauer, Phys. Rev. **B 29** (1984) 7051.

[12] K.L. Brower, Phys. Rev. **B 9**, 2607 (1974).

[13] G.D. Watkins, in *Radiation Damage in Semiconductors*, edited by P. Baruch (Dunod, Paris, 1965).

[14] P.M. Mooney, L.J. Cheng, M. Süli, J.D. Gerson and J.W. Corbett, Phys. Rev. **B 15**, 3836 (1977).

[15] D.V. Lang, J. Appl. Phys. **45**, 3014 (1974).

[16] J. Lee, N.C. Giles, D. Rajavel, C.J. Summers, J. Appl. Phys. **78**, (1995) 5669.

[17] S.D. Brotherton and P. Bradley, J. Appl. Phys. **53**, 5720 (1982).

[18] M. Asghar, M. Zafar Iqbal and N. Zafar, J. Appl. Phys. **73**, 3698 (1993).

[19] A. V. Mudryi, A. L. Pushkarchuk and A.G. Ulyashin, Phys. Stat. Sol. **b 129** (1985) K83.

[20] V.D.Tkachev, A.V. Mudryi and N.S. Minaev, Phys. Stat. Sol. **a 81** (1984) 313.

[21] A.V. Mudryi, A.L. Puschkarchuk and A.G. Ul'yashin, Sov. Phys. Semicond. **19** (1985) 225.

[22] B.G. Svensson, B. Mohadjeri, A. Allen, J.H. Svensson and J.W. Corbett, Phys. Rev. **B 43**, 2292 (1991).

[23] S.M. Sze, Physics of Semiconductor Devices (Wiley, New York, 1981), p. 37.

[24] F.D. Auret, S.A. Goodman, R.M. Erasmus, W.E. Meyer and G. Myburg, Nucl. Inst. and Meth. **B 106** (1995) 323.

[54] W. Schröter, J. Kronewitz,U. Gnauert, F. Riedel and M. Seibt, Phys. Rev. **B 52**, 13 726 (1995).

[26] T. Markvart, D.P. Parton, J.W. Peters and A.F.W. Willoughby, Materials Science Forum **143-147**, 1381 (1993).

[27] J.F. Ziegler, J.P. Biersack and U. Littmark, "*The Stopping and Range of Ions in Solids*", vol. 1, ed. J.F. Ziegler (Pergamon Press, New York, 1985).

[28] P. Sigmund, Appl. Phys. Lett. **25**, 164 (1974).

[29] W.D. Sawyer, J. Weber, G. Nabert, J. Schmälzlin and H.-U Habermeier, J. Appl. Phys. **68**, 6179 (1990).

[30] P.N.K. Deenapanray, N.E. Perret, F.D. Auret, W.E. Meyer, J.B. Malherbe and M. du Plessis, 1996 Conference on Optoelectronic and Microelectronic Materials and Devices Proceedings, (Ed. C. Jagadish) IEEE, Piscataway, NJ (USA) 1997.

[31] F.D. Auret, S.A. Goodman, G. Myburg and W.E. Meyer, submitted to Appl. Phys. Lett., (1997).

[32] J.A. Davies, MRS Bulletin **26** (June 1992).

[33] D.A. Thompson and R.S. Walker, Rad. Effects **36**, 91 (1978).

FIGURE CAPTIONS

FIG. 1.

Typical PL spectrum of silicon after implantation with 5 keV He^+ to a dose of 10^{12} cm^{-2}. The broad peak to the left is also seen in untreated material and was previously identified as a phonon replica of a bound exciton. The G- and C-lines are clearly visible. These features are completely absent in untreated material.

FIG. 2.

Position and PL intensity of the G-spectral line as a function of temperature. The measurements were made on a 1 keV He ion bombarded epitaxially grown Si, and doped to $5x10^{15}$ cm^{-3} with P, sample to a dose of $1x10^{12}$ cm^{-2}. The solid curve represents the line of fit of our experimental data to Eqn. (1) from which the activation energy E_a was extracted. At temperatures below 40 K the PL signal remains roughly constant and the peak position stays at 12 800 Å.

FIG. 3.

Plot of PL intensities of the G-line and C-line as a function of incident ion dose during 1 keV Ne ion bombardment of epitaxially grown Si doped to $5x10^{15}$ cm^{-3} with P. The PL intensities of the lines reach their maximum values for a bombardment fluence of $1x10^{12}$ cm^{-2}. Sample temperature was fixed at 11 K for these measurements.

FIG. 4.

DLTS spectra of 1 keV Ne-ion bombarded epitaxially grown n-Si, doped to $5x10^{15}$ cm^{-3} with P, to fluences of: (a) $1x10^{12}$ cm^{-2}, (b) $1x10^{13}$ cm^{-2} and (c) $1x10^{14}$ cm^{-2}. All curves were recorded at a lock-in amplifier frequency of 46 Hz (decay time constant of 9.23 ms), V_r = 1 V and V_p = 1.4 V.

FIG. 5.

Variation of PL intensities of the G- and C-lines as a function of bombarding ion mass. PL measurements were done on 1 keV He-, Ne-, Ar- and Kr-ion bombarded epitaxially grown n-si, doped to $5x10^{15}$ cm^{-3} with P, to a dose of $1x10^{12}$ cm^{-2}. The nuclear energy deposited by the 1 keV ions to recoils, as calculated from TRIM simulations, are also shown.

FIG. 6.

Influence of incident ion energy on the PL intensities of the G- and C-lines during He ion bombardment of epitaxially grown n-Si to doses of $1x10^{10}$ cm^{-2} and $1x10^{12}$ cm^{-2}.

FIG. 7.

The variation in PL intensities of the G-line and C-line with incident ion energy for He and Ar ion bombardments of epitaxially grown n-Si at a dose of $1x10^{10}$ **FIG. 1.** cm^{-2} is depicted. The solid lines show the trend in the PL intensity of the G-line.

FIG. 8.

TRIM simulations of projected range and nuclear energy deposited to recoils of He ions implanted in Si at different energies (1 - 150 keV). The error bars assigned to the projected ion ranges correspond to their straggle, as calculated by TRIM.

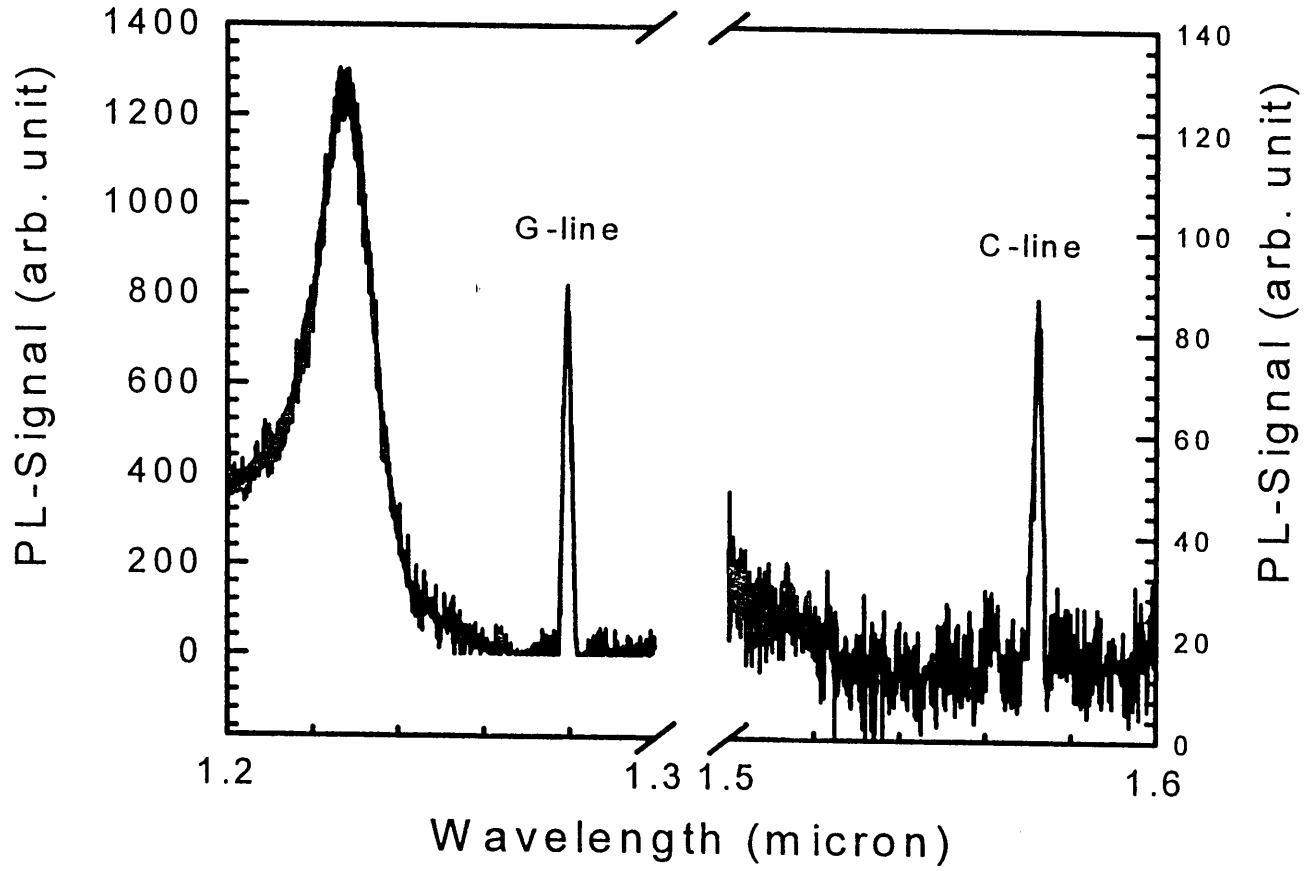

P.N.K. Deenapanray et al Fig. 1 of (8)

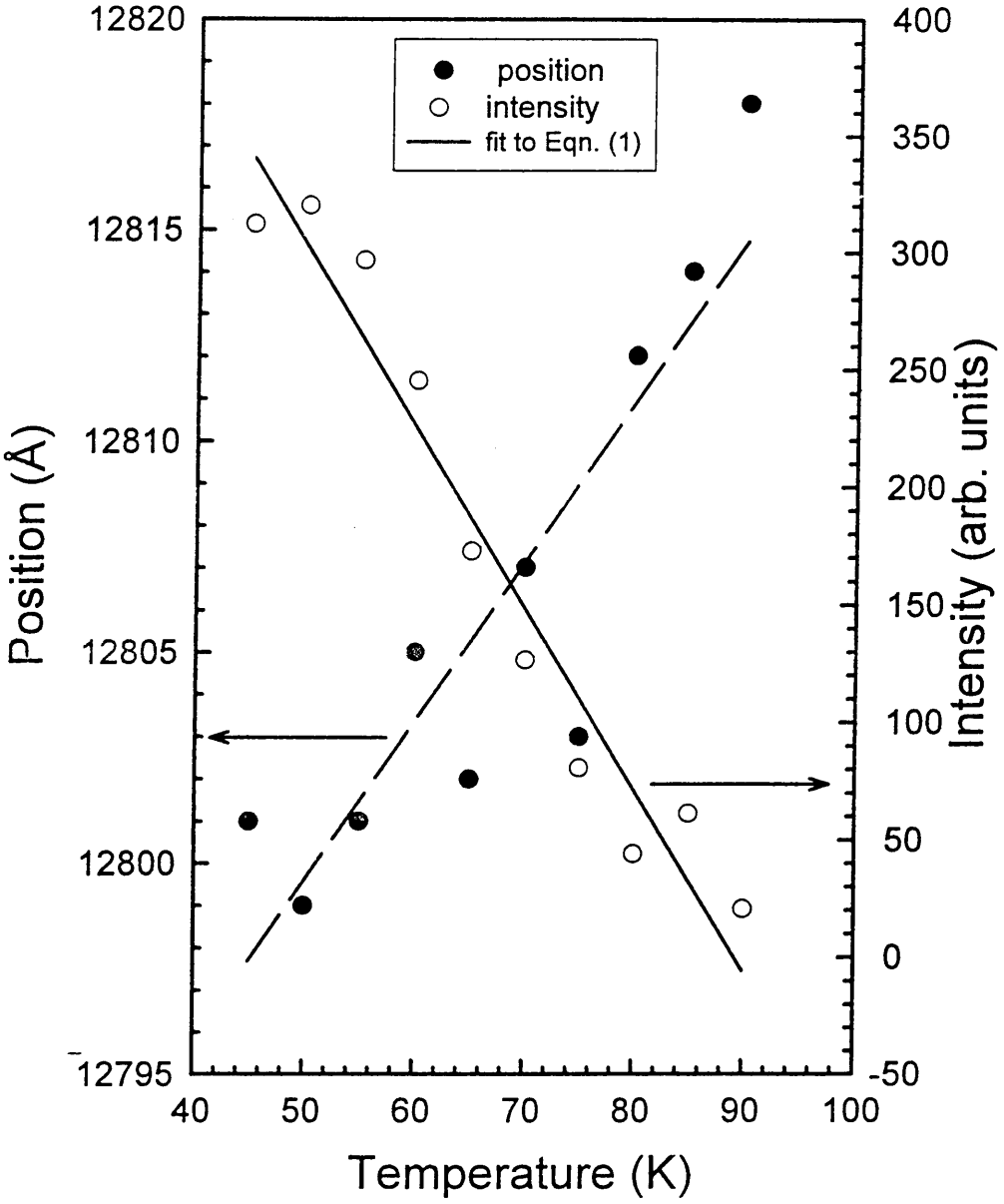

P.N.K. Deenapanray et al Fig. 2 of (8)

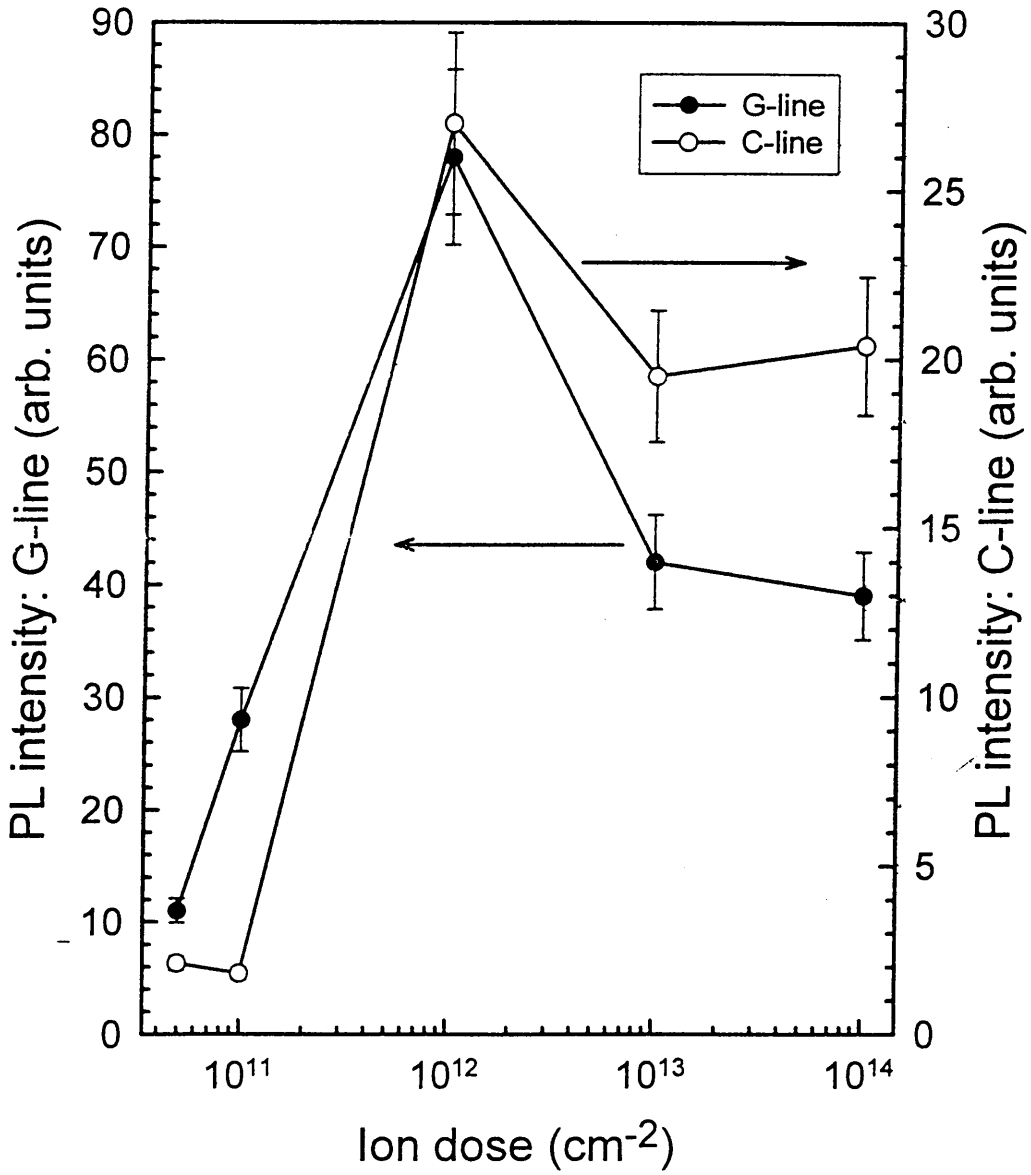

P.N.K. Deenapanray et al Fig. 3 of (8)

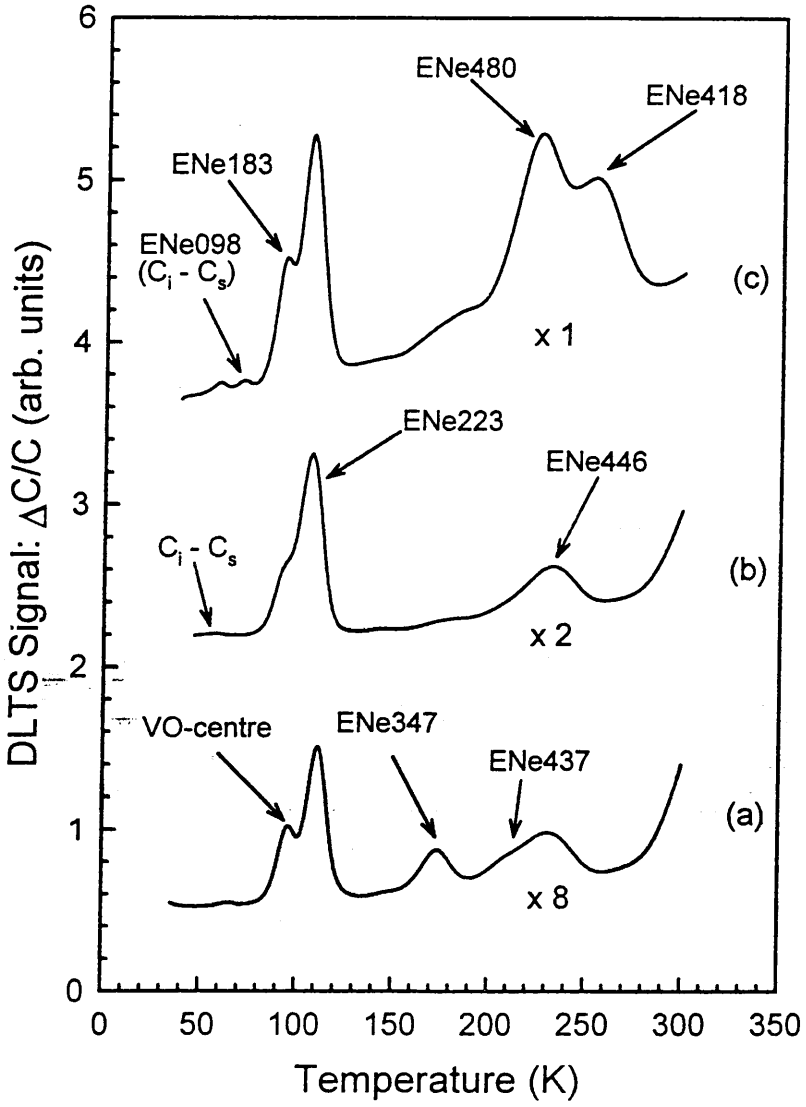

P.N.K. Deenapanray et al Fig. 4 of (8)

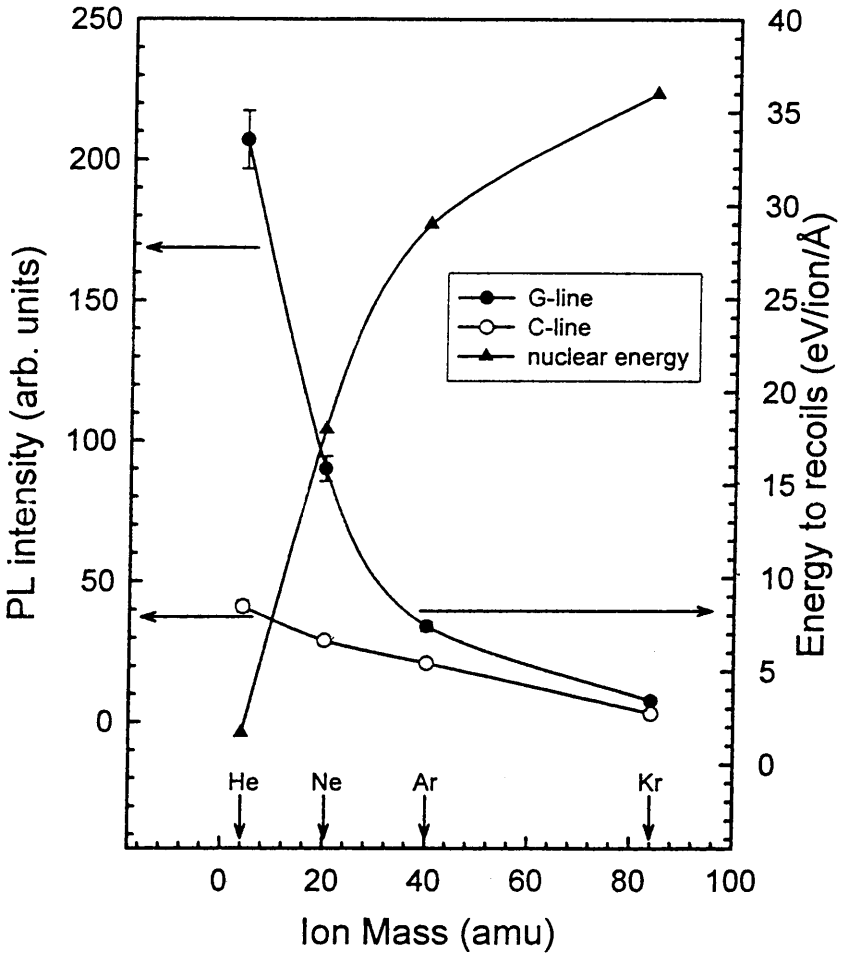

P.N.K. Deenapanray et al Fig. 5 of (8)

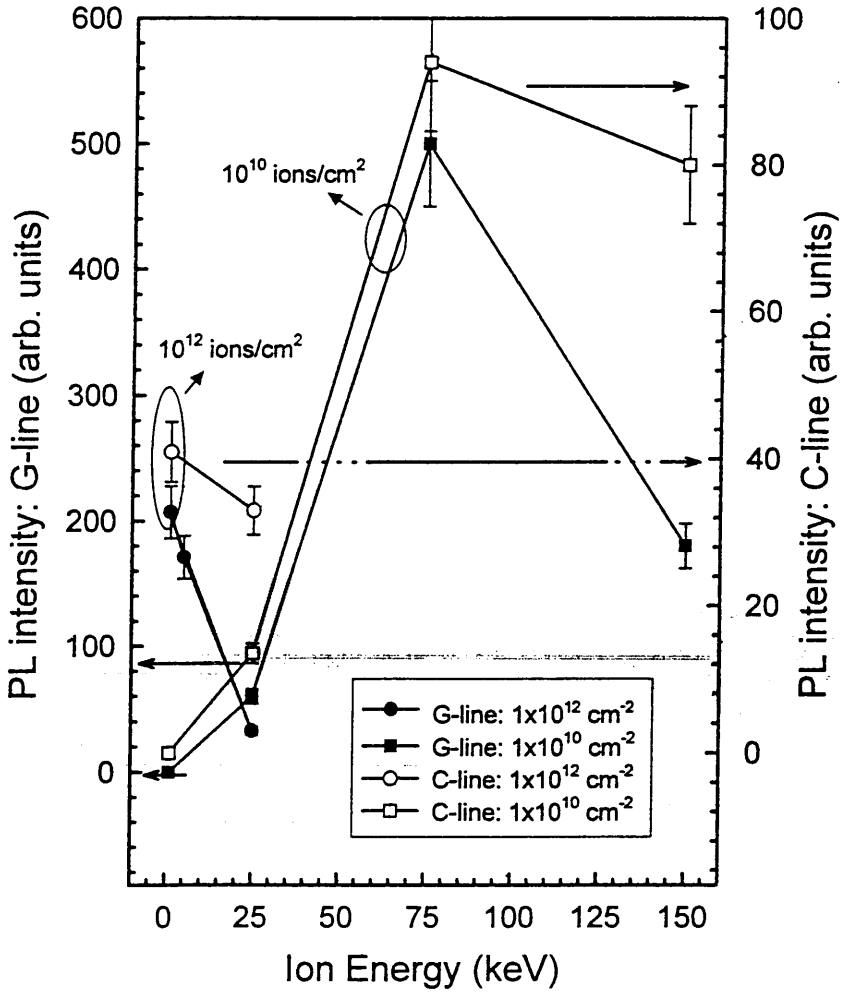

P.N.K. Deenapanray et al Fig. 6 of (8)

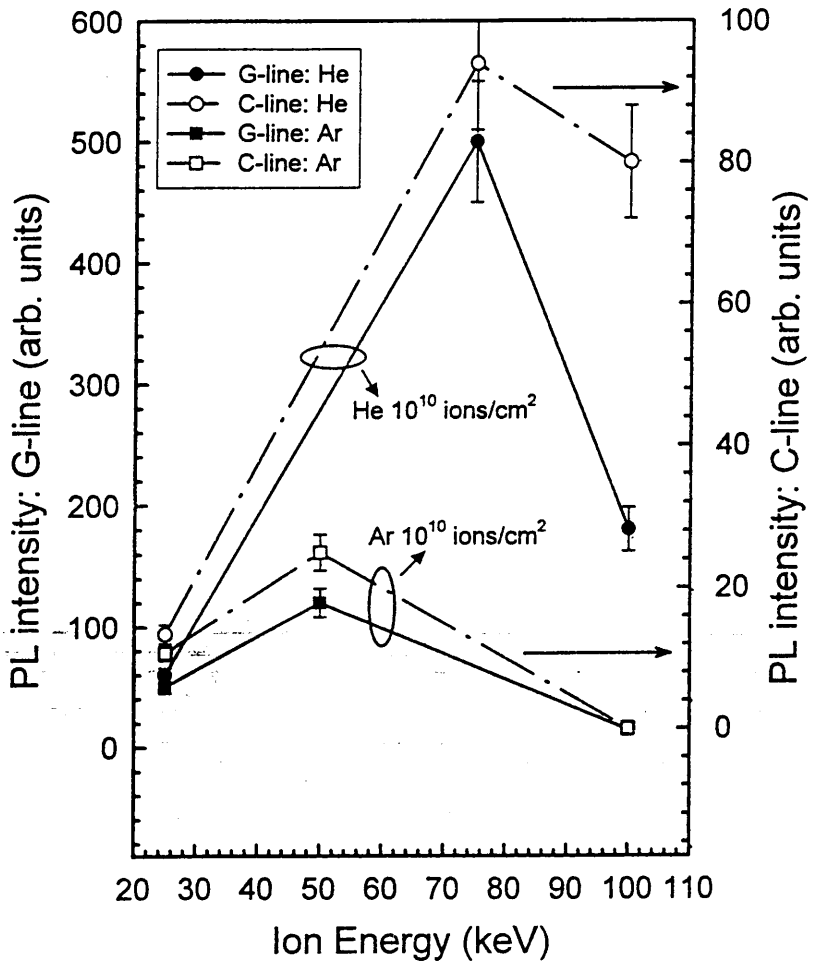

P.N.K. Deenapanray et al Fig. 7 of (8)

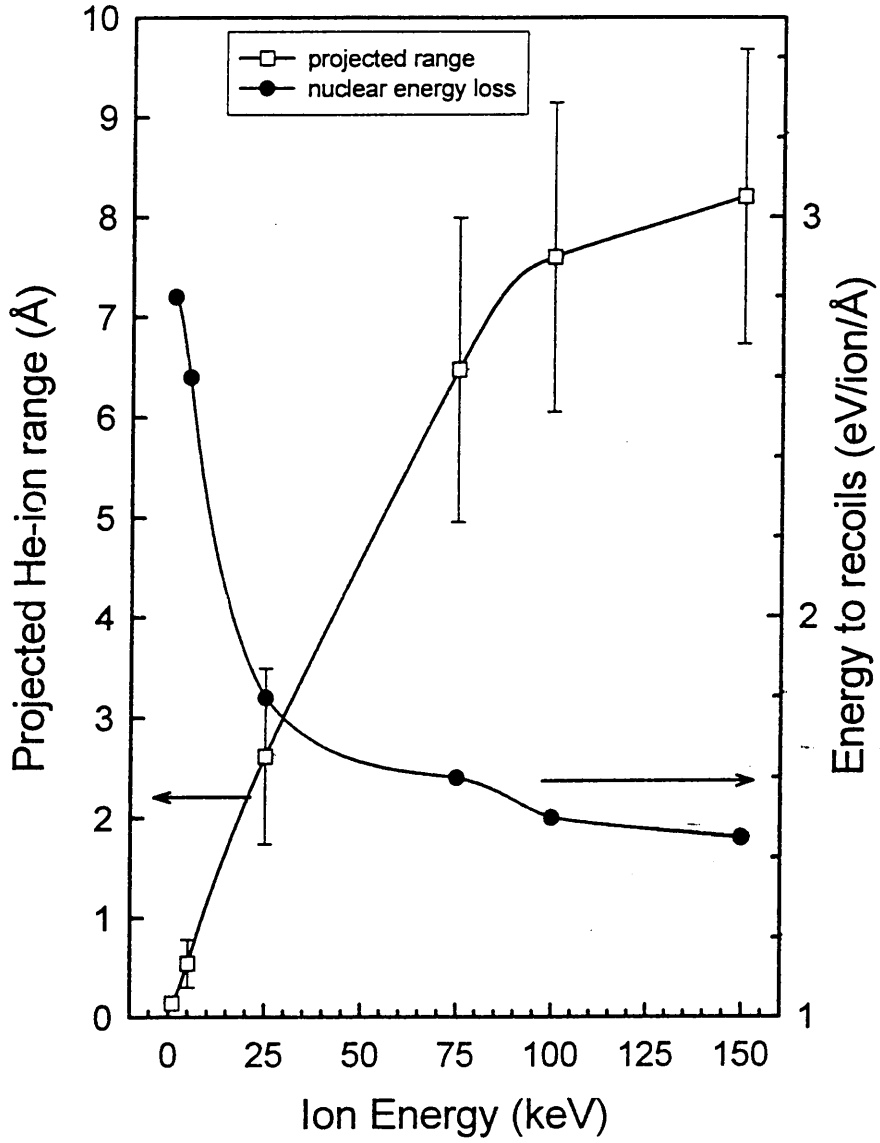

P.N.K. Deenapanray et al Fig. 8 of (8)

Electrical characterization of low-energy He-ion bombardment induced defects in epitaxially grown n-Si

F. D. Auret [(a)], P. N. K. Deenapanray , S. A. Goodman, W. E. Meyer and G. Myburg

Physics Department, University of Pretoria, Pretoria , SOUTH AFRICA

Epitaxially grown n-Si was bombarded with low energy (1 keV) He-ions. Deep level transient spectroscopy (DLTS) revealed that this introduced four prominent defects with energy levels at 0.14 eV, 0.20 eV, 0.30 eV and 0.55 eV, respectively, below the conduction band. The electronic properties and annealing behavior of these defects are different to those of the main defects, namely divacancies (V_2) and vacancy-phosphorous centers (VP), observed after 5.4 MeV He-ion bombardment of the same material. We propose that, except for the defect with an energy level at E_c - 0.14 eV, the defects introduced by 1 keV He-ion bombardment of n-Si may be related to: 1) vacancy clusters larger than divacancies but smaller than the hexavacancy; or 2) incorporation of He and H into V_2 or higher-order vacancy clusters.

[(a)] Electronic mail: fauret@scientia.up.ac.za

Low energy ion-related processing plays an important role in several areas of semiconductor device fabrication, e.g. dry etching and sputter deposition of metals. Despite the low energies (usually only a few hundred eV) of these ions, they introduce electrically active defects which alter the surface and sub-surface properties of semiconductors and thus influence the characteristics of devices, such as Schottky barrier diodes (SBDs), fabricated on them.[1,2] The degree of Schottky barrier modification was found to increase with increasing defect concentration.[3] These results suggest that the barrier height of a SBD can be tailored to specific values by exposing it to controlled amounts of low energy ions. Any such defect engineering requires two sets of parameters regarding the defects involved. Firstly, the electronic properties (energy levels and capture cross-sections) and concentrations of the defects, so that their effect on semiconductor properties and device characteristics can be predicted. Secondly, the structure and introduction rates of these defects should be known so that they can be reproducibly introduced.

The structure and electronic properties of most of the prominent defects in high energy particle-irradiated Si have been established.[4,5] Consequently, controlled modification of electronic properties of Si, such as carrier concentration and lifetime, using the known capture and emission kinetics of radiation-induced defects, is already attainable during wafer processing. However, much less is known about the nature of defects introduced by low energy particles. Weber[6] has reported the luminescence properties of defects introduced by low energy ion bombardment of Si, some of which were proposed to be complexes involving implanted noble gas ions.[7] Furthermore, much attention has recently been devoted to model the structure of certain defects created by low-energy noble gas ions using molecular dynamics simulations.[8,9] The discrepancies between the proposed models imply that more work has yet to be conducted. Up to now, no systematic study to correlate the electrical properties and structure of low-energy ion bombardment induced defects with the noble gas ion species or impurities in

Si, has yet been reported. Clearly, if defects introduced by these low energy ions are to be used to *predictably and controllably* govern the properties of semiconductors and metal-semiconductor junctions, their electrical properties *as well as their structure* must be established.

Helium is currently receiving attention as a dry etch component for some semiconductor device fabrication steps. However, little is known about the electrically active defects that low energy He-ions introduce in Si. In this letter, we report the electronic properties, determined by DLTS,[10] of defects introduced in epitaxially grown n-Si during 1 keV He-ion bombardment. We show that the main defects introduced are different from those introduced during high energy (MeV) He-ion bombardment.

Phosphorous doped (to $3x10^{16}$ cm^{-3}) n-type (111) oriented, 4 μm thick Si layers, grown by chemical vapor deposition on an n^+-Si substrate, were used for this study. After chemical cleaning, the epitaxial side of the wafer was bombarded with a fluence of $1x10^{12}$ cm^{-2} 1 keV He-ions at a dose rate of $2x10^{11}$ cm^{-2} s^{-1}. Thereafter, Pd Schottky contacts were fabricated on the bombarded surfaces by resistive evaporation. Identically fabricated Pd SBDs (without 1 keV He-ion bombardment) were irradiated with 5.4 MeV α-particles (He-ions) from an ^{241}Am source to the same fluence at a dose rate of $5.7x10^6$ cm^{-2} s^{-1}.

The DLTS "signatures" (energy level, E_t, and apparent capture cross-section. σ_a) of the defects were determined from Arrhenius plots of log (e/T^2) vs $1/T$, where e is the emission rate at a temperature T. In order to minimize electric field assisted emission,[11] small biases and pulses ($V_r = V_p = 0.3$ V) were used to determine the defect "signatures".

The DLTS spectrum in curve (a) of Fig. 1 shows that 1 keV He-ion bombardment of Si introduces four prominent electron traps, EHe136, EHe201, EHe296 and EHe554, and a trap EHe411 in a much lower concentration. In the nomenclature used here, "E" implies electron

trap, "He" means that the defect was introduced by *low energy* He-ion bombardment and the number following is its energy below the conduction band, in meV (Table I). DLTS depth profiling[12] showed that the concentration of the main defects decrease exponentially from about 10^{14} cm^{-3} at ~90 nm below the surface to 10^{12} cm^{-3} beyond 0.22 μm from the surface, showing that their migration can be modelled as "limited-source" diffusion. The chracteristic diffusion length, L, together with the extrapolated surface concentration, $N_T(0)$, of the prominent defects are also listed in Table I.

We compared the defects introduced by low energy He-ion bombardment to the primary defects[4] created during 5.4 MeV α-particle bombardment of the same material [curve (b) in Fig. 1 and Table I]. The most prominent defects thus introduced are Eα437 (VP or E center) and two of the charge states of the divacancy, Eα251 ($V_2^{=/-}$) and Eα415 ($V_2^{-/0}$). The peaks of Eα415 and Eα437 overlap and can only be distinguished after removing Eα437 by annealing above 180 °C. Two smaller peaks, Eα100 and Eα145, are also observed and may be related to C_s - Si_i - C_s.[13] The lack of VO-centres is due to the low oxygen content in the Si layers used.

The DLTS spectra in Fig. 1 and the defect "signatures" (Table I) show that, without annealing, the main defects introduced by low energy He-ion bombardment are different from the main defects introduced by high energy He-ion bombardment. In particular, we observed no V_2 or VP centres after low energy He-ion bombardment. If V_2 or VP centres are indeed present, then their concentration is one to two orders of magnitude lower than those of the EHe defects. Since V_2 and VP are formed when bombardment induced Si vacancies (V) diffuse to combine with each other or at P dopant sites, respectively, these results suggest that there are little or no free vacancies introduced by low energy bombardment. Alternatively, any single vacancies formed are trapped into other defect clusters before being able to form V_2 and VP.

Isochronal annealing (15 min periods, 50 °C intervals) showed that the concentration of the main defects in 1 keV bombarded Si decreased sharply above 200 °C, with EHe136 and EHe296 being totally removed only at 300 °C and 400 °C, respectively. EHe201 and EHe554 annealed in two stages: after an initial reduction between 200 °C and 300 °C, their concentrations remained constant up to 450 °C, above which they were removed. The EHe201 detected in *unannealed* 1 keV He-ion bombarded Si has, within experimental error, the same "signature" as Eα206 (structure unknown) detected in 5.4 MeV α-particle bombarded Si *after annealing at 180 °C*. This, and the fact that Eα206 and EHe201 are both stable up to 450 °C, imply that they are identical. After annealing at 200 °C, a defect with similar electronic properties as EHe296 and which is removed at ~400 °C is also observed in 5.4 MeV α-particle bombarded Si.

Although the structures of EHe136 and EHe296 are not yet known, their "signatures" and annealing behaviour suggest that they could be C- and H-related complexes, respectively.[13,14] Erokhin *et al*[15] recently showed that 75 keV He^+ ion implantation of Si introduced a defect with an identical "signature" as EHe554. This defect, however, was completely removed at 200 °C in their O-containing samples. Furthermore, we observe a similar defect in 1 keV He-ion bombarded epitaxially grown n-Si containing O, but in a much lower concentration and which anneals at ~200 °C. These results imply that the introduction and thermal stability of EHe554 are enhanced in the absence of O.

In order to explain why the defects in 1 keV (except for EHe136) and 5.4 MeV He ion bombarded Si are different in the region we analysed, consider the energy loss mechanisms which govern defect formation in these energy regimes. Figure 2 (compiled using TRIM[16]) shows that as a 5 MeV He-ion enters Si, electronic stopping, $(dE/dr)_e$, dominates during the first part of its path and thus only point defects can be expected in this region. Indeed, DLTS

[curve (b) in Fig. 1] shows that the main defects in this region are V_2 and VP centres. Towards the end of its range, $(dE/dr)_e$ first increases to a maximum (introducing a higher concentration of point defects), whereafter it rapidly decreases and becomes negligible. In this region nuclear stopping, $(dE/dr)_n$, increases sharply and becomes the dominant energy transfer mechanism. The initial increase in $(dE/dr)_n$ enhances point defect formation. However, after the He-ion energy has been reduced to below 12 keV (indicated as "A" in inset of Fig. 2), $(dE/dr)_n$ exceeds 1 eV $Å^{-1}$ for the rest of its path. Since 1 eV $Å^{-1}$ is the threshold for spike formation,[17] this He-ion forms mainly higher-order defects, such as vacancy clusters, to which we shall hereafter refer to as end-of-range (EOR) defects, for the remainder of its path of 0.3 μm. In this energy spike regime it is highly probable that V_2 is produced in a single event rather than by the combination of two diffusing single-vacancies. Therefore, the last part of a high energy He-ion's path is characterized by a sharp increase in the point defect concentration followed by a region containing EOR defects and a reduction in point defects. Note that, since a higher-order vacancy cluster consists of agglomerated point defects, the point defects in the preceding region will by far outnumber the EOR defects.

The inset in Fig. 2 shows that when a 1 keV He-ion enters Si (or equivalently, after a energy of a high energy He-ion has been reduced to 1 keV), $(dE/dr)_n$ is about 1.7 eV $Å^{-1}$ (position marked "B") and remains above the threshold (1 eV $Å^{-1}$) for spike formation along the remainder of its path. This suggests that whereas a high energy He-ion creates both point and EOR defects, a 1 keV He-ion creates mainly EOR defects along its range of 170 Å, on average, with 90% of all ions located in the first 300 Å (calculated using TRIM[16]). Note that since the half-angle for channeling of a 1 keV He ion is quite large (~18 °), He-ions may channel deeper into the Si than predicted by TRIM. Furthermore, the probability for channeling is increased owing to the low ion dose used here.

Where He-ions come to rest, they may be trapped by other defects. PL observations have indicated that vacancy clusters smaller than the hexavacancy[9] and combinations of these with He-atoms[6,7,8] are present in low energy He-ion bombarded Si. These studies further revealed that the noble gas ion-related defects migrated to depths of ~1 μm below the surface, and has been explained by a vacancy-enhanced diffusion model.[8] Because of these observations, the calculations above and the fact that we did not detect any VP and V_2 centers, we propose that the defects (excluding EHe136) we observed by DLTS in the 1 keV He-ion bombarded Si may be related to: 1) vacancy clusters larger than V_2 but excluding the hexavacancy (EHe201 and EHe554); or 2) incorporation of He[6,8] (EHe201) and H (EHe296) into V_2 and these higher-order vacancy clusters. Theoretical calculations have shown that the thermal stability of the divacancy is enhanced after noble gas atoms are incorporated into it.[8] Given the fact that few single vacancies are produced during 1 keV He ion bombardment and that interstitial O atoms are efficient trap for single vacancies and are absent in our samples, our results suggest that EHe554 is due most probably to the trivacancy (V_3) or pentavacancy (V_5) or complexes thereof.

The question that now arises is whether or not the EOR defects we detected in 1 keV bombarded Si can also be observed at the end of range of high energy bombarded Si. Despite the fact that several authors[14,18,19] have presented defect depth profiles extending to beyond the end of range region of high energy (5 MeV) He-ion bombarded Si, none have reported any defects other than V_2 and VO in this region. We propose that the non-detection of EOR defects in high energy He-ion bombarded Si is a consequence of the much larger straggle of high energy ions (4000 Å for 5 MeV He-ions) compared to that of low energy ions (92 Å for 1 keV He-ions) which has two effects. Firstly, whereas the defects formed by 1 keV He-ions are concentrated in the first 300 Å below the surface, the EOR defects created by 5 MeV He-ions[19] are spread out over almost 1 μm (from TRIM), reducing their concentration accordingly. Secondly, this large straggling spreads out the high concentration of point defects preceding the

EOR defects over the EOR region, and thus the DLTS signals of these point defects mask those of the EOR defects.

In conclusion, we have determined the DLTS signatures, concentration distributions and annealing behaviour of the main electron traps in 1 keV He-ion bombarded epitaxially grown n-Si. The results that we presented showed unambigiously that the main defects thus introduced are electronically, and therefore also structurally, different from V_2, VP and VO typically introduced by 5.4 MeV He-ions in the first micron below the Si surface. We suggest that, except for a defect with an energy level at E_c - 0.136 eV, the most probable origin of these defects are: 1) vacancy clusters larger than divacancies bur smaller than the hexavacancy; or 2) incorporation of He and H into V_2 and the higher-order defects. Finally, we explain that EOR defects have not been observed in high energy He-ion bombarded Si because the large straggling of these ions leads to a masking of the DLTS signals of the EOR defects by those of the high concentration of point defects prior to the EOR defects.

We gratefully acknowledge the financial assistance of the Foundation for Research Development and thank Prof. J. B. Malherbe for the He-ion bombardment.

REFERENCES

1 S. Ashok, H. Krautle and H. Beneking, Appl. Phys. Lett. **45**, 431 (1984).

2 E. Grusell, S. Berg and L. P. Andersson, J. Electrochem. Soc. **127**, 1573 (1980).

3 F. H. Mullins and A. Brunnschweiler, Solid State Electr. **19**, 47 (1975).

4 S. D. Brotherton and P. Bradley, J. Appl. Phys. **53**, 5720 (1982).

5 L. C. Kimerling, Inst. Phys. Conf. Ser. No. **31**, 221 (1977).

6 J. Weber, Physica B **170**, 201 (1991).

7 N. Burger, K. Thonke, R. Sauer and G. Pensl, Phys. Rev. Lett. **52**, 1645 (1984).

8 S.K. Estreicher, J. Weber, A. Derecskei-Kovacs and D.S. Marynick, Phys. Rev. B 55, 5037 (1997).

9 S.K. Estreicher, J.L. Hastings and P.A. Fedders, Appl. Phys. Lett. **70**, 432 (1997).

10 D. V. Lang, J. Appl. Phys. **45**, 3014 (1974).

11 J. Frenkel, *Phys. Rev.* **54**, 647 (1938).

12 Y. Zohta and M. O. Watanabe, J. Appl. Phys. **53**, 1809 (1982).

13 J. L. Benton, M. T. Asom, R. Sauer and L. C. Kimerling, in *Identification of Interstitial Carbon Related Defects in Silicon*, edited by M. Stavola, S. J. Pearton and G. Davies (Mater. Res. Soc. Proc. **104**, Pittsburg, PA, 1988) pp. 85-91.

14 A. Hallen, B. U. R. Sundqvist, Z. Paska, B. G. Svenssen, M. Rosling and J. Tiren, J. Appl. Phys. **67**, 1266 (1990).

15 Yu.N. Erokhin, J. Ravi, C.W. White, G.A.Rozgonyi, Nucl. Instrum. Methods B **96**, 223 (1995).

16 J. F. Ziegler, J. P. Biersack and U. Littmark, in *The Stopping and Range of Ions in Solids*, Vol. 1, edited by J. F. Ziegler (Pergamon Press, New York, 1985).

17 P. Sigmund, Appl. Phys. Lett. **25**, 164 (1974).

18 K. Irmscher, H. Klose and K. Maass, J. Phys. C: Solid State Phys. **17**, 6317 (1984).

19 L. Palmetshofer and J. Reisinger, J. Appl. Phys. **72**, 2167 (1992).

TABLES

TABLE I. **Electronic properties of 1 keV He-ion bombardment induced defects in epitaxially grown n-Si**

Defect	E_t *(meV)*	σ_a *(cm^2)*	T_{peak} [(a)] *(K)*	$N_T(0)$ *(cm^{-3})*	L *(μm)*	*Similar defects*	T_{in} [(b)] *(°C)*	T_{out} [(c)] *(°C)*
EHe136	136±2	6.5×10^{-16}	77	3.0×10^{15}	0.029		27	300
EHe201	201±3	1.2×10^{-15}	107	1.6×10^{16}	0.023	Eα206	27	500
EHe296	296±3	5.8×10^{-16}	158	1.1×10^{16}	0.025		27	400
EHe411	411±4	1.4×10^{-16}	226			VP?	27	180
EHe554	554±4	5.8×10^{-16}	281	1.1×10^{16}	0.021		27	500

(a) Peak temperature at a lock-in amplifier frequency of 46 Hz, i.e. a decay time constant of 9.23 ms.

(b) Introduction tempertature.

(c) Temperature where defect was removed after isochronal (15 min. periods) annealing.

FIGURE CAPTIONS

FIG. 1. DLTS spectra of 1 keV [curve (a)] and 5.4 MeV [curve (b)] He-ion irradiated epitaxially grown n-Si. Curves were recorded at a lock-in frequency of 46 Hz (decay time constant of 9.23 ms), $V_r = 0.5$ V and $V_p = 0.5$ V.

FIG. 2. Variation of the electronic [$(dE/dr)_e$, dotted line], and nuclear [$(dE/dr)_n$, thin solid line], stopping powers, as well as the energy (thick solid line) of a He-ion with an initial energy of 5 MeV, with distance into Si (calculated from TRIM[16]). The inset is an enlargement of the end of range region. "A" indicates where $(dE/dr)_n$ exceeds 1 eV $Å^{-1}$ and "B" shows the value of $(dE/dr)_n$ for a 1 keV He ion.

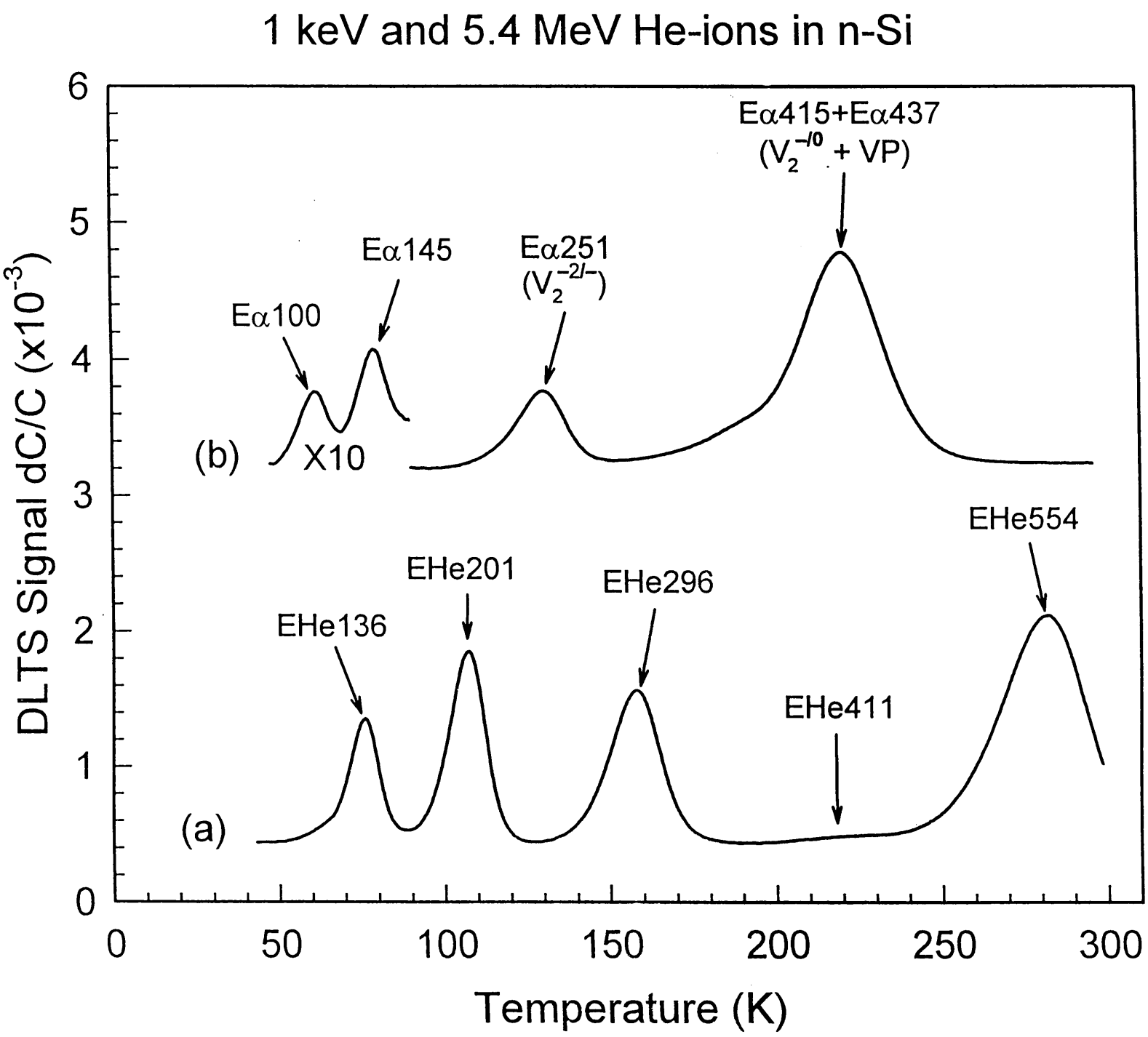

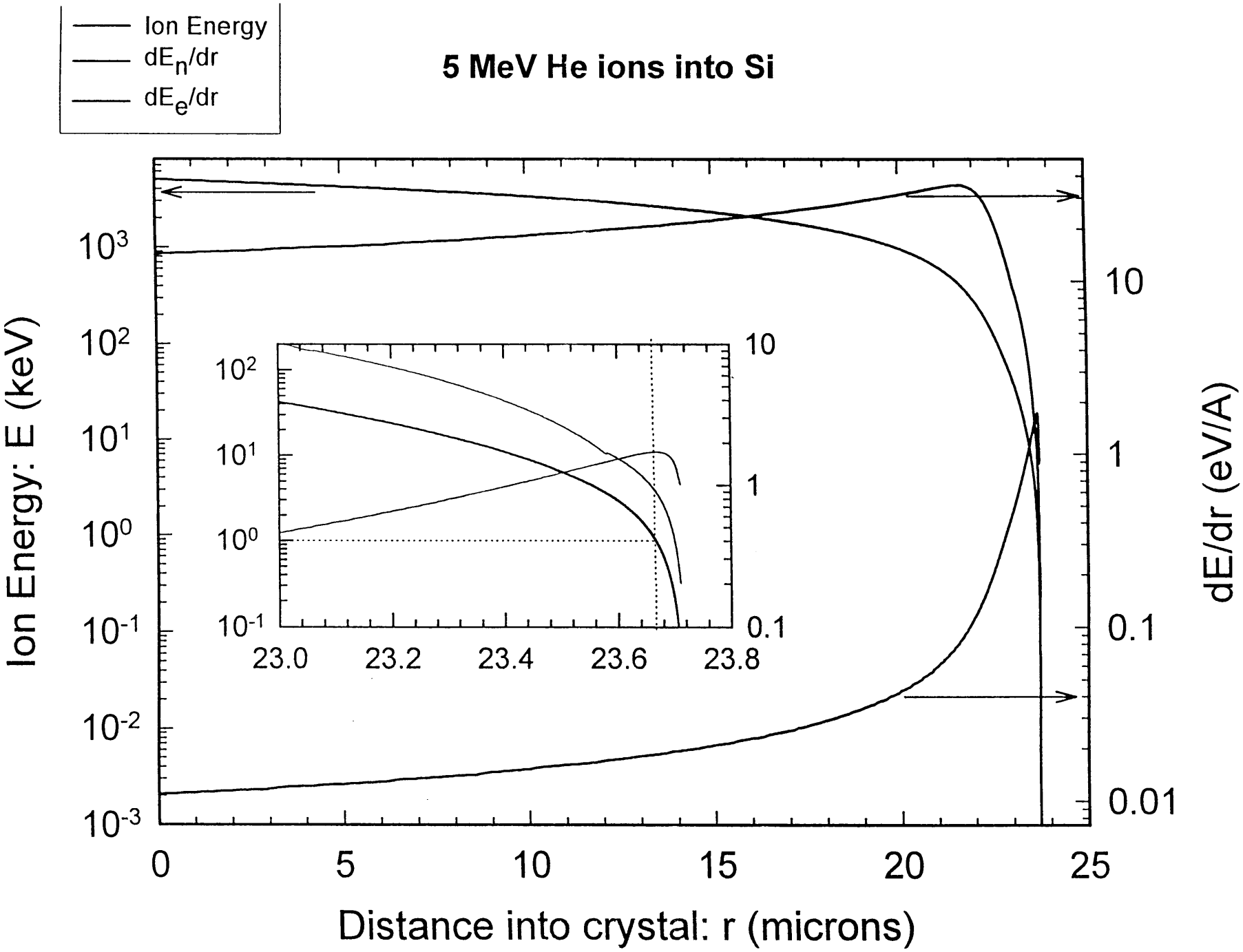

DLTS CHARACTERISATION OF 1 keV He, Ne and Ar ION BOMBARDED EPITAXIALLY GROWN n-Si

P.N.K. Deenapanray[1], F.D. Auret[1], G. Myburg[1], J.B. Malherbe[1], M.C. Ridgway[2] and S.A. Goodman[1]

[1]Department of Physics, University of Pretoria, Pretoria 0002, South Africa.
[2]Department of Electronic Materials Engineering, Australian National University, Canberra, ACT 2601, Australia

Abstract

We have investigated using deep level transient spectroscopy (DLTS) the electronic properties and isochronal annealing behaviour of the defects formed in epitaxially grown n-Si by 1 keV He-, Ne- and Ar-ion bombardment. We found that Ar-ion bombardment introduced a different set of defects compared to He- and Ne-ion bombardment, and have attributed this difference to their different stopping powers. Defects other than the VO and VP-centers detected in n-Si after high energy (5.4 MeV) alpha-particle implantation were observed after low-energy He-, Ne- and Ar-ion bombardment. A new class of related defects with energy levels at E_c - 0.203 eV (EHe203), E_c - 0.207 eV (ENe207) and E_c - 0.201 eV (EAr201) in our He-, Ne- and Ar-ion bombarded samples, respectively, were were found to be thermally stable up to ~400 °C. Annealing above 400 °C transformed them into a defect with energy level at E_c - 0.219 eV (He), E_c - 0.214 eV (Ne), and E_c - 0.219 eV (Ar). The latter defects were stable at 650 °C, and a comparison with isochronal annealing experiments on 5.4 MeV alpha-particle and $^{28}Si^{4+}$ implanted Si led us to conclude that they are high-order vacancy complexes. We have attributed EHe203, ENe207 and EAr201 to vacancy clusters smaller than the pentavacancy or to the incorporation of the noble gas species into these clusters.

I. INTRODUCTION

Noble gas ions with energies between 0.2-2 keV are routinely used during anisotropic ion beam etching (IBE) and reactive ion etching (RIE) of silicon. During these low-energy processes, energetic noble gas ions bombard the exposed semiconductor and create lattice damage. This damage alters the structural, electrical and optical properties of the semiconductor[1,2] and, therefore, affects the performance of devices fabricated on the etched surfaces. Changes in the electrical characteristics of Schottky barrier diodes (SBDs) fabricated on etched Si has shown that donor-type defects are introduced at and close to the metal-semiconductor interface which cause a lowering in barrier height of metal contacts on n-Si, whereas the opposite is observed for p-Si.[3,4] The changes in SBD characteristics have also been used to monitor the amount of damage induced in Si as a function of process parameters such as ion energy, sputtering yield (different noble gas species) and time of exposure and, in the case of plasma etching, also as a function of plasma pressure and etch rate.[5-7]

Photoluminescence (PL) measurements of silicon implanted with 20-350 keV noble gas ions (NGI) have shown that after annealing, energy shifts in the no-phonon (NP) peak of the well-known intrinsic I_1-defect (or W, 1.018 eV) occur.[8,9] These mass-dependent systematic line shifts were attributed to the incorporation of the noble gas ions into the intrinsic defect, constituting a class of related deep optical defects. Davis *et al*[10] later showed that identical shifts in the I_1-defect peak could be produced without annealing by low-energy noble gas ion bombardment of Si in the 200-2000 eV range. Furthermore, they proposed that some of the more complicated models such as, the extended pentavacancy cluster,[11,12] could not account for the I_1 defect. Sawyer and Weber[13,14] calculated the threshold energy necessary for the creation of a noble gas defect, and concluded that the noble gas-related defects could at most

contain 3 to 4 vacancies. On the basis of trigonal symmetry classification,[12] the intrinsic I_1-defect had been identified with the EPR Si-*A*3 centre - a trigonal tetravacancy cluster. However, based on theoretical modelling, Estreicher *et al*[15,16] have recently proposed that the 1018 meV line was due to the neutral divacancy and that the shifted I_1 peaks were due to the incorporation of the noble gas atoms into the neutral divacancies. Although there are uncertainties concerning the physical structure of the intrinsic I_1 defect, all the PL studies have concluded that the radiative recombination originates at impurity centres with deep energy levels. The deep energy levels E_c - 0.22 eV, E_c - 0.24, and E_v + 0.18 have been reported to be present in silicon implanted with noble gas ions.[17] Furthermore, Lalita *et al*[18] have given ample evidence for high-order vacancy complexes causing the E_c - 0.22 eV and E_c - 0.47 eV levels in 5.6 MeV $^{28}Si^{3+}$ implanted n-type Si at temperatures above 300 °C.

In order to understand the effect of defects induced during low energy NGI bombardment on the electrical properties of Si, it is necessary to know their electrical properties and structure. Furthermore, the annealing behaviour of these defects must be established so that their deleterious effects on material properties can be removed through post-bombardment high temperature treatments. Whilst most of the previous studies have investigated the changes in optical and structural properties of NGI-bombarded Si, little is known about the electrical properties and annealing behaviour of the low-energy NGI-induced defects. In this study, we report the electronic properties, determined by deep level transient spectroscopy (DLTS), and annealing behaviour of defects introduced in epitaxially grown n-Si by 1 keV He-, Ne- and Ar-ion bombardment. We demonstrate that vacancy clusters, which may be larger than the divacancy and smaller than the pentavacancy, are produced during the

low-energy NGI bombardment, and that the possibility of the implanted noble gas atoms becoming incorporated into these higher-order vacancy clusters cannot be excluded.

II. EXPERIMENT

P-doped (to $5x10^{15}$ cm^{-3}) n-type (111) oriented, 4-5 μm thick Si layers containing C and O, grown by chemical vapour deposition (CVD) on P-doped n^+-substrates, were used in this study (referred to as CO-Si in subsequent discussions). In order to investigate the influence of impurities such as C and O on some defects, we also used CVD grown n-type (100) oriented epitaxial Si layers (~3 μm), doped to $3x10^{16}$ cm^{-3} with P and with low C and O contents, on n^+-substrates. This low C and O containing n-Si will, hereafter, be referred to as HP-Si. After chemical cleaning, the epitaxial sides of the samples were bombarded to a fluence of $1x10^{12}$ cm^{-2} with 1 keV He, Ne and Ar ions at a dose rate of $1x10^{11}$ $cm^{-2}s^{-1}$. Other samples were irradiated with 5.4 MeV alpha-partilces and 5.4 MeV $^{28}Si^{4+}$ ions. The 1 keV bombardments were performed using an ion gun, while an ^{241}Am radionuclide was used as a source of 5.4 MeV alpha-particles (dose rate ~ $7.1x10^6$ $cm^{-2}s^{-1}$). The 5.4 MeV ^{28}Si implantations were done in a 1.7 MV NEC Tandem ion implanter at the Australian National University to fluences of $1x10^9$ cm^{-2} (CO-Si) and $2x10^{10}$ cm^{-2} (HP-Si) using a beam current of ~1 nA. After irradiation, circular Pd contacts, 100 nm thick and 0.77 mm in diameter, were deposited on the bombarded surface by resistive evaporation.

DLTS was used to study the bombardment-induced defects. The DLTS "signatures" (energy level, E_T, and apparent capture cross-section, σ_a) of the defects were determined from DLTS Arrhenius plots of log (e/T^2) vs $1/T$, where e is the emission rate at a temperature T. The "signatures" of the defects were extracted at a quiescent bias, $V_r = 1$ V, and a filling pulse,

V_p = 1.4 V. The high quiescent bias and pulse used here ensured optimization of the DLTS signal and did not affect the peak positions of the prominent defects. Isochronal annealing experiments were conducted on the irradiated samples from 100 °C to 650 °C in steps of 50 °C. The samples were annealed under Ar-flow at zero bias and for 20 min periods. DLTS was then used to monitor the intensities of the defects at V_r = 1 V and V_p = 1.6 V, as well as the detection of secondary defects introduced during annealing.

III. RESULTS

DLTS spectra of CO-Si bombarded with 1 keV He-, Ne- and Ar-ions to a fluence of $1x10^{12}$ cm^{-2} are shown in curves (b), (c) and (d) of Fig. 1, respectively. The defects are, for instance labelled as EHe178, where "E" denotes an electron trap, "He" for helium and "178" to the position in meV of the level below the conduction band. Curves (b) and (c) of Fig.1 reveal that a similar set of defects is introduced in low-energy He- and Ne-ion bombarded CO-Si. The peak intensities of the defects introduced by Ne ions are, however, larger in magnitude compared to those created by He ions. On the other hand, Ar-ion bombardment is found to create a more complex set of defects [Fig. 1(d)]. These observations are discussed and clarified later. In order to know more about the structure of the defects created by the NGI, we have compared their electronic properties to those of the primary defects (V_2, VO- and VP-pairs) produced by MeV electron or alpha-particle irradiation.[19,20] The DLTS spectrum of 5.4 MeV alpha-particle irradiated CO-Si is illustrated in Fig. 1(a), and shows the peaks corresponding to the VO-centre, $V_2^{=/-}$ (first charge state of the divacancy), and that due to the superposition of the VP-pair and $V_2^{-/0}$ (second charge state of the divacancy). The activation energy of $V_2^{-/0}$ was extracted after removing the VP-pair by annealing at 200 °C for 20 min.

The Arrhenius plots from which the activation energies, E_T, and apparent capture cross-sections, σ_a, of the NGI-induced defects were extracted are depicted in Fig. 2.

It is evident from Figs. 1 and 2 that the 1 keV ion bombardments introduced the VO-centre, which introduces an energy level at ~0.18 eV below the conduction band. The DLTS peaks located below 80 K are due to the well-known C_i-C_s and C_s-Si_i-C_s defects.[21] However, no direct evidence can be obtained for the presence of $V_2^{=/-}$ in these samples. Furthermore, the peak corresponding to the superimposed VP-pair and $V_2^{-/0}$ is relatively small in the low-energy NGI-bombarded samples compared to high-energy alpha-particle irradiation, and is masked by other defect peaks which we have not yet identified. A set of prominent electron traps, located at ~110 K (at a lock-in amplifier frequency of 46 Hz, i.e., a decay time constant of 9.23 ms), with energy levels at E_c - 0.203 eV (EHe203), E_c - 0.207 eV (ENe207) and E_c - 0.201 eV (EAr201) is also observed in samples bombarded with He, Ne and Ar ions, respectively. The annealing behaviour of this set of electrically active defects will be discussed in further detail below. Another pertinent remark concerns the ratio of the peak DLTS intensities of EHe203, ENe207 and EAr201 to that of the VO-centre in the respective samples. It is inferred from Fig. 1 that this ratio increases with increasing mass number of bombarding ions. The signal intensity of the VO-centre is also found to increase with increasing bombarding ion mass.

Figure 3 illustrates the DLTS spectra of 1 keV He-ion bombarded HP-Si [curve (c)] as well as those of 5.4 MeV $^{28}Si^{4+}$ implanted CO-Si and HP-Si [curves (b) and (d), respectively]. The spectrum for 1 keV He-ion bombarded CO-Si [Fig. 3(a)] has also been included for reference purposes. Due to the low C and O content in the HP-Si samples, the corresponding spectra do not show the presence of the VO-centre nor of the low-temperature C-related

peaks. Figure 3 shows that the defect with a peak at ~110 K is introduced in all the samples, which indicates that it is not related to C or O. A similar defect, labelled ESi198, is found to have an energy level at E_c - 0.198 eV in both CO- and HP-Si implanted with 5.4 MeV ^{28}Si.

Isochronal annealing experiments showed that the defect with a DLTS peak at ~110 K (at a lock-in amplifier frequency of 46 Hz) is stable up to ~450 K. In this temperature range, a set of secondary defects with energy levels at E_c - 0.219 eV (EHe219), E_c - 0.214 eV (ENe214) and E_c - 0.219 eV (EAr219) emerged in the annealed samples. Curves (a) through to (d) in Figure 4 depict the DLTS spectra of 1 keV He-ion bombarded CO-Si after annealing at 350 °C, 450 °C, 500 °C and 650 °C, respectively. It should be noted that EHe203 has a peak temperature of ~105 at a lock-in amplifier frequency of 22 Hz. Spectra (a), (b) and (c) also show that 1 keV He-ion bombardment of CO-Si introduces a defect EHe584, which appears to have similar thermal properties as EHe203. We have not yet identified this defect. The broad peak contained in Fig. 4(d) could be due to either an artefact caused by the degraded metal-semiconductor interface at 650 °C or the presence of extended defects which introduces a continuous band of defects in the band gap. EHe203 and EHe219 were observed to have the same annealing properties in HP-Si (not shown). Figure 5 shows the DLTS spectra of Ar- (LIA frequency of 46 Hz) and Ne-ion (LIA frequency of 22 Hz) bombarded CO-Si annealed at 400 °C and 500 °C, respectively. The spectra corresponding to 400 °C [curves (a) and (c)] show a high-temperature shoulder on the peak at ~110 K which indicates the emergence of a secondary peak. This latter defect is fully resolved at 500 °C, and its intensity is also observed to increase with the removal of the "110 K"-peak. Furthermore, Fig. 5(c) reveals that Ne-ion bombarded CO-Si contains a defect labelled ENeX, which has similar annealing characeristics as ENe207. Since the peak temperature of ENeX is almost the same

as that of EHe584, it is possible that they are structurally similar. The DLTS spectra of 5.4 MeV alpha-particle irradiated CO-Si [curves (a) and (c)] and HP-Si [curves (b) and (d)] annealed at 350 °C and 500 °C are illustrated in Fig. 6, while Fig. 7 shows the spectra of $^{28}Si^{4+}$ implanted CO-Si annealed at 400 °C and 550 °C. It can be seen from Fig. 6 that a defect Eα201 is produced after annealing between 300-350 °C and that its intensity increased as the two charge states of the divacancy annealed out. Furthermore, Eα201 is transformed into a defect Eα211 above 450°C. These results indicate that Eα201 and EHe201 are identical defects. The fact that ESi198 has similar electronic properties and annealing behaviour as EHe201 further indicate that they have similar structures. These results also show that the creation of the defect with a DLTS peak at ~110 K depends strongly on the amount of energy deposited through elastic recoils and is independent of C and O content.

The "signatures" of the most prominent defects created by the 1 keV NGI are listed in Table I. If defects have similar electrical properties and annealing behaviour to one another, it is indicated in the last column of the table. As the peaks are closely spaced, it was difficult to determine the positions of the peaks exactly, and consequently the error in the defect "signatures" is somewhat larger than would otherwise be expected.

IV. DISCUSSION

In order to explain why 1 keV NGI create different sets of defects compared to 5.4 MeV alpha-particles, we consider the energy loss mechanisms of these ions. The 5.4 MeV alpha-particles lose their energy predominantly by electronic stopping and, therefore, create isolated Frenkel pairs in the region probed by DLTS in this study. The fast diffusing single-vacancies are either trapped by impurities such as interstitial O and P to form VO- and VP-

pairs, or combine to form divacancies, V_2 [curve (a) in Fig. 1]. On the other hand, the low energy noble gas ions lose their energy predominantly by nuclear stopping on entering the target. The projected range, R_p, of the 1 keV ions and their nuclear energy, $(dE/dx)_n$, deposited in Si as calculated from TRIM[22] simulations are summarised in Table II. This table also gives the half-angle for channeling, $\Psi_{1/2}$, of the 1 keV ions. In this low-energy regime, the collision cascades are much denser so that the trail of an ion is characterised by large vacancy aggregates. These vacancy clusters are created either by the combination of several single-vacancies trapped in the highly damaged area or in single events. For instance, during almost the entire range of a 1 keV He ion in Si, it transfers at least 1.2 eV/Å to the lattice through elastic recoils (Table II), which is above the threshold value required for the onset of "spike" formation[23] - a non-linear effect producing extended defects, such as vacancy clusters. In fact, non-linear effects in implanted Si have previously been reported for ion energy losses as low as ~0.1 eV/Å.[24]

The displaced lattice atoms (self-interstitials) are either projected deeper into the material through momentum transfer or annihilated via recombination with vacancies or diffuse away from the highly damaged area. Abdullin *et al*[25] have shown that Si interstitials (Si_i) introduced two energy levels at E_c - 0.39 eV ($Si_i^{0/+}$ - neutral state of Si_i) and E_c - 0.25 eV ($Si_i^{+/++}$) in CZ and FZ p-Si irradiated with 4.7 MeV alpha-particles. The latter level is observed only after minority carrier injection using optical excitation. However, these levels are not detected in n-type Si because the neutral state of Si_i is ionized, and is annealed between 160-170 K owing to thermal charge transfer. Due to the large values of $\Psi_{1/2}$ of the low energy ions together with the fact that the ion dose used here is much less than the threshold for amorphisation, some of the 1 keV ions may channel deeper into the material.

These ions will, therefore, produce higher-order defects beyond the projected range given in Table II. In fact, IBE and RIE using low energy ions have shown that the processing-induced defects migrate to depths as large as 1 μm below the surface.[14,26] Vacancy-enhanced migration[15] and recombination-enhanced diffusion[26] models have been proposed to explain the long range defect diffusion.

Where the low energy ions come to rest they may be incorporated in the vacancy clusters, which is supported by the PL observations discussed above. Furthermore, since the concentration of V_2 is very low in our 1 keV ion bombarded samples, we propose that some defects observed in these samples are related to vacancy clusters or the incorporation of the noble gas atoms into these clusters and V_2. The differences between the DLTS spectra of 1 keV He-, Ne- and Ar-ion bombarded Si is attributed to the increased nuclear energy deposited to the lattice with increasing bombarding ion mass. Table II shows that the nuclear stopping of Ar ions is much higher than for He- and Ne-ions, suggesting that the former may produced larger vacancy clusters than He- and Ne-ions. Hence, the more complex DLTS spectrum [Fig. 1(d)] of 1 keV Ar-ion bombarded Si. The larger nuclear energy deposited by Ne-ions compared to He-ions is translated into the intensities of the DLTS peaks in Fig. 1(c) being larger than in Fig. 1(b).

Now we present evidence for the formation of either noble gas related defects or vacancy clusters larger than V_2 in our 1 keV noble gas ion bombarded samples. Figure 3 shows that the formation of EHe203 is not influenced by the O or C content in the starting material. Since ESi198 has similar electronic properties [Fig. 3(b) and (d)] and annealing behaviour (Fig. 7) as EHe203, we conclude that they have similar structures. It can also be concluded from these results that ESi198 is an intrinsic defect. The results shown in Fig. 4 and

Fig. 5 further reveal that EHe203, EAr201 and ENe207 constitute a class of similar electrically active defects which have similar structural properties as the intrinsic ESi198 defect.

Based on theoretical modelling, it has been suggested that the intrinsic I_1 defect is due to the neutral divacancy and that the noble gas- (NG) related defects observed using PL are caused by the incorporation of the noble gas atoms into the neutral divacancy.[15] Although it has been shown, in qualitative terms, that the neutral V_2, as well as the NG-V_2 complexes, introduce energy levels in the bandgap, no definite activation energies have been postulated for these defects.[15,27] Since the variances in the activations energies of the DLTS peak located at ~110 K (at a frequency of 46 Hz) in our 1 keV He-, Ne- and Ar-ion bombarded samples are well within the experimental error (± 5 meV), it is not possible here to certify whether these meV energy shifts could be similar those in refs. 8 and 14. However, these PL studies have revealed that the luminescence line corresponding to He is unstable above 300 °C, while that of Ne anneals out at 350 °C. The DLTS spectra depicted in Figs. 4 and 5 clearly demonstrate that EHe201 and ENe207 are thermally stable up to at least 450 °C, and cannot, therefore, be similar to the noble-gas related defects observed by PL. Hence, the non-detection or low concentrations of $V_2^{=/-}$ and $V_2^{-/0}$ in our 1 keV noble gas ion-bombarded samples cannot be explained by the incorporation of the noble-gas atoms in V_2. Since the NG-related centres are passivated by hydrogenation, and the reaction is reversible by annealing around 350 °C,[15] we plan to study the effect of low-energy hydrogen bombardment as well as MeV proton irradiation on EHe203, ENe207 and EAr201.

The results shown in Fig. 6 unambiguously demonstrate that Eα201 is produced in our 5.4 MeV alpha-particle irradiated n-Si by annealing above 300 °C. Because of their similar

electronic properties and annealing behaviour we propose that EHe203, and hence ENe207 and EAr201 to be the same defect as Eα201. Since V_2 is known to be highly mobile at ~300 °C[28,29] and that Eα201 grows at the expense of the two charge states of the V_2, we conclude that Eα201 is due to defect reactions involving divacancies. This together with the fact that very low concentrations of V_2 are present in our noble gas bombarded samples, imply that EHe203, ENe207 and EAr201 are most probably due to the tetravacancy (V_4) or pentavacancy (V_5). Divacancies could be formed directly in collision cascades during 1 keV noble gas ion bombardment of Si together with the formation of single-vacancies. Combinations of V_2 and V can then give rise to V_4 and V_5. Some of the single-vacancies are efficiently trapped by interstitial O to form the VO-pair. The fact that the ratio of the peak DLTS intensities of EHe203, ENe207 and EAr201 to that of the VO-pair increase with bombarding ion mass, suggest, as expected, that the formation of these higher-order vacancy clusters is increased when the nuclear energy deposited increases.

Finally, the possibility of noble gas atoms becoming incorporated into these higher-order vacancy clusters cannot be completely excluded. Our annealing studies further demonstrate that secondary defects are created by annealing the 1 keV noble gas bombarded samples above 450 °C. Because of their high thermal stability, we propose that EHe211, ENe214 and EAr219 are due to complexes involving vacancy clusters larger than V_4 and V_5. The presence of EAr219 in unannealed 1 keV Ar-ion bombarded CO-Si [Fig. 1(d)] suggest than vacancy clusters larger than those responsible for EAr201 may be produced when the nuclear energy loss becomes significant. The DLTS spectrum of 1 keV He-ion bombarded HP-Si features a prominent peak with an energy level at E_c - 0.552 eV which is thermally stable up to around 500 °C. Based on the fact that this level is not predominant in our low

energy ion bombarded CO-Si and has been found to be stable up to only ~200 °C in 75 keV He-implanted Si containing O,[30] we conclude that this level was most probably due to the trivacancy (V_3) or complexes thereof.[31] The somehow similar electronic properties of EHe341, ENe347 and EAr310 may suggest that they are also structurally similar. Furthermore, these defects could be similar to a H-related complex observed in MeV proton irradiated n-Si by Hallen *et al*[32]. We expect our low and high energy hydrogen irradiation studies referred to above to elucidate this speculation.

V. CONCLUSION

We have used DLTS in conjunction with isochronal annealing experiments to investigate the electronic properties and annealing behaviour of the defects introduced in n-Si by 1 keV He-, Ne- and Ar-ion bombardment. Our results have shown that most of the defects introduced by the low energy noble gas ions are different from the primary defects created by 5.4 MeV alpha-particle irradiation. Furthermore, V_2 was found to be present in very low levels in the 1 keV ion bombarded samples. Based on isochronal annealing experiments of the low energy noble gas bombarded n-Si, as well as of samples irradiated with 5.4 MeV alpha-particles and $^{28}Si^{4+}$, we have concluded that one of the defects introduced by the noble gas ions (EHe203, ENe207 and EAr201) is due to the tetravacancy (V_4) or the pentavacancy (V_5). This defect was stable up to around 450 °C after which it annealed into a secondary defect, which we propose to be a complex involving vacancy clusters larger than V_4 and V_5. The increase in the ratio of the DLTS peak intensity of EHe203, ENe207 and EAr201, respectively, to that of the VO-pair, with increasing bombarding ion mass, furthers suggest that the concentration of vacancy clusters, such as V_4 and V_5, increases with an increase in

nuclear energy deposited. The presence of a defect EAr219 in unannealed 1 keV Ar-ion bombarded n-Si implies that defect complexes involving vacancy clusters larger than V_4 and V_5 could be produced when the nuclear energy deposited by the noble gas ions becomes significant.

TABLE CAPTIONS

TABLE I Electronic properties of defects introduced by 1 keV He-, Ne- and Ar-ions, and 5.4 MeV alpha-particles in epitaxially grown CO-Si.

TABLE II Summary of projected range, R_p, energy lost to recoil atoms in Si, $(dE/dx)_n$ and half-angle for channeling, $\Psi_{1/2}$, of 1 keV He, Ne and Ar ions.

FIGURE CAPTIONS

FIG. 1 DLTS spectra of CO-Si bombarded with: (a) 5.4 MeV alpha-particles, (b) 1 keV He-ions, (c) 1 keV Ne-ions and (d) 1 keV Ar-ions. A fluence of $1x10^{12}$ cm^{-2} was used in the low energy bombardments. The spectra were recorded at a lock-in amplifier frequency of 46 Hz using a quiescent bias, V_r = 1 V, and a filling pulse, V_p = 1.6 V.

FIG. 2 Comparison of DLTS signatures of low-energy He-, Ne- and Ar-ion induced defects in CO-Si with those of the primary defects produced by 5.4 MeV alpha-particle irradiation.

FIG. 3 DLTS spectra of: (a) 1 keV He-ion bombarded CO-Si, (c) 1 keV He-ion bombarded HP-Si, and 5.4 MeV $^{28}Si^{4+}$ implanted CO-Si [curve(b)] and HP-Si [curve(d)]. The spectra were recorded using a lock-in amplifier frequency of 46 Hz, and V_r = 1 V and V_p = 1.6 V.

FIG. 4 Illustrates the isochronal annealing behaviour of EHe203. DLTS spectra (a) through to (d) correspond to annealing temperatures of 350 °C, 450 °C, 500 °C and 650 °C, respectively. Samples were annealed for 20 min periods under Ar flow and zero bias, and the spectra were recorded at a lock-in amplifier frequency of 10 Hz.

FIG. 5 DLTS spectra of 1 keV Ar- and Ne-ion bombarded CO-Si corresponding to annealing temperatures of 400 °C [curves (a) and (c)] and 550 °C [curves (b) and (d)]. Lock-in amplifier frequencies of 46 Hz and 10 Hz were employed to obtain the Ar and Ne spectra, respectively.

FIG. 6 Isochronal annealing behaviour of the primary defects induced by 5.4 MeV alpha-particle irradiation of CO- and HP-Si. A defect Eα201 is observed to emerge after annealing above 300 °C in both samples [curves (a) and (b) for CO- and HP-Si, respectively], while curves (c) [CO-Si] and (d) [HP-Si] demonstrate that Eα211 is the dominant defect after annealing at 500 °C.

FIG. 7 DLTS spectra of unannealed [curve (a)] 5.4 MeV $^{28}Si^{4+}$ implanted CO-Si, and annealed at 400 °C and 550 °C [curves (b) and (c), respectively]. A lock-in amplifier frequency of 46 Hz was used.

Table I

Noble gas species	Projected range R_p, Å	Nuclear energy loss $(dE/dx)_n$, (eV/Å/ion)	Half-angle $\Psi_{1/2}$, (degree)
He	170	1.2	~ 18
Ne	40	18	~ 35
Ar	34	31	~ 43

Table II

Ion and Energy	*Defect*	E_t (meV)	σ_a (cm^2)	T_{peak} (a) (K)	*Similar defects*
He: 1 keV	EHe087	087±2	$8.2x10^{-16}$	51	
	EHe113	113±2	$3.6x10^{-15}$	60	C_i-C_s
	EHe178	178±2	$7.5x10^{-16}$	93	VO
	EHe203	203±3	$1.1x10^{-15}$	108	EAr201/ENe207
	EHe341	341±4	$1.0x10^{-15}$	176	EAr310/ENe347
	EHe390	390±4	$6.3x10^{-17}$	225	EAr377 ?
Ne: 1 keV	ENe098	098±2	$4.4x10^{-17}$	65	C_i-C_s
	ENe183	183±2	$1.8x10^{-15}$	94	VO
	ENe207	207±3	$4.8x10^{-15}$	109	EHe203/EAr201
	ENe347	347±4	$1.9x10^{-15}$	174	EHe341/EAr310
	ENe437	437±5	$4.5x10^{-15}$	208	VP?
	ENe446	446±5	$4.4x10^{-16}$	232	
Ar: 1 keV	EAr098	098±2	$6.6x10^{-17}$	64	C_i-C_s
	EAr126	126±2	$2.2x10^{-16}$	76	
	EAr178	178±2	$7.5x10^{-16}$	93	VO
	EAr201	201±3	$9.7x10^{-16}$	108	EHe203/ENe207
	EAr219	219±4	$1.4x10^{-16}$	128	
	EAr288	288±4	$1.1x10^{-15}$	149	
	EAr310	310±4	$1.6x10^{-16}$	174	EHe341/ENe347
	EAr377	377±5	$1.1x10^{-17}$	235	EHe390 ?
He: 5.4 MeV	Eα178	178±2	$7.5x10^{-16}$	93	VO
	Eα251	251±3	$1.3x10^{-15}$	131	$V_2^{=/-}$
	Eα415	415±4	$1.9x10^{-16}$	226	$V_2^{-/0}$
	Eα437	437±4	$2.4x10^{-15}$	217	VP

(a) Peak temperature at a lock-in amplifier frequency of 46 Hz, i.e. a decay time constant of 9.23 ms.

REFERENCES

1 S.J. Fonash, Solid State Technol. **28**, 201 (1985).

2 G.S. Oehrlein, Materials Science and Engineering B **4**, 441 (1989).

3 F.H. Mullins and A. Brunnschweiler, Solid-State Electron. **19**, 47 (1976).

4 S.J. Fonash, S. Ashok and R. Singh, Appl. Phys. Lett. **39**, 423 (1981).

5 M. Hirai, H. Iwakuro, J. Ohno and T. Kuroda, IEEE Transactions on Components, Hybrids, and Manufacturing Technology **13**, 629 (1990).

6 O.O. Awadelkarim, T. Gu, P.I. Mikulan, R.A. Ditizio and S.J. Fonash, Appl. Phys. Lett. **62** (9), 958 (1993).

7 M. Balooch, M. Moalem, Wei-E. Wang and A.V. Hamza, J. Vac. Sci. Technol. A **14**, 229 (1996).

8 N. Burger, K. Thonke, R. Sauer and G. Pensl, Phys. Rev. Lett. **52**, 1645 (1984).

9 V.D. Tkachev, A.V. Mudryi and N.S. Minaev, Phys. Status Solidi A **81**, 313 (1984).

10 R.J. Davis, H.-U. Habermeier and J. Weber, Appl. Phys. Lett. **47**, 1295 (1985).

11 C.G. Kirkpatrick, J.R. Noonan, and B.G. Streetman, Radiat. Eff. **30**, 97 (1976).

12 N.S. Minaev, A.V. Mudryi and V.D. Tkachev, Phys. Status Solidi B **108**, K 89 (1981).

13 W.D. Sawyer, J. Weber, G. Nabert, J. Schmalzlin, H.-U. Habermeier, J. Appl. Phys. **68**, 6179 (1990).

14 J. Weber, Physica B **170**, 201 (1991).

15 S.K. Estreicher, J. Weber, A. Derecskei-Kovacs and D.S. Marynick, Phys. Rev. B **55**, 5037 (1997).

16 S.K. Estreicher, J.L. Hastings and P.A. Fedders, Appl. Phys. Lett. **70**, 432 (1997).

17 V.D. Tkachev, A.V. Mudryi and N.S. Minaev, Phys. Stat. Sol. A **81**, 313 (1985).

18 J. Lalita, B.G. Svensson and C. Jagadish, Nucl. Instrum. Methods B **96**, 210 (1995).

19 J.R. Troxell, Solid-State Electronics **26**, 539 (1983).

20 S.D. Brotherton and P. Bradley, J. Appl. Phys. **53**, 5720 (1982).

21 L.C. Kimerling, M.T. Asom, J.L. Benton, P.J. Drevinsky and C.E. Caefer, Materials Science Forum **38-41**, 141 (1989).

22 J.F. Ziegler, J.P. Biersack and U. Littmark, "The Stopping and Range of ions in Solids", vol. 1, ed. J.F. Ziegler, Pergamon Press, New York, 1985.

23 P. Sigmund, Appl. Phys. Lett. **25**, 164 (1974).

24 D.A. Thompson and R.S. Walker, Rad. Effects **36**, 91 (1978).

25 Kh.A. Abdullin, B.N. Mukashev, M.F. Tamendarov abd T.B. Tashenov, Mat. Res. Soc. Symp. Proc. **262**, 1109 (1992).

26 J.L. Benton, B.E. Weir, D.J. Eaglesham, R.A. Gottscho, J. Michel and L.C. Kimerling, J. Vac. Sci. Technol. B **10**, 540 (1992).

27 Hyangsuk Seong and L.J. Lewis, Phys. Rev. B **53**, 9791 (1996).

28 A.O. Evwaraye and E. Sun, J. Appl. Phys. **47**, 3776 (1976).

29 B.G. Svensson, K. Johnsson, D-X. Xu, J.H. Svensson and J.L. Lindström, Rad. Eff. and Def. in Solids **111-112**, 439 (1989).

30 Yu.N. Erokhin, J. Ravi, C.W. White and G.A. Rozgonyi, Nucl. Instrum. Methods B **96**, 223 (1995).

31 F.D. Auret, P.N.K. Deenapanray, S.A. Goodman, W.E. Meyer and G. Myburg, unpublished.

32 A. Hallen, B.U.R. Sundqvist, Z. Paska, B.G. Svensson, M. Rosling and J. Tiren, J. Appl. Phys. **67**, 1266 (1990).

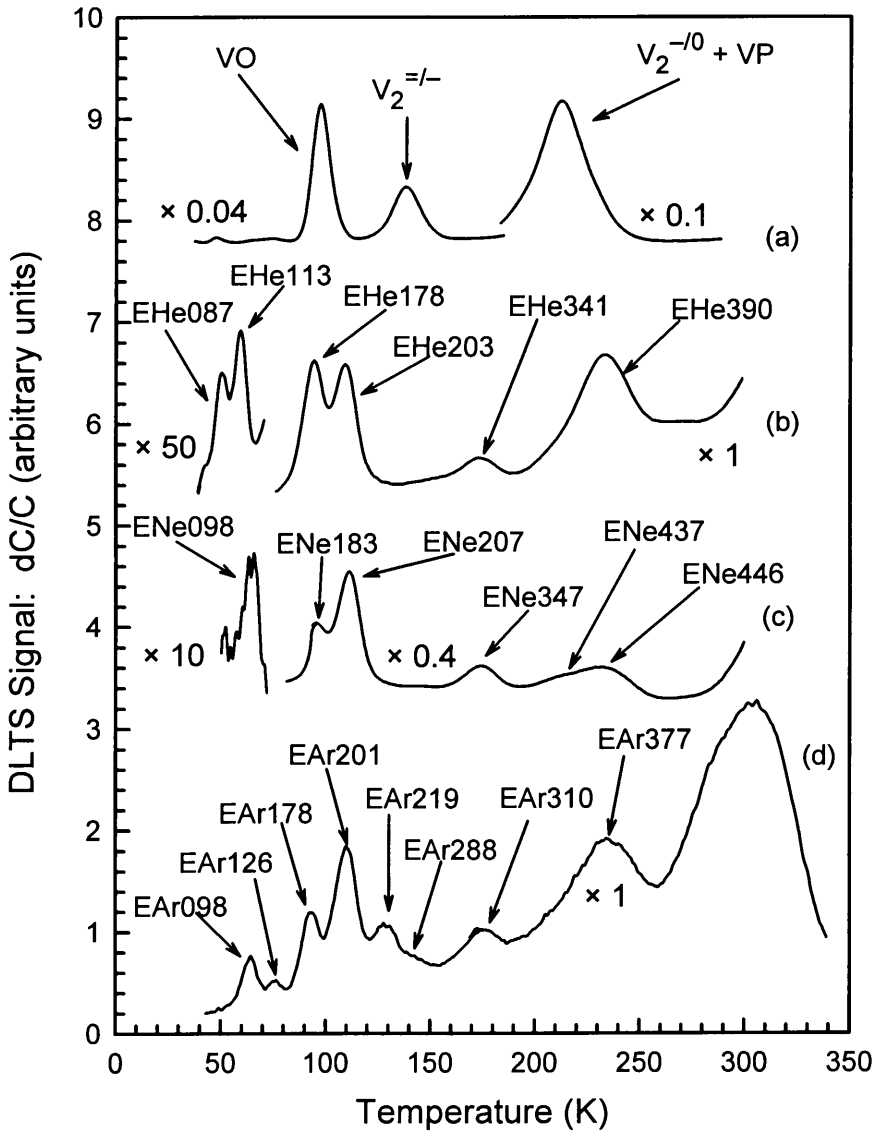

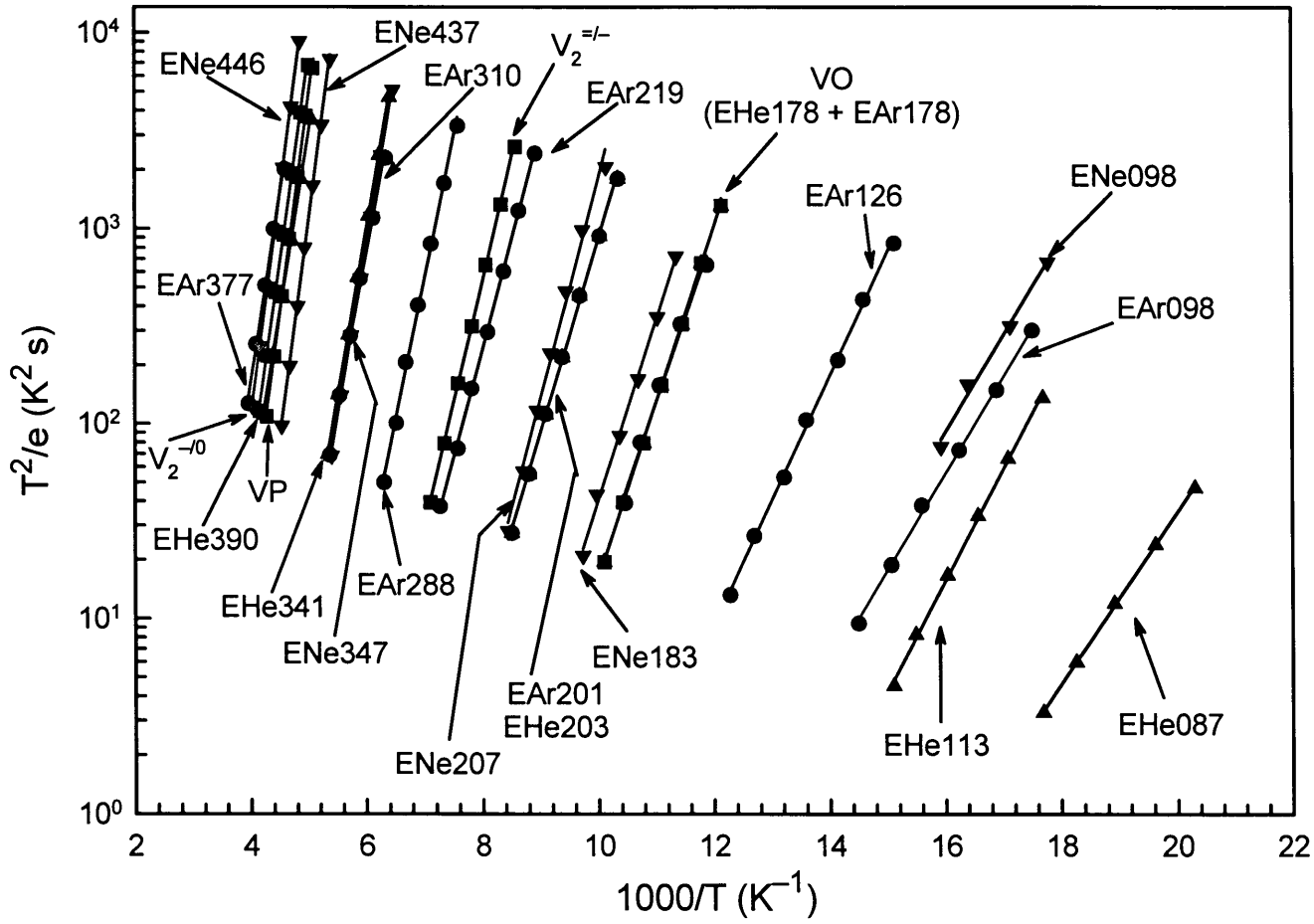

P.N.K. Deenapanray et al Fig. 2 of (7)

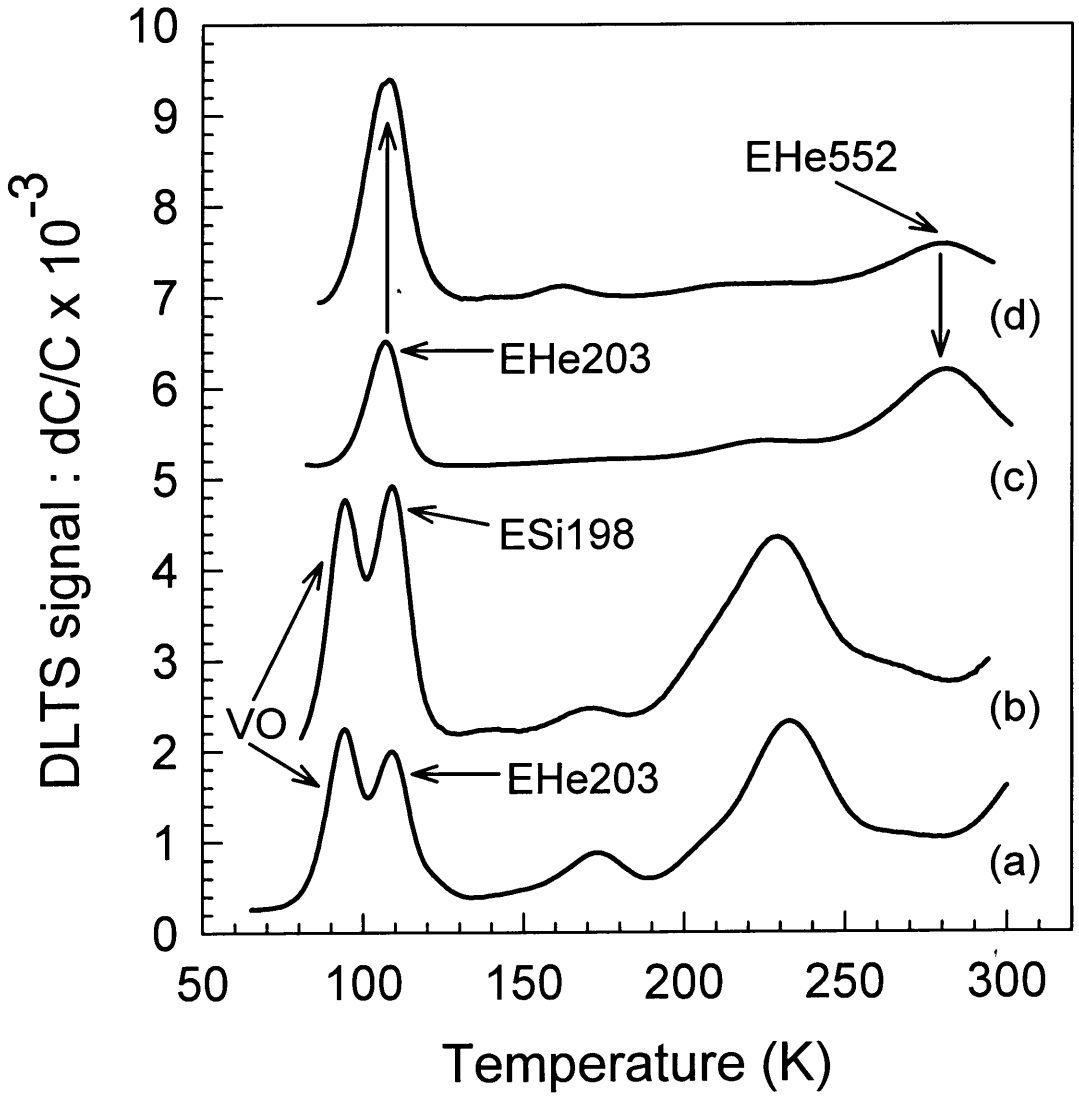

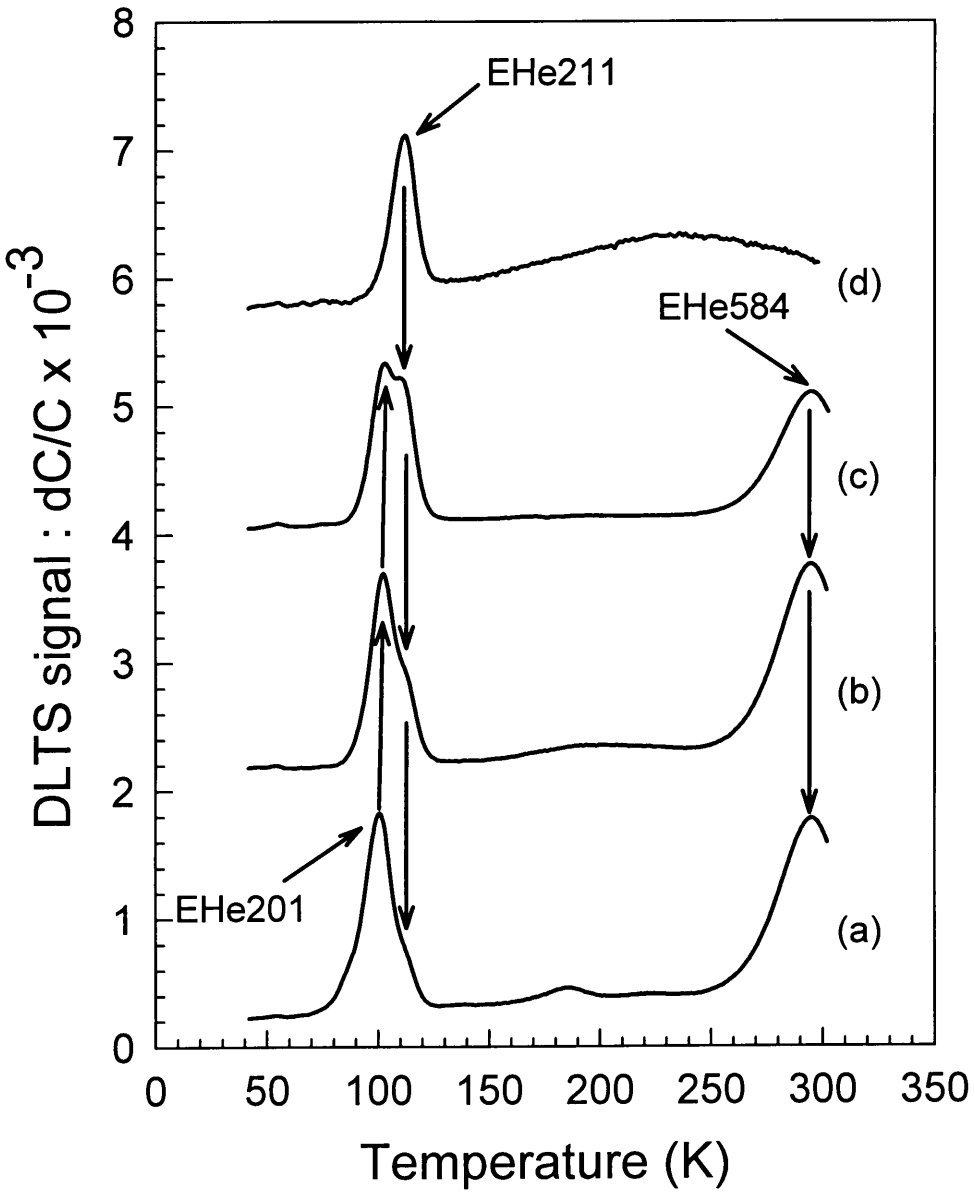

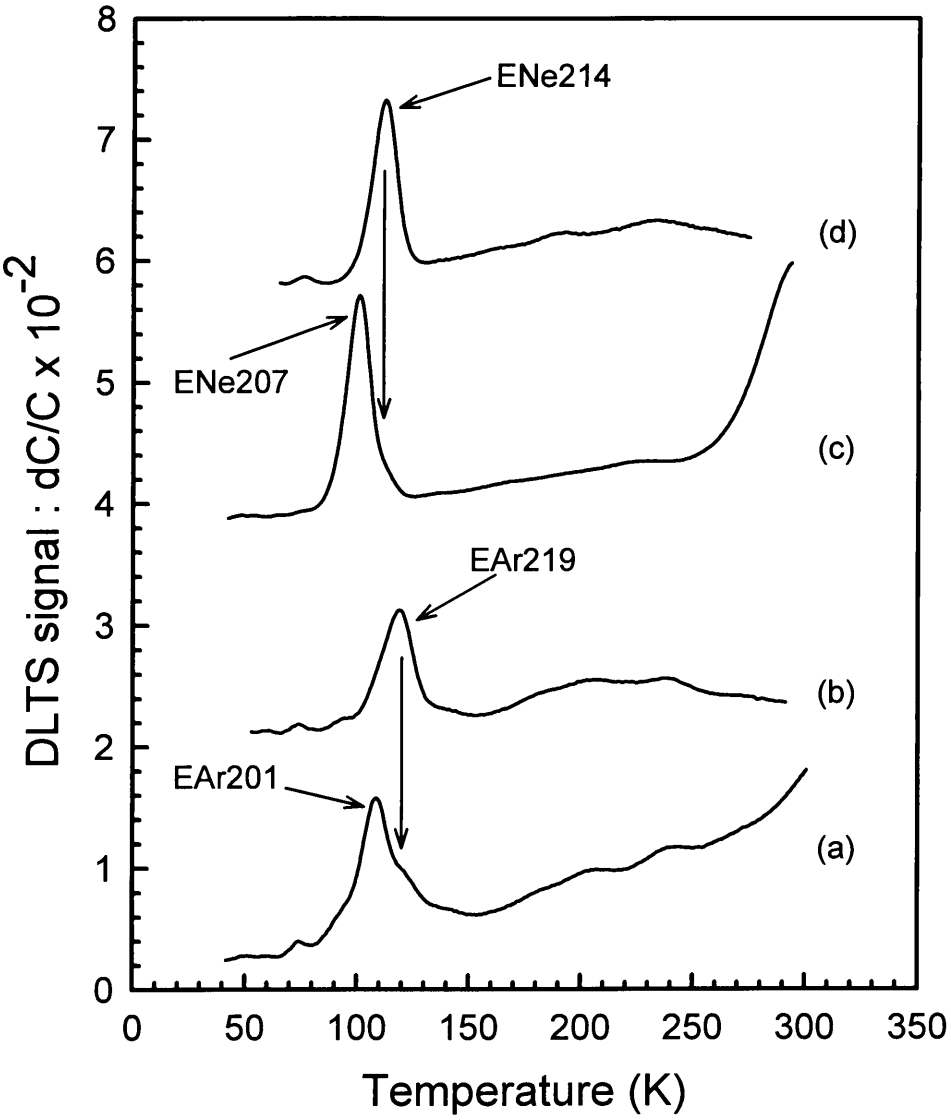

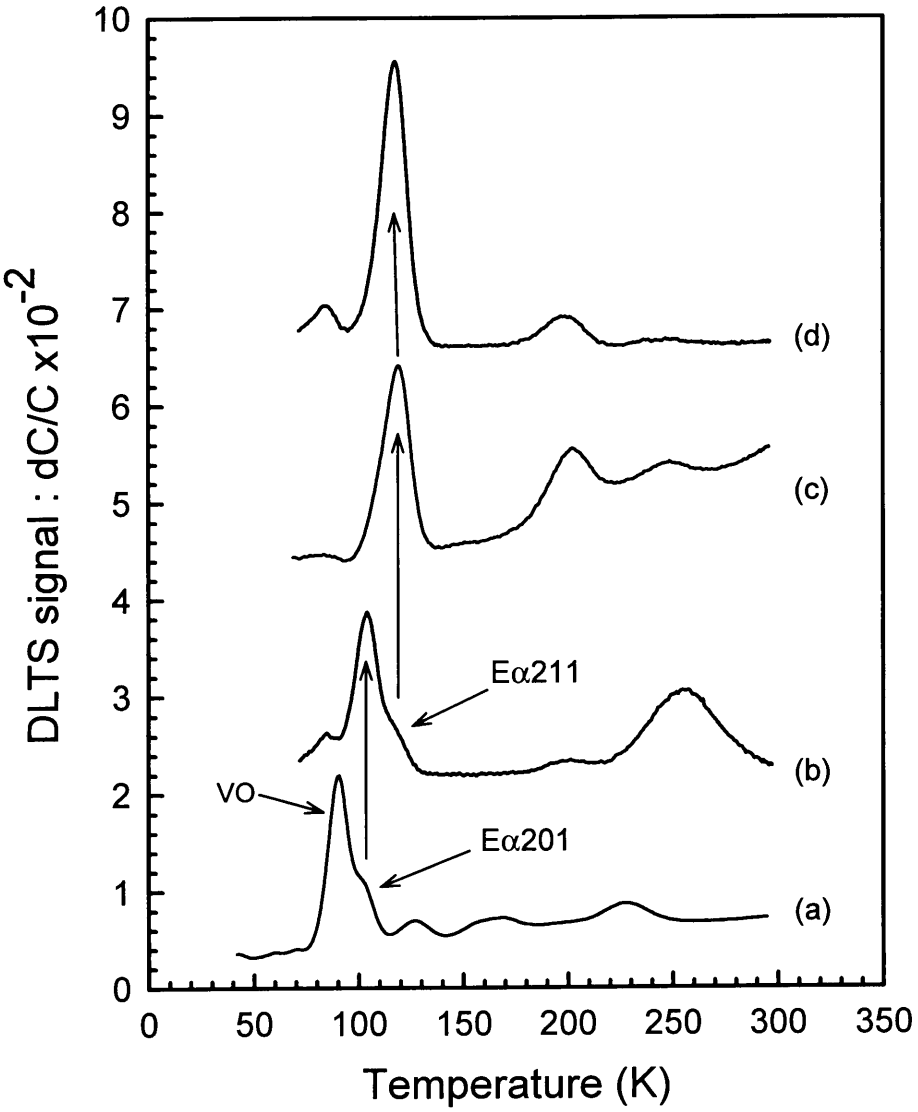

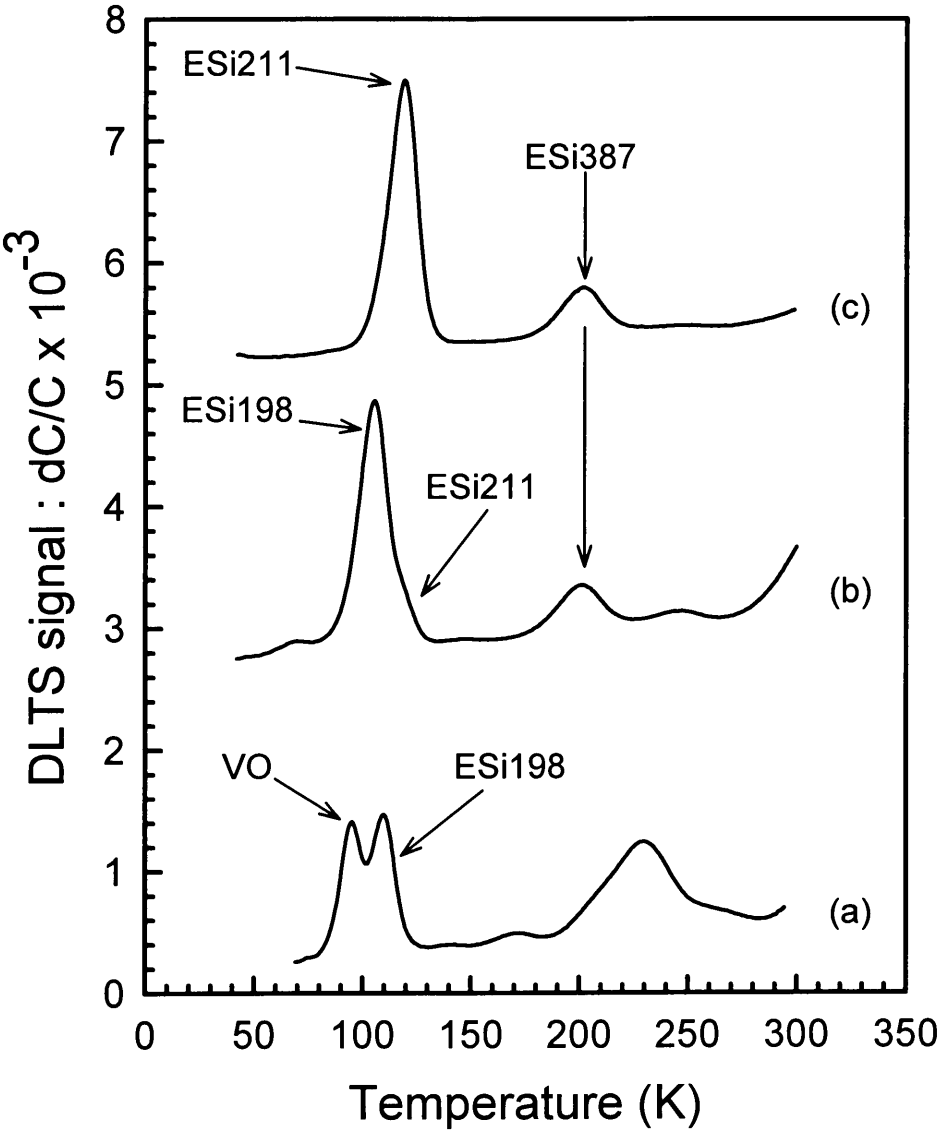

ELECTRICAL AND OPTICAL CHARACTERISATION OF DEFECTS INDUCED IN EPITAXIALLY GROWN n-Si DURING 1 keV NOBLE GAS ION BOMBARDMENT

P.N.K. Deenapanray, F.D. Auret, G. Myburg, W.E. Meyer and S.A. Goodman
Department of Physics, University of Pretoria, Pretoria 0002, South Africa

Keywords : photoluminescence, DLTS, C- and O-related defects, noble gas ion bombardment.

Abstract. The modification in the G-line (969.5 meV) and the C-line (789.4 meV) PL intensities were studied as a function of the fluence, energy and the mass of the bombarding ions (He, Ne, Ar and Kr). The intensities of the luminescent lines induced by 1 keV Ne bombardment were found to decrease with increasing dose, after reaching a maximum at about $1x10^{12}$ ions/cm^2. Considerable reductions in the intensities of the G- and C-lines were also recorded during bombardment using heavier noble gas ions. The incident ion energy at which the PL intensities of the spectral lines reached their maximum values were found to be dependent on the ion mass and fluence, and hence, on the nuclear energy deposited. The decrease in PL intensities of the G-line and C-line is explained in terms of the introduction of increased amounts of non-radiative recombination centres with increasing incident ion dose and mass.

Introduction

Low-energy noble gas ions are commonly used, for instance during ion beam etching (IBE), reactive ion etching (RIE) and sputter deposition. During these processes energetic ions create defects in the near-surface region of the exposed semiconductor. These defects can significantly alter the optical, electrical and structural properties of the material. The creation of a class of optically active noble gas (NG) related defects involving the intrinsic I_1 defect was previously reported after ion implantation and IBE using NG ions[1,2]. Besides two characteristic luminescent lines termed G (969.5 meV) and C (789.4 meV) are observed in silicon containing carbon and oxygen after dry etching using CF_4 reactive ion etching (RIE) [3] and IBE [2]. It is known that oxygen and carbon impurities play an important role in the creation of defects responsible for the G- and C-lines [4,5]. Furthermore, several studies have shown that the magnitude of G-line luminescence can be used as an accurate measure of the carbon content in Si crystals [2,6]. The G-line luminescence is attributed to an interstitial silicon atom Si_i located between two adjacent substitutional carbon atoms (C_s-Si_i-C_s) [7], while the C-line luminescence is caused by complexes composed of an interstitial carbon atom C_i and an interstitial oxygen atom O_i (C_i-O_i) [2]. The 969.5 meV PL defect has been identified with the EPR-detected G11 centre [8], whereas the 789.4 meV defect was identified as the EPR G15 centre [9].

The concentration and type of defects formed during irradiation depend on the fluence, energy and species of ions. Moreover, impurity-defect complexes are produced through the interaction between defects and impurities. It is, therefore, important to study the dependences of ion mass, dose and energy on the luminescent lines by noble gas ion implantation. In the present study, we investigated the effect of fluence, mass and energy of bombarding noble gas ions on the intensities of the G- and C-lines luminescence. The electrical properties of the low energy bombardment-induced defects have also been studied by deep level transient spectroscopy (DLTS).

Experimental procedure

Samples used were epitaxially grown (111) oriented Si layers on n^+-substrates and doped with $5x10^{15}$ cm^{-3} phosphorous. The epitaxial side of the samples were bombarded with 1 keV noble gas ions (He, Ne, Ar, Kr) at doses ranging from $1x10^{10}$ to $1x10^{15}$ ions/cm^2 using an ion gun. Photoluminescence measurements were carried out using the 514 nm line of an argon-ion laser, a 0.64 µm infra red monochromator (resolution 1.4 Å), a cooled germanium detector and conventional

lock-in amplifier technique. Samples were mounted in a closed cycle helium-cooled cryostat and the temperature could be varied between 11 K and 90 K. Circular Pd Schottky contacts of 0.77 mm diameter and 100 nm thickness were resistively deposited on the bombarded samples through a metal contact mask for DLTS analyses. The energy levels, E_T, and apparent capture cross-sections, σ_a, associated with the defects were determined from DLTS Arrhenius plots of $\log(e/T^2)$ vs $1/T$, where e is the emission rate at a temperature T. For control purposes, PL and DLTS measurements were taken using unirradiated Si samples.

Results and discussion

A. Dose dependence

Figure 1 shows the G-line and the C-line intensities after 1 keV Ne ion bombardment as a function of fluence from $5x10^{10}$ to $1x10^{14}$ ions/cm^2. It is found that the intensity of optically active defects increased with increasing Ne ion dose, and decreased after reaching a maximum at a fluence of $1x10^{12}$ ions/cm^2. A saturation in the intensity of the defects is expected at higher doses since the number of defects is limited by the concentration of carbon and oxygen atoms originally present in the Si crystals. We attribute the reduction in the PL intensities of the G- and C-lines for higher doses to the formation of non-radiative recombination centres with either discrete levels related to VO- and VP-pairs, divacancies, higher-order vacancy clusters or continuous levels related to extended defects in the band gap. Furthermore, complexes composed of vacancies and neon atoms [10,11] could also increase the number of optically inactive recombination centres for bombardment doses larger than $1x10^{12}$ ions/cm^2. The higher concentrations of defects at higher doses are due to the higher densities of collision cascades, and hence higher rates of nuclear energy deposition by the bombarding ions.

Now the presence of discrete and continuous levels in 1 keV Ne-bombarded Si is demonstrated. The electrically active defects introduced by He- and Ar-ion bombardment are discussed in the next section. Figure 2 shows the DLTS spectra obtained for n-Si after 1 keV Ne ion bombardments at doses ranging from $1x10^{12}$ and $1x10^{14}$ cm^{-2}. The VO-centre has an energy level at E_c - 0.183 eV and is labelled ENe183. In the nomenclature used, "E" denotes an electron trap, "Ne" implies the defect

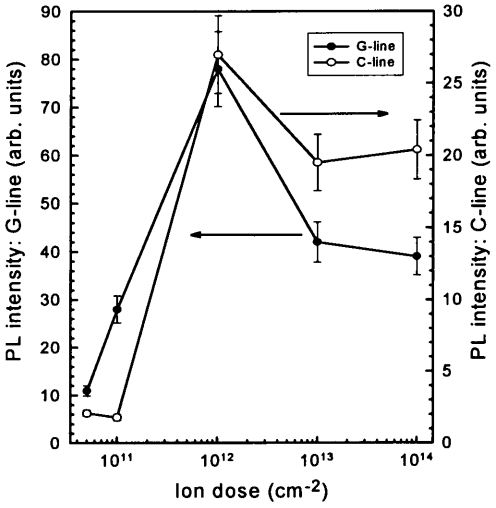

Fig. 1 Plot of PL intensities of the G- and C-line as a function of incident ion dose during 1 keV Ne ion bombardment of n-Si. Sample temperature was fixed at 11 K for the PL measurements.

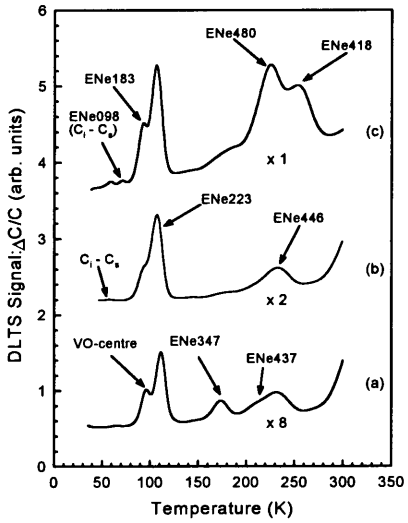

Fig. 2 DLTS spectra of 1 keV Ne-ion bombarded n-Si to fluences of: (a) $1x10^{12}$ cm^{-2}, (b)$1x10^{13}$ cm^{-2} and (c) $1x10^{14}$ cm^{-2}. All curves were recorded at a lock-in amplifier frequency of 46 Hz (decay time constant of 9.23 ms), V_r = 1 V and V_p = 1.4 V.

is introduced by Ne ions and the number gives the position of the level below the conduction band

in meV. The second charge state of the divacancy, $V_2^{-/0}$, could be observed in very low concentrations after removing the VP-centre (ENe437) by annealing at 180 °C for 30 min. The non-detection of the first charge state of the divacancy, $V_2^{=/-}$, may be attributed to the presence of stress fields in the highly perturbed region probed by DLTS [12]. The following comments can be made about the spectra to validate our discussion: Firstly, the intensities of the defect peaks (i.e., concentrations of defects) are found to increase with increasing ion dose. Secondly, a new prominent defect at E_c - 0.48 eV can be observed during bombardment at $1x10^{14}$ ions/cm^2. This defect, being close to the mid-bandgap position, could indeed be an efficient recombination centre [13]. Finally, it is clear from Fig. 2 that the baseline "skewing" of the DLTS spectra increases with increasing ion dose. The baseline "skewing" phenomenon has previously been observed in 5.4 MeV electron-irradiated GaAs and has been speculated to be due to the presence of extended defects [14]. Furthermore, the baseline "skewing" is accompanied by the broadening of some of the DLTS defect peaks such as ENe347 and those observed in the temperature range 200-280 K when the bombarding ion dose is increased. The peak broadening phenomenon is also indicative of the presence of extended defects [15].

The non-radiative defects result in an increased amount of existing or new recombination paths such that the recombination of electrons and holes between the levels responsible for the G- and C-lines is decreased. Consequently, the luminescence from the G-line and C-line defects is reduced when the irradiation dose exceeds the critical level of $1x10^{12}$ ions/cm^2.

B. Dependence on incident ion mass

Figure 3 shows the variation in the PL intensities of the G- and C-lines after 1 keV He, Ne, Ar and Kr ion bombardments. The nuclear energy deposited to recoils by each incident ion is also depicted in Fig. 3. All the low energy irradiation were done at a dose of $1x10^{12}$ ions/cm^2. The intensities of the two spectral lines were observed to decay almost exponentially with the mass of the bombarding ions. This mass dependence of the PL intensities is explained by considering the energy deposited by the different noble gas ions as they penetrate the Si lattice. Nuclear stopping is the dominant mechanism for energy transfer to the target during 1 keV He, Ne, Ar and Kr ion bombardments. As the mass of the incident ion is increased, the cross section for elastic collision is also increased. This results in a higher density of recoil atoms being produced and consequently a higher rate of energy deposition. For instance, TRIM [16] simulations reveal that the nuclear energy loss to the Si lattice increases with incident ion mass as shown in Fig. 3. Since the energy deposited by a 1 keV He ion is well above the critical value of the energy (~1 eV/Å) required for non-linear effects such as energy spikes [17] - one mechanism of forming extended defects - the amount of damage introduced to the Si lattice is expected to increase drastically with the mass of bombarding ions. The lowering in the PL intensities of the G- and C-lines can thus be explained by the introduction of increased amounts of non-radiative recombination centres with increasing incident ion mass. Since the energy deposited per unit length (eV/Å) of the incident ions

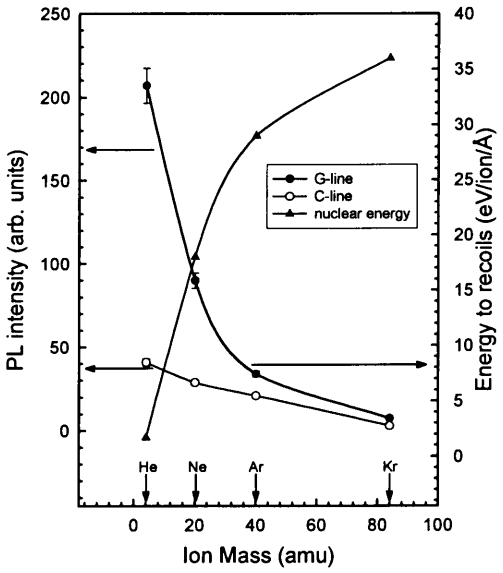

Fig. 3 Variation of PL intensities of the G- and C-lines as a function of bombarding ion mass. PL measurements were done on 1 keV He-, Ne-, Ar- and Kr-ion bombarded epitaxially grown n-Si to a dose of $1x10^{12}$ cm^{-2}. The nuclear energy deposited to recoils by the ions, as calculated from TRIM simulations, is also shown.

is much higher than the threshold for spike formation throughout their entire range, it is highly probable that non-radiative centres are produced in large concentrations during 1 keV bombardments using the noble gas ions.

DLTS measurements have shown that 1 keV He and Ne ion bombardment of Si at a dose of $1x10^{12}$ ions/cm^2 introduced the same set of defects [18]. However, the concentration of the defects were found to be relatively higher during Ne ion irradiation. On the other hand, a more complex set of defects was created in the same material during Ar [18] and Kr ion bombardments. We have also observed that, except for the VO- and VP-centres, the low energy defects created during noble gas ion irradiation are different from the primary defects introduced during high energy (MeV) electron and alpha-particle irradiation of the same wafer [19,20]. The presence of the first charge state, $V_2^{=/-}$, of the divacancy could not be observed in our low energy ion bombarded samples. However, annealing studies at 180 °C for 30 minutes have revealed the presence of the second charge state, $V_2^{-/0}$, of the divacancy produced by 1 keV noble gas ion bombardments, but in very low concentrations. We argue that $V_2^{=/-}$ could not be detected because of the presence of stress fields due to regions of high defect densities in our bombarded samples [12]. Furthermore, the low concentrations of $V_2^{-/0}$ in our samples could mean that vacancy clusters (larger than the divacancy) are predominantly formed during 1 keV noble gas ion bombardments. Low energy noble gas ion bombardment of epitaxially grown n-Si is found to introduce a class of defects similar to ENe223 (Fig. 2), the DLTS signal intensities of which increase with the mass of the bombarding ion. Based on isochronal annealing studies of both low energy noble gas ion and alpha-particle irradiated n-Si, and on epitaxial Si layers containing different O and C contents, we have proposed have that this class of defect is caused either by vacancy clusters larger than the V_2 but smaller than the hexavacancy (not electrically active) or the incorporation of the noble gas atoms into V_2 or highe-order vacancy clusters [21]. Thus our DLTS results agree with the TRIM simulation results presented above and can be used to confirm the propositions made to explain the reduction in PL intensities of the G- and C-lines with increasing bombarding ion mass. We have also noted significant baseline "skewing" of our DLTS spectra together with DLTS peak broadening during analysis of samples exposed to the heavier noble gas ions.

C. Dependence on ion energy

Figure 4 shows the PL intensities of the G- and C-lines as a function of incident ion energy for He ions at fluences of $1x10^{10}$ to $1x10^{12}$ ions/cm^2 . It is observed from Fig. 4 that the PL intensities of the G- and C-lines initially increase to maximum values and thereafter decrease. Figure 4 also suggests that the maxima are dose dependent. We explain our results by considering the energy dependence of the electronic and nuclear stopping of He ions in the Si crystal. In addition, we have considered the range of He ions with different bombarding energies together with the excitation depth of our Ar-ion laser. For any implanted ion, the nuclear stopping component of energy loss decreases as the energy of the ion is increased, whereas its electronic energy deposition increases [22]. The projected range and energy loss to recoils for He ions, as calculated from TRIM, in the energy range 1-150 keV are shown in Fig. 5.

For a given noble gas species the number of optically active defects increases with ion dose from a minimum as the energy of the incident ion is increased. It can be deduced from Fig. 5 that a 150 keV He ion will create much less energetic recoil atoms in the first 100 Å below the semiconductor surface compared to a 1 keV He ion. However, as the 150 keV ion loses energy and slows down as it penetrates further into the Si lattice, its nuclear stopping increases. As a result, the ion produces increasingly more energetic recoil atoms and, thus, introduces increasingly more damage in the semiconductor as it continues to slow down over its range of approximately 8200 Å. TRIM simulations also show that spike formation could occur when the energy of the ion is slightly less than 150 keV. Thompson and Walker [23] have shown that non-linear effects, such as the overlapping of individual collision cascades to produce higher density ones, can occur in ion

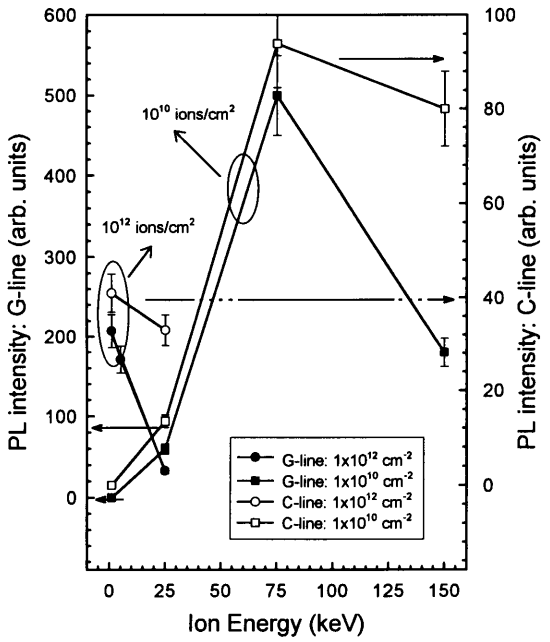

Fig.4 Influence of incident ion energy on the PL intensities of the G- and C-lines by He-ion bombardment of n-Si to doses of $1x10^{10}$ cm^{-2} and $1x10^{12}$ cm^{-2}.

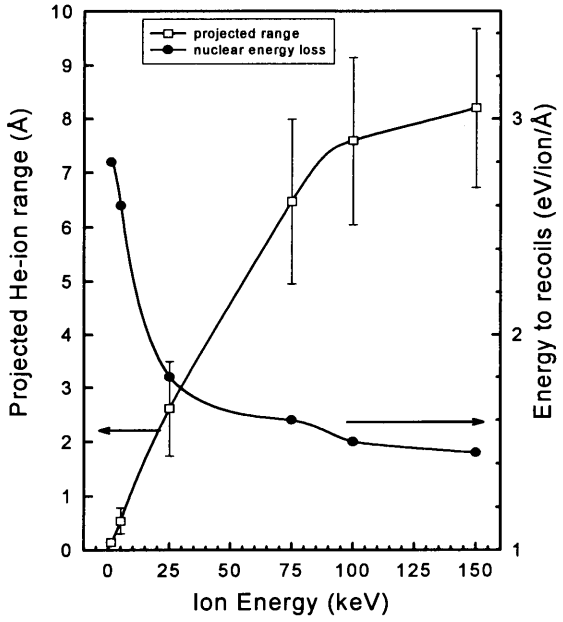

Fig. 5 TRIM simulations of projected range and nuclear energy deposited of He ions in Si for energies ranging from 1 keV to 150 keV. The error bars assigned to the projected ion range correspond to the longitudinal straggling.

bombarded Si when the average deposited energy density is as small as 0.1 eV/atom. The integral sum of defects distributed over the penetration depth of ~ $\lambda/2$ = 2570 Å of the Ar-ion laser will, therefore, be larger for the 150 keV ion than for the 1 keV ion. Consequently, the Ar-ion laser "sees" more non-radiative recombination centres when PL measurements are taken on a sample bombarded with 150 keV He ions.

For all implantation doses or noble gas ion that were used, we found that the number of optically active defects increases from a minimum as the energy of the incident ion is increased. The intensities of the two transitions start to decrease at specific ion energies, which are dose dependent, when the number of non-radiative recombination centres as discussed above provide alternative recombination paths to those responsible for the G- and C-spectral lines. For instance, the energy corresponding to maximum intensities of the G- and C-lines for a dose of $1x10^{10}$ He^+/cm^2 is about 75 keV (Fig. 4), after which the sum total of defects increases, causing a reduction in PL intensities. Since nuclear energy deposition increases with increasing bombarding ion dose, the temperature corresponding to the maximum PL intensities of the two lines is lower for an irradiation dose of $1x10^{12}$ He^+/cm^2 compared to $1x10^{10}$ He^+/cm^2. This dose dependence of the maximum is translated into a shift in the intensity curves in Fig. 4 to the left for the higher ion dose.

Conclusion

We have investigated the influence of noble gas ion species as well as their fluence and energy on the G-line and C-line luminescence in epitaxially grown n-Si. DLTS measurements of the electrical properties of the defects induced by 1 keV noble gas ion bombardment of the same material are also reported. Bombardments using 1 keV Ne ions in the dose range $1x10^{10}$ cm^{-2} to $1x10^{15}$ cm^{-2} have shown that the PL intensities of the G- and C-line luminescence increase to reach their maximum values at $1x10^{12}$ cm^{-2} and, thereafter, decrease with ion fluence. We have attributed the reduction in intensities beyond $1x10^{12}$ Ne^+cm^{-2} to be due to the introduction of higher concentrations of non-radiative recombination centres, which provide alternative recombination paths to those responsible for the G- and C-transitions. DLTS results have indeed shown that higher concentrations of defects are introduced when the ion fluence is increased for a particular noble gas species. A prominent new electron trap at E_c - 0.48 eV, which being close to the mid-bandgap position could well be an

efficient recombination centre, has been detected in $1x10^{15}$ $Ne^{+}cm^{-2}$ bombarded material. Furthermore, the baseline "skewing" and peak broadening phenomena observed in our DLTS spectra may suggest that extended defects, with a continuous distribution of deep levels in the bandgap, are introduced in our samples at irradiation doses higher than $1x10^{12}$ cm^{-2}. The PL intensities of the G- and C-lines were found to decrease almost exponentially with incident ion mass for 1 keV bombardments at $1x10^{12}$ cm^{-2}. The increasingly higher nuclear stopping component of energy deposited by the incident ions with higher mass results in larger amounts of damage to be created in the Si lattice. Consequently, the introduction of non-radiative recombination centres is increased resulting in a decrease in PL intensities of the luminescent lines. We have also observed an increase in the intensities of the prominent electrically active electron traps with increasing bombarding ion mass. Finally, we have demonstrated that the incident ion energy at which the PL intensities reach their maximum values is dose dependent. We have explained the observed trends qualitatively by considering the integral sum of defects produced over the excitation depth of the Ar-ion laser used in our PL experiments.

References

1. N. Burger, K. Thonke, R. Sauer and G. Pensl, Phys. Rev. Lett. **52**, 1645 (1984).
2. J. Weber and M. Singh, Appl. Phys. Lett. **49**, 1617 (1986).
3. R.J. Davis, H.-U. Habermeier and J. Weber, Appl. Phys. Lett. **47**, 1295 (1985).
4. J. Weber, R. J. Davis, H.-U. Habermeier, W. D. Sawyer and M. Singh, Appl. Phys. A **41**, 175 (1986).
5. W.D.Sawyer, J. Weber, G. Nabert, J. Schmalzlin and H.-U. Habermeier, J. Appl. Phys. **68**, 6179 (1990).
6. M. Nakamura, E. Kitamura, Y. Misawa, T. Suzuki, S. Nagai and H. Sunaga, J. Electrochem. Soc. **141**, 3576 (1994).
7. M. T. Assom, J. L. Benton, R, Sauer and L. C. Kimerling, Appl. Phys. Lett. **51**, 256 (1987).
8. K.L. Brower, Phys. Rev. B **9**, 2607 (1974).
9. G.D. Watkins, in *Radiation Damage in Semiconductors*, edited by P. Baruch (Dunod, Paris, 1965).
10. A.V. Mudryi, A.L. Puschkarchuk and A.G. Ul'yashin, Sov. Phys. Semicond. **19**, 225 (1985).
11. S.K. Estreicher, J. Weber, A. Derecskei-Kovacs and D.S. Marynick, Phys. Rev. B **55**, 5037 (1997).
12. B.G. Svensson, B. Mohadjeri, A. Allen, J.H. Svensson and J.W. Corbett, Phys. Rev. B **43**, 2292 (1991).
13. S.M. Sze, Physics of Semiconductor Devices (Wiley, New York, 1981), p. 37.
14. F.D. Auret, S.A. Goodman, R.M. Erasmus, W.E. Meyer and G. Myburg, Nucl. Inst. and Meth. B **106**, 323 (1995).
15. W. Schröter, J. Kronewitz,U. Gnauert, F. Riedel and M. Seibt, Phys. Rev. B **52**, 13 726 (1995).
16. J.F. Ziegler, J.P. Biersack and U. Littmark, "*The Stopping and Range of Ions in Solids*", vol. 1, ed. J.F. Ziegler (Pergamon Press, New York, 1985).
17. P. Sigmund, Appl. Phys. Lett. **25**, 164 (1974).
18. P.N.K. Deenapanray, N.E. Perret, F.D. Auret, G. Myburg and J.B. Malherbe, 1996 Conference on Optoelectronic and Microelectronic Materials and Devices Proceedings, (Ed. C. Jagadish) IEEE, Piscataway, NJ (USA) 1997.
19. S.D. Brotherton and P. Bradley, J. Appl. Phys. **53**, 5720 (1982).
20. J.R. Troxell, Solid-State Electronics **26**, 539 (1983).
21. P.N.K. Deenapanray, F.D. Auret, G. Myburg , J.B. Malherbe and M.C. Ridgway, unpublished.
22. J.A. Davies, MRS Bulletin **26** (June 1992).
23. D.A. Thompson and R.S. Walker, Rad. Effects **36**, 91 (1978).

CHAPTER 8

CONCLUSIONS

The optical and electrical properties of defects introduced in n-type silicon during various plasma processing techniques, as well as by low energy noble gas ion bombardment were investigated in this study. The effects of several chemical cleaning procedures on (111) oriented n-Si were also studied. Most of the results presented here have been presented at international conferences and have already been published. Process optimisation was achieved by monitoring the influence of plasma parameters, such as pressure and power, on the rectifying properties of Schottky diodes fabricated on the processed Si surfaces. The results presented in this study have provided and proposed new insights concerning defects properties, which will be invaluable in exploiting defect engineering to tailor the properties of semiconductors during plasma processing and ion beam etching of Si.

8.1 Plasma Processing

8.1.1 Sputter Deposition of TiW and Au

Sputter deposition of both TiW and Au contacts on n-Si introduced discrete level defects in the Si band gap. Although the VO-centre could be observed in both cases, no $V_2^{=/-}$ (first charge state of the divacancy) was introduced in detectable concentrations. The sputter deposited Schottky barriers had lower barrier heights, and hence poorer rectifying properties, compared to diodes fabricated by resistive evaporation. This result is in agreement with the generally proposed model that sputter deposition introduces donor-type defects at and close to the surface of the exposed Si substrate. Furthermore, the lowering in barrier was observed to increase with decreasing plasma pressure, suggesting that the barrier height of the deposited Schottky diodes can be tailored by varying the plasma pressure. The sputter-deposition-induced defects can be attributed to impurities (C and O) in the Si, and to point defects created by energetic metal and Ar atoms from the plasma impinging on the Si surface.

8.1.2 Sputter Etching

Sputter etching also introduced several deep levels in the Si band gap. It was found that some of the defects had similar electronic and annealing properties as those introduced during low energy Ar-ion bombardment of the same material. Our isochronal annealing experiments revealed that the VP-centre and $V_2^{-/0}$ (second charge state of the divacancy) were created in very low concentrations. The non-detection of $V_2^{=/-}$ has been attributed to its incomplete filling upon application of a forward pulse due to stress fields present in the region probed by DLTS. Discrete defect levels related to O and C were also created by the etch process. DLTS depth profiling showed that the concentration of defects produced below the semiconductor surface increased with decreasing plasma pressure. Pd Schottky diodes deposited on the etched surfaces by resistive evaporation became less rectifying with decreasing plasma pressure. These results showed that more damage was created at lower operating pressures, when the energy of the plasma particles reaching the surface increased.

The influence of etch time was found to be more severe for time periods less than 6 minutes. The sputter etching process is characterised by two competing processes, namely: (1) creation of damage close to the semiconductor surface and their in-diffusion, and (2) removal of the topmost damaged layers by physical sputtering. For relatively short etch times, the former effect is more dominant and the concentration of defects in the region probed by DLTS is larger. With increasing etch time up to 6 minutes, less residual damage is created below the surface and the diodes fabricated on the etched surfaces have, therefore, less degraded properties. The poor quality of diodes for etch times larger than 6 minutes has been attributed to the presence of structural changes, such as surface amorphization or the introduction of extended defects. We are currently conducting experiments to elucidate this observation.

Isochronal annealing experiments showed that most of the defects created by sputter etching could be removed by annealing above 500 °C. However, a prominent secondary defect is observed to emerge in this temperature range and was found to be thermally stable at 650 °C. These results have, therefore, demonstrated that sputter etching

adversely affected the material properties of etched n-Si and that annealing above 650 °C is required to remove all the defects. Low-temperature C-V measurements also showed that sputter etching introduced both donor- and acceptor-type defects in the Si matrix. The donor-type defects were found close to the metal-semiconductor interface, whereas the acceptor-type defects caused free carrier compensation to depths larger than the projected range of the low-energy Ar ions in the plasma. These donor-type defects caused degradation in the diode properties mentioned above. Furthermore, we have employed I-DLTS to demonstrate the presence of a shallow level in the sputter etched n-Si samples.

8.2 Low Energy (1 keV) Noble Gas Ion (NGI) Bombardments

1 keV He- and Ne-ion bombardment of n-Si introduced a similar set of defects, but with the latter ions creating a higher concentration of defects. On the other hand, Ar-ion bombarded n-Si contained a more complex set of defects. The low energy noble gas ion bombardment introduced the VP- and $V_2^{-/0}$-centres in very low concentrations, and the $V_2^{=/-}$ could not be observed in these samples. The well known C- and O-related defects could be observed in noble gas ion bombarded n-Si. We have also observed that different defects are created in Si containing "no" or little oxygen by 1 keV He-ion bombardment. These results have demonstrated that these low energy noble gas ions create predominantly defects related to vacancy clusters larger than the divacancy or complexes thereof. We plan to conduct hydrogen irradiations to establish whether some of the defects detected in our processed samples could be hydrogen-related. We have also established that one defect introduced during He-, Ne- and Ar-ion bombardment to be intrinsic in nature. This defect has, within the experimental error or DLTS, the same electronic property in all the low energy noble gas ion-bombarded samples. In addition, the annealing property of the defect is the same irrespective of noble gas species used. We have proposed this defect (EHe203, ENe207 and EAr201) to be a vacancy cluster larger than the divacancy but smaller than the hexavacancy. This defect anneals into a more stable defect complex associated with larger vacancy clusters above 450 °C and is stable at 650 °C.

The modification in the G-line (969.5 meV) and the C-line (789.4 meV) PL intensities were studied as a function of the fluence, energy and the mass of the bombarding ions (He, Ne, Ar and Kr). The intensities of the luminescent lines induced by 1 keV Ne bombardment

were found to decrease with increasing dose, after reaching a maximum at about $1x10^{12}$ ions/cm^2. Considerable reductions in the intensities of the G- and C-lines were also recorded during bombardment using heavier noble gas ions and these have been attributed to the higher rates of nuclear energy deposition with increasing bombarding ion mass. The incident ion energy at which the PL intensities of the spectral lines reached their maximum values were found to be dependent on the ion mass and fluence. We have explained the decrease in PL intensities of the G-line and C-line to be due to the introduction of increased amounts of non-radiative recombination centres with increasing incident ion dose and mass. Further, the integral sum of defects induced during bombardment as a function of projected ion range and excitation depth of the Ar-ion laser has been used to qualitatively describe the decrease in the intensities of the two lines.

8.3 Effect of Cleaning Procedures on the Quality of Schottky Diodes

We have used atomic force microscopy (AFM) in conjunction with I-V and C-V measurements of Pd/n-Si diodes to evaluate various cleaning procedures on Si(111). We showed that near-atomically flat surfaces ($R_{rms} \approx 1$ Å) could be obtained starting with a surface with an average roughness of 17 Å. Diodes fabricated on surfaces with roughness larger than 5 Å had poorer electrical properties compared to those fabricated on surfaces with $R_{rms} < 3$ Å. For instance, diodes corresponding to $R_{rms} \approx 16$ Å had reverse currents 20 times larger than those fabricated on a surface with $R_{rms} \approx 1$ Å. Cleaning procedures which produced near-atomically flat surfaces yielded near-ideal diodes with $n < 1.05$ and I-V barrier heights between 0.75 eV and 0.76 eV. However, cleaning procedures producing equally smooth surfaces did not yield diodes with similar electrical properties, and we have attributed this to the different densities of interfacial states introduced by the chemical procedures. We have unambiguously showed that the free carrier density can be grossly over-estimated when the surface roughness exceeds 10 Å. Buffered HF solutions used for native oxide removal produced smoother surfaces on Si(111) than diluted HF solutions, and including a heavy metal etch step yielded diodes with marginally poorer electrical characteristics.